Manager
M. J. E. Mattingly
M. C. Davis-JES 11-7

DOE/ER-0046/1

Damage Analysis and Fundamental Studies

Quarterly Progress Report
January - March 1980

May 1980

U.S. Department of Energy
Assistant Secretary for Energy Technology
Office of Fusion Energy

NOTICE

This report was prepared as an account of work sponsored by the United States Government. Neither the United States nor the U.S. DOE, nor any of its employes, nor any of its contractors, subcontractors or their employes, makes any warranty, expressed or implied, or assumes any legal liability or responsibility for any third party's use or the results of such use of any information, apparatus, product or process disclosed in this report, or represent that its use by such third party would not infringe privately owned rights.

Printed in the United States of America
Available from
National Technical Information Service
U.S. Department of Commerce
5285 Port Royal Road
Springfield, VA 22161

NTIS price codes
Printed copy: A12
Microfiche copy: A01

DOE/ER-0046/1
UC-20,20c

Damage Analysis and Fundamental Studies

Quarterly Progress Report
January - March 1980

May *1980*

U.S. Department of Energy
Assistant Secretary for Energy Technology
Office of Fusion Energy
Washington, D.C. 20545

FOREWORD

This report is the ninth in a series of Quarterly Technical Progress Reports on *"Damage Analysis and Fundamental Studies"* (DAFS) which is one element of the Fusion Reactor Materials Program, conducted in support of the Magnetic Fusion Energy Program of the U. S. Department of Energy. The first eight reports in this series were numbered DOE/ET-0065/1 through 8. Other elements of the Materials Program are:

- Alloy Development for Irradiation Performance (ADIP)
- Plasma-Materials Interaction (PMI)
- Special Purpose Materials (SPM).

The DAFS program element is a national effort composed of contributions from a number of National Laboratories and other government laboratories, universities, and industrial laboratories. It was organized by the Materials and Radiation Effects Branch, Office of Fusion Energy, DOE, and a Task Group on *Damage Analysis and Fundamental Studies* which operates under the auspices of that Branch. The purpose of this series of reports is to provide a working technical record of that effort for the use of the program participants, for the fusion energy program in general, and for the Department of Energy.

This report is organized along topical lines in parallel to a Program Plan of the same title so that activities and accomplishments may be followed readily, relative to that Program Plan. Thus, the work of a given laboratory may appear throughout the report. The Table of Contents is annotated for the convenience of the reader.

This report has been compiled and edited under the guidance of the Chairman of the Task Group on *Damage Analysis and Fundamental Studies,* D. G. Doran, Hanford Engineering Development Laboratory. His efforts and those of the supporting staff of HEDL and the many persons who made technical contributions are gratefully acknowledged. M. M. Cohen, Materials and Radiation Effects Branch, is the Department of Energy counterpart to the Task Group Chairman and has responsibility for the DAFS Program within DOE.

Klaus M. Zwilsky, Chief
Materials and Radiation
Effects Branch
Office of Fusion Energy

CONTENTS

Page

Foreword
Figures
Tables

CHAPTER 1. IRRADIATION TEST FACILITIES

1. Rotating Target Neutron Source (RTNS)-II (LLL) 3

Operation of the RTNS-11 was generally routine during the quarter. The correction of a rotating seal problem resulted in improved performance.

2. Fusion Materials Irradiation Test (FMIT) Facility (HEDL) 5

Deuteron-induced activation measurements were made on Cu, Ta, Au, and Pb.

Analysis has begun of transmission measurements of D-Li neutrons through a thick iron block.

A computer code, PRECO-D, was written to calculate angular distribution and statistical direct effects in a pre-equilibrium model of nuclear reactions.

Unperturbed neutron fluxes have been calculated for the FMIT test cell with the new microscopic d+Li neutron yield model; results are stored at the Magnetic Fusion Energy Computer Center (MFECC).

The FMIT Activation Library has been expanded and is in use for design needs.

CONTENTS (Cont'd)

Page

CHAPTER 2. DOSIMETRY AND DAMAGE PARAMETERS

1. Fission Reactor Dosimetry (ANL) 23

Helium measurements and calculations are summarized for ORR-MFE 1. Nickel two-step thermal flux calculations agree very well with the data, but titanium cross sections are seriously in error. The status of the ORR-MFE 2 and MFE 4 irradiations is presented.

Dosimetry in HFIR will be initiated with HFIR-CTR 30, 31, and 32 irradiations.

Spectral measurements are being prepared for the Omega West Reactor at LASL.

2. Helium Accumulation Neutron Dosimetry for Mixed-Spectrum Reactor Irradiations (RIES) 28

Sets of bare and platinum-encapsulated pure-element helium accumulation neutron dosimetry materials were prepared for the ORR MFE-4B irradiation, and the HFIR irradiations HFIR-CTR 30, 31, and 32.

3. Characterization of the Be(d,n) Source at U.C. Davis (ANL) 30

The joint ANL, LLL, and RIES characterization of the U.C. Davis source {Be(d,n) E_d = 30 MeV} has been completed. Fluence, damage and helium contour plots are presented based on the radiometric data. Comparisons are now being made with more detailed helium measurements by RIES.

CONTENTS (Cont'd)

Page

4. Helium Accumulation Neutron Dosimetry for the T(d,n) and Be(d,n) Neutron Irradiation Environments (RIES) 36

The helium analyses were completed for the helium accumulation neutron dosimetry materials irradiated in T(d,n) and Be(d,n) neutron environments. Analysis procedures were developed which increase the mass spectrometer system sensitivity about an order of magnitude. Comparisons between the detailed T(d,n) helium data and an initial T(d,n) neutron fluence map, generated from radiometric counting data, showed that large (~10%-20%) fluence variations can exist that are not readily discernible from the radiometric data.

5. Dosimetry Standardization (ANL) 39

The activation dosimetry cross section and cross section error files have been revised according to ENDF/B-V. All previous integral data testing is being redone to evaluate the new files; however, the changes in the nuclear data will have the most impact on fission reactor dosimetry.

6. Evaluation of Ionization-Assisted Displacements in Carbon and Al_2O_3 (BNL) 41

Ionization-assisted displacement processes involving L shell ionization of atoms by primary knock-on atoms produced during neutron irradiation of carbon and Al_2O_3 have been evaluated for a benchmark and a FMIT spectrum.

CONTENTS (Cont'd)

Page

7. Studies of Low Energy Displacement Cascades in the Binary Collision Approximation (ORNL) 55

Anomalous behavior of low energy cascades in a static lattice simulated with MARLOWE is removed by including thermal displacements in the calculations.

8. Modeling of Defect Production in High Energy Cascades in FCC Metals (HEDL) 62

Cascades generated with MARLOWE using a high displacement energy, and temperature corrected (annealed) with SCAS, are calibrated by comparison with cascades calculated with low displacement energies.

9. RTNS-II Irradiation Program (HEDL) 69

Hardening data are given for Cu. Ni, and an Fe-Ni-Cr ternary irradiated at RTNS-11 to 3 x 10^{17} n/cm^2. A high exposure elevated temperature irradiation is being prepared.

10. Microstructural Development in Copper Irradiated in RTNS-II (HEDL) 77

High purity copper irradiated at 25°C to 2.7 x 10^{17} n/cm^2 at RTNS-11 exhibits a high density of small defect clusters of both interstitial and vacancy type. Comparisons are made with calculated defect densities and with hardness measurements.

CONTENTS (Cont'd)

Page

CHAPTER 3. FUNDAMENTAL MECHANICAL BEHAVIOR

1. Segregation and Embrittlement in Cr-Mo Steels (PNL) 96

The susceptibility of 2 ¼ to 12 Cr, 1 Mo ferritic alloy steels to grain boundary chemistry induced embrittlement is reviewed. Phosphorus enrichment at grain boundaries is likely to occur as a result of equilibrium (thermal) segregation. However, radiation-induced segregation may dramatically shift both the elements which segregate and the resistance of ferritic alloy steels to intergranular failure.

2. Effects of Near Surface Damage and Helium on First Wall Performance (MIT) 110

Pressurized capsules of 316 SS were irradiated in the MITR-11 reactor under temperature and stress cycling for 9 weeks. Interim examination revealed a small amount of creep and some unexplained oxidation. A capsule failure was successfully detected.

CHAPTER 4. CORRELATION METHODOLOGY

1. Development of Fission-Fusion Correlations (HEDL) 119

Correlations are being developed for swelling, creep, and yield stress of AISI 316 stainless steel for application to ETF.

CONTENTS (Cont'd)

Page

2. Dissolution of Particles Due to Radiation Recoil (MIT) 133

The stability of a dispersion of stable particles may be affected by resolution due to radiation recoil. A simple model of the diffusion of the solute that recoils into the matrix allows an estimate of when this process will dominate over the normal thermal coarsening.

3. Development of Microstructural Evolution Models (HEDL) 149

The status of modeling of loop nucleation, network dislocation generation, and compositional effects on sink biases is outlined briefly. A discrepancy between predictions of the influence of solute elements on void nucleation is discussed in terms of the role played by bound vacancies.

4. Analysis of Radiation-Induced Microchemical Evolution in 300 Series Stainless Steels (HEDL) 158

Scanning transmission electron microscopy and energy dispersive X-ray analysis have revealed microchemical evolution to be a primary determinant of the swelling and creep response of these alloys. Analysis techniques are described in detail.

5A. The Use of Temperature Change Experiments to Determine the Maximum Equilibrium Bubble Size in 316 SS (W-R&D) 183

Estimates of critical cavity size (r_c) for bias-driven growth obtained from temperature-change experiments are in good agreement with helium inventory measurements of r_c.

CONTENTS (Cont'd)

Page

5B. Preliminary Numerical Analysis of the Temperature Dependence of Cavity and Dislocation Loop Formation in Aged 316 SS (WL - R&D) 185

A bubble growth regime at 600°C leads to double peak in temperature dependence of swelling. Cavity and interstitial dislocation loop growth rates dominate microstructural evolution; they are postulated to reflect changes in austenite matrix composition and helium partitioning to sinks.

6. Dose and Helium Injection Dependence of Swelling in Single and Dual-Ion Irradiated 316 Stainless Steel (ANL) 198

The dose and helium injection rate dependence of void swelling in 316 stainless steel irradiated simultaneously with Ni^+ and He^+ ions is compared to a parallel experiment on He preinjected and Ni^+ ion irradiated material. For dual-ion irradiation, the size and number density of small cavities in a bimodal cavity size distribution did not appear to be strongly dose dependent, but the number density increased rapidly with increasing helium injection rate. For the large size cavities (formed preferentially on precipitates), the number density remained fairly constant with dose but the size increased rapidly with dose producing rapid increases in volume swelling. The preinjected samples exhibited the lowest swelling at all doses investigated.

CONTENTS (Cont'd)

7. Characterization of Rapidly Solidified Boron Doped Stainless Steel for Synergistic Helium Production (MIT) 213

Two type 316 stainless steels with different amounts of boron and zirconium were rapidly solidified and thermochemically treated, and microstructurally characterized by means of transmission and scanning transmission electron microscopy, energy dispersive X-ray and electron energy loss spectroscopy and neutron autoradiography.

8. Determination of Helium Influence on Microstructural Development: Two Experimental Methods (HEDL) 224

Additional analysis is given of the "helium-halo" technique. Electron microscopy of the inner surface of helium pressurized tubes used in irradiation creep studies is proposed.

9. Status of the DAFS Specimens in the AD-1 Irradiation Test (NRL/HEDL) 238

One capsule containing ADIP titanium alloy specimens was opened and the specimens showed evidence of corrosion. The opening of the remaining two capsules was therefore delayed.

10. DAFS Specimen Matrix for the ORR MFE-IV Test (HEDL) 243

DAFS specimen in the ORR MFE-IV experiment include TEM and tensile specimens of several Fe-Ni-Cr ternaries and TEM specimens of ADIP Path B alloys.

CONTENTS (Cont'd)

Page

11. Path A and Path B Model Alloys (HEDL) 246

Round bar stock (1.31 in.) should be available in May 1980, of two model Path A alloys and four model Path B alloys for use in the DAFS program.

FIGURES

Page

CHAPTER 1

2. Fusion Materials Irradiation Test (FMIT) Facility (HEDL)

FIGURE 1. Thick target production rate deuterons on copper. a

FIGURE 2. Thick target production rate deuterons on tantalum. 9

FIGURE 3. Thick target production rate deuterons on gold. 10

FIGURE 4. Thick target production rate deuterons on lead. 11

FIGURE 5. Comparison between model and U.C. Davis-HEDL experiment. 15

FIGURE 6. Relationship between flux and volume. 16

CHAPTER 2

3. Characterization of the Be(d,n) Source at U.C. Davis (ANL)

FIGURE 1. Fluence contours (>1 MeV) are shown for the Be(d,n) source at U. C. Davis at E = 30 MeV. 31

FIGURE 2. Displacement-per-atom contours for copper are shown for the U. C. Davis Source [Be(d,n), E_d = 30 MeV]. 32

FIGURE 3. Helium production contours are shown for copper for the U. C. Davis Source [Be(d,n), E_d = 30 MeV]. 33

6. Evaluation of Ionization-Assisted Displacements in Carbon and Al_2O_3 (BNL)

FIGURE 1. Energy dependence of the Lindhard function L(T) and the ionization-assisted damage function L'(T). 52

FIGURE 2. Neutron spectra used to evaluate ionization-assisted damage. 53

FIGURES (Cont'd)

Page

7. Studies of Low Energy Displacement Cascades in the Binary Collision Approximation (ORNL)

FIGURE 1. The mean number of distant Frenkel pairs produced by Cu atoms recoiling in Cu. 57

FIGURE 2. The scaled variance of the number of distant Frenkel pairs produced by Cu atoms recoiling in Cu. 59

9. RTNS-II Irradiation Program (HEDL)

FIGURE 1. Normalized diamond pyramid microhardness, 50 gm load, for copper TEM disk specimens, irradiated with 14 MeV neutrons at ambient temperature. 70

FIGURE 2. Normalized diamond pyramid microhardness, 50 gm load, for nickel TEM disk specimens, irradiated with 14 MeV neutrons at ambient temperature. 71

FIGURE 3. Normalized diamond pyramid microhardness, 50 gm load for Fe-Ni-Cr ternary TEM disk specimens, irradiated with 14 MeV neutrons at ambient temperature. 72

10. Microstructural Development in Copper Irradiated in RTNS-II (HEDL)

FIGURE 1. (g,3g), g = 004, weak beam dark-field stereo micrographs showing defect clusters formed in high purity copper irradiated with 14 MeV (d,T) neutrons to a fluence of 2.7 x 10^{17} n/cm^2 at 25°C. (Negative nos. 3792 and 3803) 79

FIGURE 2. Histogram illustrating the size and frequency of defect clusters which form in the metal shown in Figure 1. 80

FIGURE 3. Dark-fie1d micrograph showing black/white contrast of defect clusters formed in the metal shown in Figure 1. 82

FIGURES (Cont'd)

Page

FIGURE 4. The increase in yield strength measured by Mitchell et al. for two heats of copper irradiated by 14 MeV (d,T) neutrons and shown on the figure as open and filled circles. 87

CHAPTER 3

1. Segregation and Embrittlement in Cr-Mo Steels (PNL)

FIGURE 1. Experimental data as compiled by Seah & Hondros showing that the enrichment of solute elements can be predicted by a linear correlation with the inverse solid solubility. 106

FIGURE 2. Data of Kaneko et al. illustrating the effect of chromium content on the solubility of phosphorus at 1000°C. 107

2. Effects of Near Surface Damage and Helium on First Wall Performance (MIT)

FIGURE 1. Details of Irradiation Unit: The SS 316 test specimens (He/Ar pressurized capsules) are held by a titanium frame which is screwed into a titanium can. 114

FIGURE 2. Typical examples of the time dependent temperatures and stresses for the pressurized tube specimens. 115

CHAPTER 4

1. Development of Fission-Fusion Correlations (HEOL)

FIGURE 1. Schematic illustration of the various phase regimes and their impact on the swelling of AISI 316. 122

FIGURES (Cont'd)

Page

FIGURE 2. Schematic illustration of the changes required in AISI 316 swelling correlation in order to apply it in ETF. 123

FIGURE 3. Outline of plan of action to develop swelling and creep correlations for ETF operations. 126

FIGURE 4. Schematic illustration of approach used to develop a microstructurally-based correlation for yield stress. The current status of the effort is also shown. 128

FIGURE 5. Yield stress of 20% cold-worked type 316 stainless steel after irradiation in EBR-II. 130

FIGURE 6. Yield stress of AISI 316 in two starting conditions after irradiation to 427°C and 538°C. 131

2. Dissolution of Particles Due to Radiation Recoil (MIT)

FIGURE 1. Concentration of oxygen from steady-state recoil resolution compared to the concentration in equilibrium with particles without irradiation, for Al_2O_3 in stainless steel. 138

FIGURE 2. Concentration of carbon from steady-state recoil resolution compared to the concentration in equilibrium with particles without irradiation, for TiC in stainless steel. 138

FIGURE 3. Concentrations versus radius for various times from a time dependent recoil resolution calculation. 141

FIGURE 4. Time it takes Dt to reach certain distances versus inverse temperature (for oxygen diffusion in austenite). 142

FIGURE 5. Time it takes to reach steady-state recoil resolution, shown on axes of particle spacing and inverse temperature. 142

FIGURE 6. Fraction of particles dissolved (or reprecipitated) when steady-state is reached, versus inverse temperature. 144

FIGURES (Cont'd)

Page

FIGURE 7. Predictions of whether thermal coarsening or recoil resolution will dominate for Al_2O_3 and TiC in stainless steel. 145

FIGURE 8. Concentration profiles at various times for a spherical particle diffusing into a spherical matrix cell. 144

4. Analysis of Radiation-Induced Microchemical Evolution in 300 Series Stainless Steels (HEDL)

FIGURE 1. Cross section and location of fixed tungsten collimator. 160

FIGURE 2. Cross section of modified specimen holder showing location in specimen holder assembly and its relationship to the collimator-detector assembly. 161

FIGURE 3. Typical microstructures observed in irradiated AISI 316 at 600°C. 162

FIGURE 4. Schematic illustration of microanalysis techniques employed by this study. 164

FIGURE 5. Schematic representation of idealized determination of line-of-sight concentration profile and its relationship to actual profile. 165

FIGURE 6. Typical line-of-sight profile measured at void surfaces in 20% AISI 316 irradiated to 1.0 x 10^{23} n/cm^2 (E>0.1 MeV) at 650°C. 166

FIGURE 7. Line-of-sight measurement of elemental profiles in the vicinity of a grain boundary in annealed AISI 316 at 520°C and 9 x 10^{22} n/cm^2 (E>0.1 MeV). 167

FIGURE 8. Determination of composition and crystal structure of G-phase found in irradiated 20% cold worked AISI 316 using the edge-foil analysis. 169

FIGURE 9. Coexistence of two precipitate phases, both rich in nickel and silicon, in one grain of 20% cold worked AISI 316 irradiated at 500°C to a fluence of 1.4 x 10^{23} n/cm^2 (E>0.1 MeV). 170

FIGURES (Cont'd)

FIGURE 10. Concentration profiles of nickel, molybdenum and silicon observed near the surface of three laves precipitate particles in 20% cold worked AISI 316 irradiated at 650°C to a fluence of 1.0 x 10^{23} n/cm^2 (E>0.1 MeV). 172

FIGURE 11. Concentration profiles of nickel, molybdenum and silicon observed near the surface of two laves precipitates in 20% cold worked AISI 316 irradiated at 650°C to a fluence of 1.4 x 10^{23} n/cm^2 (E>0.1 MeV) 173

FIGURE 12. Local-spot determinations of elemental concentrations in many regions in 20% cold worked AISI 316 irradiated at 650°C to a fluence of 1.0 x 10^{22} n/cm^2 (E>0.1 MeV). 175

FIGURE 13. Distribution of nickel content at different locations in irradiated AISI 316 specimens irradiated at 650°C to a fluence of 1.0 x 10^{23} n/cm^2 (E>0.1 MeV). 176

5A. The Use of Temperature Change Experiments to Determine the Maximum Equilibrium Bubble Size in 316 SS (W-RPO)

FIGURE 1. Schematic representation of the helium inventory method used to estimate the maximum equilibrium bubble size from measured cavity size distributions. 190

FIGURE 2. Schematic representation of the determination of the critical cavity size (r_c) by increasing the target temperature during dual-ion bombardment. 191

FIGURE 3. Comparison of the temperature dependence of the critical cavity size for dual-ion bombarded S.A. 316 and 20% C.R. 316 from (1) helium inventory method, (2) theory and (3) temperature change experiment. 192

FIGURES (Cont'd)

Page

5B. Preliminary Numerical Analysis of the Temperature Dependence of Cavity and Dislocation Loop Formation in Aged 316 SS (W-R&D)

FIGURE 4. Cavity size distributions in aged 316 SS (800°C - 10 h) after dual-ion bombardment at temperatures from 550-700°C to fluences of 8-16 dpa. 193

FIGURE 5. Temperature dependence of the mean cavity diameter and mean dislocation loop diameter in dual-ion bombarded, aged (800°C - 10 h) 316 SS. 194

FIGURE 6. Variation of cavity number density, loop number density and total dislocation density with temperature for dual-ion bombarded, aged (800°C - 10 h) 316 SS. 195

FIGURE 7. Variation of dislocation loop number density and total dislocation density with temperature for dual-ion bombarded S.A. 316 SS and 20% C.R. 316 SS. 196

6. Dose and Helium Injection Dependence of Swelling in Single and Dual-Ion Irradiated 316 Stainless Steel (ANL)

FIGURE 1. Absorption contrast micrographs of 316 stainless steel dual-ion irradiated at a nominal temperature of 625°C toanominal dose of 6 dpa at different helium injection rates. 204

FIGURE 2. Absorption contrast micrographs of 316 stainless steel dual-ion irradiated at a nominal temperature of 625°C to a nominal dose of 12 dpa. 205

FIGURE 3. Absorption contrast micrographs of 316 stainless steel dual-ion irradiated at a nominal temperature of 625°C to a nominal dose of 25 dpa. 206

FIGURE 4. Dose dependence of swelling in preinjected single-ion and dual-ion irradiated 316 stainless steel. 207

FIGURES (Cont'd)

Page

FIGURE 5. Dose dependence of cavity size in preinjected single-ion and dual-ion irradiated 316 stainless steel. 208

FIGURE 6. Dose dependence of cavity number density in pre-injected single-ion and dual-ion irradiated 316 stainless steel. 209

FIGURE 7. Acicular precipitates in a 316 stainless steel sample dual-ion irradiated to a 3 dpa dose at 610°C with 5:1 appm He:dpa. 210

FIGURE 8. Acicular precipitates in a 316 stainless steel sample dual-ion irradiated to an 8 dpa dose at 621°C with 5:1 appm He:dpa. 211

7. Characterization of Rapidly Solidified Boron Doped Stainless Steel for Synergistic Helium Production (MIT)

FIGURE 1. TEM micrograph of alloy I showing small intra-granular particles and a large grain boundary precipitate. 216

FIGURE 2a. STEM micrograph of alloy I. 217

FIGURE 2b. EELS spectrum from the particles in Figure 2a. 217

FIGURE 2c. EDXS spectrum from the particles in Figure 2a. 217

FIGURE 3a. STEM micrograph of a boron containing particle from alloy I. 218

FIGURE 3b. EELS spectrum from the particle in Figure 3a. 218

FIGURE 3c. EDXS spectrum from the particle in Figure 3a. 218

FIGURE 4a. STEM micrograph of alloy I showing a large spherical particle. 221

FIGURE 4b. EDXS spectrum obtained from the large particle in Figure 4a. 221

FIGURES (Cont'd)

		Page
FIGURE 5.	TEM micrograph of alloy II showing interdendritic precipitation of intermetallic particles.	221
FIGURE 6a.	STEM micrograph showing a 200 Å large particle.	222
FIGURE 6b.	EELS spectrum from the particle in Figure 6a.	222
FIGURE 6c.	EDXS spectrum from the particle in Figure 6a.	222
FIGURE 7.	Neutron autoradiograph obtained from alloy I showing a uniform track distribution.	223
FIGURE 8.	Neutron autoradiograph from alloy I showing a region of increased boron concentration.	223

8. Determination of Helium Influence on Microstructural Development: Two Experimental Methods (HEDL)

FIGURE 1.	Influence of particle radius on normalized deposition rate profiles of reaction products for $^{10}B(n,\alpha)$ events occurring in spherical precipitates for case where the energy deposition characteristics of alpha particles are the same in both phases.	227
FIGURE 2.	The limits of the halo are determined by (n,α) events occurring on the near and far surfaces of the precipitates.	229
FIGURE 3.	Schematic illustration of surface within precipitates capable of depositing alpha particles at point x,o within the halo.	230
FIGURE 4.	Near-surface helium profiles observed in AISI 316 cladding at the extremities of fuel pin P-238-14A.	234
FIGURE 5.	Profiles of injected helium calculated by Yamada in helium-pressurized creep capsules irradiated in EBR-II.	236

TABLES

Page

CHAPTER 2

1. Fission Reactor Dosimetry (ANL)

TABLE 1. Summary of Helium Measurements and Calculations (ENDF/B-IV) for ORR-MFE 1 — 25

2. Helium Accumulation Neutron Dosimetry for Mixed-Spectrum Reactor Irradiations (RIES)

TABLE 1. Helium Accumulation Neutron Dosimetry Materials Supplied for MFE Mixed-Spectrum Reactor Irradiations — 29

6. Evaluation of Ionization-Assisted Displacements in Carbon and Al_2O_3 (BNL)

TABLE 1. Ionization-Assisted Displacement Rates for K Shell Ionization of Carbon (K-ion), L Shell Ionization of Carbon (L-ion), and Neutron Induced Recoil Atom Damage in Carbon for an FMIT Spectrum and a Benchmark Spectrum — 50

TABLE 2. Displacement Rates of Oxygen and Aluminum in Al_2O_3 — 51

8. Modeling of Defect Production in High Energy Cascades in FCC Metals (HEDL)

TABLE 1. Comparison of High (ν_{17}) and Low (ν_5) Displacement Energy Versions of MARLOWE Cascades After Stage I Annealing (τ = 1000) — 64

TABLE 2. Comparison of High (ν_{17}) and Low (ν_5) Displacement Energy Versions of MARLOWE Cascades After Stage III Annealing — 64

TABLES (Cont'd)

TABLE 3. Distribution of Pre-Anneal Defects After Annealing 66

9. RTNS-II Irradiation Program (HEDL)

TABLE 1. Metal Composition (Weight Units) 73

TABLE 2. Prior History 74

10. Microstructural Development in Copper Irradiated in RTNS-II (HEDL)

TABLE 1. Chemical Analysis of Impurity Elements in Copper Specimens 78

TABLE 2. Room Temperature DPH Values for Copper Irradiated at 25°C with 14 MeV (d,T) Neutrons 89

CHAPTER 3

1. Segregation and Embrittlement in Cr-Mo Steels (PNL)

TABLE 1. Material Phenomena Affected by Grain Boundary Chemistry Important to Ferritic Steels 97

TABLE 2. Elements Thought to Enhance Intergranular Fracture in Steels 98

TABLE 3. Summary of the Effect Alloying and Impurity Elements are Believed to Have on the Grain Boundary Chemistry and Intergranular Embrittlement of Ferritic Alloys 108

TABLES (Cont'd)

Page

CHAPTER 4

5B. Preliminary Numerical Analysis of the Temperature Dependence of Cavity and Dislocation Loop Formation in Aged 316 SS (W-R&D)

TABLE 1. Comparison of Maximum Equilibrium Bubble Size (D_C) with Mean (6) and Maximum (D_{MAX}) Cavity Diameters for 316 SS 187

7. Characterization of Rapidly Solidified Boron Doped Stainless Steel for Synergistic Helium Production (MIT)

TABLE 1. Nominal Compositions of the Boron Doped Stainless Steels 214

TABLE 2. Measured Boron and Zirconium Concentrations in W/O 214

TABLE 3. Test Matrix for Neutron Irradiation in EBR-II 216

9. Status of the DAFS Specimens in the AD-1 Irradiation Test (NRL/HEDL)

TABLE 1. DAFS TEM Specimens in the AD-1 Test 240

TABLE 2. DAFS Tensile Specimens in the AD-1 Test 240

10. DAFS Specimen Matrix for the ORR MFE-IV Test (HEDL)

TABLE 1. DAFS TEM Specimens in the MFE-IV Test 244

TABLE 2. DAFS Tensile Specimens in the MFE-IV Test 244

CHAPTER 1

IRRADIATION TEST FACILITIES

I. PROGRAM

Title: RTNS-II Operations (WZJ-16)
Principal Investigator: C. M. Logan
Affiliation: Lawrence Livermore Laboratory

11. OBJECTIVE

The objectives of this work are operation of OFE's RTNS-II (a 14-MeV neutron source facility), machine development, and support of the experimental program that utilizes this facility. Experimenter services include dosimetry, handling, scheduling, coordination, and reporting

111. RELEVANT DAFS PROGRAM TASK/SUBTASK

TASK II.A.2,3,4.
TASK II.B.3,4.
TASK II.C.1,2,6,11,18.

IV. SUMMARY

RTNS-II is dedicated to materials research for the fusion power program. Its primary use is to aid in the development of models of high-energy neutron effects. Such models are needed in interpreting and projecting to the fusion environment engineering data obtained in other neutron spectra.

V. ACCOMPLISHMENTS AND STATUS

A. Irradiations - N. E. Ragaini, M. W. Guinan and C. M. Logan (LLL)

Irradiation of a capsule for Russ Jones (PNL) was completed. Exposure of glass-bonded mica and MACOR samples for Frank Clinard (LASL)

continued. Two irradiations were completed for researchers outside of the fusion program; semiconductors for Dawes, Ochoa, and Bacon (SLA) and liver enzymes for Vessey (V.A./SFO), Heikkinen, and Logan. HEDLIV was completed for Nick Panayotou. Exposure of HVEM tensile specimens for Bill Jesser (U. of Virginia) began. We have been irradiating pure Al wire as a piggyback since RTNS-II began. A long-lived isotope in this material will be used by Hansen for diffusion studies at LBL/LLL.

B. RTNS-II Status - C. M. Logan and D. W. Heikkinen (LLL)

The earthquakes of January were not of major consequence. We experienced unscheduled outage in Jan/Feb with rotating seal problems. The revised system is resulting in the best-ever operating pressures and beam transport. A new fiber optics control system has been designed and installed on the unused machine for checkout. It is expected to have improved radiation resistance and allow easier maintenance.

VII. FUTURE WORK

During the next quarter irradiations are scheduled for Jesser (U. of Virginia), Clinard (LASL), Guinan (LLL), Van Konynenburg (LLL), Barmore (LLL), Kneff (RI), Damask (Queens), Wilkes (U. of Wisconsin), and Panayotou (HEDLV).

VIII. PUBLICATIONS

None

I. PROGRAM

Title: Nuclear Data for Damage Studies and FMIT (WH025/EDK)
Principal Investigators: D.L.Johnson/F.M.Mann
Affiliation: Hanford Engineering Development Laboratory (HEDL)

II. OBJECTIVE

The objective of this work is to supply nuclear data needed for damage studies and in the design and operation of the Fusion Material Irradiation Testing (FMIT) facility.

III. RELEVANT OAFS PROGRAM PLAN TASK/SUBTASK

All tasks that are relevant to FMIT use, with emphasis upon:

SUBTASK	II.A.2.3	Flux spectra definition in FMIT
TASK	II.A.4	Gas Generation Rates
SUBTASK	II.A.5.1	Helium Accumulation Monitor Development
SUBTASK	II.B.1.2	Acquisition of Nuclear Data

IV. SUMMARY

Analysis of measurements of deuteron-induced activation of FMIT materials was continued in order to provide data to optimize design from the standpoint of maintenance. Results are shown for targets of Cu, Ta, Au, and Pb.

Measurements of the transmission of FMIT neutrons through thick iron were performed at U.C.Davis to verify calculations of radiation

heating in FMIT test cell walls. They will also reflect on calculational dosimetry for experiments in the FMIT test cell. These data are expected to shed light primarily on the adequacy of neutron cross section data which extend far above the 20 MeV limit in ENDF/B evaluations.

A computer code, PRECO-D, has been written to calculate angular distribution and statistical direct effects in the pre-equilibrium model of nuclear reactions.

Unperturbed neutron fluxes have been calculated for the FMIT test cell with the new microscopic d+Li neutron yield model and are at the Magnetic Fusion Energy Computer Center (MFECC).

The FMIT Activation Library has been expanded and is in use for design needs.

V. ACCOMPLISHMENTS AND STATUS

A. Measurements of Deuteron Induced Activation of FMIT Materials--

D.L.Johnson and L.G.McWethy (HEDL), C.M.Castaneda and M.L.Johnson (U.C. Davis).

A principal goal of the FMIT project is to be able to perform hands-on maintenance as much as possible. Activation of various materials will provide limitations to the ability to do hands-on maintenance, particularly in the vicinity of the test cells where the beam is deposited. In the vicinity of the accelerator and beam transport system the amount of activation will be directly related to the amount and location of losses of the deuteron beam rather than the amount transmitted. Although such beam losses are expected to be very small compared to the total beam current, large activations can result from nuclear reactions induced directly by the deuterons and also by the secondary neutrons that are prolifically produced when deuterons are

incident upon any material.

A program to provide data for evaluation of activation of FMIT materials is underway. As part of this program, measurements of deuteron induced activation were performed by observation of decay gamma rays with a high resolution Ge(Li) detector after bombardment with 35 MeV deuterons at the University of California at Davis(UCD). The objective was to measure the production rate of all significant gamma emitting isotopes in important materials with half lives longer than about an hour. The production rates coupled with known decay properties will allow calculations of radiation dose from irradiated material for any combination of incident current, irradiation time, and decay time.

Preliminary analysis of measurements for targets of Ta, Au, and Pb has been completed in addition to results shown in the last DAFS quarterly report for targets of Li and Cu.

Copper is important because it is a major material in the FMIT linear accelerator. Figure 1 shows updated results for the copper target which now include data at 35 MeV for more weakly produced radionuclides (^{60}Co, ^{61}Cu, ^{65}Ni, ^{58}Co, and ^{59}Fe). Data for ^{63}Zn was also obtained but only for 35 MeV because of its short half life (38.6 min.). In Figure 1 the data point for ^{63}Zn is superimposed on the point for ^{62}Zn at 35 MeV. Data for ^{64}Cu, ^{65}Zn, and ^{62}Zn were also shown in the last DAFS quarterly report.

For maintenance purposes, the long-lived products (65Zn, ^{60}Co, ^{58}Co, and ^{59}Fe) are most important, in roughly that order. This is because their production rates are sufficient to produce a significant buildup and they do not decay away in a reasonable time.

Figures 2, 3, and 4 show current results for targets of Ta, Au, and Pb. For some radionuclides, data are shown both with and without the effects of self absorption of the decay gamma ray observed in the measurement. In cases where the gamma ray energy is very low and the radionuclide is formed relatively deeply within the target, the self absorption is very large. See, for example, the case of ^{197m}Hg produced in the gold target which shows an apparent decrease of a factor of

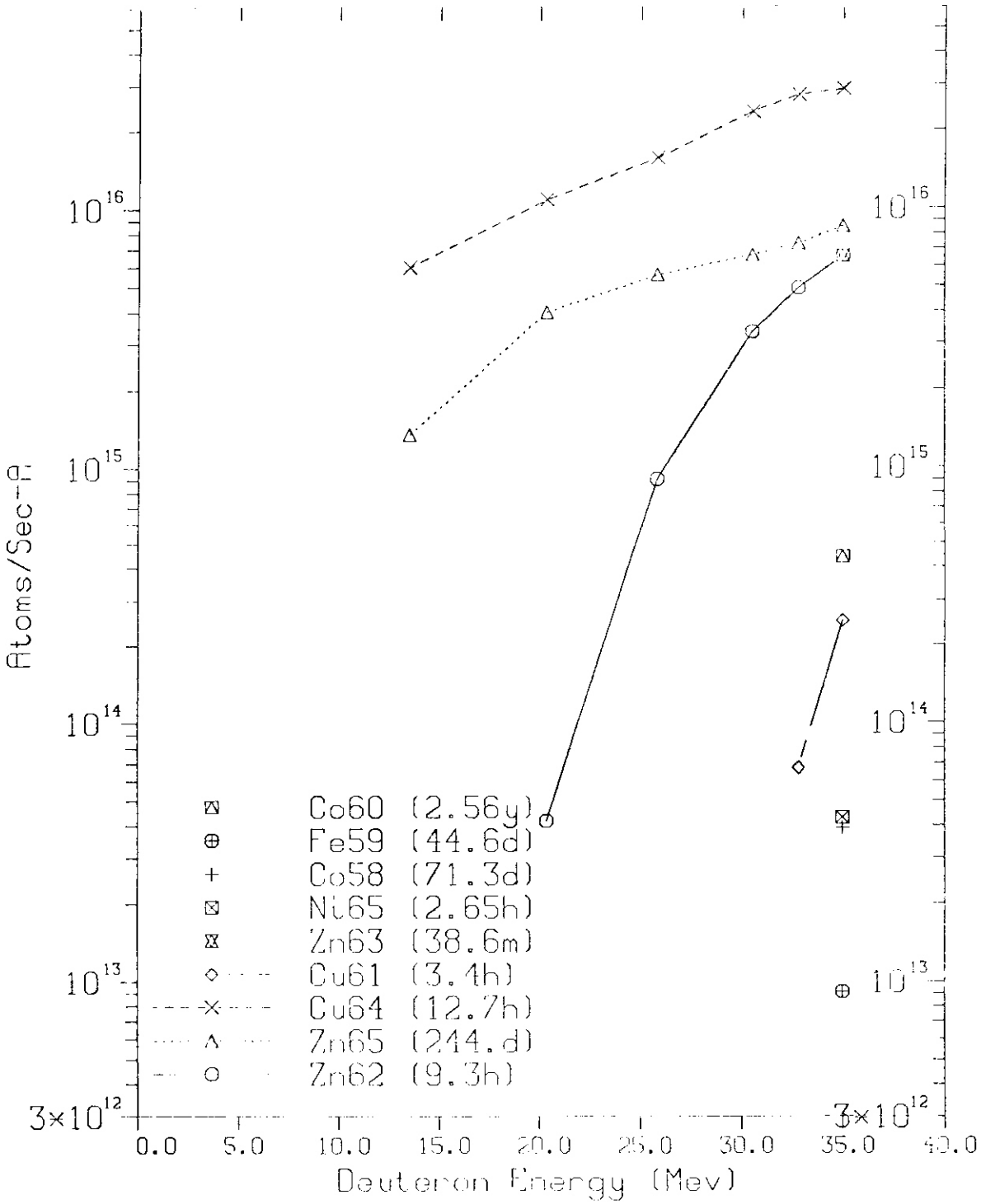

FIGURE 1. Thick Target Production Rate Deuterons on Copper.

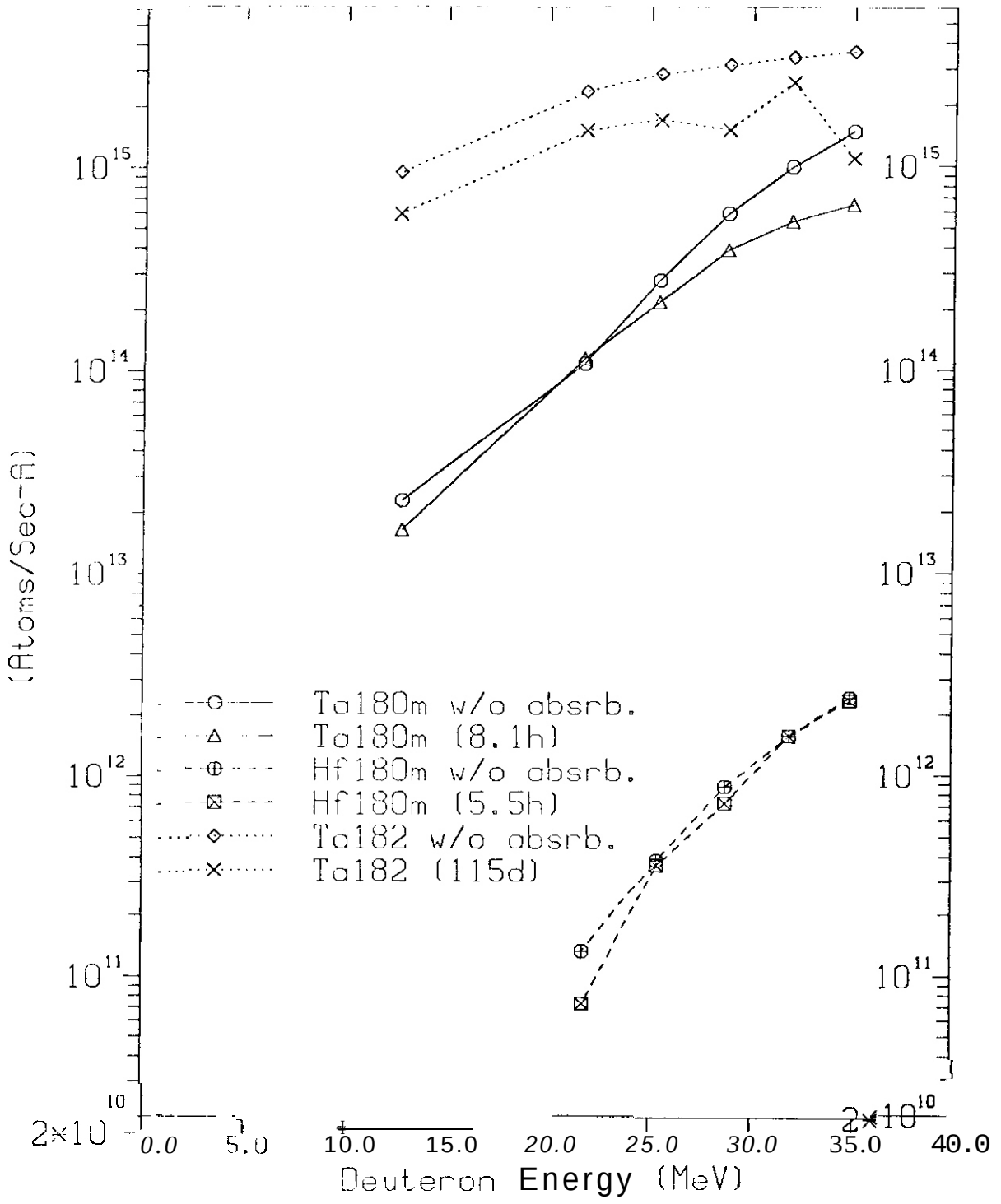

FIGURE 2. Thick Target Production Rate Deuterons on Tantalum.

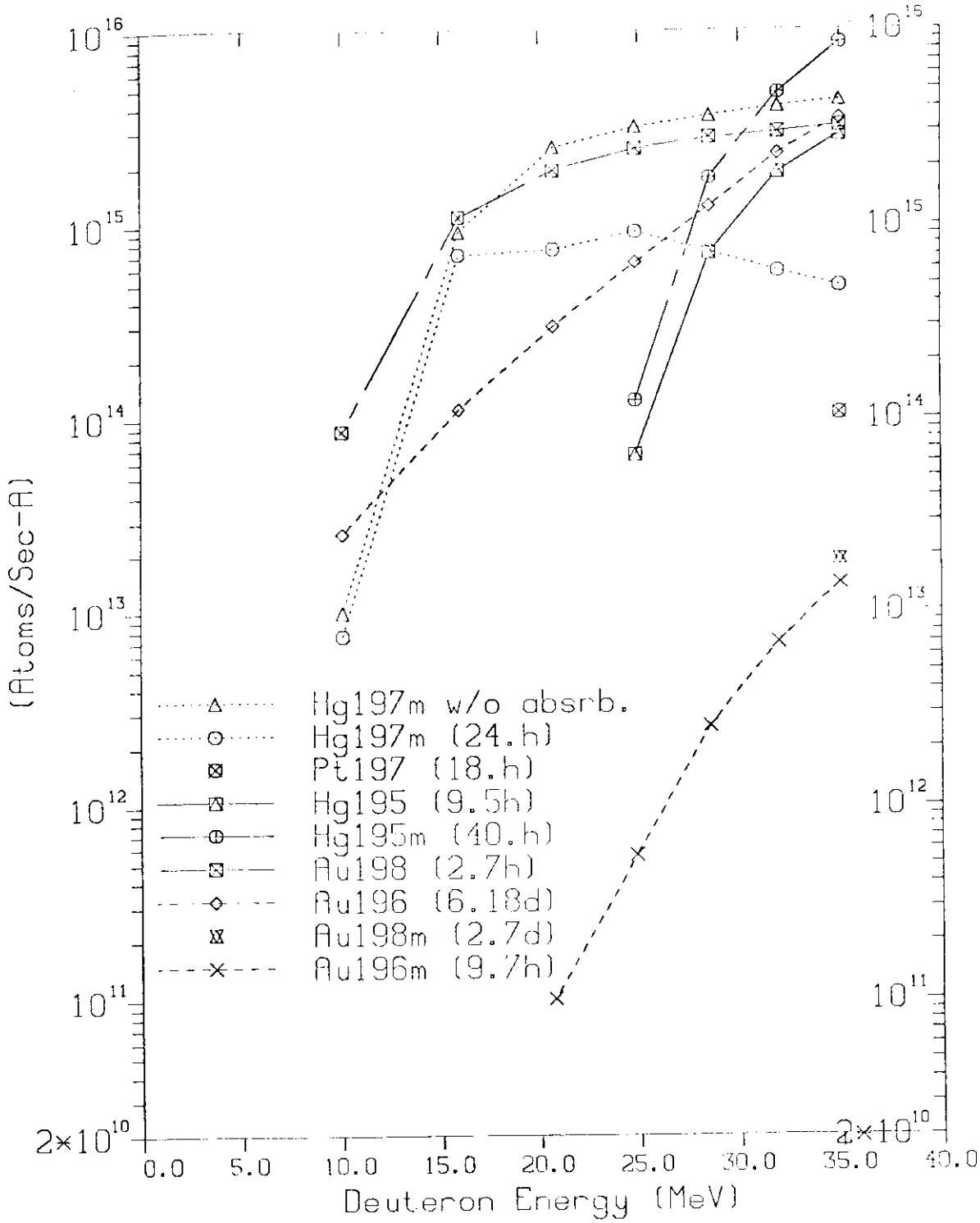

FIGURE 3. Thick Target Production Rate Deuterons on Gold.

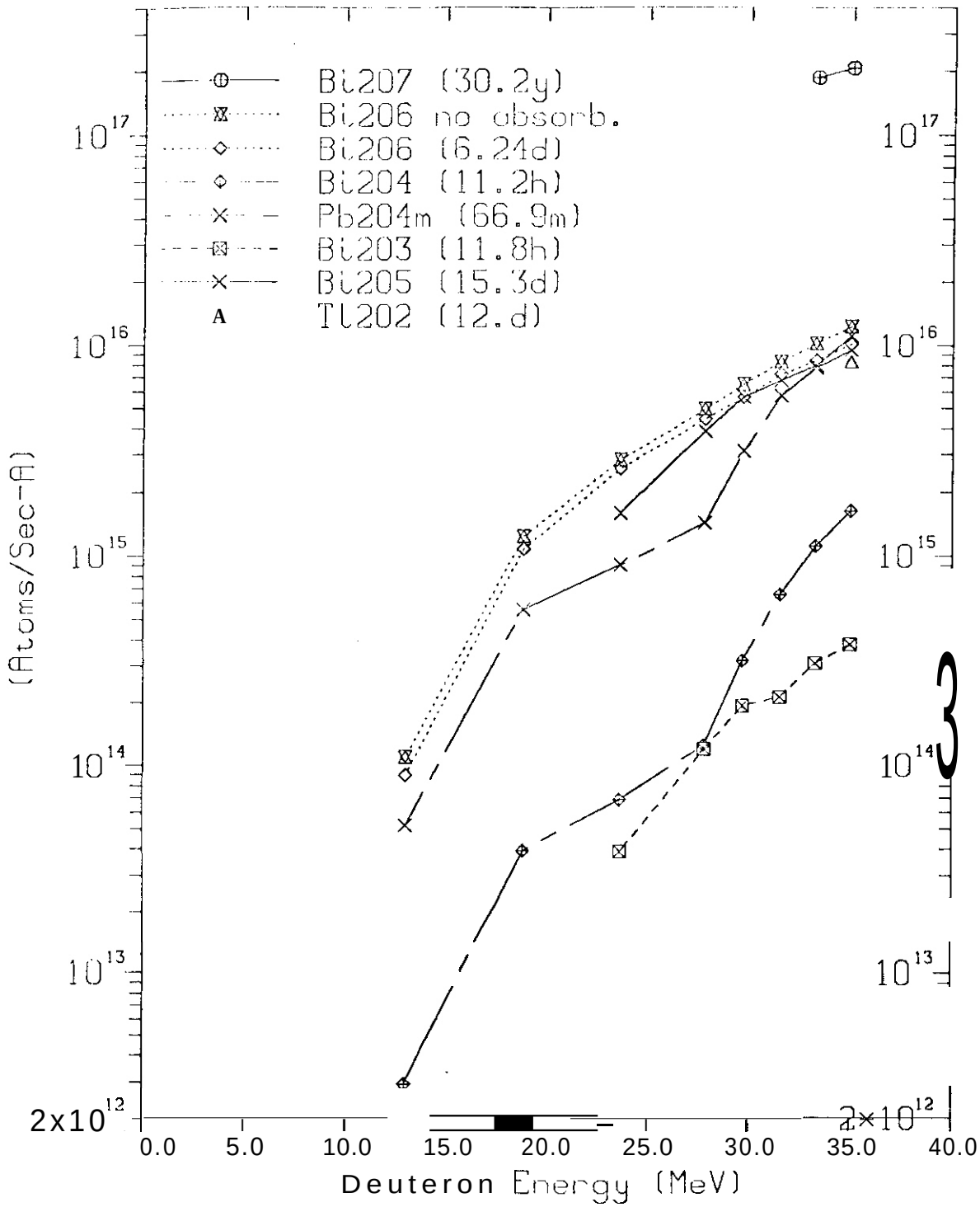

FIGURE 4. Thick Target Production Rate Deuterons on Lead.

$\sim$ 10 for 35 MeV deuterons due to self absorption of the decay gamma ray. Self absorption effects will of course help reduce the dose due to gamma radiation emitted within deuteron activated materials.

It is not yet clear that all significant radionuclides have been observed. For example in the tantalum target only three radionuclides have been positively identified. It may be necessary to supplement the measured results with calculations to provide a complete description of the important radionuclide production rates.

Qualitatively both Ta and Au appear to be reasonable materials to reduce doses from deuteron induced activation without producing copious quantities of secondary neutrons. On the other hand, lead is very bad because many long-lived isotopes are produced with fairly high energy, hence, penetrating, decay gamma rays.

A paper describing this work is in preparation for the Symposium on Neutron Cross Sections from 10-50 MeV, to be held at Brookhaven National Laboratory in May, 1980.

B. Neutron Transport Measurements -- D.L.Johnson and F.M.Mann (HEDL), G.L.Woodruff (Univ. of Washington), F.P.Brady, J.L.Romero, J.L. Ullmann, M.L.Johnson and C.M.Castaneda (Univ. of California at Davis).

Measurements of the transmission of FMIT-like neutrons through thick iron were completed at the University of California at Davis. The objective was to provide data to confirm neutron transport calculations which are used for predictions of radiation heating in the FMIT test cell walls. This comparison sheds light on the adequacy of our knowledge of the bare neutron source characteristics, nuclear data for neutrons up to 50 MeV on iron, and calculational methods. The largest uncertainties might be expected in the nuclear data which have been extended far beyond the 20 MeV limit in ENDF/B evaluations.

The neutrons were produced by a beam of 35 MeV deuterons which was stopped in a solid lithium target that was $\sim$ 2.5 cm in diameter by 2 cm thick. This target was placed close to the center of a nearly cubical

block of solid iron which was about 60 cm (2 feet) thick on each side. Neutrons from the source had to penetrate at least 30 cm (1 foot) of iron in any direction in order to escape the iron block.

Measurements of the neutron spectra were made with detectors placed ∿ 10 cm (4") outside the block at 0" and 90" with respect to the beam direction. Proton recoil proportional counters were used to measure the portion of the spectrum from ∿ 10 KeV to ∿ 1.5 MeV where most of the transmitted neutrons are found. An NE213 liquid scintillator was used to measure the spectrum from ∿ 1 MeV up to the maximum that might be observable (∿ 50 MeV).

Analysis of these data has begun using the codes PSNS and FORIST to unfold the measured spectra from the proton recoil proportional counters and the NE213 detector respectively.

Additional data were obtained from this experiment using (1) thermoluminescent dosimeters (TLD's) to measure gamma dose throughout the iron, and (2) solid state track recorders (SSTR's) and photographic emulsions to measure neutron spectra at various locations outside the iron.

It is planned that this work will be described at the BNL Symposium on Neutron Cross Sections from 10-50 MeV, in May 1980.

C. Cross Section Predictions -- F.M.Mann (HEDL), and C. Kalbach (Triangle Universities Nuclear Laboratory).

The pre-equilibrium code PRECO has been updated (PRECO-D) to include the prediction of angular distributions of the outgoing particles and the yield of statistical direct reactions.

A paper describing the underlying theory and equations of predicting angular distributions is in preparation as is a paper for the BNL conference on nuclear data from 10 to 50 MeV.

D. Microscopic Neutron Yield Model for the d,Li Reaction -- F.M. Mann and F. Schmittroth (HEDL).

The microscopic neutron yield model has been used to calculate the predicted unperturbed flux in the FMIT Test Cell. This model, which results from a generalized least squares analysis of available d+Li neutron yield data and uses the spectral data of the HEDL-U.C. Davis measurements, agrees well with most of the available data. An example of the agreement is shown in Figure 5, which compares the predicted flux at 12° with that as measured by HEOL-U.C. Davis. Figure 6 shows the predicted volumes in the FMIT Test Cell having given average and minimum fluxes. The predicted neutron yield as a function of deuteron energy, emission angle, and neutron energy is now at the MFECC (Magnetic Fusion Energy Computer Center) at Lawrence Livermore Laboratory. This work is being written up for the BNL conference on nuclear data from 10 to 50 MeV.

Displacement cross sections calculated by L.R.Greenwood (ANL) have been received. These will be folded with the predicted fluxes to obtain expected damage rates in the FMIT Test Cell.

E. FMIT Activation Library -- F.M.Mann, R.J.Morford, and L.L Carter (HEDL).

The FMIT Activation Library has been extended to four libraries (group cross sections weighted by the unperturbed FMIT flux, perturbed fluxes in the FMIT Test Cell filled with half density iron, a decay library having half-life, dose, and spectral information, and a material library). A program has been written combining the four libraries and has already been used for experimental design.

VI. REFERENCES

None

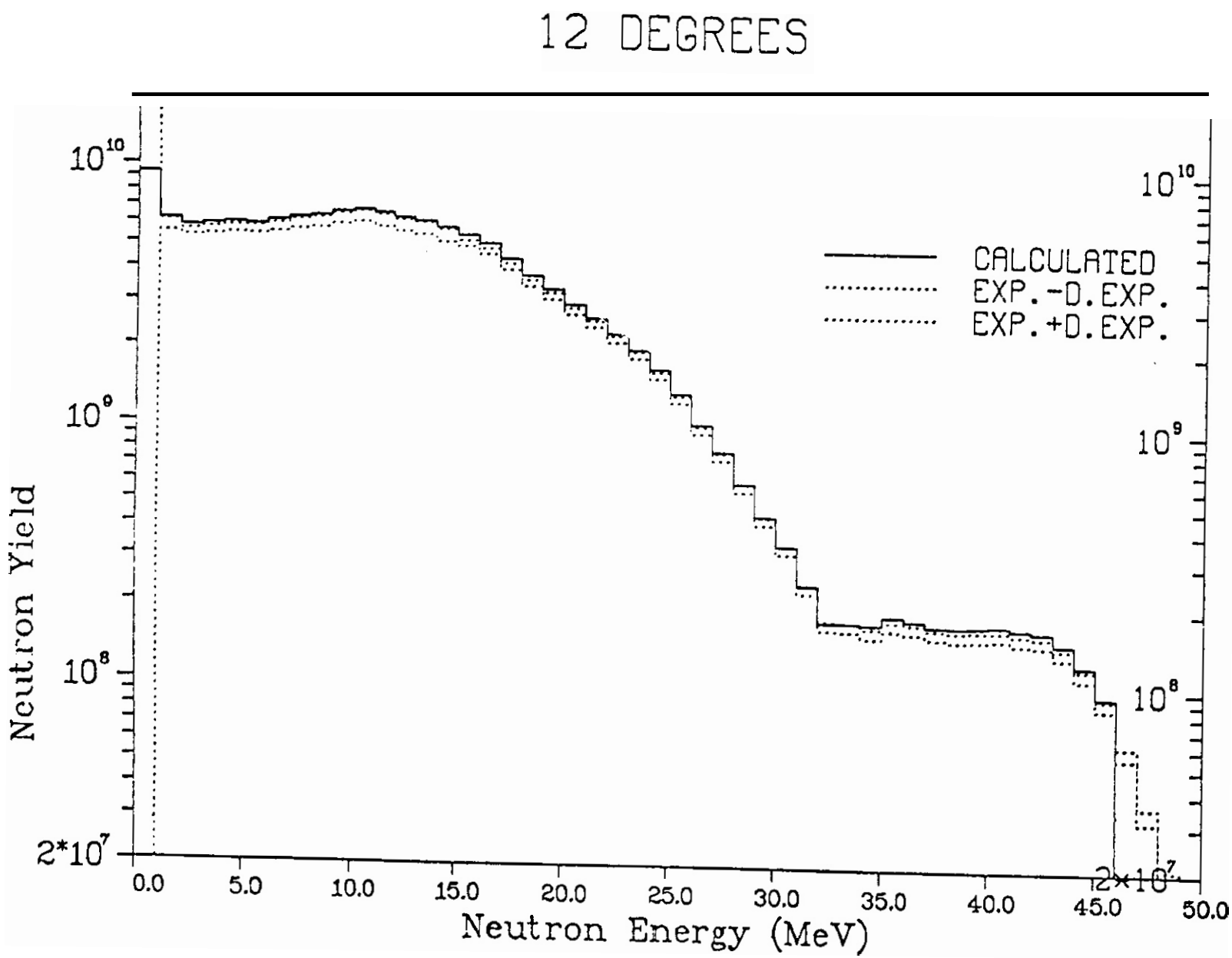

FIGURE 5 Comparison between Model and U C Davis-HEDL Experiment

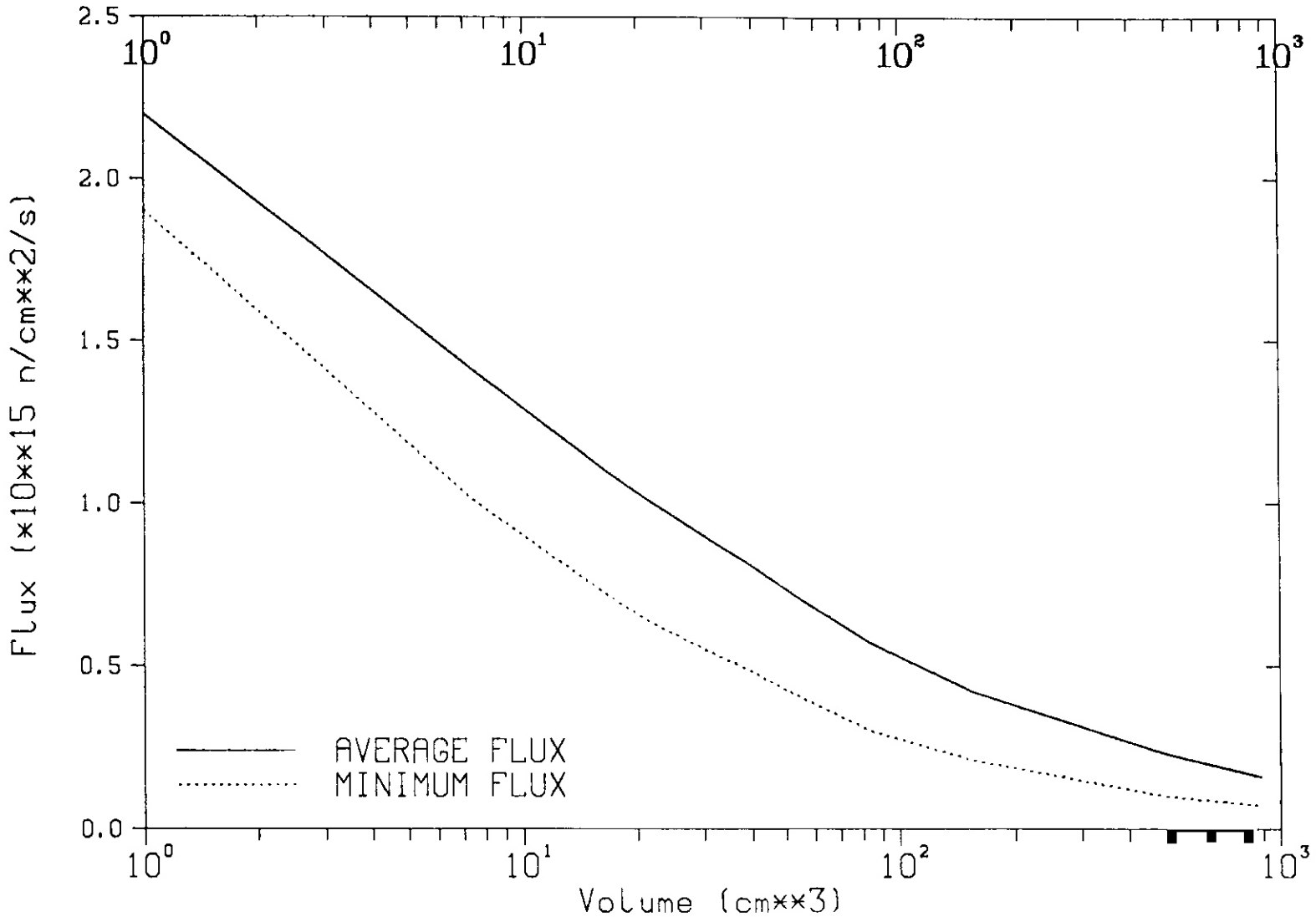

FIGURE 6. Relationship Between Flux and Volume.

VII. FUTURE WORK

Analysis of deuteron activation measurements will continue. One more set of measurements is planned to complete this program.

Improved design of a high current d+Li target for neutron activation and dosimetry studies will be completed.

Analysis of measurements of the transmission of FMIT neutrons through thick iron will begin.

The computer code HAUSER*5 will be modified to include the study of angular distributions and installed at the MFECC.

Unperturbed damage rates will be calculated for various positions in the FMIT Test Cell.

The FMIT Activation Library will be expanded and upgraded to fit construction needs.

VIII. PUBLICATIONS

1) D.L.Johnson, F.M.Mann, J.W.Watson, J. Ullman, and W.G.Wyckoff, "Measurements and Calculations of Neutron Spectra from 35 MeV Deuterons on Thick Lithium for the FMIT Facility," Jour. of Nuclear Materials 85 & 86 (1979) 467.

2) J.O.Schiffgens, R.L.Simons, F.M.Mann, and L.L.Carter, "Spatial Variations of Damage Parameters in FMIT and Their Implications: Ibid., p. 491.

3) R.E.Schenter, F.M.Mann, and D.L.Johnson, "Nuclear Data Needs for FMIT", to be published in the proceedings of the International Conference on Nuclear Cross Sections for Technology, Knoxville, Tennessee, Oct. 22-26, 1979, (also HEDL-S/A-1902FP).

4) D.L.Johnson, F.M.Mann, J.W.Watson, J.Ullmann, and W.G.Wyckoff, "Measurements of Neutron Spectra from 35 MeV Deuterons on Thick Lithium for the FMIT Facility", Ibid. (also HEDL-SA-1905FP).

5) F.M.Mann, F. Schmittroth, L.L.Carter, and J.O.Schiffgens, "The Spatial Dependence of Flux and Damage in the FMIT Test Cell", Ibid., (also HEDL-SA-1901FP).

6) D.L.Johnson, F.M.Mann, R.E.Schenter, J.W.Watson, F.P.Brady, J.L. Ullman, J.L.Romero, C.M.Castaneda, C.I.Zanelli, and W.G.Wyckoff. "Thick Target Neutron Yields and Spectra from the Li(d,xn) Reaction at 35 MeV", to be presented at the Symposium on Neutron Cross-Sections from 10-50 MeV, Brookhaven National Laboratory, May 12-14, 1980. (Also HEDL-SA-2141FP)

7) C.I.Zanelli, F.P. Brady, J.L.Romero, C.M.Castaneda, M.L. Johnson, G.A.Needham, J.L.Ullmann, P.P.Urone, D.L.Johnson. "Measurements of Neutron Total and Non-elastic Cross-sections for C, O, Ca, and Fe at U.C.Davis," Ibid., (also HEDL-SA-2144FP).

8) D.L.Johnson, F.M.Mann, R.E.Schenter. "Measurements and Evaluations of Nuclear Data to Support Early Design Needs of the FMIT Facility", Ibid., (also HEDL-SA-214DFP).

9) C. Kalbach and F.M.Mann. "Phenomenology of Preequilibrium Angular Distributions", Ibid. (also HEDL-SA-2134FP)

10) F.M.Mann and F. Schmittroth. "Neutron Environment in d+Li Facilities", Ibid. (also HEDL-SA-2123FP).

11) R.Gold, W.N.McElroy, E.P.Lippincott, D.L.Oberg, J.H.Roberts, F.H.Ruddy, and R.E.Schenter. "Cross Sections Required for FMIT Dosimetry", Ibid. (also HEDL-SA-2148FP).

CHAPTER 2

DOSIMETRY AND DAMAGE PARAMETERS

I. PROGRAM

Title: Dosimetry and Damage Analysis
Principal Investigator: L. R. Greenwood
Affiliation: Argonne National Laboratory

11. OBJECTIVE

To establish the best practicable dosimetry for mixed-spectrum reactors and to provide dosimetry and damage analysis for DFE experiments.

III. RELEVANT OAFS PROGRAM TASK/SUBTASK

SUBTASK II.A.l.l Flux-spectral definition in a tailored fission reactor.

SUBTASK II.A.1.3 Applications

IV. SUMMARY

Helium measurements are compared to calculations for DRR-MFE 1. The MFE 2 dosimeters are being shipped to ANL for analysis. Dosimeters have been prepared for MFE 4B.

Dosimeters have been provided for the CTR - 30, 31, and 32 irradiations in HFIR and more irradiations are planned. Dosimeters from the X287 irradiation in EBR II are being sent to ANL for analysis.

Plans are being made to measure the flux-spectrum in the Omega West Reactor at LASL.

V. ACCOMPLISHMENTS AND STATUS

A. Flux-spectral Measurements at ORR

L. R. Greenwood (ANL)

Helium measurements for ORR-MFE 1 are compared to calculated helium rates deduced from our flux-spectral measurements in Table I. The nickel calculations show excellent agreement for the two-step reaction, provided that the nickel cross sections for $^{58}Ni(n,\gamma)$ and $^{59}Ni(n,\alpha)$ are deduced from our measurements. Preliminary comparisons showed 15-20% differences between measurements and calculations when the nickel reaction rates were estimated from the thermal flux as suggested in ORNL/TM-6361.[1] However, this difference disappears if one estimates the nickel rates by direct comparison to measured activation rates in ORR for other reactions such as $^{58}Fe(n,\gamma)$ and $^{59}Co(n,\gamma)$. It appears that contributions to the reaction from resonance neutrons almost exactly offsets the estimated 28% difference between the thermal cross section and the 2200 m/s value. The measured thermal flux (<.5eV) times the thermal cross section thus appears to be an excellent estimate of the reaction rates for nickel in ORR. This suggests that such comparisons in the future require simultaneous dosimetry to insure that proper reaction rates are known for nickel.

Table I also shows excellent agreement for Al, probably since the $^{27}Al(n,\alpha)$ cross section is rather well-known. However, Cu and Fe show 25% differences and Ti indicates an 85% difference, suggesting serious discrepancies in the ENDF/B-IV cross sections used in the calculations.

The MFE 4A spectral-tailoring experiment has started and dosimeters are being provided for the MFE 4B irradiation. Dosimeters are being returned to ANL from the MFE 2 irradiation. Both irradiations also included helium accumulation samples from RIES.

Further attempts to improve the agreement between neutronics calculations (T. Gabriel, ORNL) and dosimetry measurements for MFE 1 have proved

Table I. Summary of Helium Measurements and Calculations (ENDF/B-IV) for ORR-MFE1

Material	Measurements[a]	Ratio of Measured-to-Calculated He
Al	2	0.95 ± .02
Fe	5	1.27 ± .07
Cu	5	1.24 ± .05
Ni[b]	5	1.00 ± .03
Ti	5	1.85 ± .07

[a] Helium measurements by O. Kneff and H. Farrar IV (RIES), DOE/ET-0065-8, February, 1980.

[b] Two-step process included using estimated spectral-averaged cross sections for nickel.

unsuccessful, probably due to significant streaming effects which are not properly accounted for in the neutronics codes. This situation is fortunately atypical for ORR since the core configuration had to be altered to reduce gamma heating in MFE1. Consequently, this situation should be a reminder of the necessity of dosimetry in materials irradiations.

B. Flux-spectral Measurements in HFIR

Argonne will provide dosimetry for future materials irradiations in the High Flux Iostopes Reactor (HFIR) at ORNL. The first experiments (CTR 30, 31, and 32) are scheduled for late April and dosimeters are now being prepared. Further irradiations are planned for May and September, 1980. The flux-spectrum will also be measured, probably using the hydraulic tube. Helium specimens will also be included for analysis at RIES.

C. Flux-spectral Measurements in EBR II

Dosimetry capsules are being returned to ANL from the X287 irradiation in EBR II. The irradiation started in 1977 and lasted about two years.

D. Dosimetry in the Omega West Reactor

Argonne will characterize the spectrum in the Omega West Reactor at LASL for experiments planned by LLL and HEDL. This reactor will replace the recently decommissioned LPTR facility at LLL in fission-fusion correlations with RTNS II. Dosimeters are now being prepared for a spectral measurement in late April and dosimeters will be included in future materials irradiations. Samples will also be sent to RIES for helium analysis.

VI. REFERENCES

1. T. A. Gabriel, B. L. Bishop, and F. W. Wiffen, "Calculated Irradiation Response of Materials Using Fission Reactor (HFIR, ORR, EBR II) Neutron Spectra," ORNL/TM-6361, August 1979; H. Farrar IV, private communication, 1980.

VII. FUTURE WORK

Several of the materials irradiations in ORR and HFIR are expected to last for 1-2 years. Detailed comparisons between neutronics and dosimetry measurements will be sought for the spectral tailoring experiments, ORR-MFE 4.

Further helium comparisons will also be obtained for all of the irradiations, improving our knowledge of gas production cross sections so that helium monitors can be used for routine dosimetry as well as helium measurement.

I. PROGRAM

Title: Helium Generation in Fusion Reactor Materials
Principal Investigators: D. W. Kneff, Harry Farrar IV
Affiliation: Rockwell International, Energy Systems Group

II. OBJECTIVE

The objective of this part of the fusion program at Rockwell International is to develop and apply helium accumulation neutron dosimetry to the measurement of neutron fluences and energy spectra in mixed-spectrum fission reactors utilized for fusion materials testing.

III. RELEVANT DAFS PROGRAM PLAN TASK/SUBTASK

TASK II.A.l	Fission Reactor Dosimetry
SUBTASK II.A.l.l	Flux-Spectral Definition in a Tailored Fission Reactor
SUBTASK II.A.1.2	Enhance Technique

IV. SUMMARY

Sets of bare and platinum-encapsulated pure-element helium accumulation neutron dosimetry materials were prepared and shipped to Argonne National Laboratory (ANL). These will be incorporated in the ORR MFE-4B irradiation, and in the HFIR irradiations HFIR-CTR-30, 31, and 32, all scheduled to commence in April 1980.

V. ACCOMPLISHMENTS AND STATUS

Helium Accumulation Neutron Dosimetry for Mixed-Spectrum Reactor Irradiations -- D. W. Kneff and Harry Farrar IV (Rockwell International, Energy Systems Group)

Four new cooperative reactor dosimetry experiments with ANL were initiated during the report period. Sets of helium accumulation neutron dosimetry materials were assembled and shipped to ANL for incorporation in the Oak Ridge Research Reactor (ORR) MFE-4B irradiation, and in the High Flux Isotopes Reactor (HFIR) irradiations HFIR-CTR-30, 31, and 32. Additional nickel wire was also sent directly to Oak Ridge National Laboratory (ORNL) for monitoring and accurately determining the helium production in nickel over the projected 10-year span of the MFE-4 experiments.

The contents of the dosimetry sets are summarized in Table 1. Platinum capsules were used to encapsulate some of the wire samples for verification of helium retention in the bare dosimetry wires. They were used for all of the chromium and molybdenum samples, which are in the form of small, irregular pure-element chips. The selection of the dosimetry materials for these experiments, as for MFE-4A,[1] was based on the use of the same specific samples for both radiometric counting and helium analysis. The Cr and Mo samples were included for helium production measurements, because of the current interest in these elements as components of candidate fusion reactor structural materials.

VI. REFERENCES

1. D. W. Kneff and H. Farrar IV. "Helium Accumulation Fluence Dosimetry for the MFE-4 Irradiation at ORR," in Damage Analysis and Fundamental Studies, Quarterly Progress Report October-December 1979, DOE/ET-0065/8, U.S. Department of Energy (1980).

TABLE 1

HELIUM ACCUMULATION NEUTRON DOSIMETRY MATERIALS SUPPLIED FOR MFE MIXED-SPECTRUM REACTOR IRRADIATIONS

Material	ORR MFE-4B	HFIR		
		CTR-30	CTR-31	CTR-32
Fe	W, C	W, C	W	W, C
Ni	W, C	W, C	W	W, C
cu	W, C	W, C	W	W, C
Ti	W, C	W, C	W	W, C
Nb	W, C	W, C	W	W, C
Cr	C	C		
Mo	C			
Pt*	C	C		C

W = Bare pure-element wires

C = Pure element in sealed Pt capsules, electron-beam welded in vacuum after loading

*Empty Pt capsules for background measurement

VII. FUTURE WORK

Helium accumulation measurements supporting the MFE experiments in mixed-spectrum reactors will continue. Additional helium accumulation neutron dosimetry materials will be prepared in April 1980 for an MFE experiment in the Omega West Reactor at Los Alamos. Helium analyses will continue, initially with the ORR MFE-2 materials when they become available.

I. PROGRAM

Title: Dosimetry and Damage Analysis
Principal Investigator: L. R. Greenwood
Affiliation: Argonne National Laboratory

II. OBJECTIVE

To establish the best practicable dosimetry for high-energy neutron facilities.

III. RELEVANT DAFS PROGRAM PLAN TASK/SUBTASK

SUBTASK II.A.2.1 - Flux-spectral Definition in Be(d,n) Field

IV. SUMMARY

The joint characterization of the Be(d,n) source at the University of California at Davis with LLL and RIES has been completed. Fluence, damage, and helium generation contour maps are presented.

V. ACCOMPLISHMENTS AND STATUS

A. Characterization of the Be(d,n) Source at U.C. Davis, E_d = 30 MeV.

L. Greenwood (ANL), M. Guinan (LLL), D. Kneff (RIES)

The joint characterization of the U.C. Davis neutron source has been completed. All radiometric data from ANL and LLL has been combined and geometric corrections have been applied. Spectral unfolding was then performed at about 25 different distances and angles from 3 to 300 mm from the source and 0 to 60 degrees from the beam axis.

Figure 1 shows constant fluence (n/cm^2) contours for neutrons above 1 MeV per Coulomb of deuterons on the Be target. A computer program (FANG) was written to calculate finite geometry corrections to the angular distributions by integrating over the source volume and sample area. The beam spot appeared to be slightly non-circular with an average radius of 2.2 mm, based on autoradiographs. The program was checked by comparing the results to measured activation rates for small radiometric foils placed close to the source.

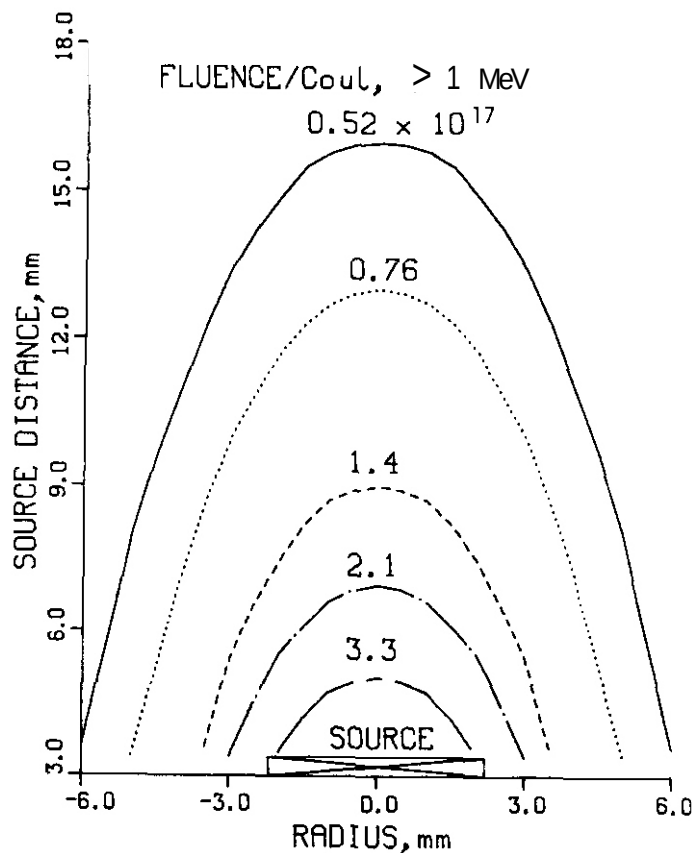

Fig. 1. Fluence contours (>1 MeV) are shown for the Be(d,n) source at U. C. Davis at E_d = 30 MeV. The beam spot was about 4.4 mm in diameter, as indicated.

As seen in figure 1, the fluence gradients are quite steep, especially away from the beam axis (R=0). Damage and helium production gradients are even steeper, as shown in figures 2 and 3, since the spectra also change rapidly with angle from the beam axis. The helium contours will be compared in detail to the helium generation measurements made by H. Farrar and D. Kneff (RIES),[1] although preliminary comparisons indicate reasonably good agreement.

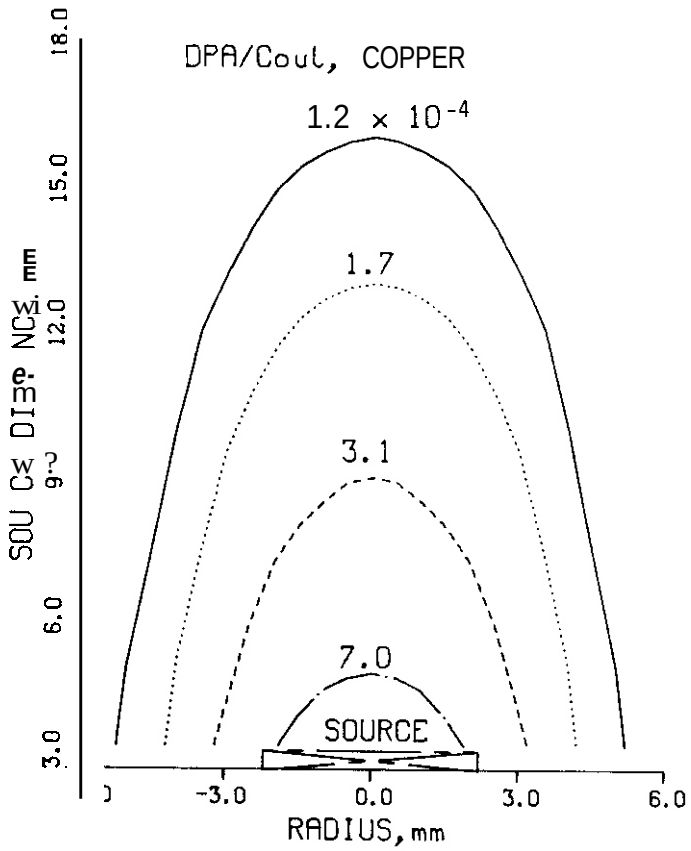

Fig. 2. Displacement-per-atom contours for copper are shown for the U. C. Davis Source [Be(d,n), E_d = 30 MeV].

The steep gradients shown in the figures indicate the need for precise dosimetry in Be(d,n) fields during materials irradiations. The gradient effects will be substantially moderated at FMIT due to the much larger source size (1x3 cm).

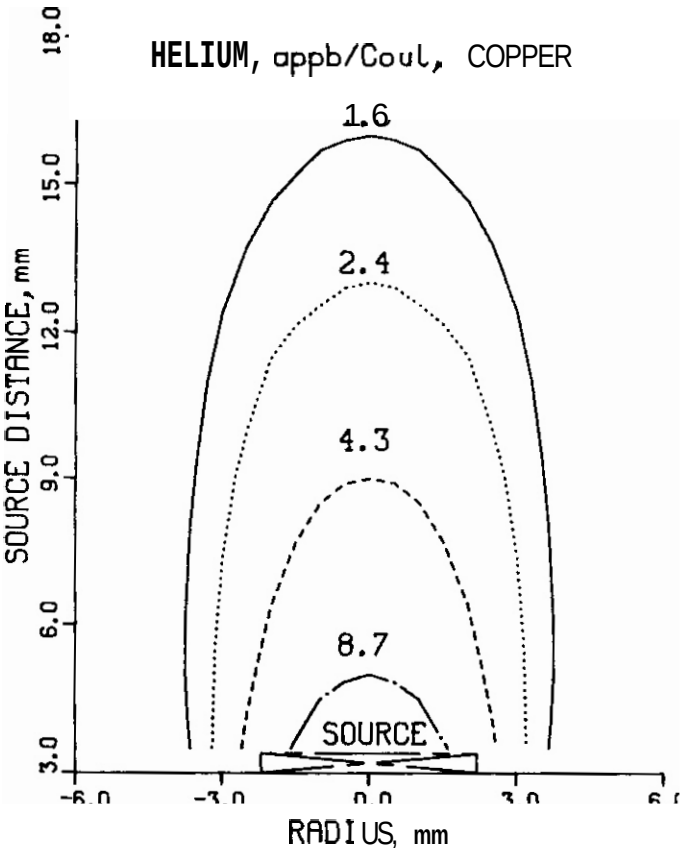

Fig. 3. Helium production contours are shown for copper for the U.C. Davis Source [Be(d,n), E_d = 30 MeV]. Note the very sharp gradients off-axis due to spectral changes.

VI. REFERENCES

1. D. W. Kneff and H. Farrar IV, DOE/ET-0065/7, p. 22, November, 1979.

VII. FUTURE WORK

A more complete compilation of our results will be presented as an ANL report and at the Symposium on Neutron Cross Sections from 10-50 MeV at BNL in May 1979. Detailed comparisons between calculated and measured

helium rates will provide a precise test of helium generation cross sections. Integral cross section evaluations will be added to our previous integral tests at E_d = 14, 16, and 40 MeV. However, all such tests are now being revised with newly available ENDF/B-V dosimetry cross sections.

I. PROGRAM

Title: Helium Generation in Fusion Reactor Materials
Principal Investigators: D. W. Kneff, Harry Farrar IV
Affiliation: Rockwell International, Energy Systems Group

II OBJECTIVE

The objectives of this part of the fusion program at Rockwell International are to measure helium generation rates of materials for Magnetic Fusion Reactor applications in the T(d,n) anu Be(d,n) neutron environments, to characterize the Be(d,n) neutron fluence and neutron energy distributions as a function of position relative to the neutron source, and to develop helium accumulation fluence monitors for neutron fluence and energy spectrum dosimetry for the various fusion program neutron test environments.

III. RELEVANT DAFS PROGRAM PLAN TASK/SUBTASK

SUBTASK II.A.4.2	T(d,n) Helium Gas Production Data
SUBTASK II.A.4.3	Be(d,n) Helium Gas Production Data
SUBTASK II.A.2.1	Flux-Spectral Definition in the Be(d,n) Field
SUBTASK II.A.5.1	Helium Accumulation Monitor Development

IV. SUMMARY

The helium analyses have been completed for the helium accumulation neutron dosimetry materials irradiated in the joint Rockwell International-Argonne National Laboratory (ANL)-Lawrence Livermore Laboratory (LLL) Be(d,n) and second RTNS-I T(d,n) irradiations. These analyses led to the development of some new helium analysis procedures to reduce background levels in the helium mass spectrometer system. The new procedures allow the measurement of helium levels of -2×10^9 atoms in selected samples

with less than 10% uncertainty. A three-dimensional neutron fluence profile is now being constructed for the T(d,n) irradiation environment.

V. ACCOMPLISHMENTS AND STATUS

Helium Accumulation Neutron Dosimetry for the T(d,n) and Be(d,n) Neutron Irradiation Environments -- D. W. Kneff, B. M. Oliver, M. M. Nakata, and Harry Farrar IV (Rockwell International, Energy Systems Group)

Helium analyses have been completed for the helium accumulation neutron dosimetry materials irradiated in the joint Rockwell International-ANL-LLL Be(d,n) and second RTNS-I T(d,n) neutron irradiations, and a detailed neutron fluence map is now being constructed for the high-flux region of the T(d,n) source environment. These experiments, described in detail in previous reports,[1,2] are being carried out to measure the spectrum-integrated helium generation cross sections of several materials, characterize the neutron environments, and develop the use of helium accumulation neutron dosimetry.

Most of the helium measurement effort during the reporting period was focused on the analysis of T(d,n)- and Be(d,n)-irradiated gold wire dosimetry rings. New helium analysis procedures were developed for determining the low helium levels in these samples, improving the mass spectrometer system detection limit by a factor of ten. The procedures, based on vaporizing the samples in tungsten coils in a copper furnace, have reduced mass spectrometer background levels to the point where $\sim 2 \times 10^9$ atoms of helium can be measured with an uncertainty of less than 10% in selected materials. These materials are presently limited to those which can be vaporized in a tungsten coil. However, the procedures are now being extended to other pure elements having higher vaporization temperatures. These procedures involve adding a second specific element, such as nickel, to the sample. The two elements form a eutectic alloy as they are heated,

releasing the sample's helium in the process. This results in less heating and therefore a lower background helium release. This has been demonstrated successfully using molybdenum samples.

The results of the gold analyses show that helium concentrations produced in the T(d,n)-irradiated gold ranged from 0.072 to 0.109 appb (atomic parts per billion, 10^{-9} atom fraction), and in the Be(d,n)-irradiated gold ranged from 0.053 to 0.39 appb. The ranges reflect the changing neutron spectra with position in the irradiation capsules. These concentrations represent helium generation rates roughly 1% and 3% of those for copper in the T(d,n) and Be(d,n) neutron environments, respectively. These results indicate, as expected, that gold has a different energy response than copper in these fast-neutron spectra, an important feature for helium accumulation fluence dosimetry. Final helium generation rates and cross sections will be determined when the neutron fluence maps for these two irradiations are completed.

The neutron fluence map for the T(d,n) irradiation environment is now being constructed. An initial fluence map was first generated using the ANL and LLL radiometric counting results. Combining these results with the helium accumulation data has shown that the irradiation capsule was offset significantly (~3.3 mm) from the neutron source axis, and was not symmetric about this axis. The asymmetry, perhaps produced by an upstream beam-line collimator attenuating the edge of the deuteron beam, was not readily discernable from the radiometric data alone, and produced fluence errors estimated to be ~10%-20% in the radiometric map. The helium results are now being folded into the map to produce a more accurate three-dimensional neutron fluence profile.

VI. REFERENCES

1. D. W. Kneff and H. Farrar IV, Helium Generation in Fusion Reactor Materials, Technical Progress Report for Period April-September 1977, AI-DOE-13219, Atomics International, Canoga Park, CA, January 1978.

2. D. W. Kneff, Harry Farrar IV, and M. M. Nakata, "Helium Accumulation Neutron Dosimetrv for the Be(d,n) Irradiation Environment," in Damage Analysis and Fundamental Studies, Quarterly Progress Report July-September 1979, DOE/ET-0065/7, U.S. Department of Energy (1980).

VII. FUTURE WORK

Detailed neutron profile maps will be generated for both the T(d,n) and Be(d,n) irradiations. Helium analyses of the other materials irradiated in these experiments will continue. The results will be combined with the maps to determine the total helium generation cross sections of a wide range of materials of interest to the fusion community.

I. PROGRAM

Title: Dosimetry and Damage Analysis
Principal Investigator: L. R. Greenwood
Affiliation: Argonne National Laboratory

II OBJECTIVE

To enhance flux-spectral unfolding techniques for OFE materials irradiations.

III. RELEVANT DAFS PROGRAM PLAN TASK/SUBTASK

TASK II.A.6 Dosimetry Standardization
TASK II.A.l Fission Reactor Dosimetry
TASK II.A.2 High-Energy Neutron Dosimetry

IV. SUMMARY

The activation dosimetry cross section and cross section error files have been revised according to ENDF/B-V. Past integral data testing is being revised to assess the impact of the new data.

V. ACCOMPLISHMENTS AND STATUS

A. Revision of ANL Dosimetry Cross Section and Covariance Files with ENDF/B-V

L. R. Greenwood - ANL

All existing dosimetry cross section files have been revised according to the recently released ENDF/B-V Dosimetry File.[1] For the first time, cross section errors have also been included in the file, thereby replacing our somewhat subjective error files used previously. Covariance effects are also being examined for use with our version of the STAYSL code for

spectral unfolding. However, programs are not presently available for computing group errors and covariances in the resonance region. Furthermore, covariance files are only available for a selected number of reactions over limited energy ranges.

It is important to note that most cross sections above about 14 MeV [e.g.--for Be(d,n) sources] are generally not included in ENDF/B-V. We are currently revising our previous integral cross section tests at E_d = 14, 16, and 40 MeV to assess the impact of these data revisions. Preliminary indications are that most changes will not be very significant, partially since some of the worst discrepancies have already been noted and changed according to preliminary ENDF/B-V data.

Several improvements in cross sections with long-lived activation products are expected to benefit reactor irradiations. In particular, the $^{63}Cu(n,\alpha)\,^{60}Co$(5.3 year) and $^{55}Mn(n,2n)\,^{54}Mn$(312 day) reactions are now being tested in our longer irradiations in ORR and HFIR.

VI. REFERENCES

1. ENDF/B-V Dosimetry File, National Neutron Cross Section Center, Brookhaven National Laboratory, 1979.

VII. FUTURE WORK

Integral data testing will be revised according to the new ENDF/B-V cross section data. A report will be published detailing our evaluations and all OFE dosimetry will be standardized.

I. PROGRAM

Title: Damage Analysis and Dosimetry Radiation Damage Analysis
Principal Investigators: A. N. Goland and G. F. Dell
Affiliation: Brookhaven National Laboratory

II. OBJECTIVE

Radiation damage analysis studies associated with the use of electrical insulators in fusion reactors.

III. RELEVANT DAFS PROGRAMS PLAN TASK/SUBTASK

SUBTASK II.A.2.3Flux Spectral Definition in FMIT

SUBTASK II.B.l Calculation of Displacement Cross Sections

IV. SUMMARY

Ionization-assisted displacement processes involving L shell ionization of atoms by primary knock-on atoms produced during neutron irradiation of carbon and Al_2O_3 have been evaluated for a benchmark and a FMIT spectrum.

V. ACCOMPLISHMENTS AND STATUS

Evaluation of Ionization-Assisted Displacements in Carbon and Al_2O_3: A. N. Goland, H. C. Berry, G. F. Dell and O. W. Lazareth (BNL).

Understanding of the radiation damage process in nonmetals is an important aspect of material development for fusion reactors. In addition to the damage processes that are important in metals, it is anticipated that additional mechanisms involving ionization will be important in some nonmetals. Our study of damage in nonmetals has included: 1) The assess-

ment of damage resulting from neutron initiated recoil atoms in monatonic and binary materials' and 2) the evaluation of damage produced by recoiling atoms following gamma ray interactions.[2] In the present report damage arising from a particular ionization mechanism associated with the inelastic energy loss of recoil atoms is estimated.

Yarlagadda and Robinson[3] have suggested that the Coulomb repulsion between a recoil atom and an atom it has ionized may he sufficient to produce displacements in nonmetals. The term ionization-assisted displacements is used to denote this process. They found that, for C^+-C ion-atom interactions, ionization-assisted processes involving the K shell of carbon should be small compared to neutron initiated recoil atom damage processes and that ionization-assisted processes involving the I, shell of silicon should exceed recoil atom damage when α particles having energy above 300 keV are incident on silicon.

We have assessed the role of ionization-assisted processes in producing displacements in nonmetals such as carbon and Al_2O_3 exposed to a typical neutron spectrum anticipated for the FMIT facility as well as to a benchmark spectrum having a wall loading of 1 MW/m^2.

The approach of Yarlagadda and Robinson has been used to determine the ionization-assisted stopping cross section $S_I(T)$:

$$S_I(T) = \sigma_I^i(T)\Delta E_d' \qquad (1)$$

where $\sigma_I^i(T)$ is the ionization cross section for the i-th electronic shell, T is the recoil energy, and $\Delta E_d'$ is the energy lost in displacing an atom from its original site to twice the nearest neighbor distance. Typically a value of 10 eV has been used for $\Delta E_d'$.

We have focussed on the evaluation of ionization-assisted displacement processes involving L shell ionization of atoms by primary knock-on atoms produced during neutron irradiation of carbon and Al_2O_3. The model

of Fortner et al.[4] has been used to estimate the L shell ionization cross sections for the ion-atom systems of interest. A function $L'(T)$, analogous to the Lindhard function, describing the fraction of the PKA energy that is dissipated in displacement production has been evaluated for each ion-atom combination.

$$L'(T) = \frac{\sum_{T'=0}^{T} S_I(T')\Delta T'}{\sum_{T'=0}^{T} [S_n(T') + S_e(T')]\Delta T'} \qquad (2)$$

In Eq. (2), $S_n(T)$ and $S_e(T)$ are the nuclear and electronic stopping cross sections, respectively, and $S_I(T)$ is defined in Eq. (1).

For ion velocities less than the Bohr velocity, $v_o = e^2/\hbar^2$, S_e has been assumed to increase linearly with velocity to the value of Land and Brennan.[5] Between v_o and $2v_o$, S_e increases linearly with a different slope, and for velocities of $2v_o$ and above Ziegler's[6] method has been used to extend the stopping cross section of protons[7] to other ions. The variation with PKA energy of the Lindhard damage function $L(T)$ and the ionization-assisted damage function $L'(T)$ is shown in Fig. 1.

The ionization-assisted damage energy function has been evaluated for carbon atoms recoiling in carbon as well as for O and Al atoms recoiling in Al_2O_3. These functions have been used in the damage program DON[8] to obtain the number of ionization-assisted displacements. The Kinchin-Pease relation has been used to relate the number of displacements N_d to the damage energy $\nu(T)$.

$$N_d = \frac{0.8\,\nu(T)}{2E_d}$$

with E_d = 10 eV.

Carbon. The ionization damage energy functions L'(T) for the K shell and the L shell were evaluated using Eq. (2). The K shell ionization cross section was obtained by using the data of Fortner et al.[4] for C^+-C ion-atom collisions with ion energies up to 1.5 MeV: above 1.5 MeV the cross section was assumed to be constant.

The L shell ionization cross section for carbon was evaluated using the model of Fortner et al.[4] The parameters used in chis evaluation will be discussed in a separate section.

The number of ionization-assisted displacements/neutron was determined for tlic FMIT spectrum as well as for a benchmark spectrum. These spectra are shown in Fig. 2. Also, the number of recoil atom displacements induced by elastic collisions was evaluated using the standard Lindhard function" in DON and a displacement energy of 25 eV.

A comparison of the displacements produced by K shell and L shell ionization with the number of recoil atom displacements is made in Table I. In agreement with the conclusions of Yarlagadda and Robinson, we find that ionization-assisted displacements involving the K shell of carbon are small compared to recoil atom displacements. On the other hand, displacements produced by L shell ionization are comparable to recoil atom displacements.

Al_2O_3. The assumption was made that tlic Bragg rule is valid for the nuclear stopping cross section S_n, the electronic stopping cross section S_e, and the ionization-assisted stopping cross section S_I. Denoting the atomic fraction of aluminum and oxygen as $\rho(Al)$ and $\rho(O)$, respectively, and the total stopping cross section $S_T = S_n + S_e$, and defining $S_k(i,j)$ as the stopping power of type k for a recoil atom of type i in material of type j, Eq. (2) becomes, for an aluminum PKA:

$$L'_{Al}(T) = L'(Al,Al) + L'(Al,O) = \frac{\sum_{T'=0}^{T} [\rho(Al)S_I(Al,Al)+\rho(O)S_I(Al,O)]\Delta T'}{\sum_{T'=0}^{T} [\rho(Al)S_T(Al,Al)+\rho(O)S_T(Al,O)]\Delta T'} \quad (4)$$

and, for an oxygen PKA:

$$L'_O(T) = L'(O,Al) + L'(O,O) = \frac{\sum_{T'=0}^{T} [\rho(Al)S_I(O,Al)+\rho(O)S_I(O,O)]\Delta T'}{\sum_{T'=0}^{T} [\rho(Al)S_T(O,Al)+\rho(O)S_T(O,O)]\Delta T'} . \quad (5)$$

Evaluation of the ionization-assisted stopping cross section $S_I(i,j)$ for the L shell requires knowledge of the four ionization cross sections $\sigma_I^L(Al,Al)$, $\sigma_I^L(Al,O)$, $\sigma_I^L(O,Al)$, and $\sigma_I^L(O,O)$. These cross sections have been evaluated using the model of Fortner et al.

The quantity $L'(i,j)$ denotes the fraction of the total energy loss by recoil atom i in material j that is dissipated through ionization-assisted processes. Each of the four functions $L'(i,j)$ was evaluated at 47 energies between 100 eV and 20 MeV. The results were used in DON to provide a lookup table for relating PKA recoil energy to damage energy. Displacements were obtained using the Kinchin-Pease relation with a displacement energy of 10 eV. DON gives the displacements per spectrum averaged neutron per cm^2 for each function $L'(i,j)$. These displacements we denote as $n'(i,j)$.

As an example, the number of oxygen atoms displaced by a recoiling aluminum atom is expressed as $disp(Al,O)$:

$$disp(Al,O) = \rho(Al)Nn'(Al,O)\Phi = 0.4Nn'(Al,O)\Phi \quad (6)$$

where N and 3 arc, respectively, the total number of atoms/cm^3 and the fluence. Tlie displacements per atom are obtained by adding the results for different species of PKA's and then dividing by N.

$$dpa(Al) = [0.4\ n'(Al,Al) + 0.6\ n'(O,Al)]\Phi$$
$$dpa(O) = [0.4\ n'(Al,O) + 0.6\ n'(O,O)]\Phi. \quad (7)$$

The importance of ionization-assistcd processes relative to other recoil atom damage processes has been assessed by using the displacement functions n(i,j) generated by Parkin and Coulter[9] for Al_2O_3. These functions are analogous in form to the ionization-assisted functions L'(i,j). They are uscd in DON, and the results are combined using Eq. (7). In this case displacement energies of 18 and 72 eV[10] have been used for aluminum and oxygen, respectively.

The results of the evaluation of ionization-assisted and rccoil atom damage proccsscs are summarized in Table II. Ionization-assisted processes appear to be important in producing oxygen displacements, hut they arc comparatively unimportant in producing aluminum displacements. This comparison will be discussed further in the section titled Conclusions.

The formalism used to obtain the ionization-assisted damage functions L'(i,j) can also be used to generate rccoil atom displacement functions similar to the Parkin-Coulter functions if the ionization-assisted stopping cross sections $S_I(i,j)$ in Eqs. (4) and (5) arc replaced with the nuclear stopping cross sections $S_n(i,j)$. Such functions have been evaluated and have been used in DON to obtain an independent estimate of rccoil atom damage. As before the displacement energies for aluminum and oxygen are 18 and 72 eV. These results also appear in Table II.

Cross Sections. Few experimental data exist for L shell ionization cross sections in ion-atom collisions. Consequently the L shell ionization cross sections used for the present evaluation were obtained by using the model

of Fortner et al.[4] The cross section is based on level crossing and is expressed as:

$$\sigma_I = 4\pi\alpha r^2[Q_3(y/v) - Q_3(2y/v)], \tag{8}$$

where v is the relative velocity at infinite separation, y is related to the coupling between the states of the ion-atom system, α is the probability that a particular level crossing occurs, and r is the separation at level crossing. The term $[Q_3(y/v) - Q_3(2y/v)]$ is a universal function with

$$Q_3(x) = \int_1^\infty \exp(-xt)t^{-3}dt. \tag{9}$$

This theory gives a good fit to the C^+-C K shell ionization cross section data when $y = 5.75(\text{kev/amu})^{1/2}$. The optimum fit to Ne-Ne K shell data is obtained for $y = 7.15(\text{kev/amu})^{1/2}$ and the optimum fit to the Ar-Ar L shell data'' is obtained with $y = 1.4(\text{keV/amu})^{1/2}$.

We have used $y = 1.4(\text{keV/amu})^{1/2}$ when evaluating the L shell cross sections for C, O, and Al. In addition, as suggested in [4], we have used $\alpha = 1$ and have used as the separation at level crossing the sum of the atomic radii of the L shells of the recoil and target atoms.

Conclusions. The ionization cross sections have been generated using "reasonable" parameters. However, these cross sections are at best approximate; the actual cross sections could be larger or smaller than those obtained from the model of Fortner et al. Since the ionization-assisted stopping cross section varies linearly with the ionization cross section, these uncertainties are propagated to our results.

On the basis of this evaluation, we draw the following conclusions concerning ionization-assisted damage:

1. Using experimentally determined cross sections for the K shell of carbon, the ionization-assisted dpa rate induced by carbon ions in carbon is less than 5% of the dpa rate produced by recoil atoms.

2. Using carbon L shell ionization cross sections evaluated from Eq. (8), the number of dpa from ionization-assisted processes is 1.6 times that produced by recoil atoms for the FMIT spectrum of Fig. 2 and is 0.85 times the number of dpa from recoil atoms for the benchmark spectrum of Fig. 2.

3. In Al_2O_3 the number of dpa for aluminum is 7.1% and 5.2% of the dpa from recoil atoms for the FMIT and benchmark spectra, respectively, and for oxygen the number of dpa is 47% and 34% of that for recoil atoms for the FMIT and benchmark spectra, respectively. Tnspection of Table II reveals that the dpa rates for aluminum and oxygen from ionization-assisted processes differ by about a factor of three; the large difference between the ratios of dpa from ionization-assisted processes *to* dpa from recoil atom damage is enhanced by the relatively small displacement energy of 18 eV used for aluminum and the relatively large displacement energy of 72 eV used for oxygen when evaluating recoil atom damage.

VI. REFERENCES

1. A. N. Goland, H. C. Berry, G. F. Dell, and O. W. Lazareth, Damage Analysis and Fundamental Studies Quarterly 'Technical Progress Report, October-December 1978, p. 26, DOE/ET-0065/4.

2. A. N. Goland, H. C. Berry, C. F. Dell, and O. W. Lazareth, Damage Analysis and Fundamental Studies Quarterly Technical Progress Report, January-March 1979, p. 42, DOE/ET-0065/5.

3. B. S. Yarlagadda and J. L. Robinson, Journal of Nuclear Elaterials 63 (1976) 466.

4. R. J. Fortner, B. P. Curry, R. C. Der, T. M. Kavanagh, and J. M. Khan, Phys. Rev. 185 (1969) 164.

5. D. J. Land and J. G. Brennan, Atomic Data and Nuclear Data Tables 22 (1978) 235.

6. F. J. Ziegler, Applied Physics Letters 31 (1977) 544.

7. H. H. Andersen and J. F. Ziegler, Stopping Powers and Ranges, Vol. 3, Pergamon Press, New York, 1977.

8. D. M. Parkin and A. N. Goland, Rad. Effects 28 (1976) 31.

9. D. M. Parkin and C. A. Coulter, Journal of Nuclear Materials 85 & 86 (1979) 611.

10. G. P. Pells and D. C. Phillips, Journal of Nuclear Material 80 (1979) 207.

11. R. K. Cacak, Q. C. Kessel, and M. E. Rudd, Phys. Rev. A 2 (1970) 1327.

VII. FUTURE WORK

Future work will include efforts to improve the assessment of ionization-assisted damage by improving the evaluation of ionization cross sections as well as by using a more realistic value than $E_d' = 10$ eV for the energy expended in displacing an atom during an ionization-assisted displacement process.

The formalism used in generating displacement functions for binary materials will be used to evaluate displacement functions for more complicated materials.

In addition, the role of Bremsstrahlung from a D-T plasma in producing defects in nonmetals will be considered.

TABLE 1

IONIZATION-ASSISTED DISPLACEMENT RATES FOR K SHELL IONIZATION OF CARBON (K-ION), L SHELL IONIZATION OF CARBON (L-ION), AND NEUTRON INDUCED RECOIL ATOM DAMAGE IN CARBON FOR AN FMIT SPECTRUM AND A BENCHMARK SPECTRUM. Φ IS THE TOTAL FLUENCE PER YEAR BASED ON A 100% DUTY FACTOR.

	FMIT Flux = $1.56 \cdot 10^{15}$ n/cm^2·sec			Benchmark Flux = $3.81 \cdot 10^{14}$ n/cm^2·sec		
	K(Ion)	L(Ion)	Recoil	K(Ion)	L(Ion)	Recoil
$\bar{\sigma}_d$(barns)	29.0	1200	730.3	8.7	547.6	642.3
$\frac{dpa}{yr}$	1.42	5'3.0	35.9	0.10	6.57	7.71
$\frac{dpa(Ion)}{dpa(Recoil)}$	0.04	1.61	----	0.013	0.85	----

TABLE 2

DISPLACEMENT RATES OF OXYGEN *AND* ALUMINUM IN Al_2O_3 FOR: IONIZATION-ASSISTED PROCESSES RESULTING FROM L SHELL IONIZATION, NEUTRON INDUCED RECOIL ATOM DAMAGE USING THE PARKIN *AND* COULTER DISPLACEMENT FUNCTIONS (P-C), AND NEUTRON INDUCED RECOIL ATOM DAMAGE USING DISPLACEMENT FUNCTIONS OBTAINED WHEN $S_I(T)$ IS REPLACED BY $S_n(T)$ IN EQUATIONS 4 AND 5 (BNL). Φ IS THE TOTAL FLUENCE PER YEAR BASED ON A 100% DUTY FACTOR.

		FMIT Flux = $1.56 \cdot 10^{15}$ n/cm^2·s Φ = $4.92 \cdot 10^{22}$ n/cm^2·yr		Benchmark Flux = $3.81 \cdot 10^{14}$ n/cm^2·s Φ = $1.20 \cdot 10^{22}$ n/cm^2·yr	
		Al	O	Al	O
Ion, Assisted	$\bar{\sigma}_d$(barns)	78.9	200.6	37.3	94.0
	dpa/yr	3.88	9.86	0.45	1.13
Recoil Parkin-Coulter	$\bar{\sigma}_d$(barns)	1115.0	428.8	723.6	280.1
	dpa/yr	54.9	21.1	8.68	3.36
Recoil BNL	$\bar{\sigma}_d$(barns)	1415.0	398.4	970.4	285.9
	dpa/yr	69.6	19.6	11.64	3.43
	$\frac{dpa(Ion)}{dpa(P-C)}$		0.468	0.052	0.336
	$\frac{dpa(Ion)}{dpa(BNL)}$	0.056	0.503	0.039	0.329

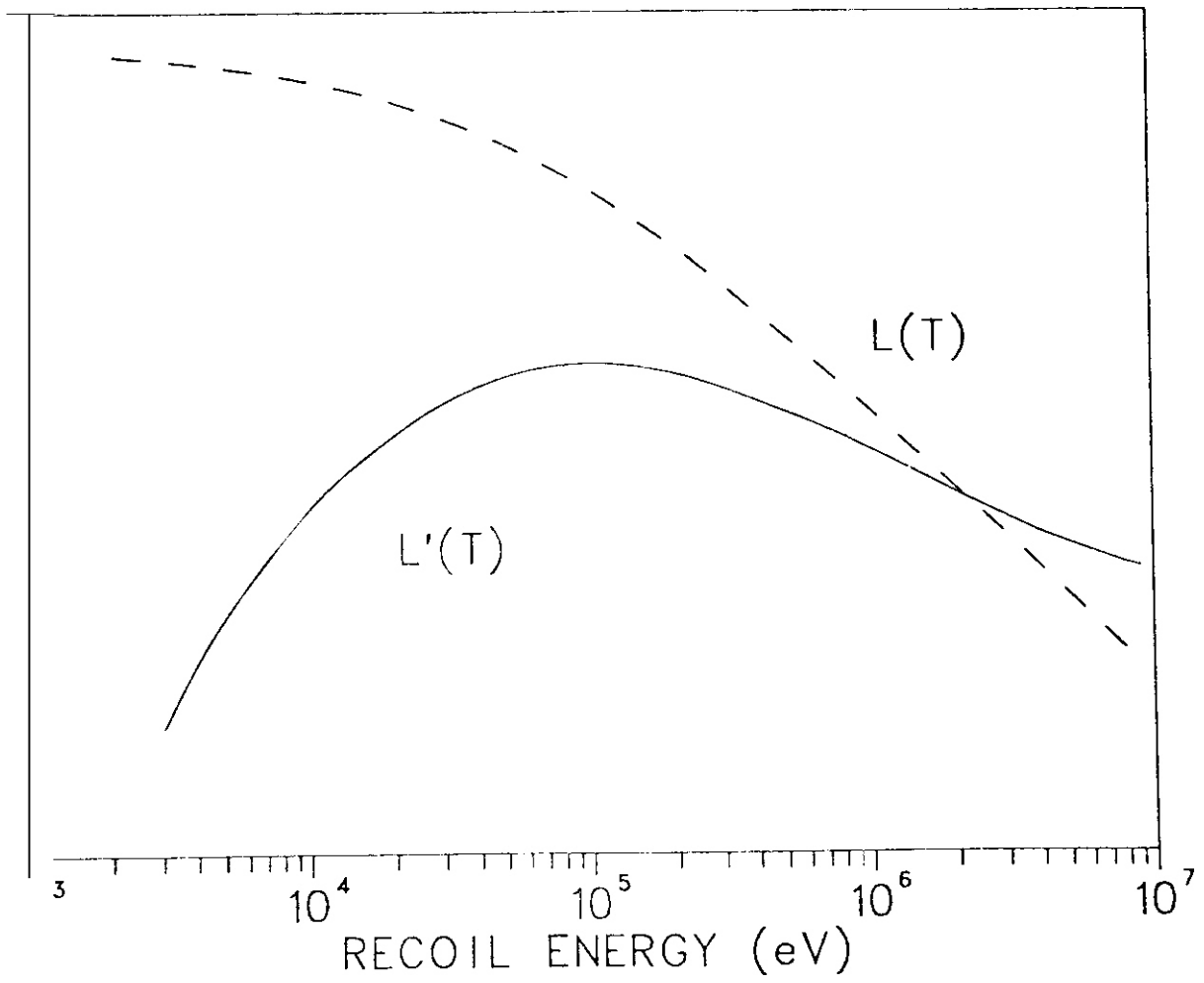

FIGURE 1. Energy dependence of the Lindhard function and the damage function L'(T).

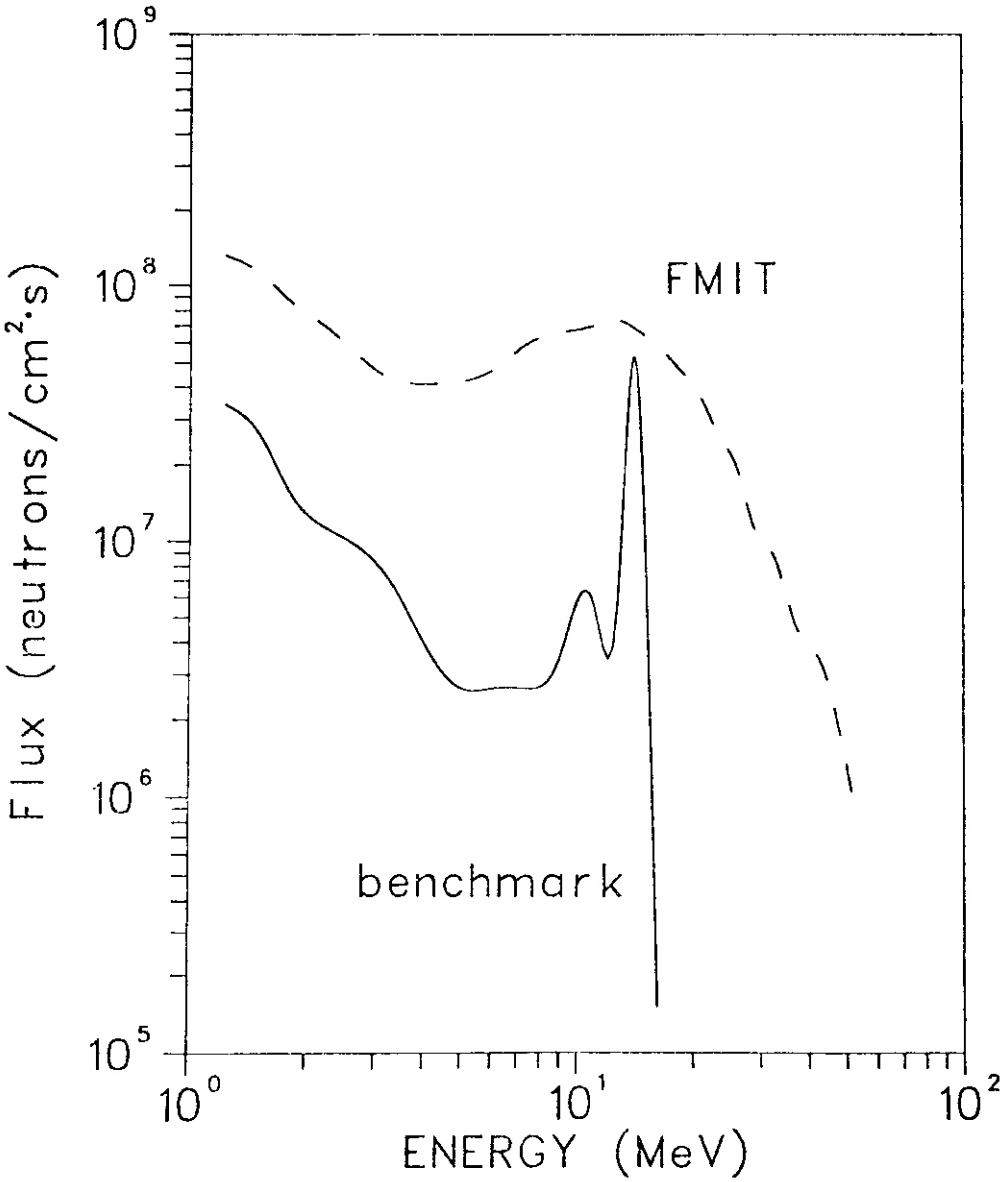

FIGURE 2. **Neutron spectra used to evaluate ionization-assisted damage. Benchmark spectrum:** 1 MW/m^2, **flux** = $3.81 \cdot 10^{14}$ n/cm^2·s. **FMIT spectrum: obtained from coupled** n-γ **transport calculation for 0.1 A of 35 MeV deuterons incident upon a 1 cm high, 2 cm thick,** and **3 cm wide lithium target. Flux** = $1.56 \cdot 10^{15}$ n/cm^2·s.

I. PROGRAM

Title: Damage Analysis
Principal Investigator: M. T. Robinson
Affiliation: Oak Ridge National Laboratory (ORNL)

II. OBJECTIVE

The objective of this work is to construct both atomistic and continuum (transport theory) models of collision cascade development in solids and to apply these models to radiation damage production, to sputtering, and to plasma particle backscattering problems.

III. RELEVANT DAFS AND PMI TASK/SUBTASK

DAFS SUBTASK II.B.2.3:	Cascade Production Methodology
PMI SUBTASK III.B.1.3:	Development of Theoretical Model Descriptions of Reflection and Backscattering
PMI SUBTASK III.C.1.6:	Development of Theoretical Models for Physical and Physichemical Sputtering

IV. SUMMARY

Recent studies of displacement cascades in copper, generated by the binary collision cascade simulation program MARLOWE, are summarized. When cascades were generated in a static lattice by primary recoils of from 100 to 500 eV, anomalous behavior of both the mean number of Frenkel pairs and its variance was observed. The anomalies could be associated with primary recoils moving initially near <111> directions, which could not produce multiple defects below the <111> focusing

energy, roughly 250 eV. The anomalies are removed by including thermal displacements in the calculations. These greatly reduce the length and the number of <111> linear collision sequences.

V. ACCOMPLISHMENTS AND STATUS

A. Studies of Low Energy Displacement Cascades in the Binary Collision Approximation -- M. T. Robinson (ORNL)

The production of radiation damage in solids has been studied by computer simulation models of varying degrees of exactness.[1-6] Only the simplest models are computationally efficient enough to be applied at the relatively high primary recoil energies characteristic of fusion neutron environments. However, simple models such as the binary collision approximation (BCA) are of limited applicability at the low recoil energies which characterize the motion of most of the particles in a displacement cascade. An important aspect of modeling fusion neutron damage production is thus an understanding of the low energy behavior of the computer simulation codes which have been developed for high energy damage studies. This report summarizes some recent work in this area with the BCA code MARLOWE.[6-8]

A detailed study has been made of collision cascades generated in copper by primary recoils of initial kinetic energies, E_0, ranging from 10 to 500 eV. At each energy, a set of 1000 isotropically distributed primary particles was used. The quasielastic scattering of particles in a cascade was governed by the Molière approximation to the Thomas-Fermi interatomic potential with the screening length a_{12} = 7.38 pm. All collisions with impact parameters less than p_m were considered, with $p_m/\underline{a}$ = 0.62, where $\underline{a}$ = 0.3615 nm is the lattice constant of Cu. Target atoms were added to the cascade if they received kinetic energy in a collision exceeding E_m = 5.0 eV. All displaced atoms were required to surmount a binding energy E_b = 0.2 eV

and were followed until their energies fell below E_c = 4.8 eV. The value of E_b was chosen by comparing six linear collision sequences (LCSs) evaluated with MARLOWE with the same events evaluated with the classical dynamical code COMENT.[3] With the parameters chosen, MARLOWE represents the length of <110> LCSs fairly accurately, but overestimates the length of <100> and <111> LCSs. Inelastic energy losses were included in the calculations using a model described previously.[6] When thermal displacements of the lattice atoms were wanted, the Oebye temperature θ_D = 314 K was used. MARLOWE organizes Frenkel defect pairs into classes based mainly on the separation between the paired interstitial and vacancy.[7] Pairs remaining after removing all interstitials located in an 18-site instability region about each vacancy are termed "distant". These in turn are organized according to whether or not their separation exceeds a vacancy capture radius r_v.

Figure 1 shows the energy dependence of $\langle\nu\rangle$, the mean number of distant Frenkel pairs, for several cases. It is convenient to discuss first the results for the static lattice with r_v = 0. In this case, the curve shows three inflections, indicated in the figure by the letters *a* (≈ 50 eV), *b* (≈ 125 eV), and c (≈ 310 eV). Below *a*, the curve shows well-marked threshold behavior, similar to that expected from a Kinchin-Pease model' with a threshold energy of about 20 eV. Near *a*, defect multiplication begins to be important and the curve rises approximately linearly to the point *b*, again consistently with Kinchin-Pease model. From *b* to c, however, although the curve is still plausibly linear, its slope is significantly less. Above c, finally, the slope increases again to something like its original value. When the value $r_v/\underline{a}$ = 2 is used to remove the Frenkel pairs of smallest separation, the energy dependence of $\langle\nu\rangle$ is similar, but the threshold is less well-marked and the inflections are moved to different values, marked *d* and *e* in the figure. The introduction of thermal displacements corresponding to room temperature completely

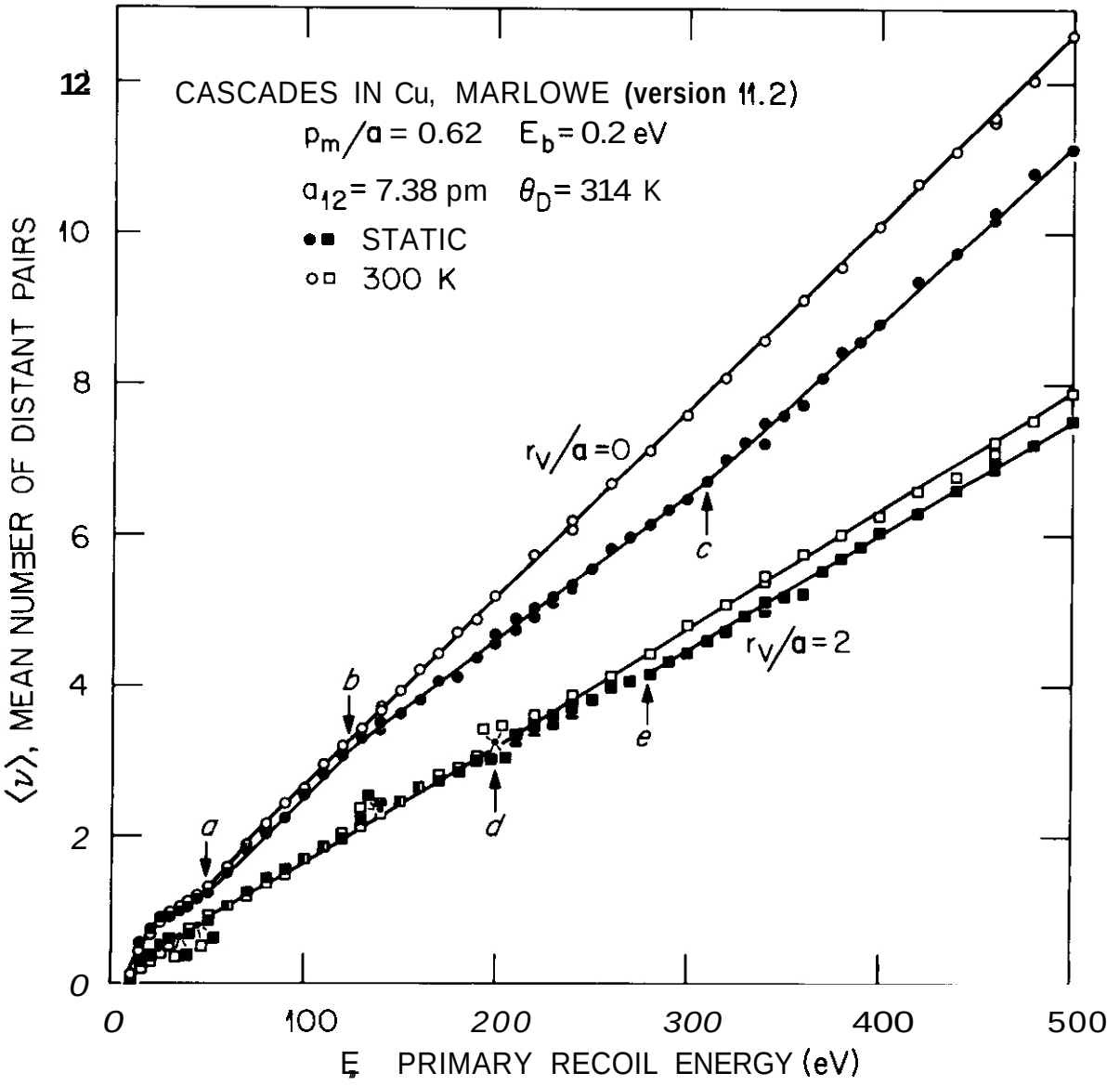

FIGURE 1. The mean number of distant Frenkel pairs produced by Cu atoms recoiling in Cu.

eliminates the inflections *b*, *c*, *d*, and *e*, without altering much the threshold region.

Leibfried[10] found that for the Kinchin-Pease model, the variance of the number of distant pairs was a linear function of the energy, that is, that

$$\sigma^2/m \equiv [\langle\nu^2\rangle - \langle\nu\rangle^2]/\langle\nu\rangle = 4 \ln 4/3 - 1 = 0.1507 \quad \ldots \quad E > 4\,E_d \,.$$

This quantity, the scaled variance, is plotted in Fig. 2 for the MARLOWE cascades with $r_v = 0$. The hard-core result is shown for an assumed E_d value. Below about 80 eV, the computer simulations are all much alike and differ from the hard-core result only because there is no sharp threshold in the calculation. The simulations including thermal displacements show σ^2/m to **be** constant above about 80 eV at 300 K or about 140 eV at 0 K. In sharp contrast to this behavior, however, is that of the static lattice simulations. Here, σ^2/m continues to rise until a maximum is reached near 260 eV and then decreases. The behavior above 500 eV has not yet been examined.

Detailed examination of the simulations shows that the anomalies in both figures can be associated with primary recoils starting near the <111> directions. Multiple defects are substantially prevented from being formed as long as E_0 is less than the <111> focusing energy, about 250 eV for the potential used in the calculations.[3,11] At higher energies, multiple defects are formed by <111> primaries, but, up to 500 eV, not as copiously as for primaries starting in other directions. Approximately 5 percent of the primary particles can be assigned to the <111> region, that is, to a cone about a <111> direction with a half-angle of about 9 degrees.

The static crystal results may be interpreted in terms of a simple modification of the Kinchin-Pease model originally proposed to describe the effects of channeling.[7,8] In this model, in addition to

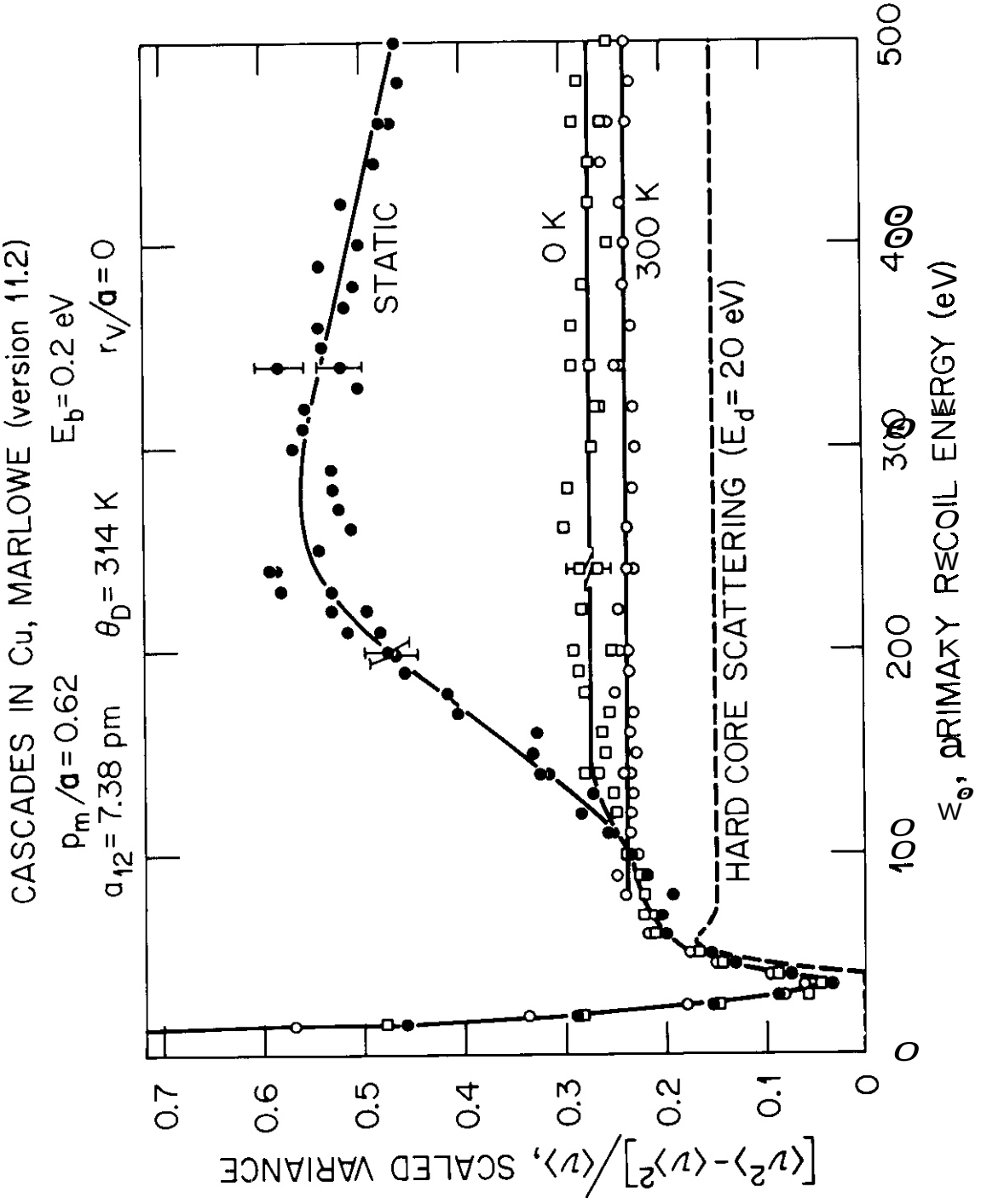

FIGURE 2. The scaled variance of the number of distant Frenkel pairs produced by Cu atom recoiling in Cu.

the usual assumptions, it is imagined that each particle in the developing collision cascade has an energy-independent probability p of slowing down to rest without producing further displacements. This feature, though originally assigned a different physical origin, can clearly be assigned equally well to <111> LCS production. In this model,[12]

$$\langle\nu\rangle \sim [E/2E_d]^{1-2p}$$

and the scaled variance can be written as[13]

$$\sigma^2/m \sim \langle\nu\rangle \ .$$

The latter dependence accounts for the results in Fig. 2. Furthermore, if the data from Fig. 1 are replotted bilogarithmically, the static crystal results are fit very well over the energy range up to about 350 eV by the value p = 0.05, in complete agreement with the size of the <111> region. The 300 K results, in contrast, require p = 0.

Thus, a consistent picture emerges in which all of the anomalies shown in Figs. 1 and 2 for the static lattice simulations can be attributed to the dynamics of <111> LCSs. The introduction of thermal displacements into the model removes the anomalies by interfering with the propagation of these sequences. It seems probable, therefore, that thermal energy plays a significant role in the development of displacement cascades in the energy range below ~ 1 keV and must be included in computer simulation models to obtain correct results.

VI. REFERENCES

1. J. B. Gibson, A. N. Goland, M. Milgram, and G. H. Vineyard, Phys. Rev. 120, 1229 (1960).

2. A. Scholz and C. Lehmann, Phys. Rev. B 6, 813 (1972).

3. J. O. Schiffgens, O. M. Schwartz, R. G. Ariyasu, and S. E. Cascadden, Radiation Effects 39, 221 (1978).

4. H. L. Heinisch, J. O. Schiffgens, and D. M. Schwartz, J. Nucl. Mater. 85/86, 607 (1979).

5. J. R. Beeler, Jr., Phys. Rev. 150, 470 (1966).

6. M. T. Robinson and I. M. Torrens, Phys. Rev. B 9, 5008 (1974).

7. M. T. Robinson, Solid State Oiv. Annu. Proq. Rep. April 30, 1977, ORNL-5328, pp. 12-15.

8. M. T. Robinson, Damage Analysis and Fundamental Studies Quart. Prog. Rep., October-December 1978, DOE/ET-0065/4, pp. 73-76.

9. G. H. Kinchin and R. S. Pease, Rep. Prog. Phys. 18, 1 (1955).

10. G. Leibfried, Nukleonik 1, 57 (1958).

11. D. K. Holmes and M. T. Robinson, Solid State Div. Annu. Rep. Oec. 31, 1975, ORNL-5135, pp. 16-18.

12. O. S. Oen and M. T. Robinson, Appl. Phys. Lett. 2, 83 (1963).

13. M. T. Robinson, Phil. Mag. 12, 741 (1965).

I. PROGRAM

Title: Irradiation Effects Analysis (AKJ)
Principal Investigator: D. G. Doran
Affiliation: Hanford Engineering Development Laboratory

II OBJECTIVE

The objective of this work is to develop computer models for the simulation of high energy cascades which will be used to generate defect production functions for correlation analyses of radiation effects.

III. RELEVANT DAFS PROGRAM TASK/SUBTASK

SUBTASK II.B.2.3 Cascade Production Methodology

IV. SUMMARY

Cascades generated with two versions of MAKLOWE, using high and low displacement energies, are compared. Raising the displacement energy makes feasible the simulation of higher energy cascades. Defect yields consistent with resistivity measurements are obtained from both models by application of different energy independent recombination volumes. The resulting cascades are then compared after annealing with the stochastic cascade annealing simulation code SCAS, and calibration factors are determined for the high displacement energy version. The factors are independent of energy over the calibration range of 5 to 30 keV.

V. ACCOMPLISHMENTS AND STATUS

A. Modeling of Defect Production in High Energy Cascades in FCC Metals - H. L. Hcinisch, Jr. (HEDL)

1. Introduction

As reported in an earlier DAFS Quarterly Progress Report, (1) cascades generated with two versions of MARLOWE, using high and low displacement energies, E_d, were compared before and after annealing with the simulation code SCAS. The nature of the relatively small differences between defect yields by the two versions suggested that a simple adjustment scheme, based on defect yields, would allow the more efficient high E_d versions to be simply calibrated against the lower version, which has been carefully checked against dynamical simulations. Progress toward that calibration is reported on here.

2. Calibration Procedure

In the earlier report only two different primary knock-on atom (PKA) energies had been used in the comparison of high and low E_d versions, 5 and 20 keV. Sets of 30 keV cascades have now been generated with the two versions. Also, cascades of 60 and 100 keV have been generated using only the high E_d version.

The calibration of the high E_d version against the low E_d version was accomplished by determining multiplicative correction factors for the defect yields at three stages of cascade development. The first stage is the pre-annealing or "quenched cascade" stage. This represents the cascade, produced at low temperature (4 K), such that no thermally activated annealing takes place. The cascades calculated with MARLOWE are first reduced so that the numbers of defects are consistent with resistivity measurements on specimens ion irradiated at 4 K. This is done by imposing an effective spontaneous recombination radius, R, to simulate the recombination which occurs during the localized quenching of the highly excited cascade region.

Defect yields as a function of R were determined in both versions of MARLOWE at intervals of 0.25 lattice parameters, and the values of

PKA Energy (keV)	Defect Pairs		
	ν_5	1.22 ν_{17}	.87 ν_{exp}
5	18	17	17
20	59	55	57
30	78	77	79
60	-	154	153
100	-	233	231

TABLE 2

COMPARISON OF HIGH (ν_{17}) AND LOW (ν_5) DISPLACEMENT ENERGY VERSIONS OF MARLOWE CASCADES AFTER STAGE III ANNEALING

PKA Energy, keV	Defect Pairs			Free Vacancies		Free Interstitals	
	ν_5	1.31 ν_{17}	.7 $\nu_{e:}$	V_5	V_{17}	I_5	1.38 I_{17}
5	16	14	14	8	5	10	14
20	50	52	46	17	20	41	41
30	65	64	63	23	20	50	50
60	-	116	123	-	44	-	81
100	-	189	186	-	77	-	144

R giving yields closest to the measured value were used. For high E_d (E_d = 17 eV) R is 3.0 lattice parameters, and for low E_d (E_d = 5 eV) R is 5.5 lattice parameters. For both high and low E_d the recombination radius is independent of energy.

The second stage at which the two versions were compared is at a simulated time (τ) equal to 1000 jumps of a single interstitial. This corresponds to Stage I annealing of isolated cascades, about 50 K in copper. In Table 1 the numbers of pairs at τ = 1000 determined from the E_d = 5 eV version (ν_5) are compared to those for the E_d = 17 eV version (ν_{17}) multiplied by a factor of 1.22 to make them agree with ν_5. In addition, the "experimental" values from resistivity data, ν_{exp}, are shown, multiplied by 0.87 to illustrate that the fraction of pairs recombined is constant at least in the energy range from 5 to 100 keV.

Table 2 contains defect pair yields, as well as free vacancy and free interstitial yields, at τ = END ($\sim 10^{12}$ interstitial jumps). This corresponds to about the end of Stage III annealing for an isolated cascade. At this stage of the simulation all mobile defects (interstitial clusters of size 3 or less and vacancy clusters of size 4 or less) have either clustered, recombined, or left the cascade region. No dissociation of clusters has taken place. At this stage a somewhat larger factor, 1.31, is needed to correlate the number of pairs produced b.v the hiqh and low E_d versions. The yields are still a constant fraction of the experimental values at all energies.

The number of free vacancies is about the same by either version, while the number of free interstitials gives the best fit when adjusted by the factor 1.38. Since the pairs and the free interstitials are adjusted by about the same factor, the fraction of remaining interstitials which is free is about the same for both high and low E_d versions. However, for E_d = 17 eV the fraction of remaining vacancies which is mobile is much larger than for E_d = 5 eV, although the total numbers are about the same for each version.

3. Discussion

The high E_d value effectively truncates long replacement sequences. With high E_d the interstitials of a cascade are in closer proximity to the vacancies as well as to each other. Therefore, one expects and observes more recombination and more clustering of interstitials hence fewer free interstitials, with the high value of E_d. The additional recombination evidently changes the average density of the vacancy distribution as well as its size. Once the vacancies become mobile the number which forms clusters is a smaller percentage of the pre-anneal number of defects. The distribution of pre-anneal defects after annealing is given in Table 3. The values are averages for a total of thirty cascades from 5 to 30 keV for each of the E_d values. The average pre-anneal number of defects at each energy is the same for both values of E_d.

TABLE 3

DISTRIBUTION OF PRE-ANNEAL DEFECTS AFTER ANNEALING

E_d(eV)			
5	Recombined	30%	
	Clustered	42%	11%
	Mobile	28%	59%
17	Recombined	47%	47%
	Clustered	25%	14%
	Mobile	28%	39%

The two sets of cascades at the pre-anneal stage are defined by two parameters, E_d and R. In the calibration described above, the values of R are set so that each set of cascades has the "measured" number of defects before annealing. The adjustment factors applied after annealing make the number of defects correlate, but do not provide the locations of the added defects. An alternate method of calibrating the defect yields of high E_d MARLOWE cascades would be to increase the pre-anneal number of defects by decreasing R, such that the number of defects remaining after annealing is the same for both values of E_d. This has the advantage of maintaining some spatial distribution for all the residual defects. A first attempt at this procedure with 30 keV cascades indicates that the clustering of interstitials increases by about 50%. A comprehensive graphical analysis may be the best way to resolve the differences in spatial distribution resulting from using higher values of E_d.

VI. REFERENCES

1. H. L. Heinisch, Jr., DAFS Quarterly Progress Report, October-December 1979, DOE/ET-0065/8.

VII. FUTURE WORK

Techniques of graphical analysis of cascades are being developed to aid in further calibration of MARLOWE for high energy cascades.

I. PROGRAM

Title: Irradiation Effects Analysis (AKJ)
Principal Investigator: D. G. Doran
Affiliation: Hanford Engineering Development Laboratory

11. OBJECTIVE

The objective of this work is to determine the effects of high energy neutrons on damage production and evolution, and the relationships of these effects to effects produced by fission reactor neutrons. Specific objectives of current work are the planning and performance of an irradiation program at the Rotating Target Neutron Source (RTNS)-II at the Lawrence Livermore Laboratory (LLL) and postirradiation testing.

III. RELEVANT OAFS PROGRAM TASK/SUBTASK

SUBTASK II.B.3.2 Experimental Characterization of Primary Damage State; Studies of Metals

II.C.6.3 Effects of Damage Rate and Cascade Structure on Microstructure; Low-Energy/High-Energy Neutron Correlations.

II.C.11.4 Effects of Cascades and Flux on Flow; High-Energy Neutron Irradiations.

II.C.18.1 Relating Low- and High-Exposure Microstructures; Nucleation Experiments

IV. SUMMARY

Two additional ferritic alloys have been obtained for the RTNS-II metal stockpile. Preparations for HEDL 5, a high dose elevated temperature experiment at RTNS-II, are continuing. HEDL 4, the irradiation of both microtensile and disk specimens, was completed. Hardening has been

observed for copper, nickel and an Fe-Ni-Cr ternary, irradiated at RTNS-II to a fluence of about 3 x 10^{17} n/cm^2.

V. ACCOMPLISHMENTS AND STATUS

A. RTNS-II Irradiation Program - N. F. Panayotou (HEDL)

1. Specimen Preparation

Specimen fabrication for future irradiations is continuing. Stock material for two ferritic alloys, 057-B and 9A-1Mo, has been obtained from the Breeder Reactor Program advanced alloy stockpile.

A supply of Nb and Fe dosimetry foils were received from LLL. These foils will be laser engraved and stored for use in future HEDL irradiations at RTNS-II.

2. Status of Irradiations

HEDL-4, a dual purpose irradiation containing both microtensile and disk specimens was initiated and completed during this reporting period. This experiment will permit the direct correlation of tensile data with microhardness data on specimens fabricated from the same heat of material.

The HEDL-4 capsule was received on site, disassembled, and dosimetry foils returned to LLL for analysis. Preliminary microhardness testing is in progress.

3. Elevated Temperature Irradiation

HEDL-5, our first elevated temperature irradiation, is currently scheduled to begin in June. The objective is to accumulate exposure of at least 3 x 10^{19} ($\sim$0.1 dpa) at temperatures below 350°C on materials under consideration for the first wall of the ETF. Because of the long irradiation time required, the possibility of employing a dual-temperature zone furnace is currently being explored.

4. Microhardness Data

The results of microhardness testing of copper, nickel and an Fe-Ni-Cr ternary irradiated at RTNS-II are shown in Figures 1 to 3. The increase in diamond pyramid hardness is plotted as a function of fluence over the range of 2 to 12 x 10^{17} n/cm^2. E $\sim$14 MeV. The composition

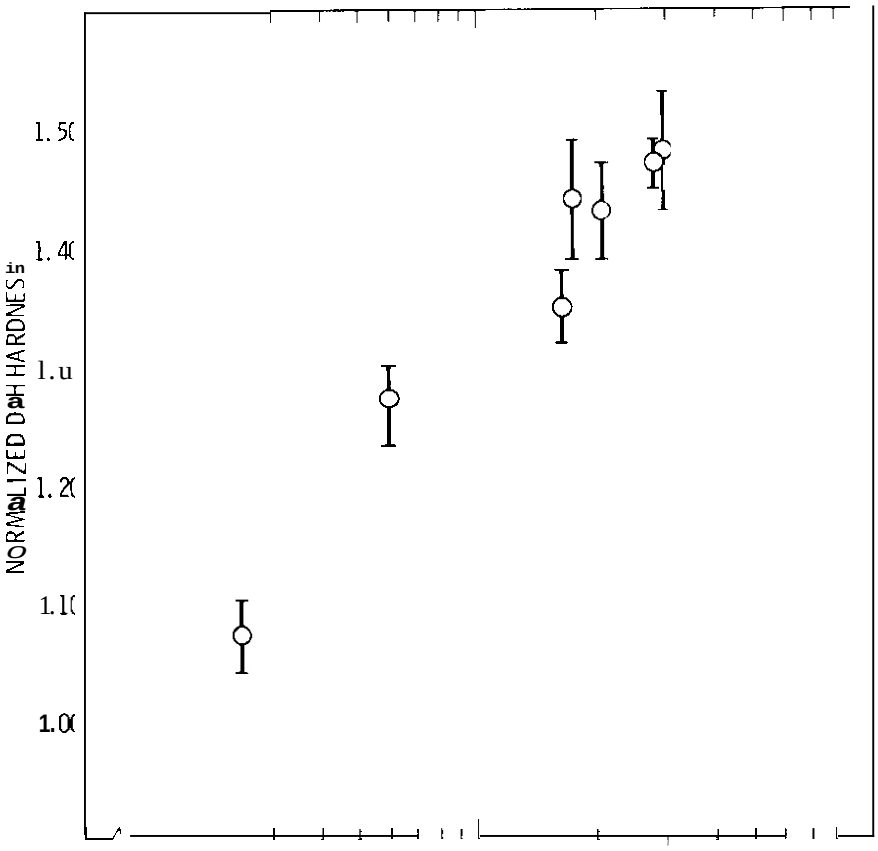

FIGURE 1. Normalized Diamond Pyramid Microhardness, 50 gm Load, for Copper TEM Disk Specimens, Irradiated with 14 MeV Neutrons at Ambient Temperature.

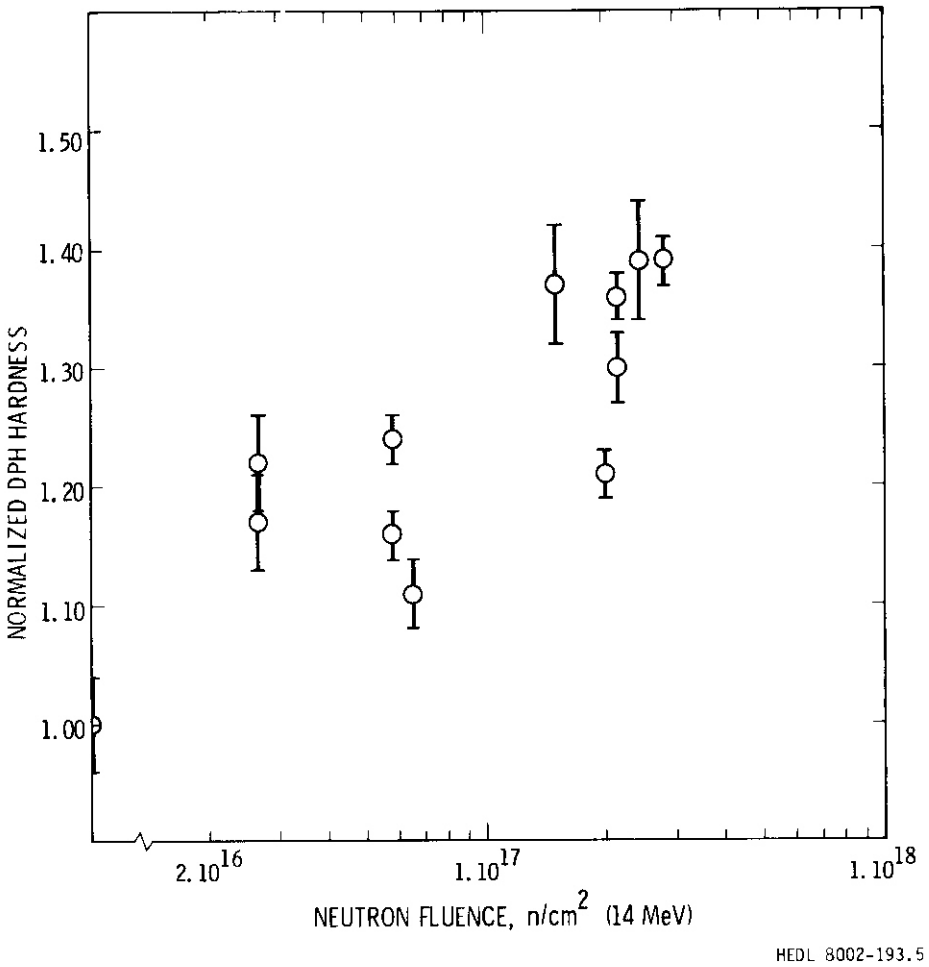

FIGURE 2. Normalized Diamond Pyramid Microhardness, 50 gm Load, for Nickel TEM Disk Specimens, Irradiated with 14 MeV Neutrons at Ambient Temperature.

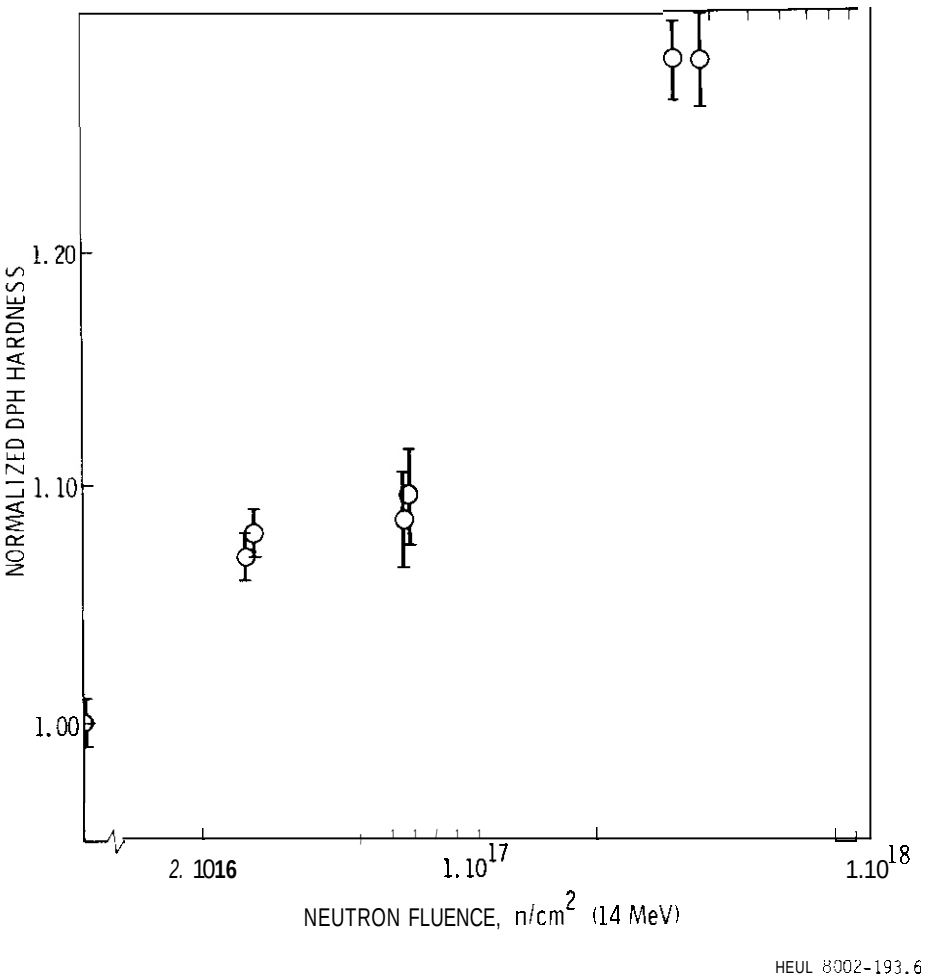

FIGURE 3. Normalized Diamond Pyramid Microhardness, 50 gm Load for Fe-Ni-Cr Ternary TEM Disk Specimens, Irradiated with 14 MeV Neutrons at Ambient Temperature.

of the metals tested is given in Table 1.

TABLE 1

METAL COMPOSITION[t]

ELEMENT	COPPER (ppm)	NICKEL (ppm)	Fe-Ni-Cr (percent)
Ni	<0.1	Balance	19.4
Cr	0.3	2.0	14.9
Mo	<0.1	0.25	--
Nb	<0.1	<0.1	--
Si	0.3	17	--
Mn	0.3	---	--
Zr	<0.1	0.65	--
Ti	<0.1	<0.1	--
Al	1.0	0.9	--
C	<10	15	0.003
B	---	---	--
W	<0.1	<0.1	--
O	2.0	12	0.018
Cu	Balance	---	--
Fe	0.8	20	Balance

[t]Weight Units

The prior histories of the specimens used for this study are given in Table 2.

TABLE 2

PRIOR HISTORY

METAL	AS RECEIVED CONDITION	HEAT TREATMENT
Copper	Annealed	400°C/15 min/FC
Nickel	Cold Worked	500°C/10 min/FC
Fe-Ni-Cr	Cold Worked	975°C/10 min/FC

FC: Furnace Cool

The heat treatments used for the Fe-Ni-Cr alloy and the nickel were sufficient to recrystallize the materials. Since the copper stock was received in an annealed condition our heat treatment served only as a stress relieving treatment.

Each data point shown in Figures 1 to 3 represents the average and range of at least three indents made on TEM disk specimens. The minimum load employed for microhardness testing was 50 gms. Tests were performed at room temperature using a standard Tukon microhardness testing instrument. Fluence data was derived from niobium dosimeters which bracketed the positions of the specimens.

Over about the same range in fluence the Fe-Ni-Cr alloy has sustained a thirty percent increase in hardness while the nickel and copper have sustained forty and fifty percent increases, respectively.

No hardening has been observed over the same range in fluence for the Path A and Path B alloys.

VI. REFERENCES

None

VII. FUTURE WORK

Microhardness testing on key disk specimens up to and including those irradiated in HEDL-4 will be completed. Irradiation experiments at Omega West Reactor at Los Alamos will be initiated. A high dose, elevated temperature experiment (HEDL-5) will be initiated at the RTNS-II.

I. PROGRAM

Title: Irradiation Effects Analysis (AKJ)
Principal Investigator: D. G. Doran
Affiliation: Hanford Engineering Development Laboratory

II. OBJECTIVE

The purpose of this study is to determine the effect of 14 MeV (d,T) neutron irradiation on the microstructural development and to correlate the microstructural development to mechanical property changes in metals of interest to the Fusion Reactor Development program. These results are to be compared with microstructural and mechanical property changes produced in specimens irradiated with fission reactor neutrons.

III. RELEVANT DAFS PROGRAM TASK/SUBTASK

SUBTASK II.B.3.2 Experimental Characterization of Primary Damage State; Studies of Metals

II.C.6.3 Effects of Damage Rate and Cascade Structure on Microstructure; Low-Energy/High-Energy Neutron Correlations

IV. SUMMARY

High purity (>99.99 wt.%) copper was irradiated at 25°C to a neutron fluence of 2.7 x 10^{17} n/cm^2 (E = 14 MeV) in the Rotating Target Neutron Source II (RTNS-II). The irradiation produced a high density (8 x 10^{16}/cm^3) of small (1 to 7 nm in diameter) defect clusters. For a given dynamical diffraction condition, the defect clusters produce black/white contrasts which are parallel to specific crystallographic directions. The defect clusters are considered to he platelets with Burgers vectors of $\frac{a}{2}$<111> and $\frac{a}{2}$<110>. Preliminary analysis of the defects by the "2-1/2 D" technique has

identified both vacancy and interstitial types of defect clusters. These visible defect clusters can account for about 80% of the increase in the yield strength of the irradiated material. However, they account for only about 40% of the estimated number of defects produced by the irradiation.

V. ACCOMPLISHMENTS AND STATUS

A. Microstructural Development in Copper Irradiated in RTNS-II - H. R. Brager, H. L. Heinisch and N. F. Panayotou (HEDL)

1. Introduction

Designing fusion reactor components requires estimates of the effects that high energy neutrons have on macroscopic material properties. The RTNS-II facility permits studies of the effect of 14 MeV neutron irradiation on material behavior. The limited high-flux test volume encourages strong emphasis on microstructural studies since the specimens are small in size. Mechanical behavior can be inferred from microhardness measurements on the same specimens.

This report is the initial contribution of a series of examinations which will describe the microstructural development in metals irradiated with 14 MeV (d,T) neutrons in RTNS-II. The material, high purity copper, was chosen (1) to provide a base point for comparing the TEM results with (a) theoretical modeling predictions of defect clusters formed in a simple material bombarded with high energy particles and with (b) macroscopic material property changes, and (2) to determine the influence of minor and major alloying additions on the microstructure which evolves during high energy neutron irradiation.

2. Experiment

Table 1 gives the compositions of the copper specimens studied at HEDL and LLL. The preparation of samples and their irradiation with 14

TABLE 1

CHEMICAL ANALYSIS OF IMPURITY ELEMENTS IN COPPER SPECIMENS

Element	Mackay (RTNS-II) (HEOL)	LLL Stores Grade[6]	Cominco (LLL)[6]
Be	-	30.	<1.
O	2.00	-	-
Mg	<0.10	4.	10.
Si	0.30	100.	150.
Al	1.00	<3.	<3.
S	0.50	-	-
Ca	0.40	25.	2.
Cr	0.30	-	-
Fe	0.80	300.	400.
Co	-	<10.	<10.
Ni	<0.10	5.	<3.
Zn	4.50	-	
Ag	0.50	50.	2.
Pb	0.70	-	-
Analysis Total:	11. ppm	514. ppm	564. ppm

MeV (d,T) neutrons at RTNS-II have been described previously.[1] The TEM specimens were prepared by electropolishing using a solution (in vol.%) of 5% isopropyl alcohol, 24% phosphoric acid, 24% ethyl alcohol and 47% water at 20°C at a potential of 12 VDC. Specimens were examined in a JEOLCO 100CX electron microscope. Foil thicknesses were determined by stereoscopic measurements.

3. Experimental Results

The microstructure of an unirradiated control sample showed no unusual features: the matrix grains were clean, about 10 to 40 μm in size, and contained relatively few dislocations ($\leq 10^8$ cm/cm^3). The microstructure of specimens made from the same material and irradiated at room temperature at RTNS-II to a fluence of 2.7 x 10^{17} n/cm^2 (E = 14 MeV) contained a very high density (about 8 x 10^{16} cm^{-3}) of very small defect clusters. A stereo

,structure typically present in this irradiated copper is
. The defect clusters produced in the metal do not appear
stributed. Localized regions of high defect cluster den-
subcascades[2] formed by high energy primary knock-on
he superposition of defect clusters formed by several high
At the present time, no attempt has been made to estimate
tion of defects that can be grouped into these multiple
scades. Other specimens of the same material which have
an order of magnitude lower neutron fluence to decrease
f defect cluster overlap will be examined during the next

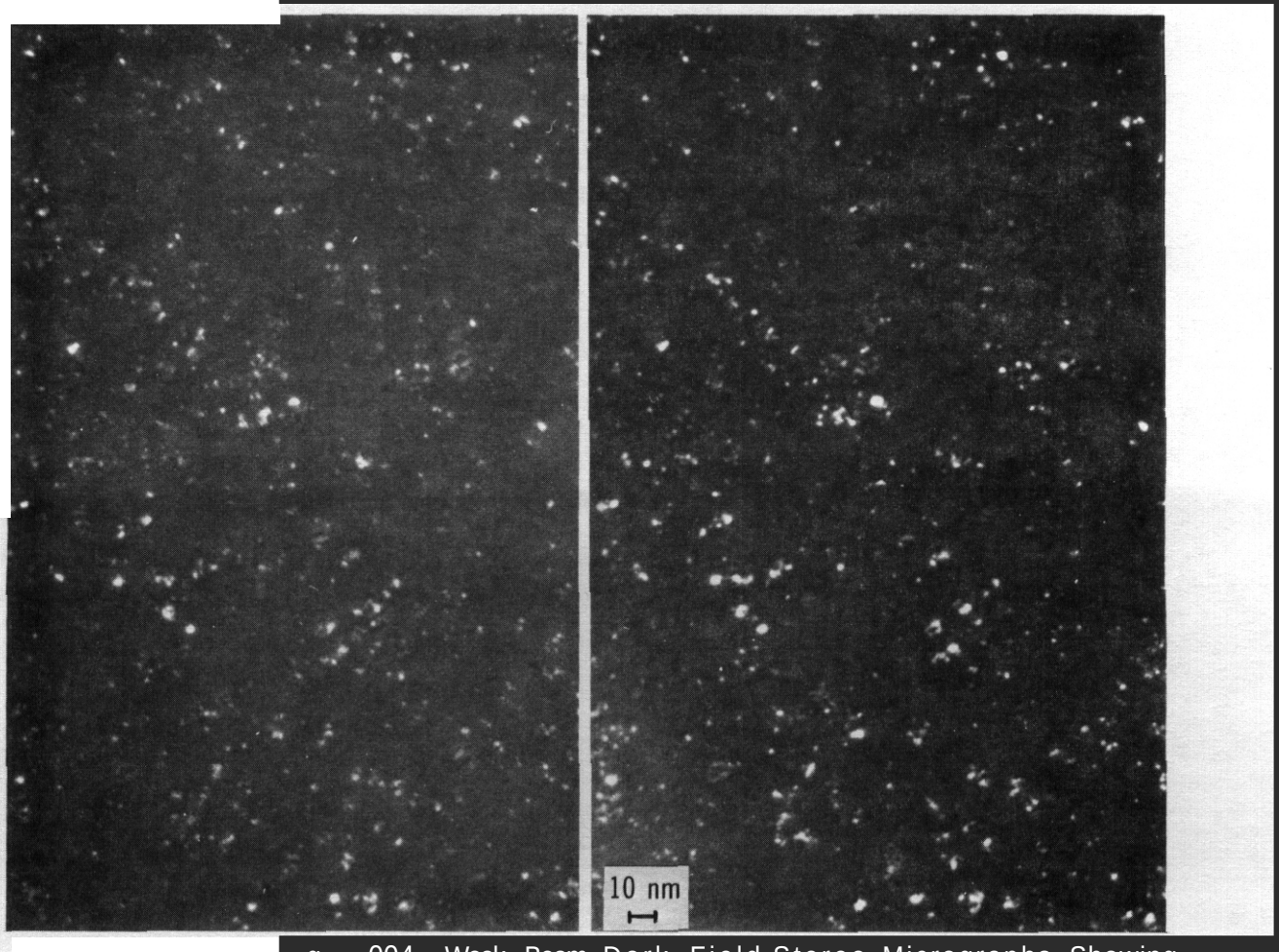

, g = 004, Weak Beam Dark-Field Stereo Micrographs Showing
Clusters Formed in High Purity Copper Irradiated with 14
,T) Neutrons to a Fluence of 2.7 x 10^{17} n/cm^2 at 25°C.
ive Nos. 3792 and 3803.)

Figure 2 is a histogram showing the size and frequency of the defect clusters observed. The measurements of the clusters were made from micrographs similar to those illustrated in Figure 1. The small size scale of the defect clusters is emphasized by comparing the increment size of the histogram with the corresponding "mean diameter" of a copper atom (based on a lattice parameter for copper of 0.361 nm). The number density of defects (8×10^{16} cm^{-3}) is the mean of three determinations (7, 7 and 10×10^{16} cm^{-3}). Each density estimate consisted of counting more than 300 defect clusters that were visible in a randomly selected area in a given stereo pair of micrographs. Three to six foil thickness measurements were obtained in and around each region analyzed.

In addition to conventional stereo micrographs, weak beam dark-field micrographs were taken with the objective lens of the electron microscope set to different values. The changes in objective lens current cause movement in the relative positions of certain features, such as those due to the lattice straining from small dislocation loops surrounding planar

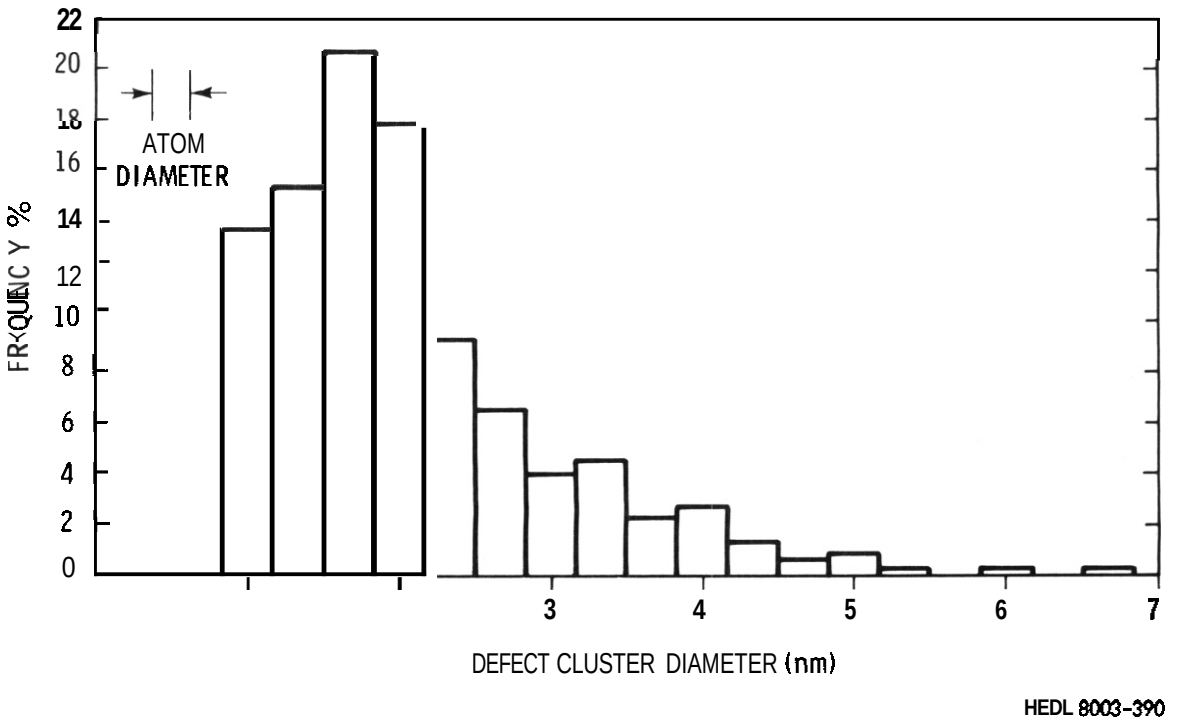

FIGURE 2. Histogram Illustrating the Size and Frequency of Defect Clusters Which Form in the Metal Shown in Figure 1.

vacancy or interstitial clusters. The relative movement of the images corresponds to a topographic elevation shift in the position of defect clusters when viewed on a stereo viewer. These "2-1/2 D" micrographs[3] can be analyzed to provide information on the vacancy and interstitial nature of defect clusters.[4] The micrographs taken in this work using the "2-1/2 D" technique exhibit topographical variations which are consistent with defects being both vacancy and interstitial types. However, the reciprocal lattice vector used was too small to differentiate definitively as to the type of the Burgers vector: ($\frac{a}{3}$<111> or $\frac{a}{2}$<110>).

Regions of the irradiated specimens were also examined with the foil oriented to a position very near the strongly diffracting Bragg condition, Figure 3. For this dynamical diffraction condition, shown with $\bar{g}$ = <002>, the defects exhibit black/white (B/W) contrast with the direction of the B/W contrast of some of the defects being indicated by black lines drawn on the micrograph. All of the B/W contrast directions are nearly parallel with projections of the specific low order crystallographic directions on the <110> plane of the micrograph. Analysis of the black/white contrast indicates that most are planar defects and have Burgers vectors that are consistent with both $\frac{a}{3}$<111> and $\frac{a}{2}$<110> loops. A thorough analysis of the types of loops using B/W contrast conditions[5] is planned for comparison with the analysis by the simpler 2-1/2 D method.[4]

4. Discussion

a. Size Distribution of Defect Clusters

The size distribution of defects shown in Figure 2 should not be interpreted to imply that the most probable diameter of observed defect clusters is about 1.5 to 2 nm. Examination of typical defect clusters, as shown in Figure 1, illustrates that a very high density of the defects exist at a size scale which approaches the resolution limit of the analysis technique being used. Accordingly, the size distribution should be interpreted as providing a lower limit to the size of the visible defects produced by the irradiation conditions noted. A more realistic size distribution would

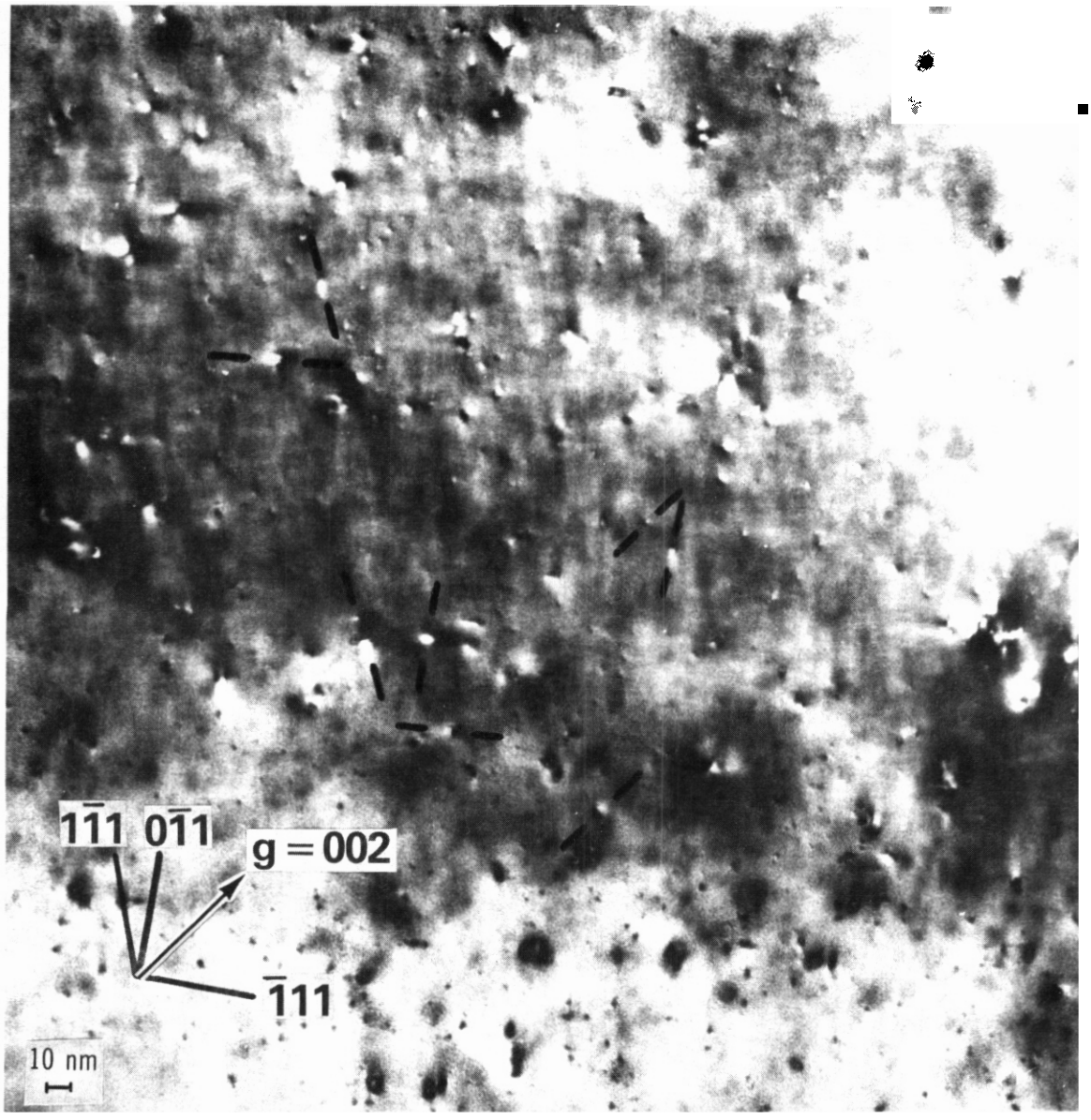

FIGURE 3. Dark-Field Micrograph Showing Black/White Contrast of Defect Clusters Formed in the Metal Shown in Figure 1. The foil is oriented near the <110> zone axis and imaged under a strong dynamical contrast condition with $\bar{g}$ = <002>. Projections of several low order crystallographic directions as well as black lines are shown to indicate the orientation of the B/W contrast for some of the defect clusters. (Negative No. 4188.)

be one which has a larger defect density than shown for cluster diameters less than about 1.5 nm.

The high number density and size distribution of small-sized defect clusters formed in the high purity copper bombarded with 14 MeV (d,T) neutrons at ambient temperature appear to be consistent with previously reported TEM data when differences in experimental procedures are taken into account. In the present study, very thin (about 35 to 40 nm) regions of TEM specimens were examined and photographed under weak beam dark-field high order diffraction conditions. Both of these conditions are particularly essential for examining and obtaining information on small-sized defect clusters.

Mitchell et al,[6] using the same weak beam dark-field diffraction conditions, reported that about 3×10^{16} defects/cm^3, with a mean size of about 3 nm, were formed during neutron irradiation of high purity copper to a fluence of 1.3×10^{17} n/cm^2 (E = 14 MeV). The size frequency distribution of defect clusters, grouped into sizes in increments of 2.5 nm, exhibited an increasing number density of defect clusters with decreasing cluster size. Based on a nearly linear increase in the strengthening of 14 MeV (d,T) neutron irradiated copper with increasing neutron fluence, it appears reasonable to linearly extrapolate the number density of clusters observed by Mitchell et al[6] to the fluence of the present study, which gives a value of about 7×10^{16} clusters cm^{-3} with a mean cluster size of about 3 nm. These values are to be compared with the defect concentration of 8×10^{16} cm^{-3} and mean cluster size of 2 nm reported here. Mitchell,[6] using the 2-1/2 D technique for identifying the small defect clusters,[4] reported that about half of the defects were vacancy and half were interstitial and that the vacancy and interstitial cluster size distributions were similar.

Cluster formation in high purity copper irradiated by (d,T) neutrons at room temperature to a fluence of 1.8×10^{17} n/cm^2 (E = 14 MeV) was also reported by Narayan et al.[7,8] They determined the types of defect clusters by dynamical B/W contrast techniques and found that about three-fourths of the loops were interstitial and about one-fourth were vacancy.[7] They also reported,[8] for 15 MeV (d,Be) neutron irradiation, that the defect cluster size distribution was analyzed by high order diffraction, weak beam, dark-field microscopy as well as by X-ray diffuse

scattering. While both methods showed that the number density of clusters increased with decreasing size, the two methods produced significantly different values for the number density of the small-sized defect clusters. The density of defects determined by TEM and by X-ray diffuse scattering was about 2 x 10^{16} cm^{-3} and 5 x 10^{16} cm^{-3}, respectively, with mean defect sizes of about 6 nm and 3 nm, respectively. Again, if the number density of defect clusters increases linearly with increasing neutron fluence, the TEM and X-ray diffuse scattering data would extrapolate to about 3 x 10^{16} cm^{-3} and about 6 x 10^{16} cm^{-3}, as compared with the value of 8 x 10^{16} cm^{-3} reported here. Narayan et al's[8] X-ray data on defect number density and mean size are in good agreement with those reported by Mitchell[6] and those found in the present study. However, their TEM data[7] are not. Furthermore, the factor of three difference between the number of interstitials in the visible interstitial clusters and the number of vacancies in the vacancy clusters does not appear to be explained by long range diffusion of defects to the few preirradiation dislocations, to the small number of impurity atoms or to the grain boundaries. The results suggest that a large fraction of the small vacancy loops are simply not visible by the B/W contrast techniques used by Narayan et al.[7,8]

b. Comparison of Visible Defect Clusters with Calculated Damage

A simple estimate can be made of the number of vacancies and interstitials in the observed defect clusters. If one assumes that all the defect clusters are on <111> planes, that there are 8 x 10^{16} defect clusters/cm^3, and that the lattice parameter of copper is 0.361 nm, then approximately 5.6 x 10^{18} defects/cm^3 are needed to fill the defect cluster histogram shown in Figure 2.

The number of defects produced by the interaction of 14 MeV neutrons with copper, based on an average displacement cross section of 3690 b[9] and a cascade efficiency factor of 0.31,[10] is 2.8 x 10^{19} Frenkel pairs/cm^3, or 5.6 x 10^{19} total defects/cm^3. An estimate of the number of residual defects, for an irradiation at 25°C, can be obtained by calculating the change

in electrical resistivity in copper irradiated at 4.2°K and heated to 25°C. Roberto et al[11] irradiated high purity copper at 4.2°K with 15 MeV (d,Be) neutrons to about 4 x 10^{15} n/cm^2 and determined that 75% of the resistance change was recovered by annealing to about 25°C. With the resistance per defect reported to be insensitive to the degree of clustering,[26] the 75% recovery of the electrical resistance change is taken as a reasonable estimate of the number of defects that are annihilated during defect cluster formation. The number of defects that survive in the form of defect clusters for irradiation at 25°C is therefore estimated to be about 25% of the total defects or about 1.4 x 10^{19} defects/cm^3.

From the above, it follows that about 40% of the number of Frenkel defects that survive the 25°C irradiation are in the form of visible defect clusters. These calculations indicate that there are many defect clusters that are smaller than the resolution limit of the TEM technique used in this study.

c. Relationship Between Microstructure and Mechanical Properties

High energy neutron irradiation of metals produces defect cascades consisting of subcascades, immobile defect agglomerates, mobile interstitials and vacancies.[12] At temperatures where both vacancies and interstitials are mobile, these defects are expected to form clusters, in a range of sizes, which impede the movement of dislocations. This manifests itself as an increase in the strength, or hardness, of the material. Most dislocation models that relate the hardening in metals to dislocation obstacles are of the form[13,14]

$$\Delta\tau = \frac{\mu b}{\beta \bar{\ell}} ,$$

where τ = shear stress, μ = shear modulus, b = Burgers vector, $\bar{\ell}$ = average interbarrier spacing, and β = constant.

Fleischer[15] developed a hardening model for neutron irradiated copper in which the loops are regarded as centers of tetragonal distortion

that interact with straight dislocations. While controversy still exists as to the exact hardening mechanism,[16,17,19,20] the Fleischer model appears to correlate well a wide range of data and should be applicable to the present experiment in which a high density of small loops exist. Assuming a square array of small loops, clusters and point defects, Fleischer[15] estimated $\bar{\ell}$ to be $[\Sigma\, n_i\, d_i]^{-1/2}$ where n_i is the concentration of defect clusters with the diameter d_i. Values of β for most fcc metals and alloys normally fall into the range of 2 to 4.[13,14] Values of β were calculated by Fleischer[15] and Foreman[21] for neutron irradiated copper and are 3.7 and 4.0, respectively.

For the TEM data of Figure 2, β = 3.7 and the Von Mises criterion[22] to relate yield strength to shear stress, the estimated increase in yield strength is

$$\Delta\sigma_o = \sqrt{3}\,\Delta\tau = \frac{\sqrt{3}}{\beta\bar{\ell}}\mu b = \frac{(\sqrt{3})(6.0 \times 10^6\ \text{psi})(2.556 \times 10^{-8}\ \text{cm})}{(3.7)[(8 \times 10^{16}\ \text{cm}^{-3})(2.18 \times 10^{-7}\ \text{cm})]^{-1/2}}$$

$$= 9{,}500\ \text{psi}.$$

Figure 4 shows the increase in yield strength measured by Mitchell et al[6,18] for specimens made from two heats of copper (depicted in Figure 4 as open and filled-in circles) which were irradiated at 25°C with 14 MeV neutrons. For a neutron fluence corresponding to the present experiment (2.7×10^{17} n/cm^2), the increase in the yield strength is about 12,000 psi. Then the calculated increase in yield strength obtained by applying the Fleischer hardening model[15] to the visible defect clusters reported here is in fair agreement with the increase measured by Mitchell et al.[6,18]

A similar estimate can be made of the increase in yield strength caused by dislocation interaction with irradiation produced defect clusters, using the Mitchell et al[6,18] TEM data, the Fleischer hardening model,[15] and the Von Mises criterion[22]

$$A_o = \frac{\sqrt{3}\ \mu b}{\beta \bar{\ell}} = \frac{(\sqrt{3})(6.0 \times 10^6\ \text{psi})(2.556 \times 10^{-8}\ \text{cm})}{(3.7)[(3 \times 10^{16}/\text{cm}^3)(3 \times 10^{-7}\ \text{cm})]^{-1/2}} = 6{,}800\ \text{psi}$$

Figure 4 shows that the increase in yield strength of copper irradiated to a fluence of 1.3×10^{17} n/cm^2 (E = 14 MeV) is about 7,500 psi or that the observed clusters can account for about 90% of the measured increase in yield strength (with β = 3.7).

An estimate can also be made of the defect cluster density and mean size needed to increase the yield strength, via the Fleischer hardening model, from 9,500 to 12,000 psi. An iterative set of simple calculations

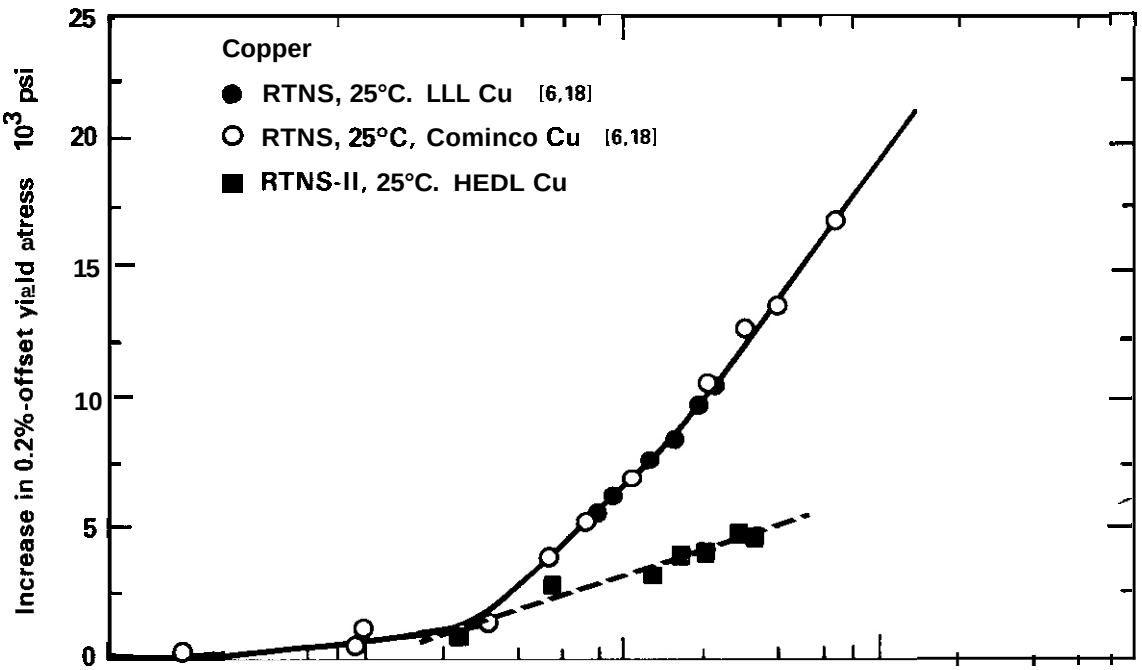

FIGURE 4. The Increase in Yield Strength Measured by Mitchell et al[6,18] for Two Heats of Copper Irradiated by 14 MeV (d,T) Neutrons and Shown on the Figure as Open and Filled-in Circles. The square symbols show the calculated increase in yield strength of high purity copper based on increases in DPH measurements[24] induced by 14 MeV (d,T) neutron irradiation.

was performed balancing the size and concentration of invisible and observed defect clusters, the experimentally measured hardening and the mean barrier size. For a mean cluster diameter of 1.5 nm

$$\rho = \frac{1}{d}\left[\frac{\beta\ \Delta\sigma}{\sqrt{3}\ \mu b}\right]^2 = \frac{1}{(1.5 \times 10^{-7}\ \text{cm})}\left[\frac{(3.7)(12{,}000\ \text{psi})}{\sqrt{3}\ (6.0 \times 10^{6}\ \text{psi})(2.556 \times 10^{-8}\ \text{cm})}\right]^2$$

$$= 1.9 \times 10^{17}\ \text{cm}^{-3}.$$

This concentration is consistent with invisible defect clusters having a 1.0 nm mean diameter and concentration of $1.1 \times 10^{17}/\text{cm}^3$. Thus, only a small number of additional defects, about 30% of those in visible clusters, would be needed to form small, invisible clusters sufficient to account for the 12,000 psi change in yield strength.

In the previous section of this report on Calculated Damage, it was estimated that perhaps 60% of the defects that survived the 25°C irradiation are in the clusters that are in or are smaller than the size range of the TEM technique used (1.0 nm resolution limit). In order to estimate their effect on strengthening, two cases were considered. It was assumed that the unresolved defect clusters are in the form of a close-packed planar array and have a mean diameter of either 1.02 nm or 0.76 nm, corresponding to fourteen or seven atoms, respectively. The corresponding densities of these unresolved defect clusters are $5 \times 10^{17}\ \text{cm}^{-3}$ and $1.0 \times 10^{18}\ \text{cm}^{-3}$, respectively. These concentrations of barriers to dislocation motion would produce a total increase in the yield strength of about 16,000 psi and 20,000 psi, respectively. This is much more hardening than is observed. It is likely that a smaller number of defects survive the 25°C irradiation as clusters than was estimated based on the recovery of resistivity of material irradiated at 4°K and annealed to 25°C.

Due to the very limited irradiation volume of the 14 MeV neutron source, one of the major mechanical property measurements of RTNS-II irradiated specimens is microhardness measurements. The microhardness data on

the HEDL copper samples irradiated at RTNS-II, listed in Table 2,[24] show a monotonic increase in hardness with increasing neutron fluence in direct analogy with the yield strength increase with fluence, Figure 4.

TABLE 2

200M TEMPERATURE DPH VALUES FOR COPPER IRRADIATED AT 25°C WITH 14 MeV (d,T) NEUTRONS[24]

ϕt 10^{17} n/cm^2 (E = 14 MeV)	DPH (kg/mm^2)	DPH (ksi)
0	56	80
0.25	61	87
0.59	71	101
1.66	75	107
1.74	80	114
2.05	80	114
2.83	83	118
2.99	83	118

In addition to the well-recognized relationship between hardness and ultimate tensile strength, Cahoon et al,[25] using the correlation summarized by Tabor,[23] derived an expression relating yield strength (σ_Y) to diamond pyramid hardness (H)

$$a_Y = (H/3)(0.1)^n ,$$

where n equals the strain hardening coefficient. For n = 0.414 for copper,[23] the changes in yield strength corresponding to the increase in microhardness of the RTNS-II irradiated copper specimens are plotted in Figure 4 as solid squares. At low fluence, these microhardness data correlate well with the yield strengthening data of Mitchell et al[6] but exhibit a clear difference in hardening rate with fluence. This difference is in spite of the fact that the microstructure observed in the present work is consistent with that observed by Mitchell et al.[6,18] If defect clusters too small to be resolved exist, as is probably the case, one would expect the hardness data to give a change in yield strength which is in excess of that deduced from

the observed microstructure, rather than a value which is a factor of two lower. The source of this discrepancy is being investigated.

5. Conclusions

The size and number density of defect clusters formed in high purity copper irradiated with 14 MeV (d,T) neutrons at 25°C have been obtained; they compare favorably with previously reported results.

The number of defects needed to fill the observed defect clusters are significantly smaller (about a factor of two) than the number of defects currently predicted to survive and to form clusters during a 25°C irradiation.

The experimentally determined size and concentration of defect clusters correlate fairly well (within about 20%) with the increase in yield strength predicted by the Fleischer hardening model over the fluence range investigated. Only a small (30%) increase in the number of defects in the form of small, unresolved clusters with a density of about 1.1×10^{17} cm^{-3} and size near 1.0 nm is needed to reasonably account for the balance of the increase in yield strength observed after irradiation.

At present, it does not appear that an accurate estimate can be made of the number of defects which form during irradiation and which survive to form clusters, as a factor of two discrepancy exists. For the calculated number of defects to exist as small, unresolved clusters, the yield strength increase should be larger than what has been reported.

VI. REFERENCES

1. N. F. Panayotou et al, "RTNS-II Irradiation Program Status," (a) DAFS Quarterly Progress Report, DOE/ET-0065/5 (January-March 1979), p. 112, (b) DAFS Quarterly, DOE/ET-0065/6 (April-June 1979), p. 84, (c) DAFS Quarterly, DOE/ET-0065/7 (July-October 1979), p. 65, (d) OAFS Quarterly, DOE/ET-0065/8 (October-December 1979), p. 113.

2. K. L. Merkle, "Defect Production by Energetic Particle Bombardment," Radiation Damage in Metals, N. L. Peterson and S. 0. Iiarkness (Eds), ASM (1975).

3. W. L. Bell, "2-1/2 D Electron Microscopy Through Focused Dark-Field Image Shifts," J. Appl. Phys., 47, 1676 (1976).

4. J. B. Mitchell and W. L. Bell, "Characterization of Point Defect Clusters by 2-1/2 D TEM," Acta Met., 24, 147 (1976).

5. S. M. Ohr, "Direction of the Black/White Contrast of Dislocation Loops," Phys. Stat. Sol., 38, 553 (1976).

6. J. B. Mitchell et al, "DT Fusion Neutron Radiation Strengthening of Copper and Niobium," Radiation Effects and Tritium Technology for Fusion Reactors, J. S. Watson and F. W. Wiffen (Eds), Gatlinburg, Tennessee (October 1-3, 1975), Vol. II, p. 172.

7. J. Narayan and S. M. Ohr, "The Nature of High Energy Damage in Copper and Gold," J. Nucl. Mat., 85 & 86, 515 (1979).

8. J. B. Roberto, J. Narayan and M. J. Saltmarsh, "15 MeV Neutron Damage in Cu and Nb," ibid. Ref. 6, p. 159.

9. D. G. Doran and N. J. Graves, "Displacement Cross Sections and PKA Spectra: Tables and Applications," USERDA Report HEDL-TME 76-70 (December 1976).

10. R. S. Averback, R. Benedek and K. L. Merkle, "Efficiency of Defect Production in Cascades," J. Nucl. Mat., 69 & 70, 786 (1978).

11. J. B. Roberto et al, "Isochronal Recovery of High-Energy d-Be Neutron Damage in Cu, Nb and Pt from 8 to 400°C," J. Nucl. Mat., 73, 97 (1978).

12. A. N. Goland, "Experimental Evaluation of the Primary Damage Process-Neutron Energy Effects," J. Nucl. Mat., 85 & 86, 453 (1979).

13. A. L. Bement, Jr., "Fundamental Materials Problems in Nuclear Reactors," 2nd International Conference on the Strength of Metals and Alloys, CONF-700819-5, ASM, Vol. II (1970), p. 693.

14. J. Moteff, D. J. Michel and V. K. Sikka, "The Influence of Irradiation Temperature on the Hardening Behavior of the Refractory bcc Metals and Alloys," J. Nucl. Mat., 18, 198 (1973).

15. R. L. Fleischer, "Solution Hardening by Tetragonal Distortions: Applications to Irradiation Hardening in fcc Crystals," Acta Met., 10, 835 (1962).

16. M. J. Makin, "The Obstacles Responsible for the Hardening of Neutron Irradiated Copper Crystals," Phil. Mag., 18, 1245 (1968).

17. R. J. Koppenaal, "The Strengthening Mechanism in Neutron Irradiated Copper Single Crystals After Mild Annealing," Acta Met., 16, 89 (1968).

18. J. B. Mitchell, "Exploratory Experiments Comparing Damage Effect of High-Energy Neutrons and Fission-Reactor Neutrons in Metals," ERDA Report UCRL-52388 (January 12, 1978); also, OAFS Quarterly Progress Report, DOE/ET-0065/1 (January-March 1978), p. 187.

19. T. J. Koppenaal and R. J. Arsenault, "Neutron-Irradiation-Strengthening in fcc Single Crystals," Review #157, Met. Rev., 16, 175 (1971).

20. W. Frank, M. Rühle and M. Saxlova, "Radiation Hardening of Neutron-Irradiated Copper Single Crystals," Phys. Stat. Sol., 26, 671 (1968).

21. A. J. E. Foreman, "Junction Reaction Hardening by Dislocation Loops," Phil. Mag., 17, 353 (1968).

22. G. E. Dieter, Jr., Mechanical Metallurgy, McGraw-Hill (1961).

23. D. Tabor, "The Hardness and Strength of Metals," J. Inst. Metals, 79, 1 (1951).

24. N. F. Panayotou, "RTNS-II Irradiation Program Status," OAFS Quarterly Progress Report, DOE/ET-0065/9 (January-March 1980).

25. J. R. Cahoon, W. H. Broughton and A. R. Kutzak, "The Determination of Yield Strength from Hardness Measurements," Met. Trans., 2, 1979 (1971).

26. R. S. Averback, R. Benedek and K. L. Merkle, "Ion-Irradiation Studies of the Damage Function of Copper and Silver," Phys. Rev. B, 18, 4156 (1978).

VII. FUTURE WORK

The microstructural development in various metals and alloys irradiated in HEDL I through IV at RTNS-II with 14 MeV (d,T) neutrons will be examined and the results correlated with microhardness measurements. A copper specimen irradiated to a low neutron fluence of about 2 x 10^{16} n/cm^2 (E = 14 MeV) will be examined to investigate subcascade formation.

CHAPTER 3

FUNDAMENTAL MECHANICAL BEHAVIOR

I. PROGRAM

Title: Mechanical Properties
Principal Investigator: R.H. Jones
Affiliation: Battelle, Pacific Northwest Laboratory

II. OBJECTIVE

1. Assess the susceptibility of ferritic alloy steels with 2 1/4 - 12 Cr, 1 Mo to grain boundary chemistry induced intergranular embrittlement.

2. Identify impurity and alloying elements which segregate to and enrich grain boundaries and discern their effects on embrittlement.

III. RELEVANT DAFS AND ADIP TASK/SUBTASK

DAFS Subtask II.C.l.l, II.C.1.2, II.C.8.2, II.C.14.1
ADIP Subtask I.C.1.3, I.C.1.5, I.C.1.6

IV. SUMMARY

Phosphorus is the primary element responsible for segregation-induced embrittlement of Cr-Mo steels at low temperatures. Its segregation is enhanced by the presence of chromium in solution and to a lesser degree by manganese, nickel and silicon. Molybdenum reduces both the segregation and embrittling effect of phosphorus. In 2 1/4 Cr steels, the optimum molybdenum content is 0.7% and the content of manganese, nickel and silicon should be minimized. For higher Cr steels, the presence of elements as molybdenum is essential because the susceptibility of these alloys to embrittlement due to phosphorus segregation increases with chromium content.

Radiation-induced segregation may alter which elements will partition to the grain boundaries and therefore may affect embrittlement. Enrichment of undersized elements as sulfur, phosphorus, silicon, nitrogen, boron and nickel could dramatically increase the alloy's susceptibility to intergranular failure.

V. ACCOMPLISHMENTS AND STATUS

A. Segregation and Embrittlement in Cr-Mo Steels -- S.M. Bruemmer

1. Introduction

Considerable interest has been generated recently concerning the use of ferritic 2 1/4 - 12 Cr steels for the first wall and shield of the Engineering Test Facility (ETF) and in future fusion reactor designs. This interest stems from a possible significant increase in component lifetime, relative to that of 316SS. However, uncertainties exist regarding the susceptibility of these alloys to grain boundary chemistry - induced embrittlement. Grain boundary chemistry is known to affect a wide range of material phenomena. Table 1 lists several of these which may be important to the application of ferritic alloy steels for fusion reactors.

The enrichment of solutes at interfaces can result from two types of segregation:

- Equilibrium Segregation - due to the interaction between the solute and the interface.

- Non-Equilibrium Segregation - due to the flux of point defects to sinks and the interaction between the solute and point defects.

Both of these mechanisms of solute enrichment are present in the fusion reactor environment. This review identifies certain impurity and alloying elements which may have an effect on the integrity of 2 1/4 - 12 Cr steels at temperatures where creep processes are not significant (below 300°C).

TABLE 1. MATERIAL PHENOMENA AFFECTED BY GRAIN BOUNDARY CHEMISTRY IMPORTANT TO FERRITIC STEELS

	Temper Embrittlement	
	Tempered Martensite Embrittlement	
	Weld Re-heat Cracking	
	Creep Embrittlement	
Intergranular		Fatigue/Corrosion Fatigue
		Corrosion/Stress Corrosion
		Hydrogen Embrittlement
		Radiation-Induced Embrittlement

2. Identifying Embrittling Elements

In order to identify elements that may prompt intergranular embrittlement in steels it is essential to know: (i) the embrittling potency of the element, (ii) its segregation propensity and (iii) the amount in solution available for segregation. From temper embrittlement results, the solute species which are thought to reduce grain boundary cohesion can be listed (Table 2). Much less is known concerning their particular embrittling potency. However, it has been shown in Ni-Cr steels[1] that antimony is more potent than tin and that both of these elements are considerably more potent than phosphorus on the basis of ductile-brittle transition temperature. Within the group VI A elements, the order of increasing potency when comparing the effects on toughness,

is: sulfur, selenium and tellurium.[2,3] This suggests, at least in a general sense, that embrittling potency increases as one moves left to right or top to bottom through the elements displayed in Table 2.

TABLE 2. ELEMENTS THOUGHT TO ENHANCE INTERGRANULAR FRACTURE IN STEELS

GROUP		
IV A	V A	VI A
Si	P	S
Ge	As	Se
Sn	Sb	Te
	Bi	

An indication of the segregation propensity of solutes may be determined from figure 1. This diagram from the work of Seah and Hondros[4,5], allows the identification of elements which have the potential to enrich grain boundaries as a result of thermal treatment. It also illustrates the inverse relationship between solubility and segregation. This relationship can be formulated using the analogue to the Brunauer, Emmett and Teller (BET) isotherm[6-8] which has been described in a previous quarterly.[9] As shown in figure 1, the grain boundary enrichment ratio (boundary content ÷ bulk content in solution) increases as solubility decreases. However, the actual amount enriched at the interface will also depend on the solute content in the grain available to segregate. This quantity is not only dependent on the bulk composition, but on the solid solubility. As the solubility limit drops below the bulk composition, the amount of free solute in solution decreases. This may reduce the actual boundary enrichment as was shown for sulfur at below 500°C.[9] A practical example of this is the addition of manganese to

commercial steels to tie up sulfur. Sulfur strongly segregates to the grain boundaries of iron, but in most steels the chemical reaction between manganese and sulfur leaves very little sulfur in solution, thereby minimizing or eliminating segregation.

3. Embrittling Elements in Cr-Mo Steels

Using the criteria outlined in the previous section, phosphorus and tin are expected to have the dominant effect on segregation induced embrittlement of the ferritic alloys of interest. Both of these elements are potent embrittlers, segregate strongly in iron and are present in significant amounts as impurities. Phosphorus has been reported to contribute to or cause the embrittlement of both 2-3% Cr[10-12] and 11-13% Cr[13-14] ferritic steels. The addition of molybdenum to these steels reduces the embrittlement due to phosphorus segregation, but does not eliminate it. Tin segregates less in 2 1/4 Cr steels than phosphorus, but is a more potent embrittler.[1] In a 2 1/4 Cr - 1 Mo steel, 0.04% Sn did not affect the transition temperature.[11] Apparently the presence of molybdenum and lack of nickel in this steel limited the segregation of tin. The effect of alloying elements on segregation and embrittlement will be discussed in the following section.

Other solute elements which may effect intergranular cohesion (Table 2) should not become sufficiently enriched at the grain boundaries to cause embrittlement if kept at current commercial levels. However, non-equilibrium segregation as a result of neutron irradiation may considerably alter this. Enrichment of undersized elements such as boron, nitrogen, silicon and phosphorus appears possible and potentially deleterious. Additional solutes normally tied up in solution such as sulfur and oxygen may also become enriched during elevated temperature irradiation. Intergranular precipitation of compounds as Cr_2N could significantly reduce ductility. The segregation of boron to grain boundaries may lead

to embrittlement due to the transmutation of boron to helium and lithium.

4. Effect of Alloying Elements on Segregation and Embrittlement

Alloying elements such as chromium, nickel, manganese and molybdenum have a significant effect on the segregation of the embrittling elements in iron. One example noted previously is manganese additions removing sulfur from solution and decreasing segregation. Unfortunately these elements can also increase both the kinetics and equilibrium grain boundary concentration of certain solutes. This behavior results from an attractive interaction between the alloying element and solute, thereby increasing the segregation of both elements. The thermodynamics of this interaction and the theory which serves to explain the co-segregation effect will not be considered in this review. It is suggested that one of the several papers by Guttman[15-17] be consulted for this purpose. A simple method of rationalizing the effect of alloying elements is by examining their effect on impurity element solubility. Referring back to the relationship between solubility and segregation in figure 1, as the solubility decreases, the enrichment ratio increases. Whether the grain boundary concentration increases or decreases depends on the quantity in solution available for segregation. Using phosphorus as an example in figure 2,[18] raising the bulk content of chromium rapidly drops the solid solubility of phosphorus. Thus the use of higher chromium alloys leads to an enhanced susceptibility of phosphorus segregation and embrittlement. In plain 12% Cr steel (without molybdenum), considerable embrittlement is possible after tempering, welding and service temperatures above 500°C.[13]

Nickel and manganese will also increase the segregation of phosphorus, but will enhance the segregation of tin and antimony to a much larger degree, thereby increasing their importance. Another common element in these steels, silicon, has been shown to augment the embrittlement presumably by raising the activity of phosphorus.[21] The addition of

these elements will probably have a more significant effect on the lower Cr alloys, but the amount in solution should be minimized in either case.

If the interaction between alloying element and impurity is strong enough (eg. Mn-S), segregation can be reduced. Unfortunately, elements which interact in this manner with embrittling species as phosphorus also strongly interact with interstitial elements as carbon, nitrogen and oxygen. Thus, the effectiveness of such an addition depends on the amount dissolved in the matrix. Molybdenum has long been recognized as inhibiting temper embrittlement in low alloy steels. In 2 1/4 Cr steels, the ability of molybdenum to reduce phosphorus segregation and embrittlement depends on its relative partitioning to carbides. The optimum molybdenum content in this steel is 0.7%,[10,11] above this concentration molybdenum replaces chromium in the carbides, enabling chromium to enhance phosphorus segregation. In the higher Cr steels, this optimum content will probably not exist and larger amounts of molybdenum could be added. The alloying of a 12% Cr steel with 1 3/4% Mo (along with 3% Ni and 0.3% V) eliminated the intergranular embrittlement due to phosphorus segregation.[15] Niobium, titanium and zirconium also interact very strongly with phosphorus; however, they tend to preferentially combine with interstitial elements.

5. Effect of Neutron Irradiation on Embrittlement

It is important to note when considering alloying effects on embrittlement, that the strength level (and grain size) of the steel has a direct bearing on its susceptibility. Thus, the addition of elements such as carbon or vanadium or the use of heat treatments which raise the strength level will make the steel more prone to intergranular embrittlement. Since neutron irradiation will strengthen steels, it may prompt failures at impurity concentrations considered immune in thermal applications. In particular, elements such as copper, which induce significant

matrix strengthening during irradiation dramatically increase susceptibility. In summary, irradiation could enhance segregation-induced intergranular fracture by:

- non-equilibrium segregation of embrittling elements
- non-equilibrium segregation of alloying elements (as Ni) which increase thermal segregation of embrittling elements.
- altering the solubility of carbides or other phases, enriching co-segregating elements as Cr in solution or removing alloying elements as Mo from solution.
- precipitation of brittle second phase as Cr_2N at grain boundaries.
- transmutation of elements enriched at grain interface to an embrittling species.
- increasing the strength such that intergranular fracture occurs with smaller grain boundary enrichments.

The enrichment of helium and the formation of helium bubbles at grain boundaries which also promotes intergranular failure in irradiated materials can occur simultaneous with the impurity segregation effects. Which process will dominate the embrittlement of ferritic alloy steels is not known and is one of the many questions which needs to be answered.

6. Conclusion

The segregation-induced embrittlement of ferritic Cr-Mo steels results from complex interaction between impurity elements and alloying elements. Table 3 gives a brief summary of the effect that certain alloying and impurity elements are believed to have on this embrittlement. Other elements which are not listed are thought to have only a minor effect if present in compositions representative of commercial ferritic steels.

Phosphorus segregation is likely to occur in ferritic alloy steels as a result of equilibrium segregation. It's magnitude and effect on embrittlement will depend primarily on the bulk compositions of phosphorus, chromium and molybdenum, the thermal history, and the strength level of the steel. While phosphorus is expected to predominate during thermal processing, radiation-induced segregation may dramatically shift both the elements which enrich the grain boundary and the alloy's susceptibility to intergranular failure.

VI. REFERENCES

1. A.K. Cianelli, H.C. Feng, A.H. Ucisik, and C.J. McMahon, Jr., Met. Trans. A, Vol. 8A, p. 1059 (1977).

2. P. Jolly and C. Goux, Mem. Sci. Rev. Met., 66, p. 605 (1969).

3. C. Pichard, J. Rieu and C. Goux, Mem. Sci. Rev. Met., 70, p. 13 (1973).

4. M.P. Seah and E.D. Hondros, Proc. R. Soc., 335A, p. 191 (1973)

5. E.D. Hondros, M.P. Seah and C. Lea, Metals and Materials, p. 26, January (1976).

6. S. Brunauer, P.H. Emmett and E. Teller, J. Am. Chem. Soc., 60, p. 309 (1938).

7. S. Brunauer, L.S. Deming, W.E. Deming and E. Teller, J. Am. Chem. Soc., 62, p. 1723 (1940).

8. E.D. Hondros and M.P. Seah, Met. Trans. A, vol. 8A, p. 1363 (1977).

9. S.M. Bruemmer and R.H. Jones, OAFS Quarterly Report, DOE/ET-0065/5, p. 147, January - March (1979).

10. Ph. Dumoulin, M. Guttman, M. Foucault, M. Palmier, M. Wayman, and M. Biscondi, Metal Sci., p. 1, January (1980).

11. Jin Yu and C.J. McMahon, Jr., Met. Trans. A, vol. 11A, p. 277 (1980).

12. M. Guttman, Ph. Oumoulin, M. Palmier, P. LeBlanc and M. Biscondi, Mem. Sci, Rev. Met., p. 377, June (1977).

13. Ph. Lemble, A. Pineau, J.L. Castagne, Ph. Sumoulin, and M. Guttman, Metal Sci., p. 496, August (1979).

14. B.C. Edwards and E.A. Little, Ferritic steels for fast reactor steam generators. BNES, London, paper 22 (1978).

15. M. Guttman, Surf. Sci., 53, p. 213 (1975).

16. M. Guttman, Met. Trans. A, vol. 8A, p. 1383 (1977).

17. M. Guttman and D. McLean in Interfacial Segregation, ASM, Metals Park, p. 261 (1979).

18. H. Kaneko, T. Nishizawa, T. Tamaki and A. Tanifuji, J. Jpn. Inst. Met., vol. 29, p. 166 (1965).

19. S.M. Bruemmer, R.H. Jones, M.T. Thomas and D.R. Baer, Scr. Met., vol. 14, p. 137 (1980).

20. S.M. Bruemmer, Battelle Pacific Northwest Laboratory, unpublished research.

21. Jin Yu and C.J. McMahon, Jr., Met. Trans. A, vol. 11A, p. 291 (1980).

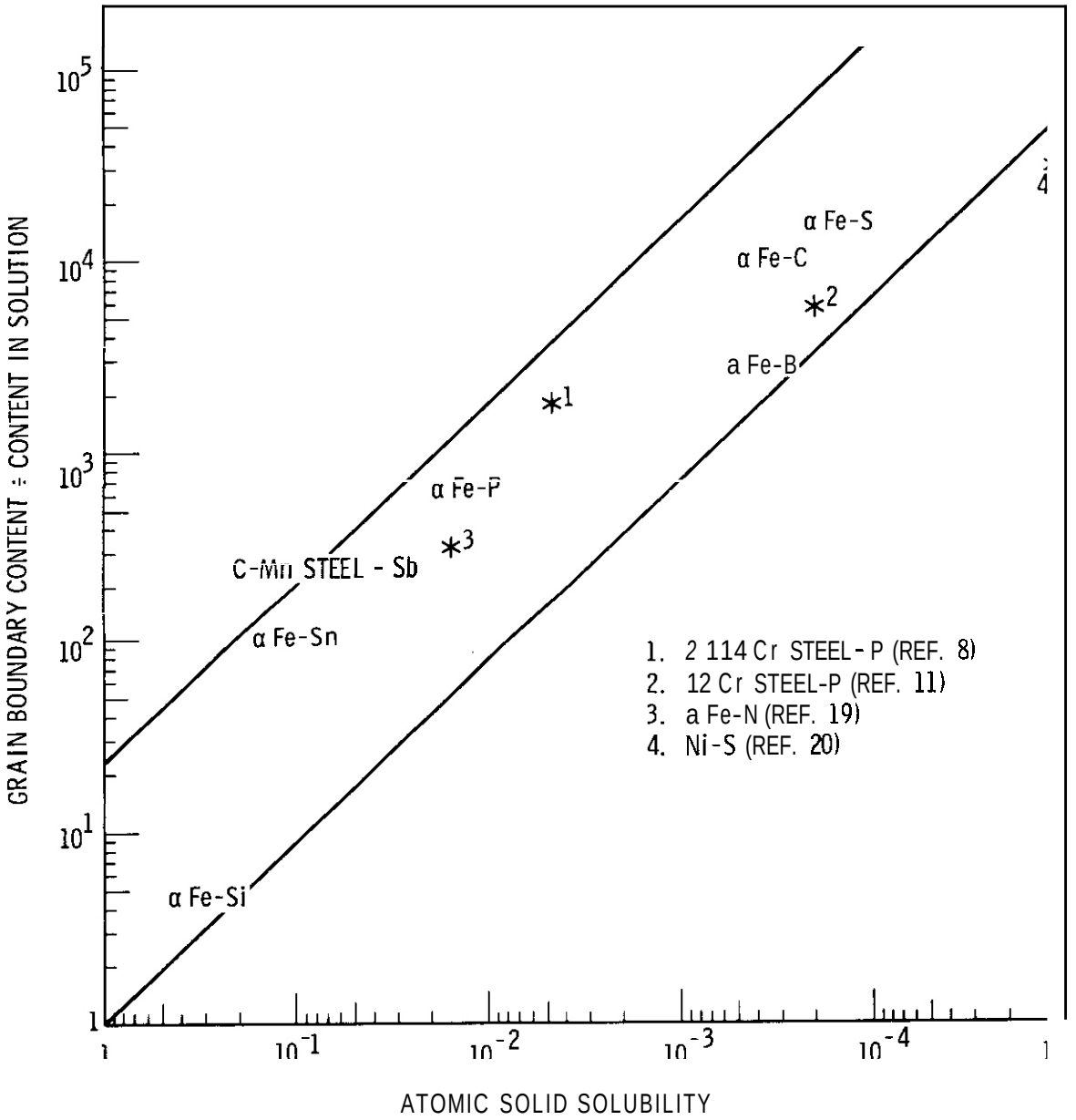

Figure 1. Experimental data as compiled by Seah & Hondros[5] showing that the enrichment of solute elements can be predicted by a linear correlation with the inverse solid solubility. Some more recent experimental results are shown as *.

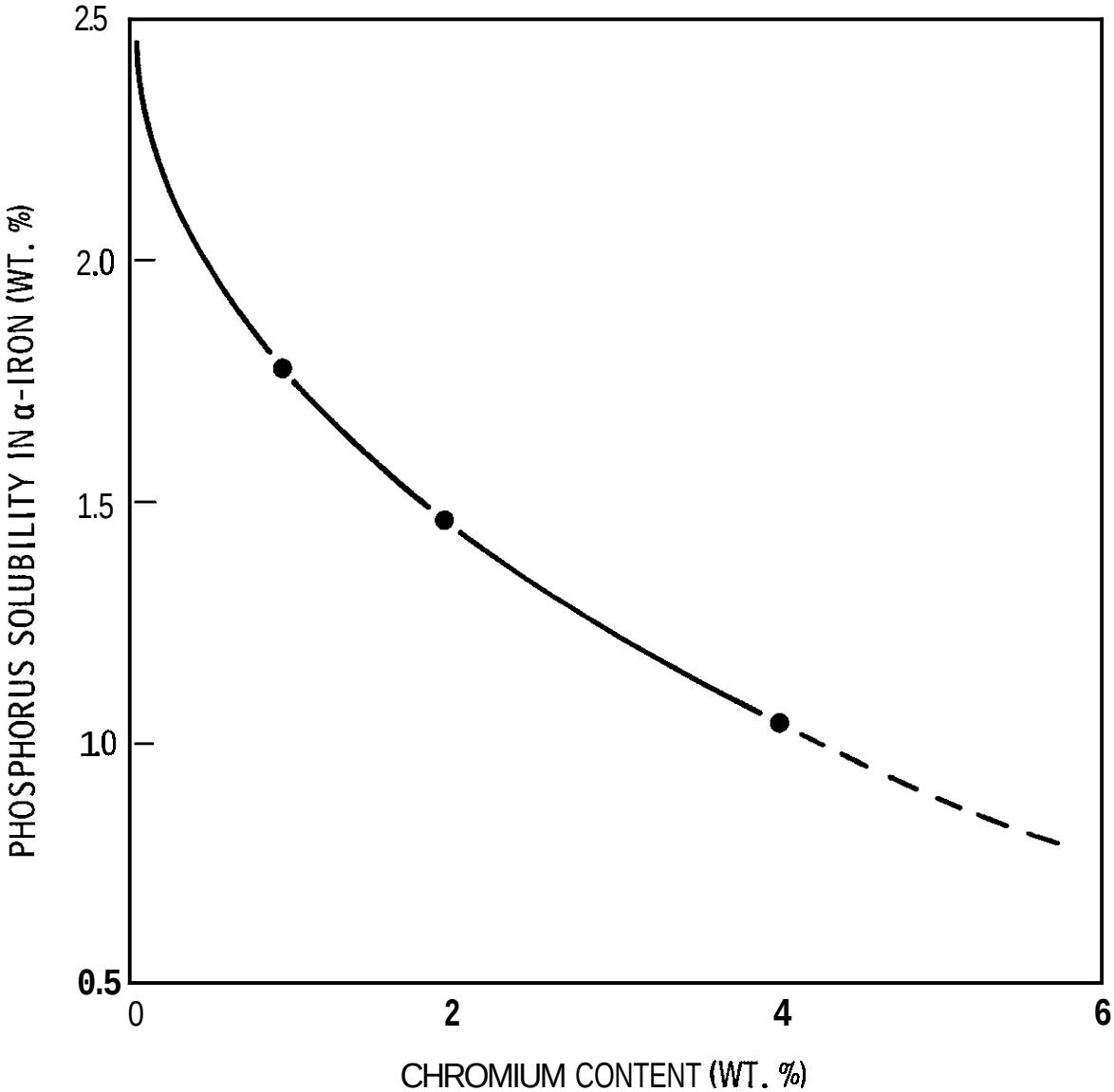

Figure 2. Data of Kaneko, et al.[18] illustrating the effect of chromium content on the solubility of phosphorus at 1000°C.

TABLE 3. SUMMARY OF THE EFFECT ALLOYING AND IMPURITY ELEMENTS ARE BELIEVED TO HAVE ON THE GRAIN BOUNDARY CHEMISTRY AND INTERGRANULAR EMBRITTLEMENT OF FERRITIC ALLOYS

Alloying or Impurity Element	Effect on Segregation and Embrittlement
Chromium	Increases impurity element segregation.
Molybdenum	Decreases impurity element segregation and embrittlement, 0.7 wt. % optimum content for 2 1/4 Cr steel.
Manganese	Minimizes sulfur segregation via precipitation, free Mn increases segregation of other impurities.
Nickel	Increases impurity element segregation.
Vanadium	Increases embrittlement without Mo in steel.
Tungsten, Niobium, Titanium	Decreases impurity segregation and embrittlement if not precipitated in carbides.
Silicon	Increases P segregation, may segregate and contribute to embrittlement.
Phosphorus	Segregates strongly and embrittles due to large bulk content and interaction between Cr and P.
Tin	May segregate and embrittle due to large bulk content, susceptibility increases with Ni and Mn content.
Sulfur	Potentially a potent embrittler, but should be immobilized due to precipitation.
Nitrogen	May segregate and contribute to embrittlement.
Boron	Segregates and may embrittle as a result of neutron irradiation.

VII. FUTURE WORK

The enrichment of embrittling elements at the grain boundaries of iron and nickel as a result of both thermal and irradiation environments is being analyzed. Elements of interest have been selected and initial experiments are underway to measure the irradiation-induced grain boundary segregation of sulfur in nickel. Theoretical predictions of solute segregation in pertinent systems such as Ni-S will compare the grain boundary enrichments due to thermal treatment and irradiation. The predictions of the segregation models will be examined relative to the experimental results.

I. PROGRAM

Title: Effects of Near Surface Damage and Helium on the Performance of the First Wall

Principal Investigator: O. K. Harling

Affiliation: Nuclear Reactor Laboratory, Massachusetts Institute of Technology

11. OBJECTIVE

The objective of this study is to understand and quantify the effects of near surface damage and implanted gas on the performance of the fusion first wall.

III. RELEVANT DAFS PROGRAM TASK/SUBTASK

TASK II.C.5 Effects of Cycling on Microstructure

II.C.8 Effects of Helium and Displacement on Fracture

II.C.12 Effects of Cycling on Flow and Fracture

II.C.13 Effects of Helium and Displacement on Crack Initiation and Propagation

II.C.15 Effects of Near Surface Damage on Fatigue

IV. SUMMARY

Capsules of 316 SS, pressurized with a He/Ar mixture were irradiated in the core of MITR-II under temperature and stress cycling for a total of nine weeks. Between irradiations the capsules were measured and the surface was observed. A small amount of creep and no asymmetric deformation was found; the specimens showed some oxidation. The addition of some Argon to the pressurizing gas led to early detection of a capsule failure and could be used to follow the growth of the tiny leak over two days. The microstructure and microhardness of the 316 SS test material was

determined after anneals at different temperatures and creep data were determined for later comparison with the irradiated material. The preparations for cutting the hot samples in a hot cell and TEM work are well advanced.

V. ACCOMPLISHMENTS AND STATUS—H. Andresen (M. I. T./Hahn Meitner Institute); G. Kohse, A. Argon, O. Harling, M. I. T.

Starting November 1, 1979, pressurized capsules made of SS 316 were irradiated in the core of the MITR-II with a fast flux of ~ 10^{14} n/cm^2-sec (E>0.1 MeV) and a thermal flux around 3 x 10^{13} n/cm^2-sec under temperature and pressure cycling. The cycling was obtained by rapid changes of the helium pressure in the irradiation thimble, which causes rapid changes in the heat transport for the y-heating, which stays constant. The control system has been described in an earlier quarterly report [1]. Design details of the irradiation capsule are given in Fig. 1.

Minimum conductance along the metal paths was an important design criterion for the frame, together with the requirement of maximum optical access to the sample surface and adequate mechanical stability required by safety considerations (protection against missile effects) and precise positioning in the measurement steps. The heat transfer characteristics of the irradiation unit (Fig. 1) during cycling and under equilibrium conditions have been measured. Evaluation of the data will soon be completed and will then allow precise predictions about the maximum temperature range and minimal cycle times which are achievable in this and somewhat similar geometries. Presently used cycles are shown in Fig. 2.

Periodic removal of the irradiation unit from the core for careful examination was planned and has been executed successfully. The radioactive irradiation capsule was transferred from the core to the hot cell for disassembly (removal of the titanium can) and then inserted into the precision measurement/observation setup described in Ref. [2]. Only a

small amount of creep and no asymmetries in the deformation were measured. The specimen surfaces show evidence of oxidation, which was not expected because very pure helium was used in the cyclic irradiation. An explanation for this phenomenon is not yet known. Mass spectrometric analysis of the residual gases in the irradiation thimble will be carried out during the next irradiation run. This data about the maximum level of oxygen in the thimble during the low pressure (i.e. high temperature) part of the cycle will allow evaluation of the effect.

As indicated in Fig. 1, the capsules are pressurized with a He/Ar mixture. This results in a few hundred microcuries Ar-41 activity per specimen under irradiation with $3 \times 10^{13} cm^{-2}$ thermal neutrons. If a pressurized capsule fails, the released Argon activity is pumped from the thimble during the low pressure part of the cycle and detected with a GM tube in the exhaust lines of the pumps. With this setup the failure of one of the two specimens after about seven weeks of irradiation was detected. During ongoing irradiation the gas release from the defective specimen could be measured quantitatively and even the growth of the small leak during the first 40 hours was observed.

The 316 SS material used for the experiments has been characterized with several methods, both for determination of an adequate pre-irradiation annealing treatment and for later comparison with data on the irradiated material. Changes in the microstructures and microhardnesses after 30 min anneals at different temperatures between 750°C and 1100°C were examined. Some creep data were measured on 750°, 800" and 980" annealed material with standard specimens. Some TEM work was done on as received, 20% CW and post creep test material. For post irradiation examination and testing, the pressurized capsules must be cut in a hot cell. Preparations for this step are well advanced.

VI. REFERENCES

1. H. Andresen, O. K. Harling, "Effects of Near Surface Damage and Helium on the Performance of the First Wall," DAFS Quarterly Progress Report, October – December 1978.

2. H. Andresen (M. I. T./Hahn-Meitner-Institut), G. Kohse, K. Kwok, A. Argon, O. K. Harling (M. I. T.), DAFS Quarterly Progress Report, April – June 1979.

VII. FUTURE WORK

In the near future we expect to begin testing with pressurized capsules in-core under alpha particle bombardment from ^{10}B layers as well as stress and temperature cycling. Simultaneous out-of-pile experiments on pressurized capsules will simulate the thermal and stress environment without the alpha bombardment and radiation environment of the reactor core.

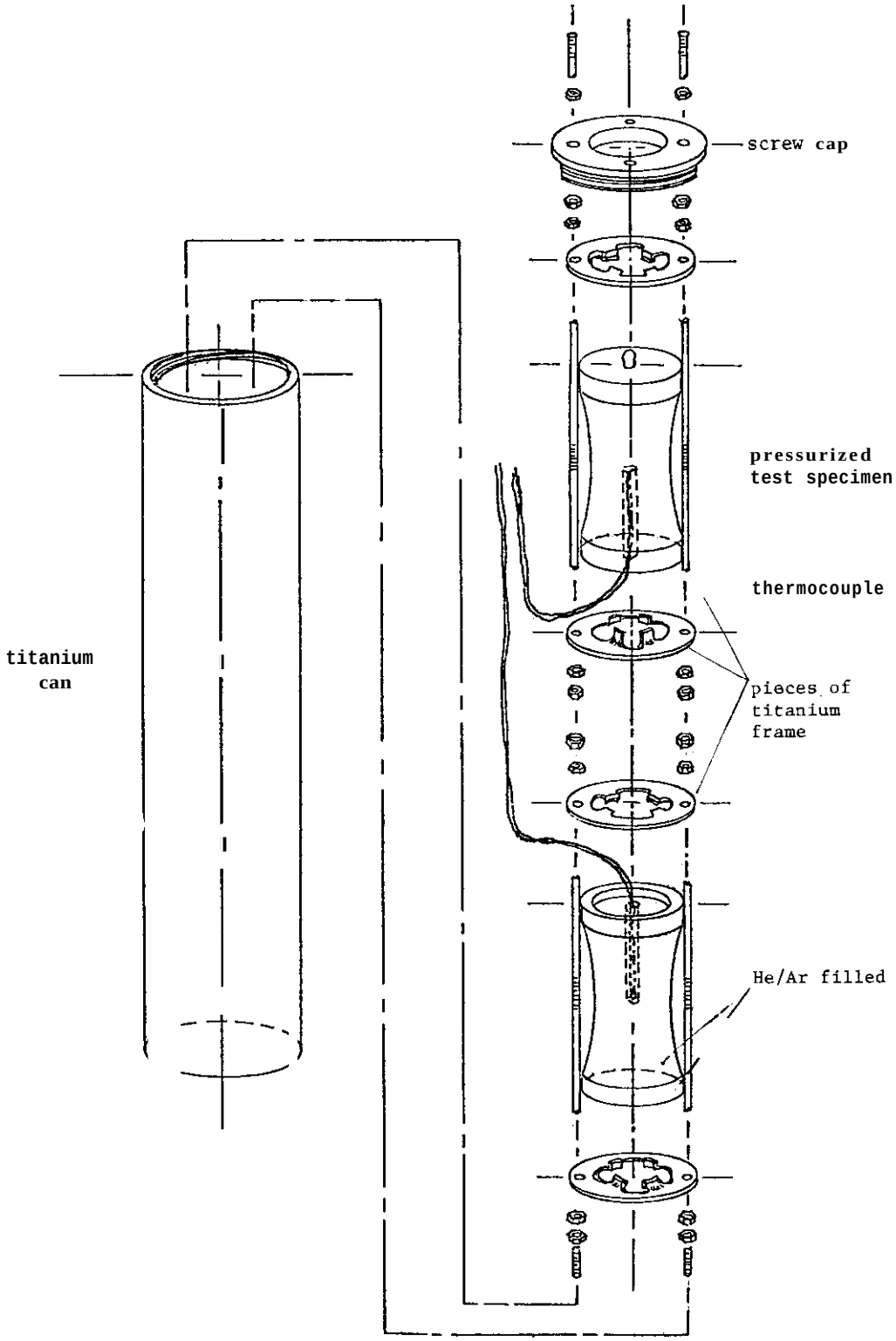

FIGURE 1. Details of Irradiation Unit: The SS 316 test specimens (He/Ar pressurized capsules) are held by a titanium frame which is screwed into a titanium can.

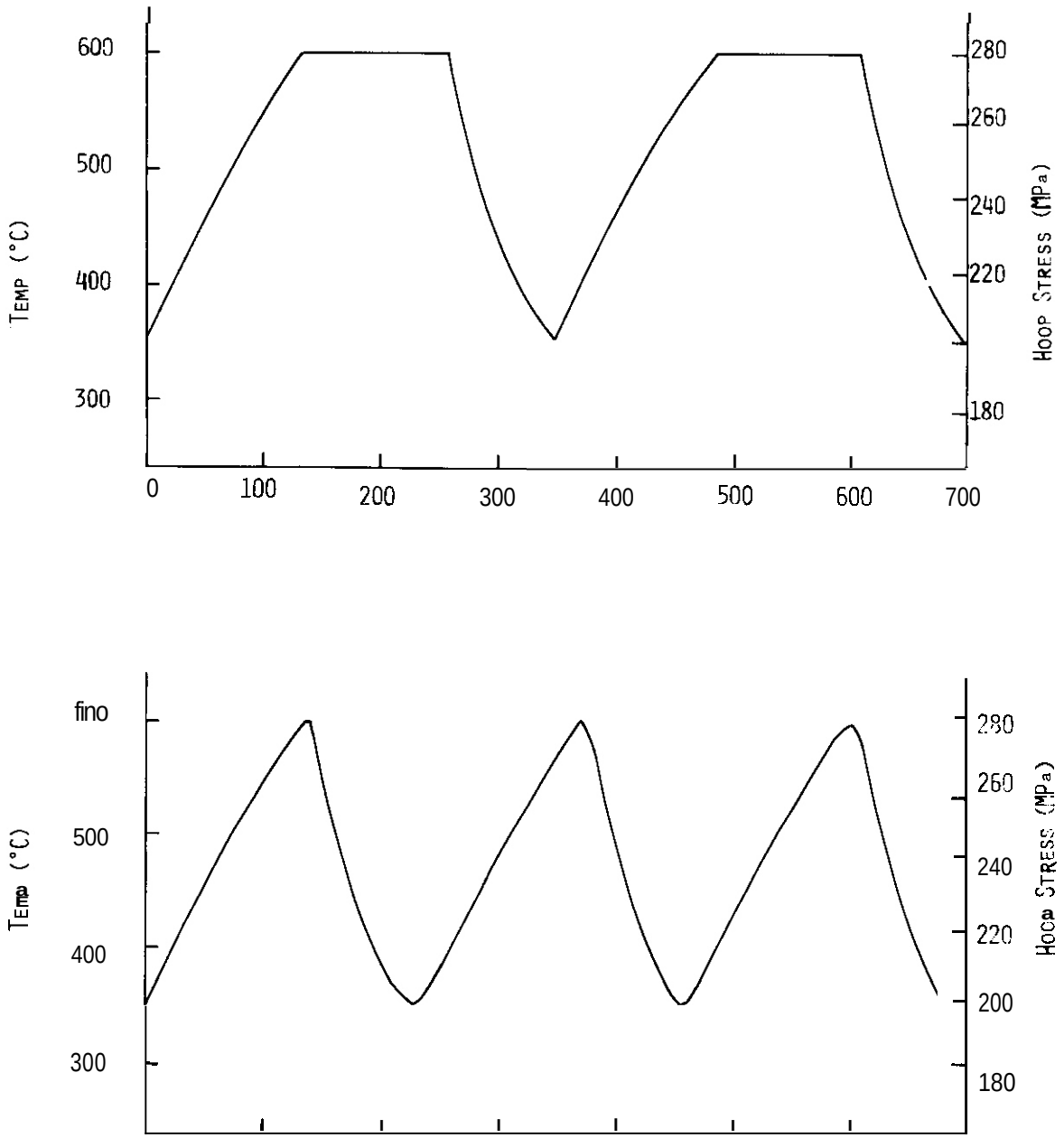

FIGURE 2. **Typical Examples of the Time Dependent Temperatures and Stresses for the Pressurized Tube Specimens.**

CHAPTER 4

CORRELATION METHODOLOGY

I. PROGRAM

Title: Irradiation Effects Analysis
Principal Investigator: D. G. Doran
Affiliation: Hanford Engineering Development Laboratory

II OBJECTIVE

The objective of this effort is to develop dimensional and property change correlations for fusion environments utilizing data derived from fission neutron and charged particle irradiations.

III. RELEVANT DAFS PROGRAM TASK/SUBTASK

II.C.l Effects of Material Parameters on Microstructure
II.C.2 Effects of Helium on Microstructure
II.C.1.4 Models of Flow and Fracture Under Irradiation
II.C.16 Composite Correlation Models and Experiments
II.C.17 Microstructural Characterization

IV. SUMMARY

The current status of three fission-fusion correlation efforts is outlined. Efforts are currently underway to develop correlations for swelling, irradiation creep and yield stress of AISI for application to the design of the Engineering Test Facility (ETF). Each of these correlations is based on an assessment of the microstructural and microchemical evolution of this alloy and is anticipated to be substantially different from that currently employed to describe the isothermal and flux-independent behavior predicted in breeder reactors.

V. ACCOMPLISHMENTS AND STATUS

A. Development of Fission-Fusion Correlations - F. A. Garner (HEDL)

1. Introduction

In an earlier report it was noted that the correlations currently available for radiation-induced dimensional and mechanical property changes of AISI 316 could not be directly utilized for ETF design studies without modification.[1] The current correlations were developed from breeder reactor data and require reformulation in order to incorporate the anticipated differences in flux, spectrum and helium generation. It is also anticipated that the pulsing inherent in Tokamak-type reactors will lead to some difference in behavior when compared to the essentially continuous irradiation typical of fast breeder reactors.

In addition, the current correlations are based on empirical descriptions of data extracted from isothermal irradiations. While the correlations reproduce the data trends, the empirical description selected is not unique and there are other descriptions that would fit the data equally as well. Each possible correlation is based on a different conception of the physical processes involved, however. Since the various descriptions would only diverge beyond the data base one might argue that all were equally valid for their intended purposes. In fact, however, the accumulated swelling data for other starting conditions of the AISI 316 alloy[2] or for non-isothermal irradiation histories[3] argues for a substantially different swelling correlation, and it is suspected that the irradiation creep correlation also requires similar modification.[3] The anticipated changes will significantly affect the predictions of the derived correlation when applied to fusion environments.

The primary insight leading toward a reformulation of fission-based correlations arises from recent advances in the understanding of the microchemical and microstructural evolution of AISI 316 stainless steel.[2-6] It has been shown that much of the observed response of this steel to irradiation can be correlated directly to the evolution of a number of phases and the subsequent extensive repartition of various elements between the alloy austenite matrix and these phases. Each of these phases exhibits a

different sensitivity to the large number of variables known to influence radiation-induced property changes. The relationship of the microchemical evolution to swelling is schematically shown in Figure 1.

Therefore the differences in the fission and fusion environment will lead to differences in each property change correlation that are specific to the temperature and fluence regime in which each phase develops. For instance, some phases are sensitive to displacement rate and others to time at temperature; some are sensitive to stress and some are not, and some phases are stable (once formed) over a wide temperature range, while others are stable only in or below the temperature range in which they formed.[6] The various phases also exhibit different sensitivities to various compositional modifications.

In the following sections the progress attained on three current fission-fusion correlation efforts is outlined. The approach taken in each is to first develop a reformulated correlation capable of describing the breeder-generated isothermal data equally as well as the current correlation, but one which is also capable of describing the non-isothermal and starting condition data as well. These correlations will be developed in cooperation with the individuals in the Breeder Reactor Program responsible for the particular property change under investigation. Each correlation will be written in a format which allows incorporation of variables relevant to fission-fusion correlations. The available data relevant to environments with high helium/displacement ratios will then be assessed and used along with simulation data and theoretical modeling to modify the reformulated breeder correlations to make them applicable to fusion environments.

2. Swelling Correlation

As shown in the inset of Figure 2 and Equation 1 the current design swelling correlation for 20% cold-worked AISI 316 describes the

ANALYSIS OF BREEDER DATA NECESSARY FOR ETF CORRELATIONS

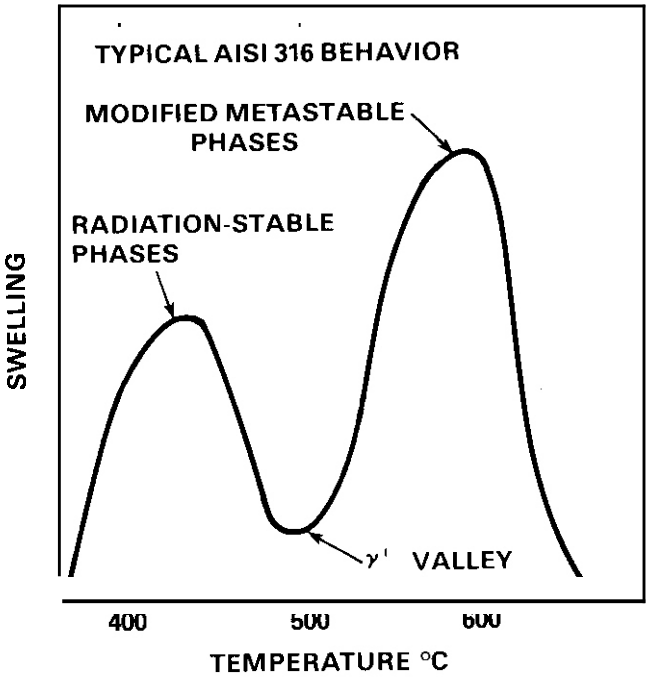

- MICROCHEMICAL INSIGHT VALUABLE
- REFORMULATION OF BREEDER CORRELATION REQUIRED
- SENSITIVITIES OF SWELLING TO COLD-WORK, AGEING, STRESS, FLUX, TEMPERATURE HISTORY ARE BEING DEVELOPED
- CORRELATION OF PHASES WITH SENSITIVITIES IN PROGRESS
- EXTEND REFORMULATED EQUATION TO ETF BASED ON HFIR DATA AND PROPERTY PHASE SENSITIVITIES

FIGURE 1. Schematic Illustration of the Various Phase Regimes and Their Impact on the Swelling of AISI 316. The elements of an effort to reformulate the correlations for use in ETF are also outlined.

REFORMULATION OF SWELLING CORRELATION

MICROCHEMICAL INSIGHT REQUIRES ALL TEMPERATURE AND HISTORY DEPENDENCE TO RESIDE IN THE INCUBATION PARAMETER

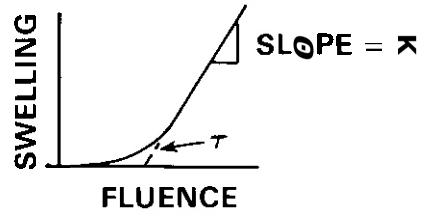

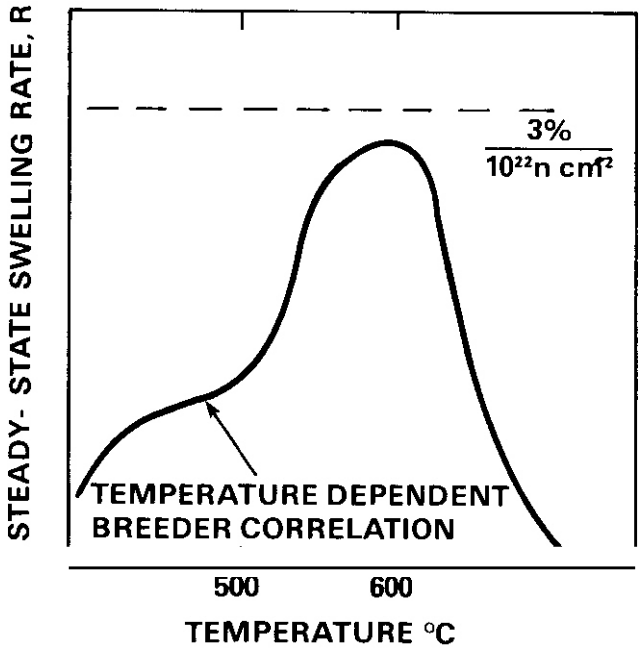

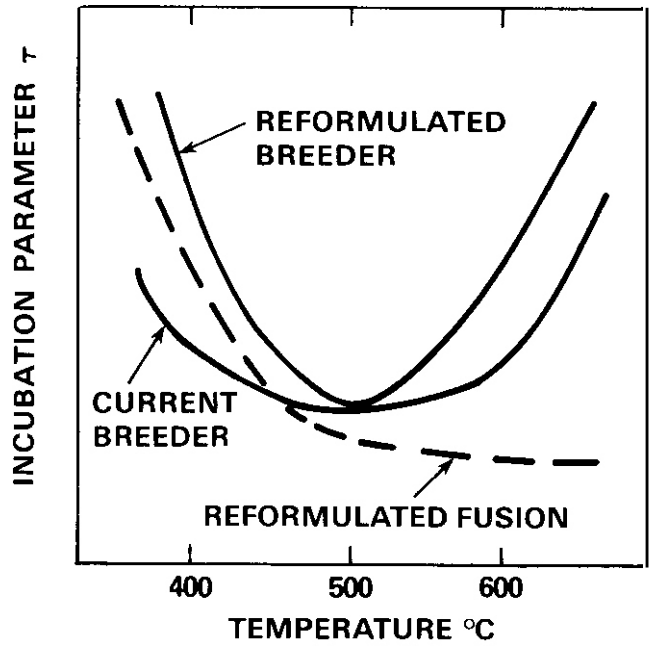

FIGURE 2 Schematic Illustration of the Changes Required in UNS 316 Swelling Correlation in Order to Apply it in ETF.

development of steady-state swelling at a rate $R(\%\Delta V/V_o$ per 10^{22} n/cm^2[E>0.1 MeV]) after a relatively large incubation period.[7] The incubation behavioi is described by an incubation parameter τ (which is essentially the extrapolated fluence intercept of the steady-state swelling regime) and a transition parameter α which governs the transition region between no swelling and steady-state swelling. The low or zero swelling regimes for isothermal irradiations are rather large and range from 4 to 9 x 10^{22} n/cm^2 (E>0.1 MeV) depending on the heat under consideration.

$$\text{Swelling} = R\left[\phi t + \frac{1}{\alpha}\ln\left(\frac{1 + \exp[\alpha(\tau - \phi t)]}{1 + \exp(\alpha\tau)}\right)\right] \qquad [1]$$

For reasons to be documented in depth in a later report, the current temperature-dependent steady-state swelling rate curve shown in Figure 2 is being replaced with a swelling rate that is independent of temperature. The best current estimate is R = 2.92%/10^{22} n/cm^2 but the final value may be as high as R = 4.0%/10^{22} n/cm^2. This necessitates that $\tau(T)$ be reformulated in order to fit the available data, as shown in Figure 2. Within the regime of the available data, this latter expression has been found to fit the data as well as the current correlation. At fluences above the data regime the predictions diverge substantially, particularly for temperatures above ~625°C and also for temperatures below ~525°C.

ETF will operate primarily at lower temperatures[1] (<350°C) with only some experimental regions operating in the temperature regime typical of breeder reactors, i.e., 300-700°C. Therefore the reformulated equation must first be checked to *see* what adjustments are necessary to describe other non-breeder data in 300-700°C range. Several problems have been identified and are now being addressed.

First, the majority of non-breeder data in AISI 316 was generated from irradiation of the DO heat of steel. With hindsight derived from the Breeder Reactor Program it appears that the DO heat is different in composition from both the reference N-lot and first. core FFTF steels.

It contains sixty percent more silicon, an element identified as playing a large role in the microchemical evolution, a higher level of manganese and a measurable amount of titanium. All of these elements participate strongly in the formation of the radiation-stable phases found in low temperature irradiations of AISI 316 and are expected to foster somewhat earlier swelling.

A second problem is that there appears to be some uncertainty in the swelling levels measured for the DO heat in HFIR. The reported microscopy and immersion density measurements vary.[8,9] Discussions with P. Mazaisz of ORNL indicate that difficulties were encountered in early immersion density measurements and that microscopy measurements require substantial judgment in weighting the relative contributions of void swelling in the matrix and cavity swelling at the grain boundaries. This poses a third problem in that the breeder correlation includes no grain boundary cavity contribution. It is also unlikely that the large cavity contribution observed in HFIR irradiations can be related to microchemical processes. Therefore, a reassessment of data generated in HFIR is in progress. In addition some additional data on the swelling behavior of DO heat in EBR-II is being gathered for analysis. There are also some swelling data on U.K. steels obtained at temperatures as low as 270°C (the inlet temperature of DFR) which are being analyzed. The plan of attack in development of the swelling correlation is shown in Figure 3.

3. Irradiation Creep Correlation

Irradiation creep in ETF will be much more difficult to model than swelling since there are currently no irradiation creep data available from HFIR. It is anticipated that swelling and creep correlations must exhibit some parallels, particularly in their temperature dependences, since both processes are manifestations of the same microstructural and microchemical processes. It is also anticipated from analysis of breeder data that the creep correlation must be reformulated if it is to successfully predict the response of AISI 316 to temperature history. There are also

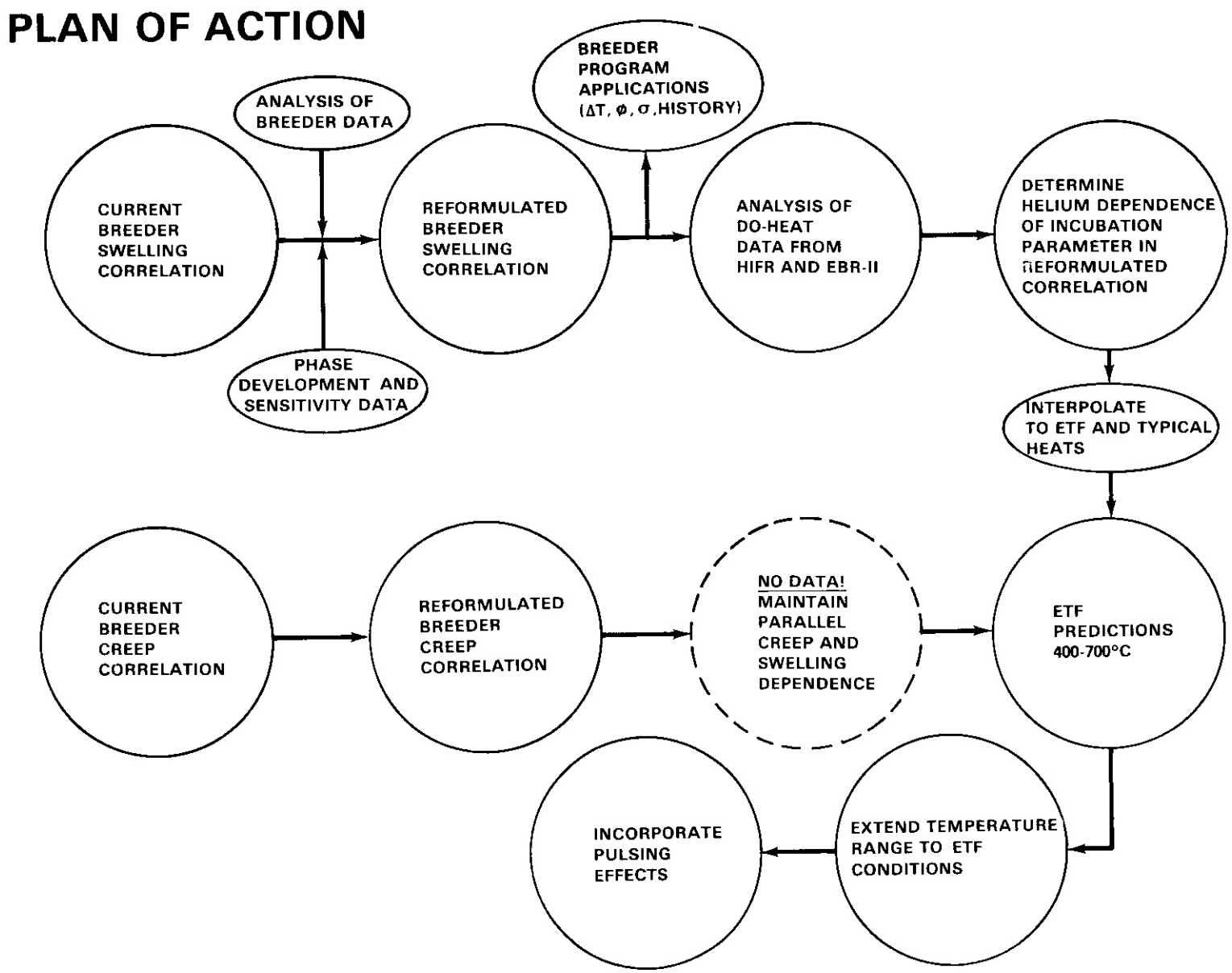

FIGURE 3. Outline of Plan of Action to Develop Swelling and Creep Correlations for ETF Operations.

data which indicate that irradiation creep is sensitive to flux[10] and increases at lower temperatures.[10,11]

Figure 3 illustrates the parallel approach to be used in development of fission-fusion correlations for irradiation creep. Note that pulsing effects are anticipated in both irradiation creep and swelling. Recent publications by Gurol and Ghoniem suggest that the potential effect of pulsing can be large depending on the exact nature of the microstructure and pulse history.[12,13] Collaboration with Gurol has yielded the preliminary result that irradiation of AISI 316 in ETF at the upper end of that facility's anticipated temperature regime may lead to enhancement of creep by a factor of two or three. This effort is now being expanded to incorporate all anticipated creep mechanisms, as well as microstructural scenarios typical of AISI 316 in its various starting conditions. It is anticipated that the results will provide guidance for incorporation of pulsing effects on creep and swelling.

4. Yield Stress Correlation (with G. D. Johnson)

There currently exists for AISI 316 a correlation for yield stress based on a flow-law equation of state of model. This correlation in its present formulation allows no extrapolation to helium-rich environments where the microstructural evolution is known to be substantially altered. Nor does it contain any dependencies on flux, temperature history or pulsing. Since the microstructure of irradiated AISI 316 has been more extensively characterized than any other alloy, an effort has been initiated to develop a microstructurally-based correlation to complement the flow-law equation. Although the microstructurally-based equation will not offer any better predictive capability for isothermal irradiations in breeder reactors, it can be used in conjunction with microstructural data generated in thermal or mixed spectrum reactors to provide guidance for extrapolation to this type of environment. An outline of this approach and its status is shown in Figure 4.

DEVELOPMENT OF MICROSTRUCTURAL BASED YIELD STRESS CORRELATION

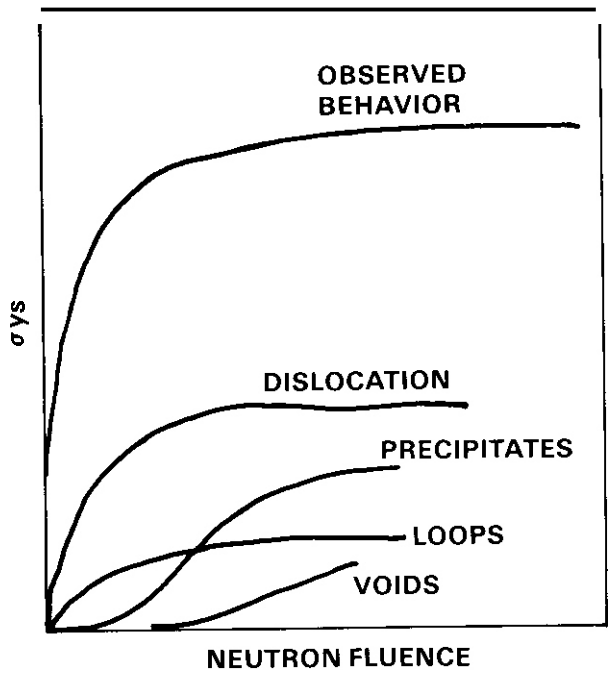

BREEDER DATA ANALYSIS

- PROVIDE MICROSTRUCTURAL CORRELATION TO AID EXTRAPOLATION OF EXISTING BREEDER CORRELATION BASED ON FLOW LAW / EQN. OF STATE
- CORRELATION WITH VARIOUS MICROSTRUCTURAL COMPONENTS ESTABLISHED
- FLUX AND TEMPERATURE-SENSITIVE COMPONENTS IDENTIFIED
- HELIUM BUBBLE AND VOID ROLES ESTABLISHED

ETF CORRELATION

- EXTRAPOLATE FROM HFIR / ORR MICROSTRUCTURES OBSERVATIONS AND FLUX / HELIUM DEPENDENCIES

FIGURE 4. Schematic Illustration of Approach Used to Develop a Microstructurally-Based Correlation for Yield Stress. The current status of the effort is also shown.

The development of the microstructurally-based correlation is nearing completion and will be reported in depth in the next report. Preliminary results demonstrate that the major features and magnitude of the curves[14] shown in Figure 5 can be reproduced. As shown in Figure 6, this effort was aided greatly by the fact that solution-annealed 316 saturates at the same level of yield stress as does cold-worked steel.[15] Since it arrives at this point by an entirely different microstructural route, it is possible to more clearly isolate the action of each microstructural component and to determine the best hardening parameters with which to describe that component.

VI. FUTURE WORK

Each of these efforts will continue. It is anticipated that the first generation swelling and yield stress correlations will be completed and documented in the next quarterly report. A correlation for irradiation creep will be developed on a slower time scale.

VII. REFERENCES

1. F. A. Garner, "Review of Needs for Developing Fission-Fusion Correlations," DAFS Quarterly Progress Report, October-December 1979, DOE/ET-0065/8, p.

2. H. R. Brager and F. A. Garner. "Dependence of Void Formation on Phase Stability in Neutron-Irradiated Type 316 Stainless Steel," ASTM-STP 683, p. 207.

3. F. A. Garner, E. R. Gilbert and D. S. Gelles, "The Effect of Temperature Changes on Swelling and Creep of 316 Stainless Steel," HEDL-SA-2003, November 1977.

4. H. R. Brager, F. A. Garner, E. R. Gilbert, J. A. Flinn and W. G. Wolfer, in Radiation Effects in Breeder Reactor Materials, M. L. Bleiberg and J. W. Bennett, eds., AIME, 1977, pp. 727-755.

5. H. R. Brager and F. A. Garner, J. Nucl. Mat. 73, p. 9.

6. H. R. Brager and F. A. Garner, "Analysis of Radiation-Induced Microchemical Evolution in 300 Series Stainless Steel," this report.

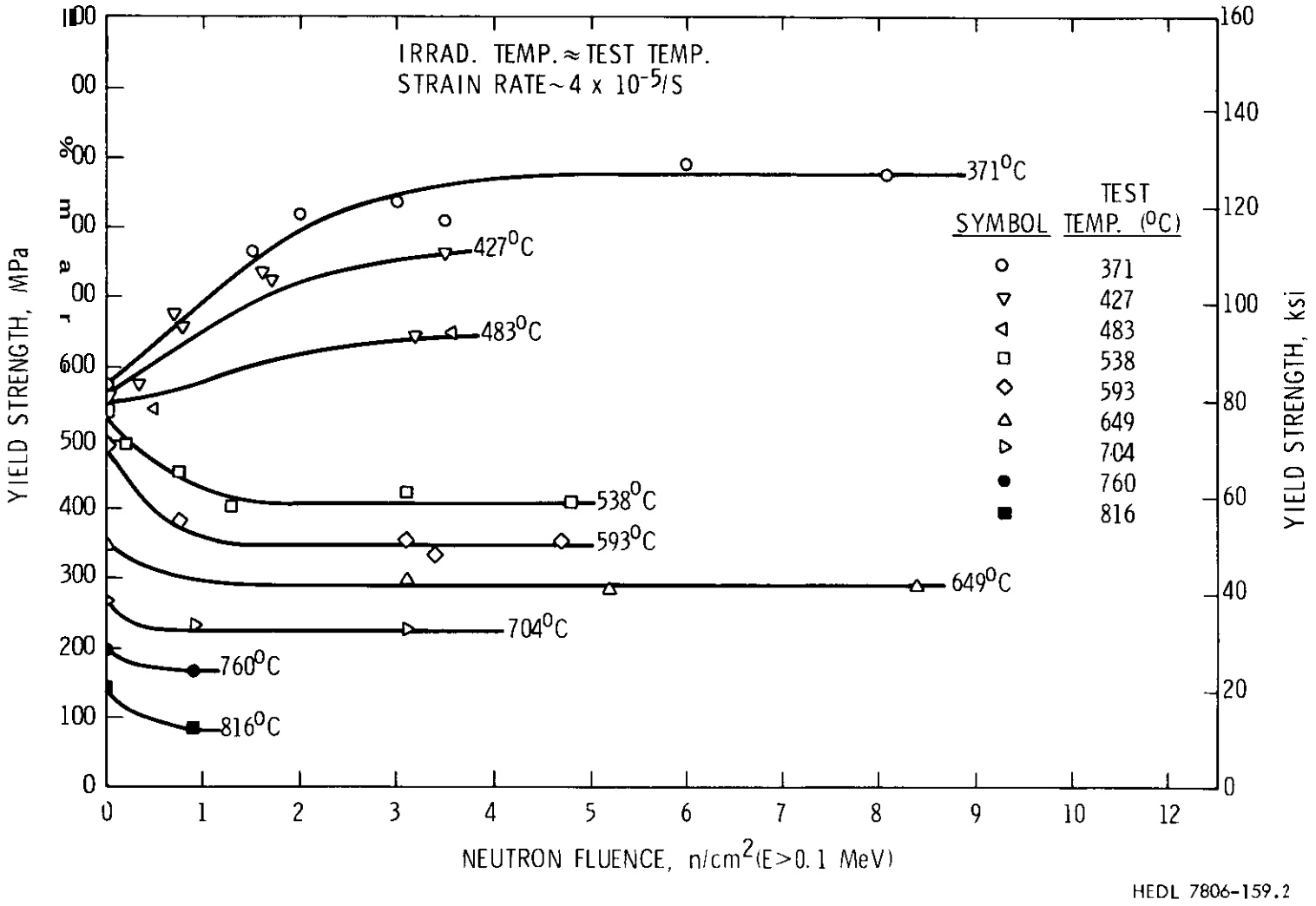

FIGURE 5 Yield Stress of 20% Cold-Worked Type 316 Stainless Steel After Irradiation in EBR-II.[14]

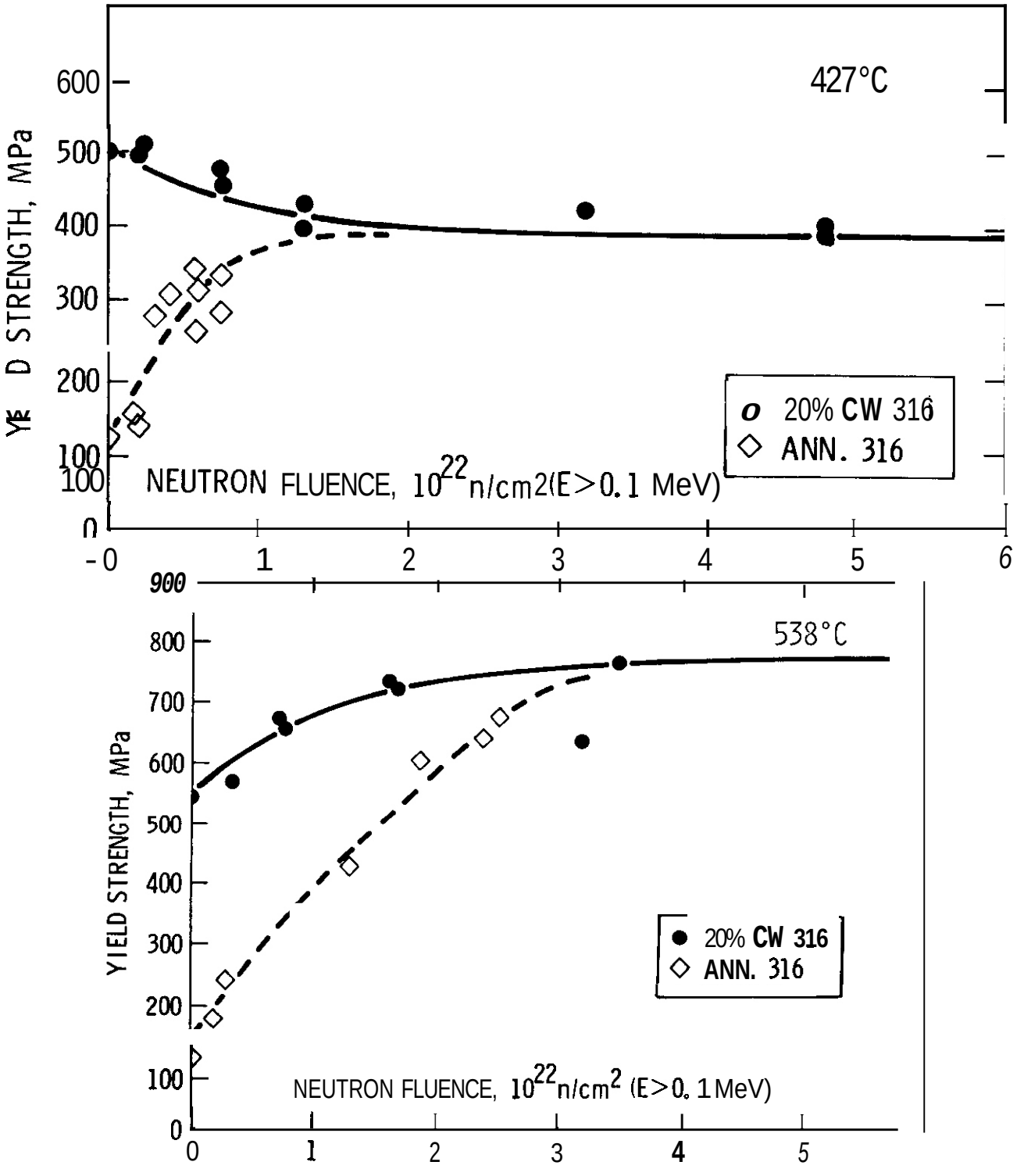

FIGURE 6. Yield Stress of AISI 316 in Two Starting Conditions After Irradiation to 427°C and 538°C.(15)

7. J. F. Bates and M. K. Korenko, "Empirical Development of Irradiation-Induced Swelling Design Equations," accepted for publication in Nuclear Tech.

8. P. J. Maziasz, F. W. Wiffen and E. E. Bloom, "Swelling and Microstructural Changes in Type 316 Stainless Steel Irradiated Under Simulated CTR Conditions," ORNL/TM-5396, May 1976.

9. J. A. Horak, E. E. Bloom, M. L. Grossbeck, P. J. Maziasz, J. O. Steigler and F. W. Wiffen, "Swelling, Mechanical Properties and Microstructure of Type 316 Stainless Steel at Fusion Reactor Damage Levels, Int. Conf. on Behavior of Metallic Materials for Fast Reactor Core-Components, Corsica, France, June 4-8, 1979.

10. G. W. Lewthwaite and D. Mosedale, "The Effects of Temperature and Dose Rate Variations on the Creep of Austenitic Stainless Steels in the Dounreay Fast Reactor," accepted for publication in J. Nucl. Mat.

11. G. W. Lewthwaite and D. Mosedale, "Irradiation Creep of Nimonic PE16 Alloy in the Dounreay Fast Reactor," ibid., Reference 9.

12. H. Gurol and N. M. Ghoniem, "Irradiation Creep by the Climb-Controlled Glide Mechanism in Pulsed Fusion Reactors," accepted for publication in Radiation Effects.

13. N. M. Ghoniem and H. Gurol, "An Analytical Approach to Void Growth in Inertial Confinement Fusion Reactor First Walls," U. of California Engineering Report, UCLA ENG 7984 (1979).

14. R. L. Fish, N. S. Cannon and G. L. Wire, ASTM-STP 683, pp. 450-465.

15. G. D. Johnson, F. A. Garner, H. R. Brager and R. L. Fish, "A Microstructural Interpretation of the Fluence and Temperature Dependence of the Mechanical Properties of Irradiated AISI 316," HEDL-SA-2045.

I. PROGRAM

Title: Phase Stability Under Irradiation
Principal Investigator: K. C. Russell
Affiliation: Massachusetts Institute of Technology

II. OBJECTIVE

To understand and model the effects of irradiation on microstructural stability.

III. RELEVANT DAFS PROGRAM PLAN TASK/SUBTASK

SUBTASK II.C.1.2 Modeling and Analysis of Effects of Material Parameters on Microstructure

IV. SUMMARY

The stability of a dispersion of stable particles may be affected by resolution due to radiation recoil. A simple model of the diffusion of the solute that recoils into the matrix allows an estimate of when this process will dominate over the normal thermal coarsening.

V. ACCOMPLISHMENTS AND STATUS

A. Dissolution of Particles Due to Radiation Recoil -- H. J. Frost and K. C. Russell (Massachusetts Institute of Technology, Cambridge, MA)

1. Introduction

There has recently been considerable interest in the stability of particles and precipitates in alloys subjected to intense irradiation. Particles can be restructured, or even entirely dissolved. Coarsening can be enhanced or reversed. The topic has recently been reviewed by Wilkes[1],

who described the simple model of precipitate dissolution originally put forward by Nelson, Hudson, and Mazey.[2] In the simplest model a particle loses solute into the matrix by recoil from radiation at a rate proportional to its surface area, or radius squared. The solute removed is assumed to be evenly distributed as a supersaturation in the matrix. Solute will then diffuse hack to the particle and make it grow in volume at a rate proportional to its radius. A balance between these two processes will occur at some stable steady-state radius. Larger particles would shrink by resolution, smaller ones would grow by accretion. Following this simple model, Wilkes adds explicit consideration of the diffusion of solute in the matrix cell surrounding the particle. He also describes the situation in which the solute reprecipitates as small sub-particles surrounding the main particle. Such reprecipitation has been observed by Jones [3] surrounding ThO_2 particles in a nickel matrix when subjected *to* 50 dpa ion bombardment.

The above models neglect the growth or dissolution of particles caused by the variation in equilibrium solute concentration with particle radius (normal thermal coarsening). This is usually justified at low and moderate temperatures and high radiation fluxes, except for the very smallest particles, as we will show later. For now, we accept the approximation that the solute maintains a constant concentration in the matrix just adjacent to the particle.

One shortcoming of the previous models is that they give no explicit estimate of the time required to reach the predicted steady-state behavior, and no description of the situation that pertains in the interim. To address this problem, this paper presents some simple models of these processes under conditions in which the dominant mechanism is recoil resolution.

2. Steady-State

Let us first estimate how much solute will be in the matrix bv the following simple model of the steady-state situation. Assume a

regular array of particles of equal radius r_p with interparticle spacing of 2L. Each particle may be modeled as being in the center of a spherical region of radius L. Assume for now that the concentration of solute in the matrix is initially zero and grows because atoms accumulate there. These recoil atoms may either diffuse back to the particle, diffuse away from the particle into the matrix, or reprecipitate as new sub-particles in the matrix. Although reprecipitation may often be an important process, we will start with the simpler model which assumes it does not occur. The problem then becomes a straightforward diffusion problem.

To attack the problem we also assume a constant recoil distance, R. This is not physically correct, of course, because irradiation cascades produce an entire spectrum of recoil distances. From the model we will find that it is the longest recoils (primary knock-ons) that are most important, and the general trend would not be changed if a spectrum of recoil distances were used. For numerical simplicity we have assumed that R = 100 Å.

Given the particle radius, r_p, and the recoil distance, R, we can find the rate of deposition in the matrix, G, as a function of radius from the particle center, r, by geometry, as has been done by Garner and Gelles.[4]

$$G(r) = \frac{S}{4rR}\left[r_p^2 - (r - R)^2\right] \tag{1}$$

where S is the volumetric birth rate of solute recoil atoms in the particle. Since no deposit occurs farther away from the particle than the recoil distance, $G(r) = 0$ for $r \geq r_p + R$. We do not include the second-order effect of recoils of solute atoms that are already in the matrix.

The solute atoms that diffuse back to the particle may be assumed to recombine at the interface and return to the particle phase. If some approach to local equilibrium is maintained, then we may assume that a boundary condition of constant concentration, c_o, occurs at the particle

surface, $r = r_p$. Solute atoms that diffuse away from the particle will eventually enter the region of other particles. If particles are identical we would expect symmetry midway between them, which we can model by using the boundary condition $\frac{dc}{dr} = 0$ at $r = L$.

When the radiation is turned on, a halo of solute will start to build up around the particle and diffuse into the matrix. Eventually at long times the concentration in the matrix (at more than one recoil distance from the particle) will approach a high constant level which we may call steady-state. The steady-state matrix concentration is such that as much material diffuses down the concentration gradient back to the particle as is being deposited into the matrix by the recoil. The steady-state concentration profile can be found from the diffusion equation

$$\frac{\partial c}{\partial t} - D\nabla^2 c + G = 0$$

with boundary conditions:

1. $c = c_o$ at $r = r_p$

2. $\frac{\partial c}{\partial r} = 0$ at $r = r_p + R$ [because $G(r \geq r_p + R) = 0$]

The concentration is linear in recoil rate, S, (or the flux of radiation), and inverse in the diffusion coefficient of the solute, D. The exact steady-state solution (which appears at long tines in Figu[illegible]s:

$$c_{ss}(r) = c_o + \frac{S}{48RD}\left[r^3 - r_p^3 - 4R(r^2 - r_p^2) - 6(r_p^2 - R^2)(r - r_p) - (3r_p - R)(r_p + R)^3\left(\frac{1}{r} - \frac{1}{r_p}\right)\right] \quad (2)$$

The maximum concentration is:

$$c(r \geq r_p + R) = c_o + \frac{SR^2}{48Dr_p}(4r_p - R) \quad (3)$$

As long as the particle is much larger than the recoil distance, the maximum concentration depends only very weakly on the particle size, and depends directly on the recoil distance squared.

3. Applicability

The conditions under which this mechanism is likely to be important can be shown by comparing the matrix concentration in thermal equilibrium with the particles, to the maximum steady-state recoil resolution concentration. For example, consider a dispersion of Al_2O_3 particles in an austenitic stainless steel that has an additional 0.1 atomic percent aluminum as a substitutional solute in the matrix. With excess aluminum available in the matrix, the coarsening or redistribution of particles will depend on the oxygen transport. The equilibrium oxygen concentration in the matrix can be found using the free energy of formation of Al_2O_3, and the activity coefficients of aluminum and oxygen in austenite, and assuming that the matrix concentration of aluminum does not change much from 0.001 atom fraction. The local equilibrium concentration near a particle will be slightly enhanced over the Concentration near a flat interface because of the surface tension of the particle interface, σ. This concentration is plotted against inverse temperature in Figure 1 for particles of 100Å and infinite radius. The same figure shows the maximum concentration from steady-state recoil resolution (using an extrapolation of oxygen diffusion in y-iron). This figure assumes that the diffusion coefficient of oxygen is not appreciably changed by the irradiation. This may be accurate if oxygen diffuses as an interstitial without any strong interaction with the defects produced by the irradiation.

Figure 1 demonstrates three different temperature regimes. At temperatures near 700°C the two concentrations are roughly comparable, and coarsening will be effected by both mechanisms. Below about 500°C the recoil resolution concentration so vastly exceeds the equilibrium concentration that any nucleation barrier to reprecipitation should be

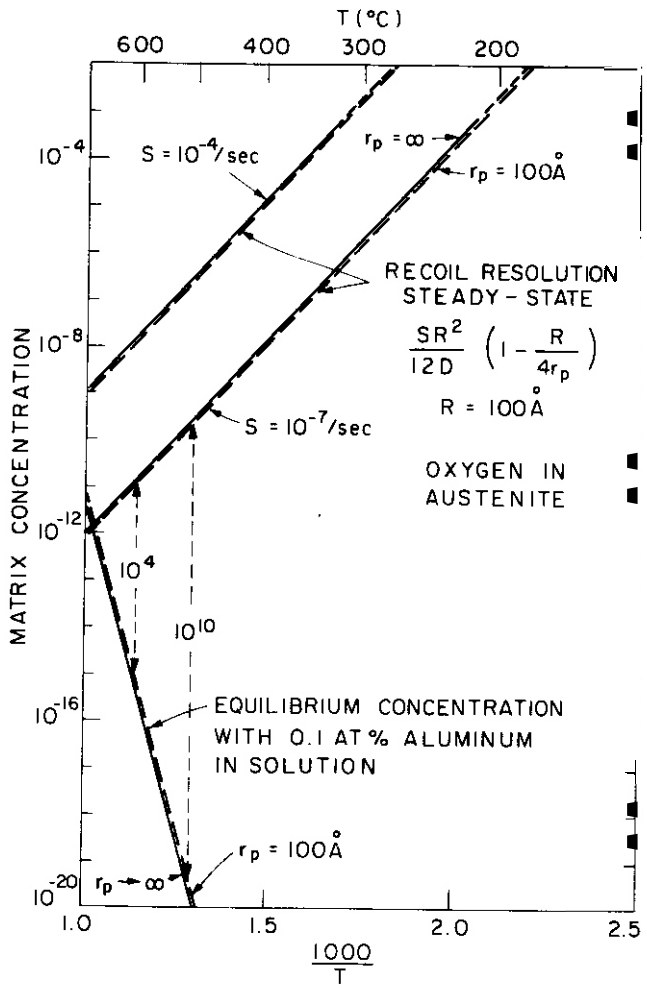

FIGURE 1. Concentration of oxygen from steady-state recoil resolution compared to the concentration in equilibrium with particles without irradiation, for Al_2O_3 in stainless steel.

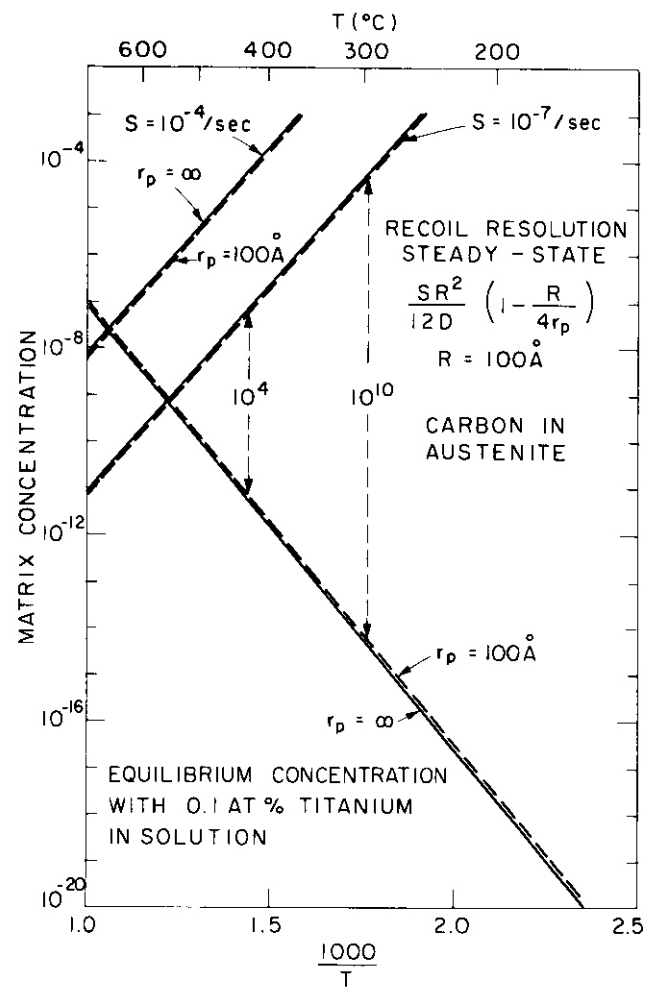

FIGURE 2. Concentration of carbon from steady-state recoil resolution compared to the concentration in equilibrium with particles without irradiation, for TiC in stainless steel.

immediately overcome and the process should be dominated by the growth of reprecipitated sub-particles around each original particle. This will be modeled in more detail in section 5. In between, around 600°C, is a region in which we might expect the simple model to apply. The figure demonstrates that the difference between concentrations near large and small particles (which is the driving force for normal coarsening) becomes insignificant compared to the recoil resolution effects. In Figure 2 the same quantities are plotted for the case of TiC particles in austenite stainless steel, assuming an excess of titanium and control by carbon diffusion. The different regions are shifted to lower temperatures, mostly because of the higher carbon matrix concentration.

4. Transient Behavior

To proceed with this simple model we must find how long it takes to reach the steady-state, and what exactly occurs during the transient. It turns out to be possible to solve the diffusion problem in a closed form series [Carslaw and Jaeger[5]]. For a continuous deposition (at rate unity) in an incremental shell at $r = r_d$, starting at $t = 0$, the concentration will be:

$$c(r,t,r_d) = \frac{2r_d}{r} \sum_{n=1}^{\infty} \frac{(1 + L^2 a_n^2) \sin[\alpha_n(r - r_p)] \sin[\alpha_n(r_d - r_p)]}{[(L - r_p) L^2 \alpha_n^2 - r_p] \alpha_n^2}$$

$$\cdot [1 - \exp(-\alpha_n^2 Dt)] \qquad (4)$$

If the deposition rate varies according to radius as expected from recoil (equation 1), the concentration will be:

$$c(r,t,R) = \frac{S}{2rRD} \sum_{n=1}^{\infty} \frac{(1 + L^2\alpha_n^2) \sin[\alpha_n(r - r_p)]}{[(L - r_p) L^2 \alpha_n^2 - r_p] \alpha_n^5} [1 - \exp(-\alpha_n^2 Dt)]$$

$$\cdot [a_n^2 R(2r_p - R) - 2\cos(\alpha_n R) - 2r_p a_n \sin(\alpha_n R) + 2] \quad , \qquad (5)$$

where a_n, n=1,2 are roots of $\tan[\alpha(L - r_p)] = \alpha L$. This concentration is plotted against radius from the particle center for various values of $\sqrt{Dt}$ for the case of $R = 0.5\ r_p$ and $L = 10\ r_p$ in Figure 3. The same is plotted for $R = 0.2\ r_p$ and $L = 10$, 5 and 3 r_p. With both R and L normalized to r_p we may think of solutions with different R as representing particle radii (with the same recoil distance), and solutions with different L as representing different volume fractions.

The maximum concentration at steady-state does not depend on L at all, but depends on recoil distance as approximately R^2. The time to reach steady-state does not depend on R at all, but does depend directly on L. Steady-state is reached when the characteristic diffusion distance, $\sqrt{Dt}$, is comparable to the interparticle half-spacing, L, times some geometric factor which accounts for the ratio of particle radius to spacing. If we just consider how much material will diffuse away from an isolated sphere with constant surface concentration, we would estimate that enough material had diffused out when $Dt = L\sqrt{\frac{L}{3r_p}}$. In Figure 3 it appears that a closer approach to steady state occurs at $Dt = L\sqrt{\frac{L}{r_p}}$. To find when steady-state will be experimentally important we can plot the time it takes $\sqrt{Dt}$ to reach certain distances versus inverse temperature, as in Figure 4. At 600°C steady-state should be reached within an hour, even for large interparticle spacings. At 200°C we would not expect steady-state to be reached in a year, except at the smallest interparticle spacings.

The same information can be plotted showing contours of the different times it takes to reach steady-state, on axes of particle spacing versus inverse temperature, as in Figure 5.

It should be pointed out that the same diffusion that leads to the steady-state for recoil resolution would be the diffusion responsible for thermal coarsening. There can therefore be no appreciable thermal coarsening in times less than those required to reach steady-state.

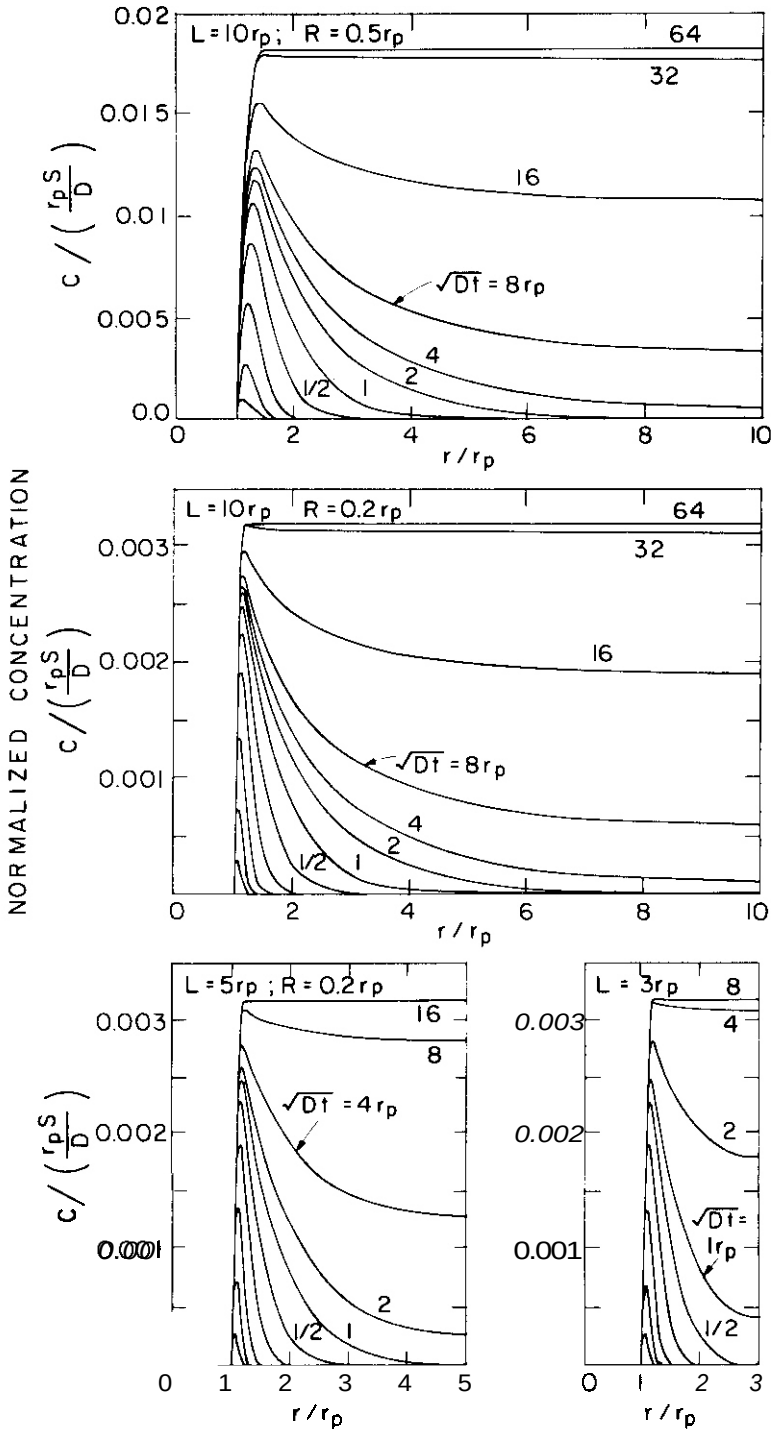

FIGURE 3. Concentrations versus radius for various times from a time dependent recoil resolution calculation. R = 0.5 r_p, L = 10 r_p; and R = 0.2 r_p, L = 10, 5, and 3 r_p.

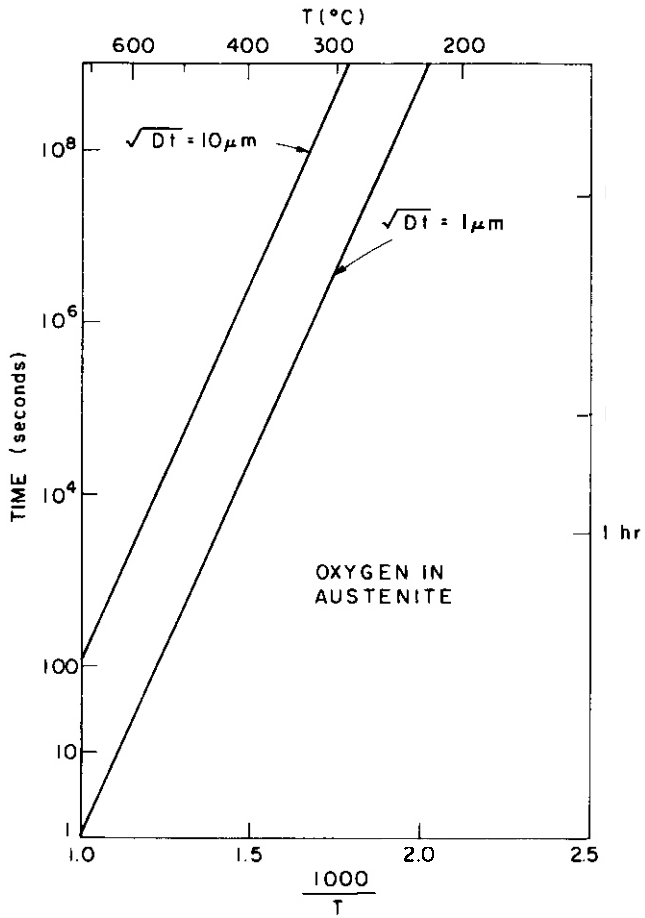

FIGURE 4. Time it takes Dt to reach certain distances versus inverse temperature (for oxygen diffusion in austenite).

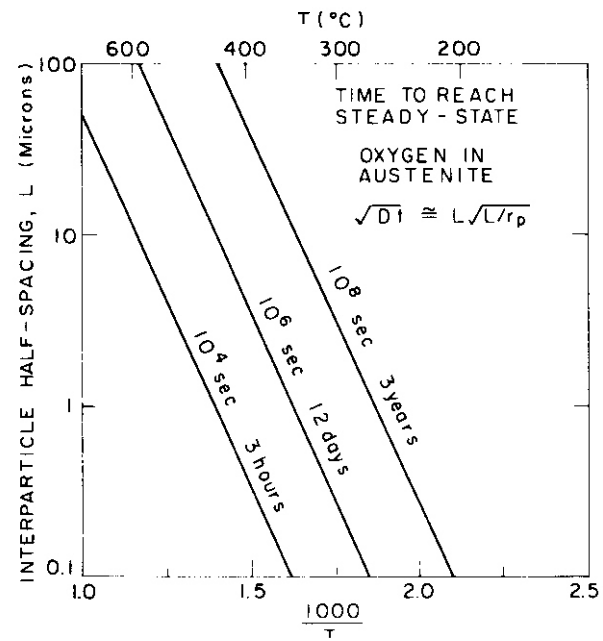

FIGURE 5. Time it takes to reach steady-state recoil resolution, shown on axes of particle spacing and inverse temperature.

One limitation of the model is that it has not used any conservation of solute criterion. That is, we assume that the particle volume fraction does not change because the concentration of solute in the matrix is so low that it constitutes negligible total solute. This would not be true if the steady-state matrix concentration (by atom fraction) approached the initial volume fraction of particles. When this would happen can be derived from Figure 1; the fraction of particles that can be expected to be dissolved (or reprecipitated in the matrix) is shown in Figure 6. This figure is meant only to show the limit of the simple model. It is misleading when reprecipitation is dominant because reprecipitated particles will appear essentially the same as the original particles, except smaller.

A major prediction of this model is whether a dispersion will coarsen in the usual way (driven by the surface tension of the particle—matrix interface, u) or not coarsen (or reverse coarsen) because of recoil resolution. Although this is generally indicated in Figures 1 and 2, it can be more explicitly described. Coarsening will occur when the concentration in the matrix near a large particle is lower than for a small particle. We can add the two effects together and find the net dependence on particle radius:

$$c(r_p) = c_o\left(1 + \frac{2\sigma V_m}{r_p(R_g T)}\right) + \frac{SR^2}{12D}\left(1 - \frac{R}{4r_p}\right) \tag{6}$$

where V_m is the molar volume of the particle phase and R_g is the gas constant. The boundary where the dependence on particle size changes sign is therefore when:

$$s = c_o \frac{96D\sigma V_m}{R^3(R_g T)} \tag{7}$$

In Figure 7 this boundary is plotted for Al_2O_3 and TiC. The boundary is about 100°C higher for typical heavy ion irradiation than for typical fast reactor irradiations. It is independent of particle size.

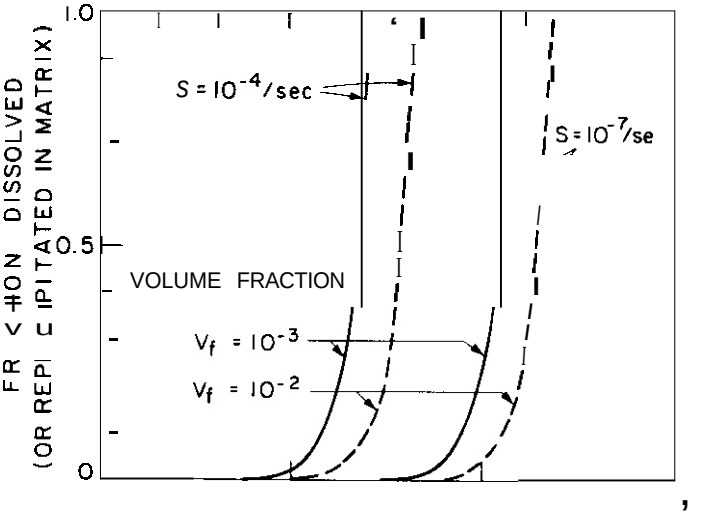

FIGURE 6. Fraction of particles dissolved (or reprecipitated) when steady-state is reached, versus inverse temperature.

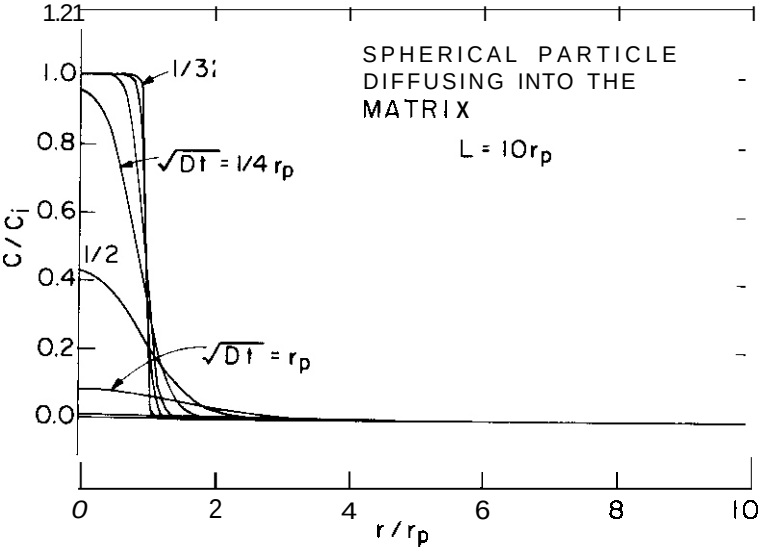

FIGURE 8. Concentration profiles at various times for a spherical particle diffusing into a spherical matrix cell.

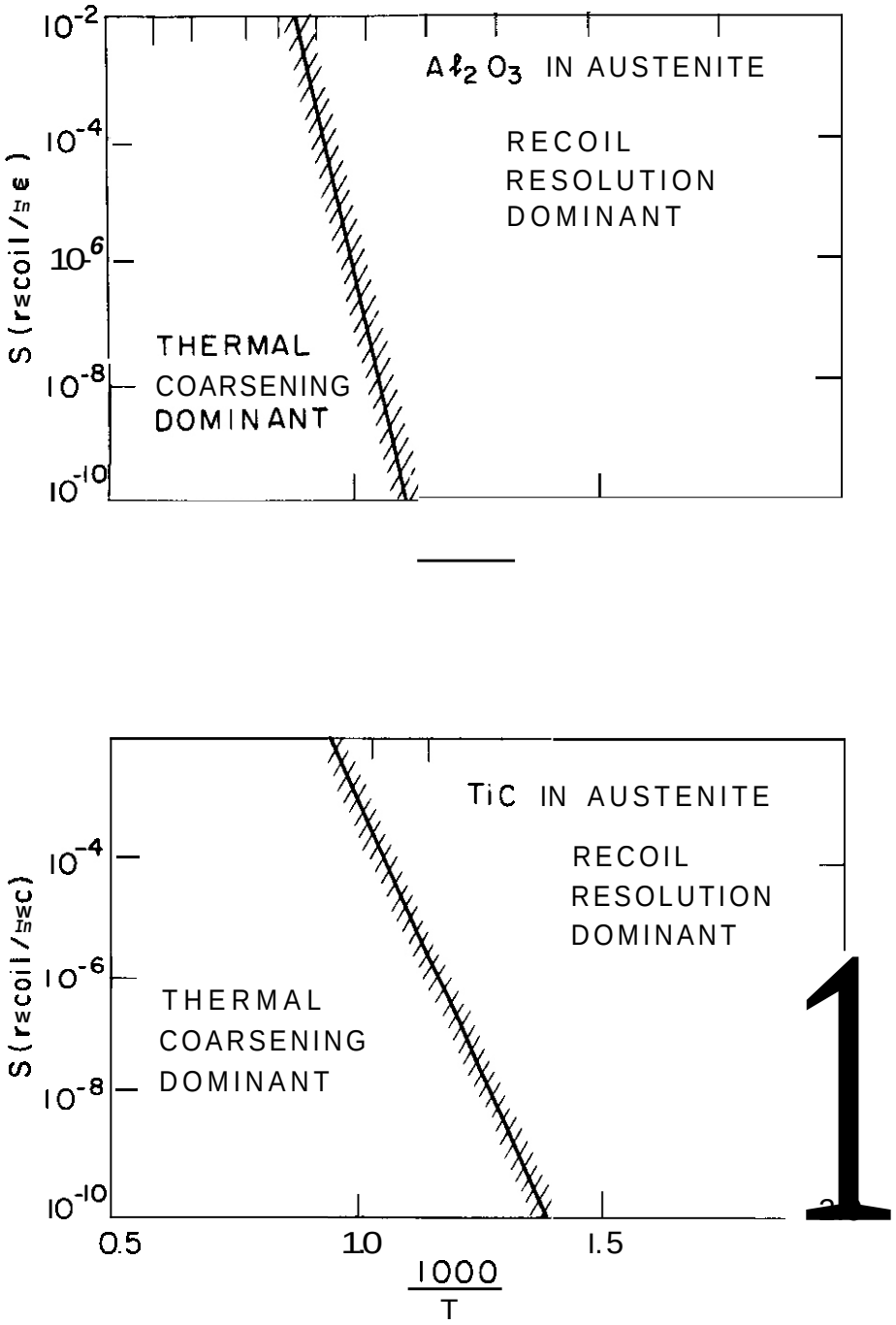

FIGURE 7. Predictions of whether thermal coarsening or recoil resolution will dominate for Al_2O_3 and TiC in stainless steel.

This analysis differs from that of Nelson, Hudson, and Mazey[2], in that we have used a more precise geometric analysis for the resolution rate (theirs is proportional to r_P^2, which is strictly true only if $r_P >> R$), and we do not assume that the dissolved material is uniformly distributed, but have directly modeled its diffusion. If a number of particles is held constant, then our model would lead to the same result that all particles approach a constant volume (when recoil resolution is dominant) which would be the average volume of the initial distribution. If the number of particles is not held constant (for instance, if new particles can be easily nucleated) it is not obvious what lower limit to the particle size will apply.

5. Reprecipitation Dominant Regime

Let us now consider in more detail the extreme condition of reprecipitation dominance. If there is a very large driving force to reprecipitate, then the concentration in the matrix will be limited to the nucleation concentration for sub-particles, which may be orders of magnitude less than the steady-state discussed above. In this case, each original particle will become surrounded by a tight halo of sub-particles. This appears to be the case for the ThO_2 particles observed by R. H. Jones.[3] As the irradiation continues, there will be recoils from the sub-particles in this halo, which would start another sub-halo of sub-particles about one recoil distance farther out. There is no obvious reason why this process should not continue until the entire volume is filled with an even distribution of sub-particles. The size and spacings of such sub-particles are determined by kinetic and nucleation considerations. We expect that the spacing would be very few recoil distances.

This redistribution from a relatively few large particles to an array of sub-particles can be modeled approximately as a diffusion problem. The typical solute atom will spend a very small fraction of its time diffusing in the matrix. It will sit in a sub-particle until it is displaced as a recoil, and before diffusing very far it will get caught in another

sub-particle. *An* effective diffusion coefficient can then be defined based on a jump distance, d, (about one or two recoil distances), and a jump frequency, Γ, (the recoil frequency):

$$D = \frac{\Gamma d^2}{6}$$

Using $d = 2\times10^{-6}$ cm, $\Gamma = 10^{-7}$/sec, we would have $D \cong 10^{-19}$ cm2/sec, which is considerably slower than interstitial diffusion in the usual high temperature experiment (above 300°C) and is the same as the extrapolation of oxygen diffusion in austenite to below 200°C.

Using this diffusion coefficient, the problem can be treated as diffusion in a solid sphere of radius L with the initial solute distribution of

$$c(r) = c_i \quad ; \quad 0 < r < r_p$$
$$= 0 \quad ; \quad r_p < r < L$$

The boundary condition is the same as before: $\frac{\partial c}{ar} = 0$ at $r = L$. The solution is given by Crank[6] (page 97):

$$c(r,t) = c_i \left\{ \frac{r_p^3}{L^3} + \frac{2}{Lr_p} \sum_{n=1}^{\infty} \frac{\exp(-\alpha_n^2 Dt)}{\alpha_n^2} \frac{\sin(\alpha_n r)}{\sin^2(a_n L)} \cdot [\sin(\alpha_n r_p) - r_p a_n \cos(\alpha_n r_p)] \right\} \tag{8}$$

where the a_n's are the roots of $La_n = \tan(\alpha_n L)$.

This solution is shown in Figure 8 as several contours of concentration at different times. As expected, the time to reach an approximate steady-state is when the characteristic diffusion distance approaches the cell size: $\sqrt{Dt} = L$. This time turns out *to* be long compared to typical

experimental times. For an initial interparticle half-spacing of 0.1 micron (which is fairly small) and the recoil rate from typical fast neutron irradiation, we approach steady-state in 10^9 seconds (30 years). For heavy ion irradiations the time required drops to about 10^6 seconds (11 days) which is longer than typical heavy-ion irradiations. We are therefore not surprised that only the beginning of the process has been observed so far. It is not impossible, however, that the steady-state could be approached in fusion first-wall materials in service for several years.

VI. REFERENCES

1. P. Wilkes, J. Nucl. Mat. 83, 166 (1979).
2. R. S. Nelson, J. A. Hudson and D. J. Mazey, J. Nucl. Mat. 44, 318 (1972).
3. R. H. Jones, J. Nucl. Mat. 74, 163 (1978).
4. D. S. Gelles and F. A. Garner, J. Nucl. Mat. 85 and 86, 689 (1979).
5. H. S. Carslaw and J. C. Jaeger, Conduction of Heat in Solids, Clarendon Press, Oxford, 1959.
6. J. Crank, The Mathematics of Diffusion, 2nd edition, Clarendon Press, Oxford, 1975.

VII. FUTURE WORK

The next step in this modeling is to consider explicitly the solute drag caused by the interaction with excess interstitials and vacancies.

I. PROGRAM

Title: Irradiation Effects Analysis (AKJ)
Principal Investigator: D. G. Doran
Affiliation: Hanford Engineering Development Laboratory

II. OBJECTIVE

The object of this effort is to provide the fundamental models which will form the basis of correlations between property changes observed in fission environments and those anticipated in projected fusion devices.

III. RELEVANT DAFS PROGRAM TASK/SUBTASK

Task II.C.l Effects of Material Parameters on Microstructure

IV. SUMMARY

An outline is presented of the fundamental modeling efforts being initiated in support of the DAFS program on radiation-induced microstructural development and its consequences on dimensional and mechanical properties. Progress in three areas is briefly outlined. Another area, previously presented in some detail, is discussed further in order to resolve an apparent discrepancy between predictions of the influence of solute elements on void nucleation.

V. ACCOMPLISHMENTS AND STATUS

A. Development of Microstructural Evolution Models - F. A. Garner (HEDL) and W. G. Wolfer (University of Wisconsin)

1. Introduction

In an earlier report,[1] an assessment was presented of the modeling needs of the DAFS program in support of its objective to provide fission-fusion correlations for application to the Engineering Test Facility (ETF) and other proposed fusion devices. In the area of radiation-induced microstructural/microchemical evolution of AISI 316 a number of required modeling needs were outlined along with a description of ongoing or projected activities to address these needs. In addition to DAFS-sponsored activities, these efforts included cooperative efforts with individuals in other programs with an interest in either the description of fundamental radiation damage or the response of AISI 316 to radiation.

In this report the developing framework of a coordinated fundamental modeling effort on the evolution of AISI 316 is described along with the results of a second assessment of the role played in this evolution by various solute atoms.

2. Current Modeling Efforts

As discussed elsewhere,[2-5] the evolution of AISI 316 involves two concurrent and interactive evolutions, one involving the microstructural components associated with swelling and irradiation creep, and another which involves an extensive repartitioning of elements between various phases. This latter evolution has been shown to be the primary determinant of the alloy behavior in response to the large number of variables which influence void swelling and irradiation creep. It is necessary to describe both evolutions in detail, however, since the microchemical evolution exhibits its effects through the action of the microstructural components, and these components in turn often influence the course of the microchemical evolution.

Currently models of four aspects of "simple" alloy behavior are being developed in cooperative efforts with individuals at various

laboratories. Each of these is described briefly. This work is to be incorporated directly or indirectly in correlation models under development for complicated alloys such as AISI 316, as is described in another report.[6]

(a) Loop Nucleation. The sources of radiation-induced dislocations and their influence on swelling, creep and various mechanical properties arise from the radiation-induced generation of Frank dislocation loops. The factors which determine the number density, orientation and growth rate of Frank loops are subject to some controversy, however, as evidenced by the divergence of opinion expressed on this subject at a recent symposium.[7] In an attempt to discriminate between the action of the various mechanisms and to incorporate them into a loop nucleation code, several data sets derived from irradiations of AISI 316 and Nimonic PE16 have been provided to individuals at three laboratories (HEDL, University of Wisconsin, and ORNL) who are currently modeling loop evolution. These loop data sets, published elsewhere,[8,9] are comprised of complete size and orientation-dependent information for nicrostructures which were both stressed and unstressed during irradiation. Not only are the other microstructural components, such as voids and network dislocations, also complete1 characterized in these data sets but the relationship between loop orientation and stress state is preserved. The principle being applied here is that it is often easier to study and describe a perturbation of a physical mechanism than it is to describe the mechanism itself. In this case the applied stress is the perturbation. The data generated at zero stress will be used to determine parameters needed to model loop capture efficiencies and the data generated under appiied stress will be used to study not only the creep response but also the validity of the zero-stress description.

Another loop modeling effort involves the response of both Frank and diamond loops to intersection with small precipitates. This phenomenon also functions as a perturbation on the normal growth habit from which insight on the processes governing loop growth can be gained. This work is nearing completion.

(b) Network Generation. As shown elsewhere[2] the neutron-induced dislocation densities of both cold work and annealed AISI 316 stainless steel converge to the same steady-state level (6 i3 x 10^{10} cm^{-2}) which appears to be independent of irradiation temperature in both the stressed and unstressed conditions. Similar trends are observed in simulation experiments of simple alloys. Models which describe the relaxation of the cold worked dislocation density (1.7 x 10^{11} cm^{-2}) and the build-up of the annealed density (10^8 to 10^9 cm^{-2}) have been developed. Current efforts are now focused on analyzing data sets available in the Breeder Reactor Program which allow identification of the mechanisms of network generation, particularly the development of network anisotropy in Burgers vector. This effort will form a basic building block for modeling of irradiation creep processes.

(c) Compositional Effects on Sink Biases. In simple ternary alloys the swelling and creep rates are known to be strong functions of composition.[10] As shown in References 2 through 5, dissolved solutes such as silicon are known not only to influence point defect diffusion but to cause major modifications of the matrix composition upon their removal into radiation-induced precipitates. Since the onset of swelling and accelerated irradiation creep have been correlated with changes in matrix composition, an effort has been initiated in which the sink biases are modeled to determine their dependence on matrix composition. Wolfer and Mansur[11] have recently shown that the interstitial capture efficiency or bias of a void is very sensitive to gradients in composition, lattice parameter and elastic moduli near the void surface. Recent data by Brager and Garner[5] have shown that gradients in composition of the required magnitude do indeed develop near void surfaces during irradiation.

(d) Solute Effects on Void Nucleation and Irradiation Creep. As described in an earlier report'[12] solutes in solution in an alloy matrix have a large influence on point defect diffusivities and concentrations. Two major effects have been identified. One of these is the effect of solute-defect binding and is adequately described by a number of authors.

The work of Mansur[13] is a good example. The action of a solute can also be felt as an influence on the diffusivity of the alloy without involving the binding concept. This phenomenon was dealt with in detail in an earlier report[12] in which both the basic diffusivity and binding concepts were studied. In the following section this work is expanded somewhat to address an apparent discrepancy between this work and that of Mansur.

3. The Effect of Solute Additions on Void Nucleation

In a previous report[11] it was shown that the steady-state nucleation rate I of voids is given by

$$I = 2\,(6\pi^2\Omega)^{1/3}\,D_V^{eff}\,(\Delta C_V + C_V^{eq})^2 \left\{ \sum_{x=2}^{\infty} \frac{\exp\left[\Delta G(x)/kT\right]}{x^{1/3}\,Z_V^{o}(x)} \right\}^{-1}, \qquad (1)$$

where Ω = atomic volume,

D_V^{eff} = effective vacancy diffusion coefficient including solute effects,

ΔC_V = radiation-produced vacancy concentration in excess of average thermal vacancy concentration $\bar{C}_V^{eq}$,

$\Delta G(x)/kT$ = nucleation barrier, and

$Z_V^{o}(x)$ = vacancy capture efficiency of the void at size x.

Mansur[12] predicted that immobile traps would decrease void nucleation, whereas in this effort slowly-diffusing elements are predicted by equation (1) to enhance void nucleation. The apparent contradiction arises not from the treatment of migration or binding energies but in the assumed role of bound vacancies as nucleation sites. The consequences of the different assumptions employed in this treatment and that of Mansur can be easily demonstrated. Note that in equation (1) the nucleation rate depends on the second power of the vacancy concentration $C_V = \Delta C_V + \bar{C}_V^{eq}$. The second power expresses the requirement that the nucleation rate is proportional to the number of vacancies C_V and the number of impinging vacancies

$D_v^{eff} C_v$. In this work it is assumed that C_v is composed of the sum of free vacancies C_v^f and bound vacancies C_v^b. In contrast the bound traps of Mansur are considered to be saturable and therefore not available for void nucleation. Therefore, in comparable notation, Mansur's nucleation rate I' is given by

$$I' = 2\,(6\pi^2\Omega)^{1/3}\, D_v^{eff}\,(C_v\, C_v^f)\,\left\{\sum_{x=2}^{\infty} \frac{\exp\,[\Delta G(x)/kT]}{x^{1/3}\, Z_v^{o}(x)}\right\}^{-1} \tag{2}$$

The ratio of the two predicted nucleation rates is

$$\frac{I}{I'} = \frac{C_v}{C_v^f} = 1 + \frac{C_v^b}{C_v^f} \tag{3}$$

The effective vacancy diffusive coefficient[12] is defined by

$$D_v^{eff}\, C_v = D_v\, C_v^f + D_s\, C_v^b\ , \tag{4}$$

where D_s was earlier defined as the solute diffusion coefficient. Thus,

$$\frac{C_v^b}{C_v^f} = \frac{D_v - D_v^{eff}}{D_v^{eff} - D_s}\ . \tag{5}$$

The effective diffusion coefficient is also defined in equation (1), leading to the conclusion that for a given solute concentration C_s

$$\frac{I}{I'} = 1 + K\, C_s\ . \tag{6}$$

For strong binding conditions typical of that considered by Mansur the nucleation rate ratio

$$\frac{I}{I'} \approx K\, C_s\ , \tag{7}$$

and is always larger than unity. Thus, the nucleation rates defined in this study are always larger than those of Mansur for conditions of strong binding. The assumption that both bound and free vacancies can function as nucleation sites is considered to be the more realistic assumption.

VI. FUTURE WORK

Each of the areas covered in this report will continue with primary emphasis placed on the modeling of compositional effects on sink biases.

VII. PUBLICATIONS

A paper has been prepared entitled "The Effect of Solute Additions on Void Nucleation," HEDL-SA-2155, by F. A. Garner and W. G. Wolfer. It is being submitted to the Journal of Nuclear Materials.

VIII. REFERENCES

1. F. A. Garner, "Review of Needs for Developing Fission-Fusion Correlations," DOE/ET-0065-8, p. 64.

2. H. R. Brager, F. A. Garner, E. R. Gilbert, J. E. Flinn and W. G. Wolfer, Radiation Effects in Breeder Reactor Structural Materials, M. L. Bleiberg and J. W. Bennett (Eds), The Metallurgical Society of the American Institute of Mining, Metallurgical and Petroleum Engineers (1977), pp. 727-755.

3. H. R. Brager and F. A. Garner, "Dependence of Void Formation on Phase Stability in Neutron-Irradiated Type 316 Stainless Steel," Effects of Radiation on Structural Materials, ASTM STP 683, J. A. Sprague and D. Kramer (Eds), American Society for Testing and Materials (1979), pp. 207-232.

4. H. R. Brager and F. A. Garner, J. Nucl. Mat., 73, 9 (1978).

5. H. R. Brager and F. A. Garner, "Analysis of Radiation-Induced Microchemical Evolution in 300 Series Stainless Steel," Proceedings of Symposium on Advanced Techniques for the Characterization of Irradiated Materials, 109th AIME Annual Meeting, Las Vegas, Nevada (February 24-28, 1980), in press.

6. F. A. Garner, "Development of Fission-Fusion Correlations," this report.

7. Proceedings of International Conference on Fundamental Mechanisms of Radiation-Induced Creep and Growth (May 8-10, 1979), Chalk River, Ontario, Canada (in press).

8. F. A. Garner, W. G. Wolfer and H. R. Brager. "A Reassessment of the Role of Stress in Development of Radiation-Induced Microstructure," ibid. Ref. 3, pp. 160-183.

9. D. S. Gelles, F. A. Garner and H. R. Brager, "Frank Loop Formation in Response to Applied and Internal Stresses," Proceedings, ASTM 10th International Symposium on Effects of Radiation on Materials, Savannah, Georgia (June 3-5, 1980), HEDL-SA-2002.

10. J. F. Bates and W. G. Johnston, "Effects of Alloy Composition on Void Swelling," ibid. Ref. 2, p. 625.

11. W. G. Wolfer and L. K. Mansur, "The Capture Efficiency of Coated Voids," University of Wisconsin Report UWFDM-329 (November 1979).

12. F. A. Garner and W. G. Wolfer, "Effect of Solute Additions on Void Nucleation," DOE/ET-0065/8, p. 71.

13. See Review by L. K. Mansur, J. Nucl. Mat., 83, 109 (1979).

I. PROGRAM

Title: Irradiation Effects Analysis (AKJ)
Principal Investigator: D. G. Doran
Affiliation: Hanford Engineering Development Laboratory

II. OBJECTIVE

This work was initially conducted under the support of the Breeder Reactor Program and is now being extended toward the development of fission-fusion correlations. The objective of this work is to determine the identity of the radiation-activated processes responsible for the dimensional and mechanical property changes observed in irradiated AISI 316.

III. RELEVANT DAFS PROGRAM TASK/SUBTASK

TASK II.C.l
TASK II.C.16
TASK II.C.17

IV. SUMMARY

The irradiation of 300 series stainless steel by fast neutrons leads to an evolution of alloy microstructures that involves not only the formation of voids and dislocations, but also an extensive repartitioning of elements between various phases. This latter evolution has been shown to be the primary determinant of the alloy behavior in response to the large number of variables which influence void swelling and irradiation creep. The combined use of scanning transmission electron microscopy and energy-dispersive X-ray analysis has been the key element in the study of this phenomenon. Problems associated with the analysis of radioactive specimens are resolved by minor equipment modifications. Problems associated with spatial resolution limitations and the complexity and heterogeneity of the microchemical evolution have been overcome by using several data acquisition

techniques. These include the measurement of compositional profiles near sinks, the use of foil-edge analysis, and the statistical sampling of many matrix and precipitate volumes.

V. ACCOMPLISHMENTS AND STATUS

A. Analysis of Radiation-Induced Microchemical Evolution in 300 Series Stainless Steels - H. R. Brager and F. A. Garner (HEDL)

1. Introduction

The irradiation of metastable alloys such as AISI 316 and 304 has recently been shown to lead to two concurrent and interactive evolutions, one involving the microstructural components associated with swelling and irradiation creep, and the other involving extensive repartitioning of elements between the matrix and various phases.[1-5] Presented in this paper is the key role played by scanning transmission electron microscopy (STEM) and energy-dispersive X-ray (EDX) analysis in the identification and study of this latter phenomenon. The following sections discuss the modifications of commercially-available STEM/EDX equipment necessary to overcome the difficulties associated with examination of radioactive specimens, and the types of data acquisition procedures used to determine the complex nature of the microchemical/microstructural evolution. Finally, a summary is presented of the radiation-induced evolution of AISI 316 as revealed by a combination of STEM/EDX and other techniques, and the impact of this evolution on dimensional and mechanical properties.

2. Modification of STEM/EDX Equipment

The majority of the measurements described in this study were performed on a JSEM-200 STEM equipped with a Kevex energy-dispersive X-ray detector system connected to a Tracor-Northern 880 multichannel analyzer. As described elsewhere,[6] the analysis of radioactive specimens is complicated by the presence of both gamma radiation and characteristic X-radiation. Typical activities due to long-lived isotopes in AISI 316 specimens

(nominally 3 mm in diameter and 0.25 mm thick) measure about 10 Rad/hr at 2.5 cm after irradiation to 1×10^{23} n/cm^2 (E>0.1 MeV). The decay-gamma rays contribute to increased deadtime in the X-ray detector system and a decreased spectral resolution, while the X-rays characteristic of various decay-daughter isotopes provide a false indication of elemental composition.

The majority of the decay radiation directed toward the detector is prevented from reaching it by placing a conical-shaped 16 mm long tungsten collimator between the specimen and the detector. The collimator also attenuates photons generated by other sources in the microscope. Shown in Figure 1, the collimator is mounted at a fixed location on the microscope column at the same elevation as the specimen. As discussed elsewhere,[6] the attainment of an adequate signal-to-noise ratio at the detector requires a trade-off between the specimen-to-detector distance and the intensity of the beam on the specimen. The beam intensity and beam spreading determine the spatial resolution. The specimen/detector configuration used in this study requires a relatively intense electron beam and thus leads to a spatial resolution on the order of 30 to 50 nm.

In order to determine the various elemental concentrations in an area under examination, the X-ray signal is analyzed by the detector circuitry and resolved as a function of X-ray energy. The characteristic decay X-rays are then measured for an equal amount of time when the electron beam passes through the hole in the center of the specimen. The decay spectra are comprised principally of mid-range (about 8 keV) X-rays which, for most cases, are less than 1% of the total signal. The resolved decay spectrum is then "stripped" or subtracted from each energy channel. Correlation factors between X-ray intensities and composition are determined from analysis of unirradiated homogeneous metal standards of known composition. The measurement uncertainties were determined to be about $\pm 2\%$ for major alloy components and about $\pm 10\%$ for minor solute components.

Two other modifications were made to the STEM. First, the vendor-supplied double-tilt specimen holders used in the side entry

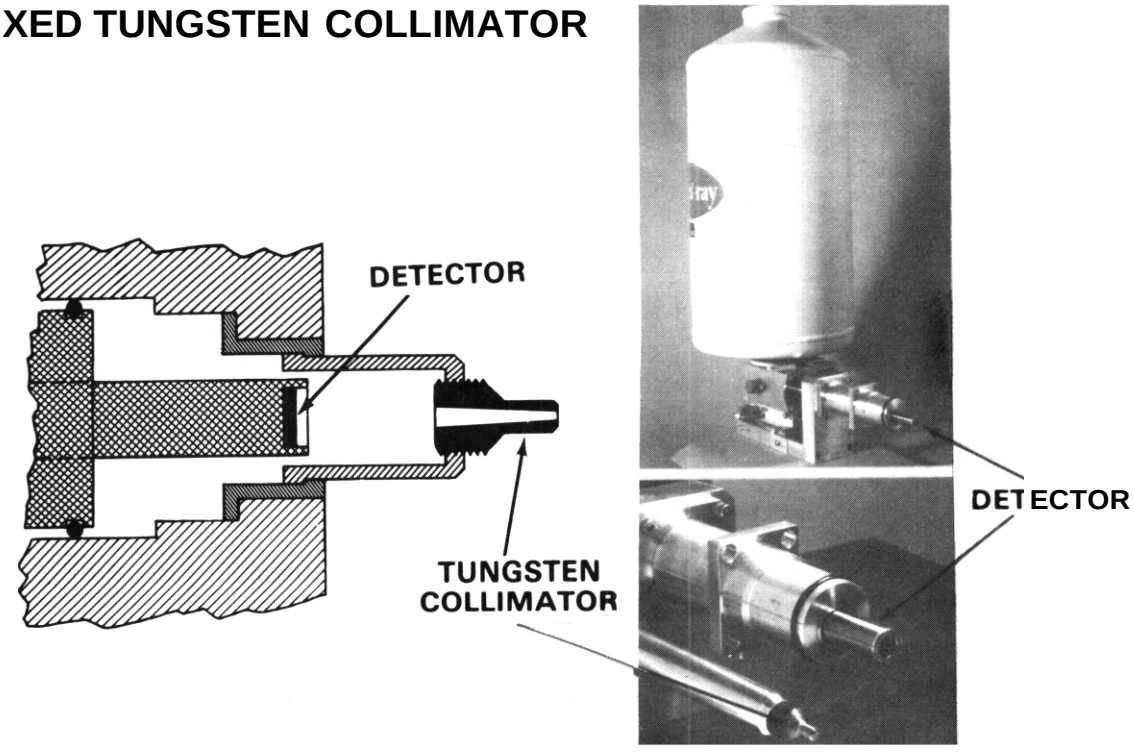

FIGURE 1. Cross Section and Location of Fixed Tungsten Collimator. Note that the detector-specimen distance is variable.

goniometer which are constructed of copper were replaced by a modified holder constructed of beryllium. This holder is shown in Figure 2 and possesses both a threaded cap to securely hold the specimen and a larger solid angle for uninterrupted line-of-sight between the specimen and detector. Beryllium was chosen to eliminate the generation of copper X-rays and to eliminate their second-order influence on the apparent concentration of other elements.[7] The second modification was to alter one of the fixed resistors of the first condenser lens control to provide a continuous variation of lens current. This allows an optimization of the signal-to-noise ratio at the X-ray detector while also allowing maximum resolution of the STEM-generated image on the CRT screen.

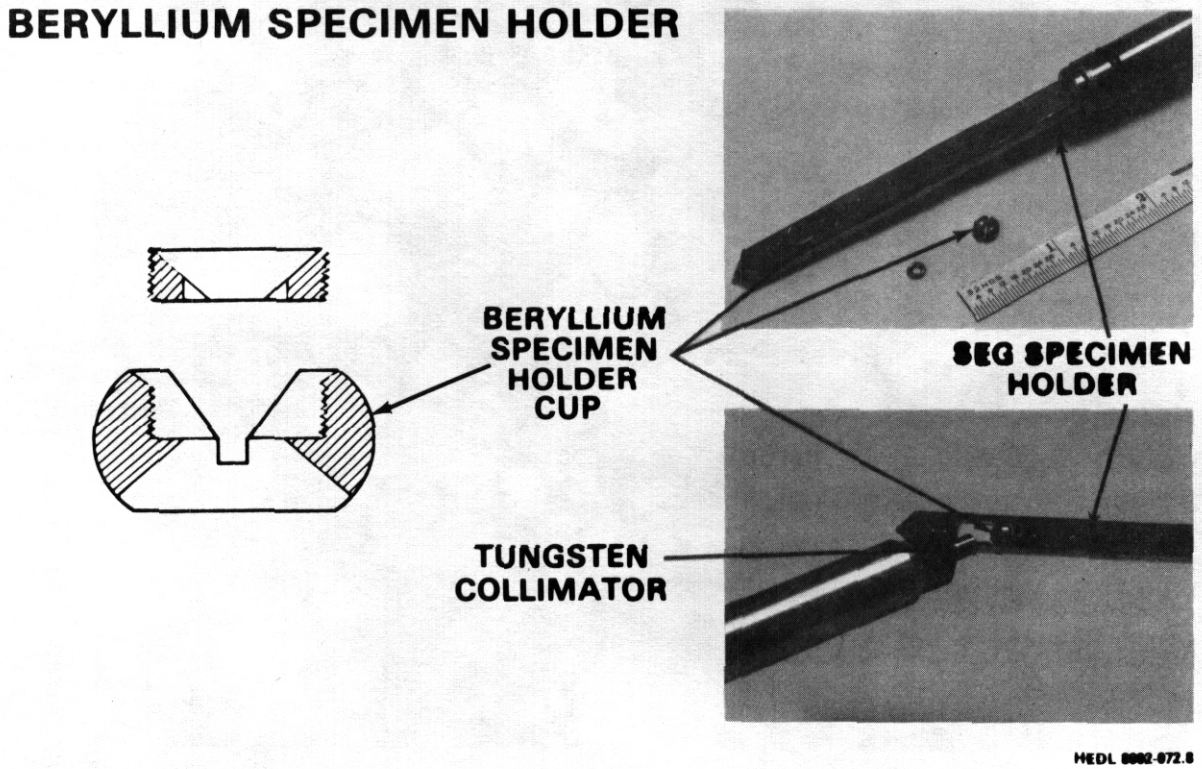

FIGURE 2. Cross Section of Modified Specimen Holder Showing Location in Specimen Holder Assembly and Its Relationship to the Collimator-Detector Assembly.

3. Data Acquisition Strategy

There are a number of factors which complicate the analysis of radiation-induced evolution in 300 series stainless steel. First, the resolution limit of 30 to 50 nm is rather large compared to the scale of the microstructure that develops at relatively low irradiation temperatures. It is also often large with respect to some of the concentration gradients found to develop near microstructural sinks during irradiation. Second, the microstructure under examination is often quite complex as shown in Figure 3, and the many phases are not only sensitive to irradiation

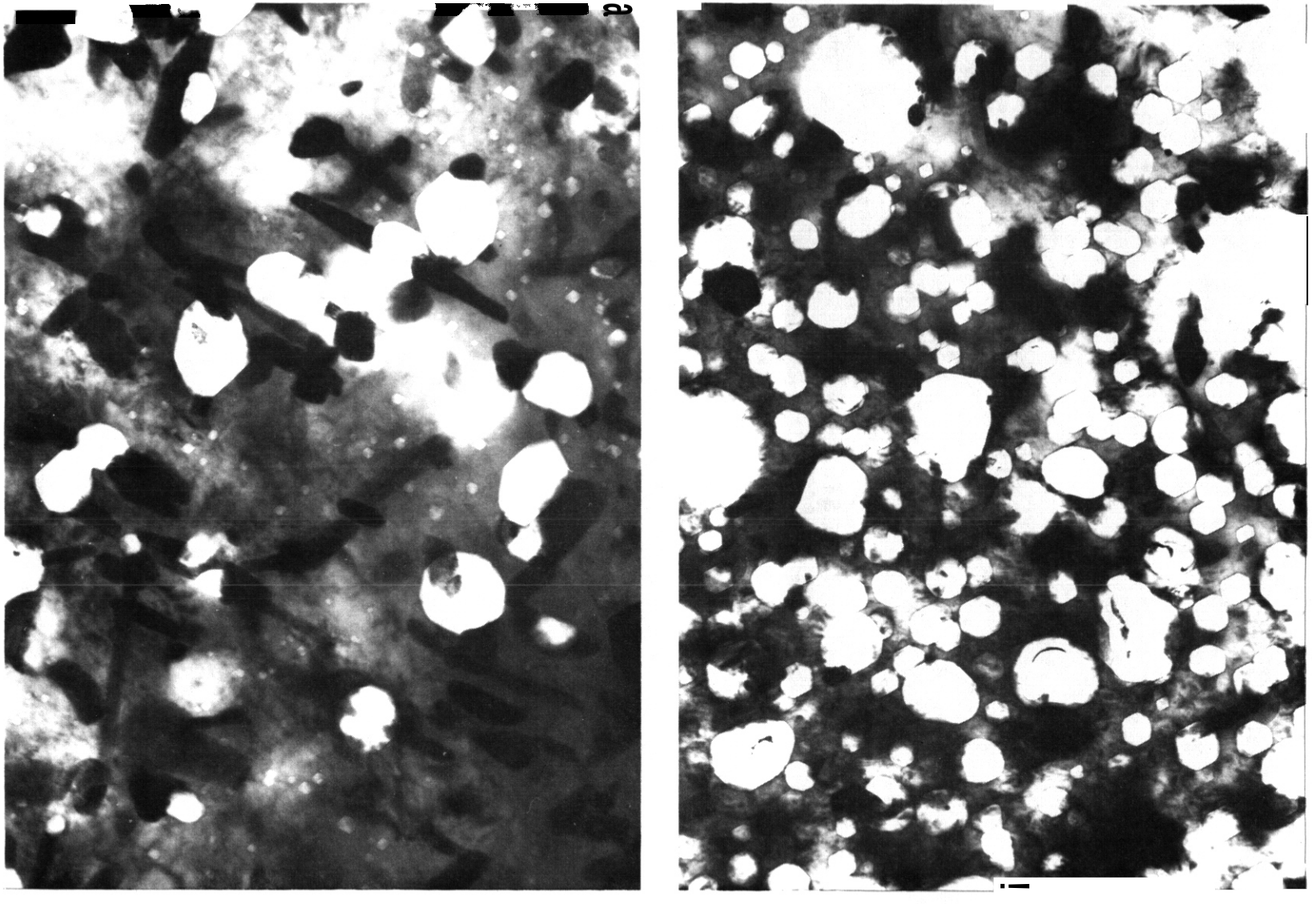

FIGURE 3. Typical Microstructures Observed in Irradiated AISI 316 at 600°C

temperature but are undergoing continuous evolution during irradiation. The evolution is quite heterogeneous in nature, however, progressing at different rates and sometimes by different paths in each small volume sampled. Therefore, conclusions about the nature of the evolution cannot be safely deduced from a single or small number of determinations. Third, the major microstructural participants in the evolution are frequently small with respect to the usual foil thickness employed. This factor often does not allow determination of the composition of a small precipitate, but yields an average composition of the surrounding matrix volume. Another problem is that light elements such as carbon, nitrogen and oxygen cannot be detected with the presently available commercial EDX equipment, a problem which complicates the analysis of the various carbon-rich phases that develop in these steels.

A number of data extraction techniques have evolved in order to study the nature of the radiation-induced evolution and overcome some of the complications discussed above. These involve both different specimen preparation methods, statistical sampling techniques and the use of bulk extraction techniques which complement the microanalysis methods.

a. In-Foil Analysis

Figure 4(a) illustrates representative microstructural features which can be studied using microanalysis techniques. Two of these features, voids and grain boundaries, obviously cannot be extracted and must be examined in-foil. The nature of adjacent composition gradients is of primary interest but the X-ray signal generated by the electron beam will represent a line-of-sight average over the composition gradient as it extends through the matrix. It will also represent an average over the width of the excited volume, which increases with depth in the foil due to scattering of electrons out of the incident beam. Figure 5 illustrates this point, showing the relationship of line-of-sight averages to the actual profile for a highly idealized void, foil and electron beam. If the measured profile can be unfolded, it represents a microstructural record[8] of

IN-FOIL ANALYSIS

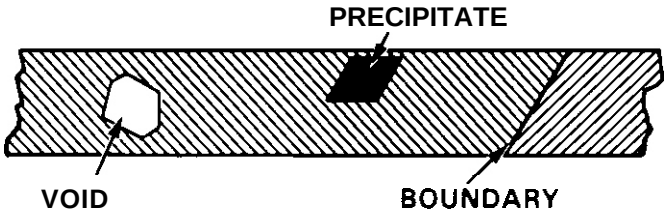

[a]

EXTRACTION REPLICA ANALYSIS

[b]

FOIL - EDGE ANALYSIS

[c]

HEDL 8003-310.1

FIGURE 4. Schematic Illustration of Microanalysis Techniques Employed by This Study.

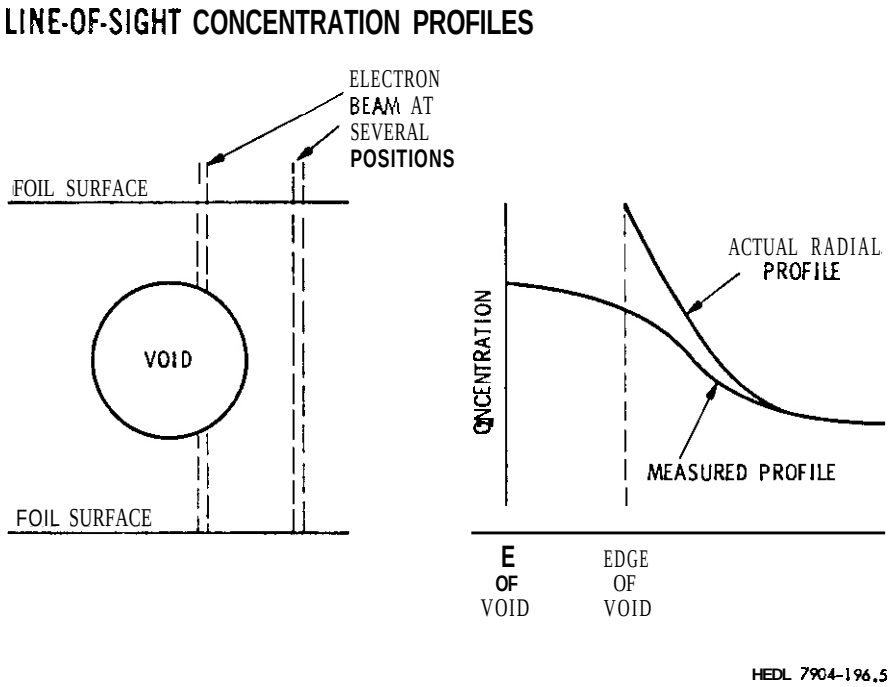

FIGURE 5. Schematic Representation of Idealized Determination of Line-Of-Sight Concentration Profile and Its Relationship to Actual Profile.

the diffusional processes in progress during irradiation. Figure 6 shows typical measured concentration profiles for nickel and chromium in the vicinity of void surfaces in AISI 316 at a high neutron fluence and temperature. The segregation of nickel at void surfaces is primarily balanced by an outflow of chromium. There is also a lesser outflow of iron, but no measurable gradients were found to exist in other major components such as molybdenum or silicon. This microstructural record therefore provides data which can be used to validate and rank the operation and relative contribution of various diffusional processes postulated to operate during irradiation. For instance, the segregation of the slow-diffusing nickel and the compensating outflow of the faster diffusing chromium offer substantial support for the proposed inverse Kirkendall effect,[**] wherein slow-diffusing species are concentrated by default at the bottom of vacancy gradients as a consequence of the selective outflow of faster-diffusing elements.

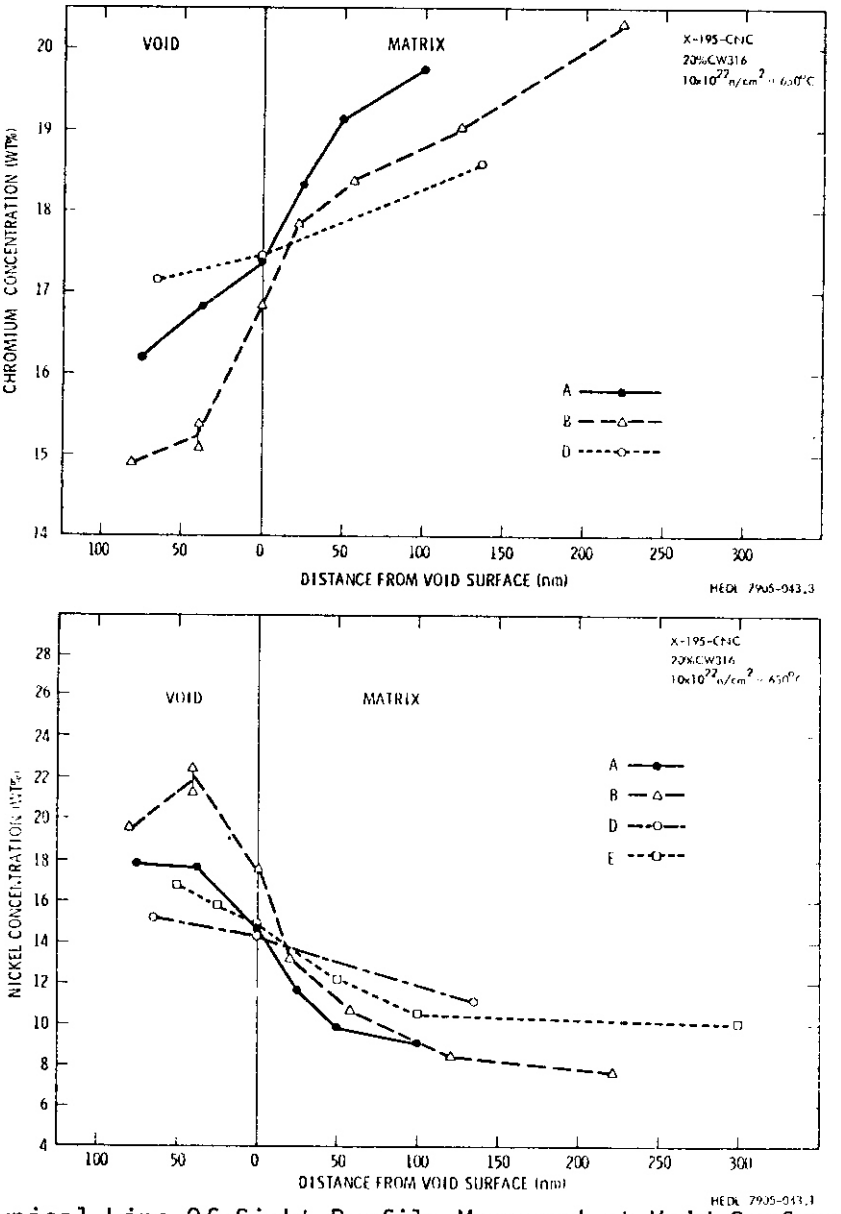

FIGURE 6. Typical Line-Of-Sight Profile Measured at Void Surfaces in 20% AISI 316 Irradiated to 1.0 x 10^{23} n/cm^2 (E>0.1 MeV) at 650°C.

Similar microstructural profile records can be developed from regions adjacent to and within precipitates, but this subject will be developed in a later section. Grain boundaries also participate in the segregation process but the microanalysis results can sometimes be misleading. Figure 7 shows the segregation profiles observed at 520°C in annealed AISI 316. The apparent decline in nickel content near the boundary is illusory

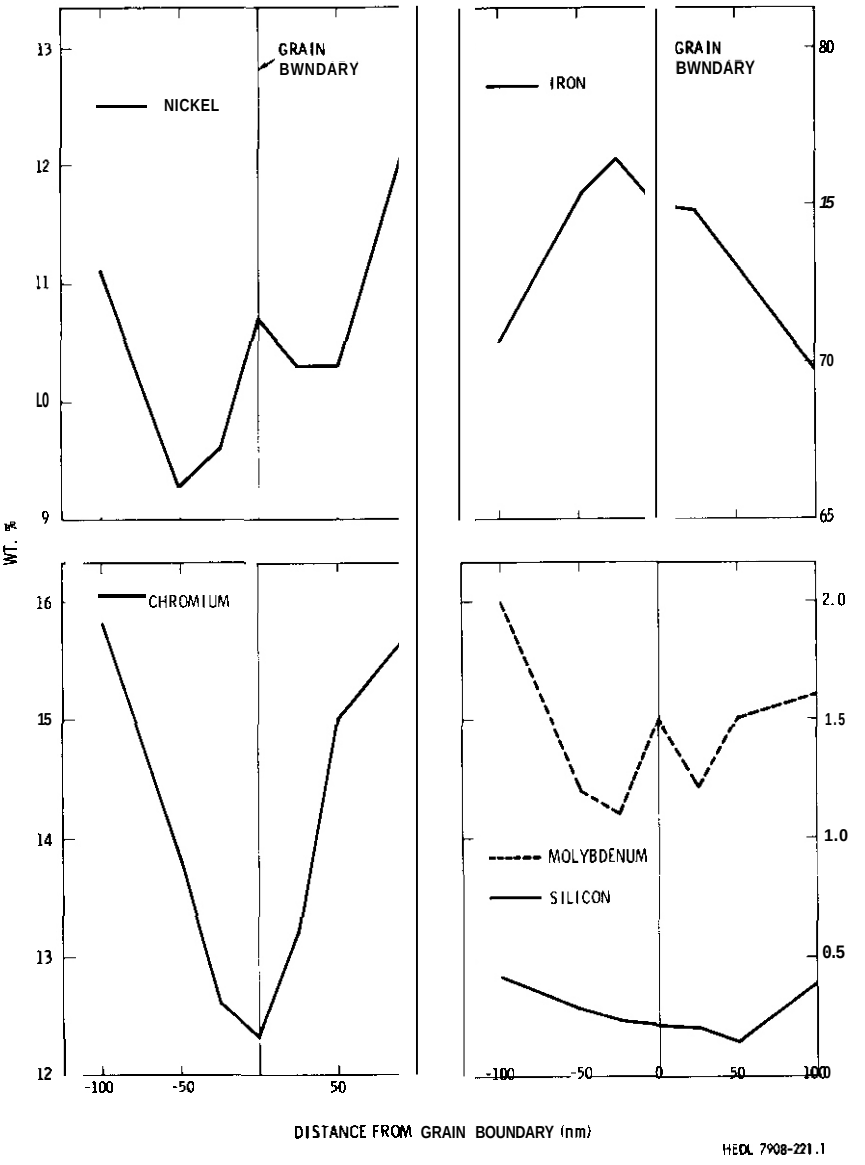

FIGURE 7. Line-Of-Sight Measurement of Elemental Profiles in the Vicinity of a Grain Boundary in Annealed AISI 316 at 520°C and 9 x 10^{22} n/cm^2 (E>0.1 MeV).

and reflects a problem peculiar to analysis of thin microstructural features The relatively thick foils needed for boundary analysis and the 30 to 50 nm resolution limit tend to obscure the presence of small γ' precipitates within the foil. These precipitates are denuded near the boundary, however. The large decrease in nickel content in the vicinity of the boundary is due to the local absence of γ' while the small peak at the boundary represents

the inverse Kirkendall concentration of nickel

b. Extraction Replica Analysis

Figure 4(b) illustrates the use of extraction replicas as a method of analyzing precipitates without the influence of the surrounding matrix. An advantage of this technique is that the influence of decay radiation is decreased substantially. The disadvantage of this technique is the partial or sometimes total loss of some kinds of precipitates due to selective dissolution. For instance, the normal procedure for thin foil preparation (electrolytic thinning in 10% perchloric and 90% glacial acetic acid) appears to dissolve the γ' or Ni_3Si phase while preserving most carbide and intermetallic phases. Since the irradiation-induced γ' phase is usually distributed as very small precipitates, it was necessary to extract this phase using another electrolyte.[1] Cawthorne and Brown[10] were able to tentatively identify this phase in the foil by analysis of the moire fringe without specifying its exact composition, but extraction replication and EDX microanalysis were necessary to establish the elemental composition.[1]

c. Foil-Edge Analysis

If a given precipitate is not selectively attacked by the electrolyte used to prepare the thin foil, then microanalysis can proceed on precipitates of reasonable size which are attached to the edge of the foil. Illustrated in Figure 4(c), analysis near the foil edge not only reduces the influence of the matrix but preserves a record of the compositional gradients in the adjacent matrix. Figure 8 illustrates the use of this technique in the examination of an irradiation-induced fcc precipitate (G-phase) formed in 20% cold worked AISI 316 irradiated to high fluence and moderate temperature. It is not unusual, however, to find several kinds of precipitates co-existing in the same grain, with each type exhibiting a different solubility in the electropolishing procedure. Figure 9 shows that both the γ' and G-phase populate the grain located near the foil edge, but of the two only the G-phase is both sufficiently large and stable during

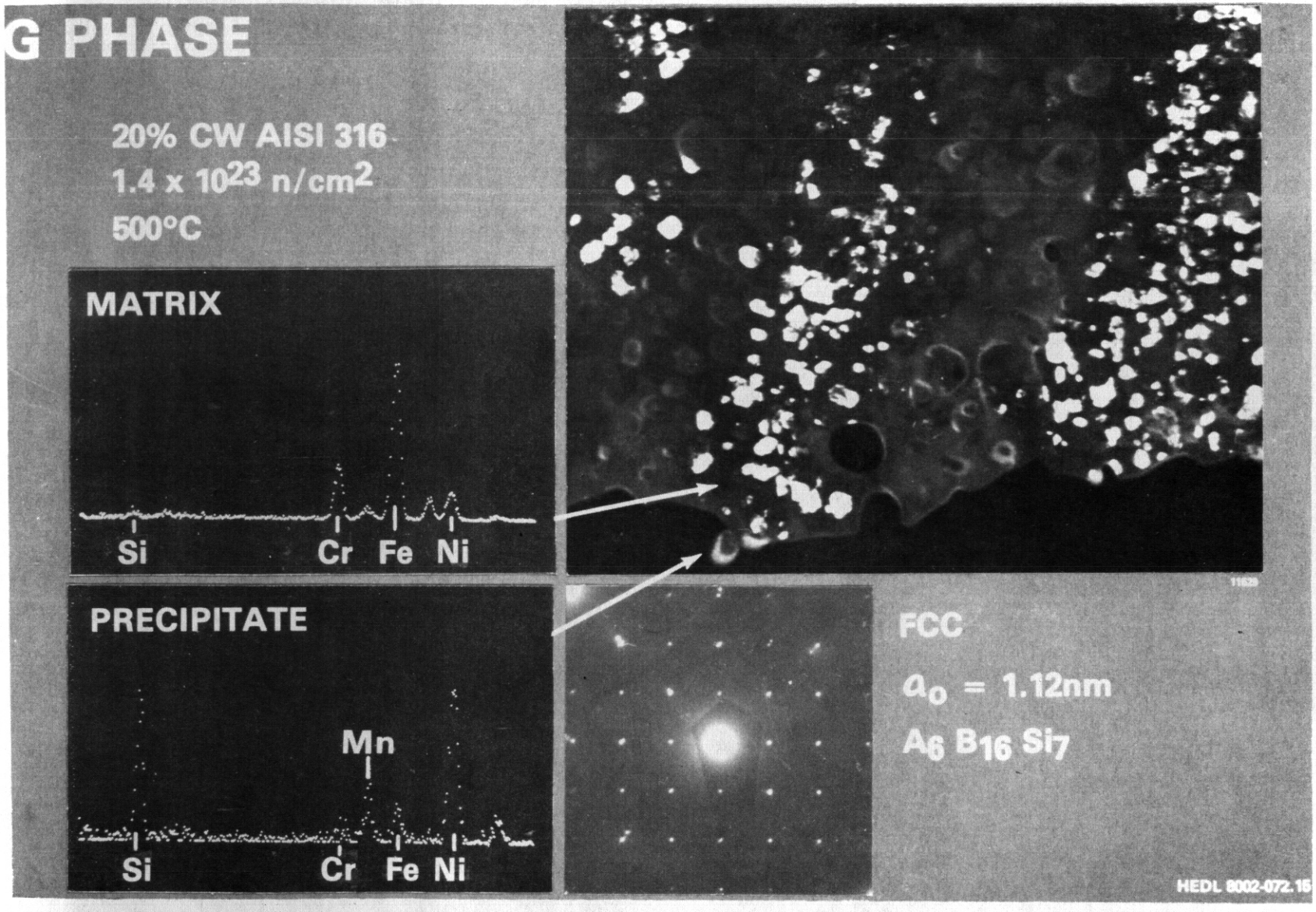

FIGURE 8. Determination of Composition and Crystal Structure of G-Phase Found in Irradiated 20% Cold Worked AISI 316 Using the Edge-Foil Analysis. The adjacent matrix composition is also shown.

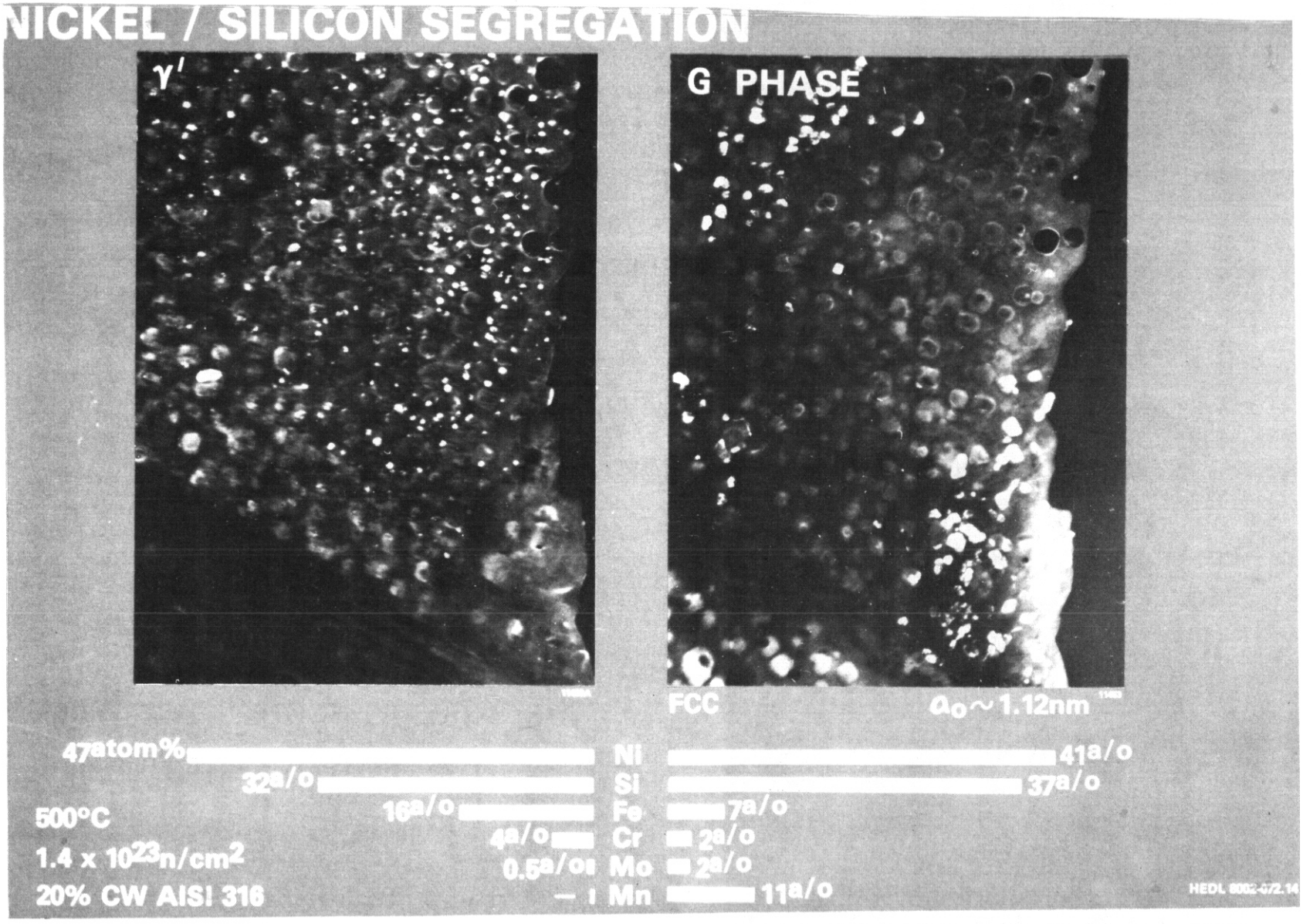

FIGURE 9. Coexistence of Two Precipitate Phases, Both Rich in Nickel and Silicon, In One Grain of 20% Cold Worked AISI 316 Irradiated at 500°C to a Fluence of 1.4 x 10^{23} n/cm^2 (E>0.1 MeV).

electropolishing to allow the foil-edge analysis approach.

When the foil-edge technique was first employed in the study of the elemental flow sequence in precipitates, several unexpected observations were made. First of all, Laves precipitates (nominally Fe_2Mo) appeared to be changing in composition during irradiation. Although diffraction analysis indicated the presence of Laves at all fluences above 5×10^{22} n/cm^2 (E>0.1 MeV) at temperatures over 600°C, foil-edge microanalysis showed a steady reduction in iron and molybdenum in these precipitates with increasing fluence and a concurrent increase in nickel and silicon. It was not known, however, whether Laves of traditional composition was continually dissolving and nickel-rich Laves precipitating, or whether nickel and silicon were infiltrating the precipitates and either diluting the precipitates or replacing iron and molybdenum. The first composition profiles from the adjacent matrix indeed exhibited gradients in nickel composition which were indicative of nickel flow into the precipitates. The profiles shown in Figure 10 are not so illuminating on the direction of flow of molybdenum and silicon, however. The lower level of these elements, their higher diffusivity and the heterogeneity of the microchemical evolution all combine to yield an ambiguous record of the elemental flow. The direction of flow can be inferred from comparison of the mean matrix compositions of these elements at different fluence levels, however. Note in Figure 11 that in at least one matrix area the molybdenum level has risen during irradiation to its average bulk composition while the precipitate molybdenum level is rather low, indicating that molybdenum has substantially deserted the Laves phase. The nickel level of the matrix has also fallen somewhat. It is very difficult to draw a clear conclusion from a few such profiles since the variability of the segregation process is expressed throughout the irradiated volume, and the precipitate particle density is sufficiently heterogeneous to preclude a simple determination of the total amount of any one element in the precipitates.

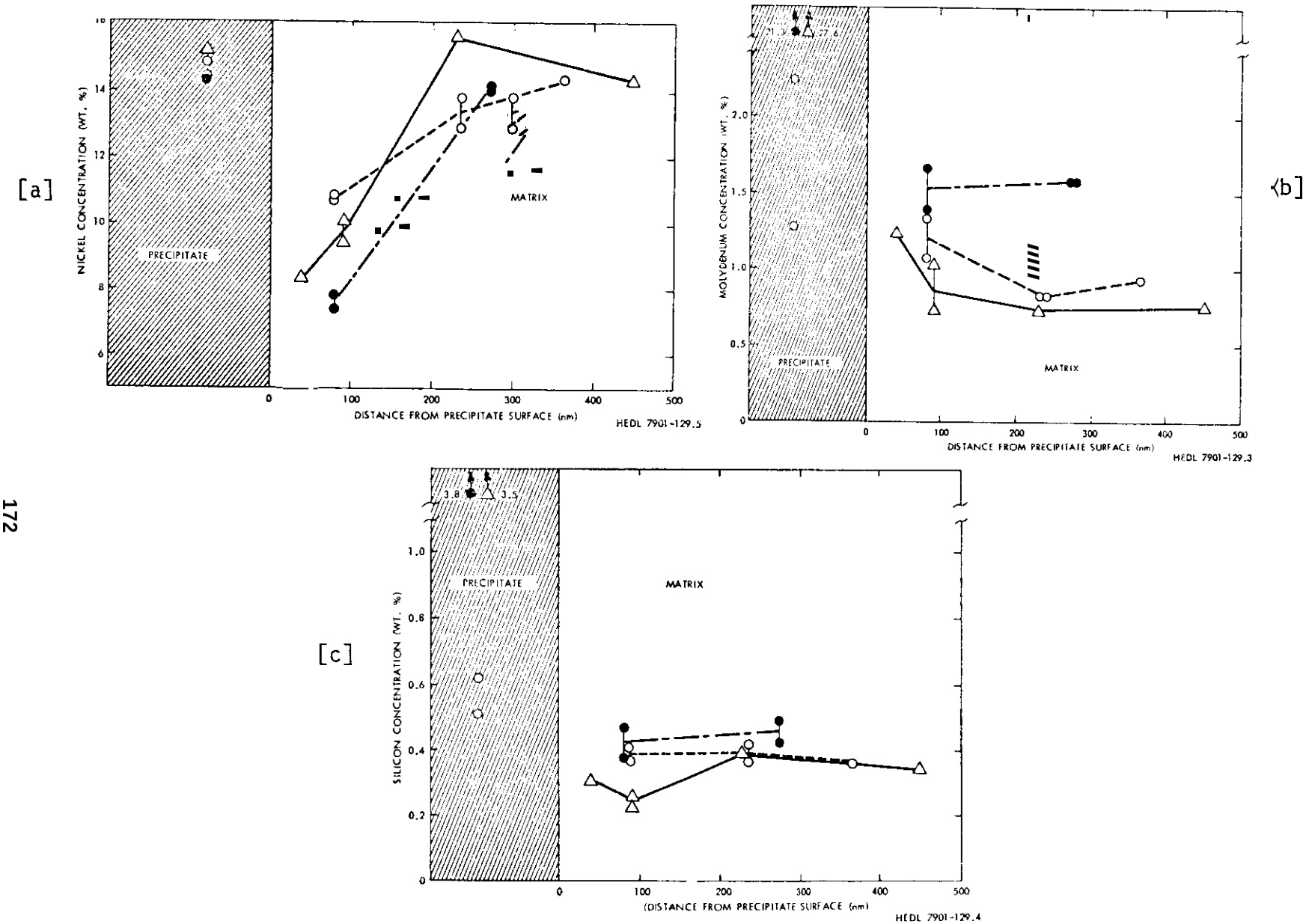

FIGURE 10 Concentration Profiles of Nickel, Molybdenum and Silicon Observed Near the Surface of Three Laves Precipitate Particles in 20% Cold Worked AISI 316 Irradiated at 650°C to a Fluence of 1.0×10^{23} n/cm^2 (E>0.1 MeV).

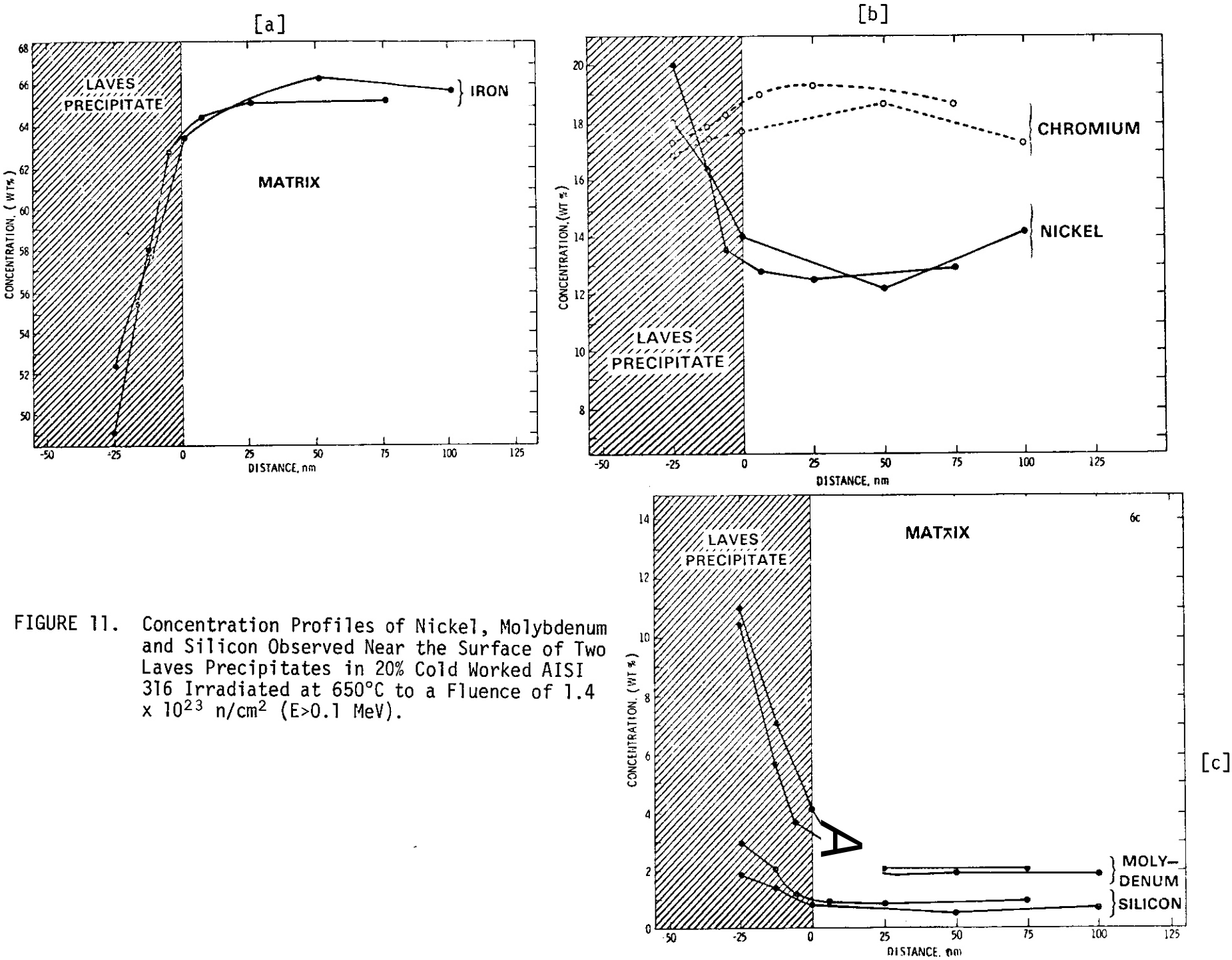

FIGURE 11. Concentration Profiles of Nickel, Molybdenum and Silicon Observed Near the Surface of Two Laves Precipitates in 20% Cold Worked AISI 316 Irradiated at 650°C to a Fluence of 1.4 x 10^{23} n/cm^2 (E>0.1 MeV).

d. Statistical Sampling Analysis

Additional information on the direction of elemental flows can be gained from the random spot analysis of many small representative matrix volumes. These volumes are chosen to be large enough to measure a substantial volume of material, but small enough to avoid including features such as precipitates. As shown in Figure 12, the many areas sampled in one specimen exhibit a large range of local concentration levels for each of the elements nickel, silicon and iron. While this observation underscores the heterogeneity of the evolution, it is rather obvious that nickel and silicon flow in the same direction with respect to the precipitates, while molybdenum flows in the opposite direction.

When this information was obtained it provided an explanation for some initially perplexing data published by Porter and McVay.[5] Using bulk extraction techniques they reported that the precipitates formed in 20% cold worked AISI 316 during irradiation at 550°C gradually increased in volume but suffered substantial and progressive decreases in iron and molybdenum while gaining nickel. Whereas it was previously assumed that molybdenum, nickel and silicon were all concentrated into precipitates during irradiation,[3] the molybdenum concentration in the precipitates actually peaks at some moderate fluence and declines thereafter during irradiation.

Another application of the sampling procedure is demonstrated in Figure 13, in which the distribution of matrix nickel contents is presented for two AISI 316 specimens of different starting conditions which were exposed to identical irradiation conditions. The solution annealed specimen contained Laves precipitates which were substantially enriched in nickel and silicon, with some indication that the mean levels of these elements were higher than that of the 20% cold worked specimen. Note that the average matrix nickel level of the annealed specimen has been reduced from the original. 13.5% level to about 9%. The cold worked specimen at these conditions has a matrix nickel content that has been reduced to an

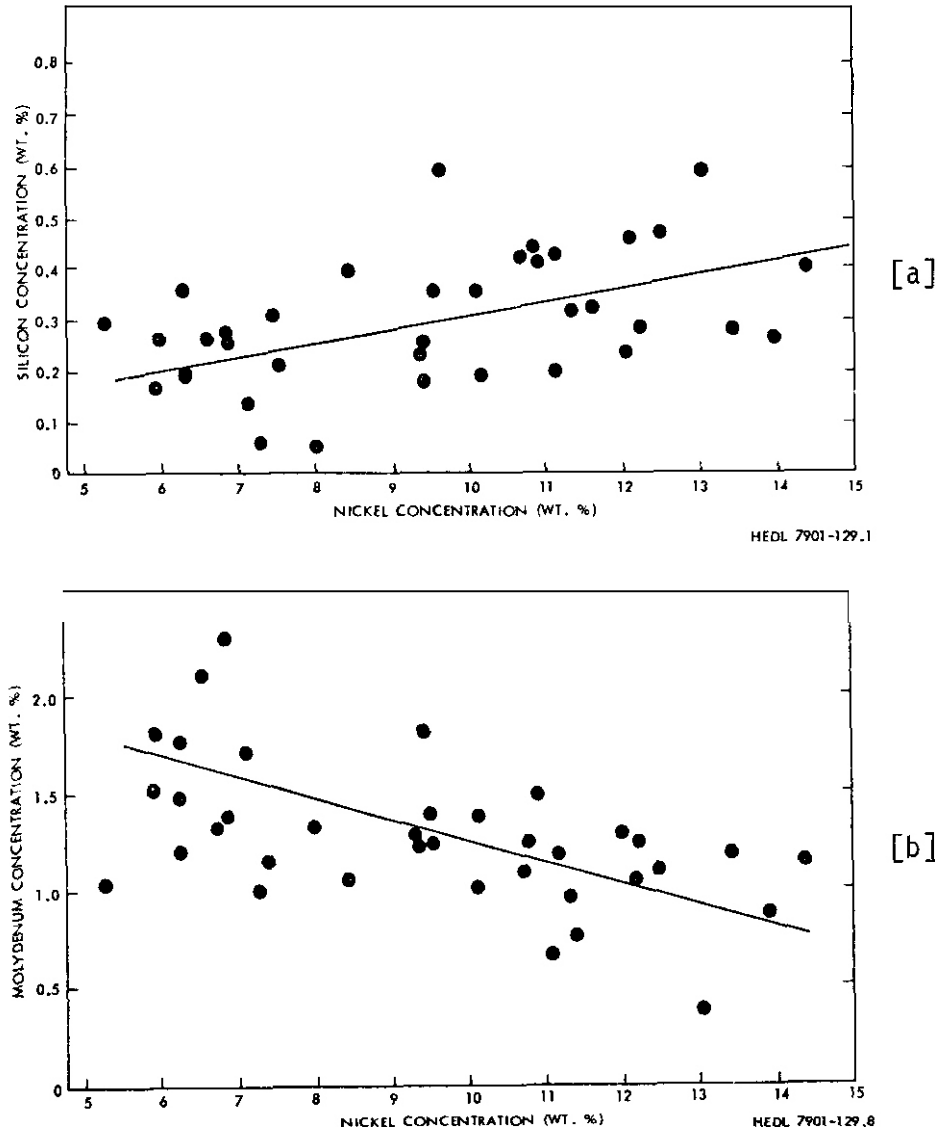

FIGURE 12. Local-Spot Determinations of Elemental Concentrations in Many Regions in 20% Cold Worked AISI 316 Irradiated at 650°C to a Fluence of 1.0 x 10^{22} n/cm^2 (E>0.1 MeV). Note that nickel and silicon concentrations tend to increase together while nickel and molybdenum do not. This indicates that nickel and silicon flow together and against the flow of molybdenum. There are large local variations in all elements, however. The trend lines were established by a least squares analysis.

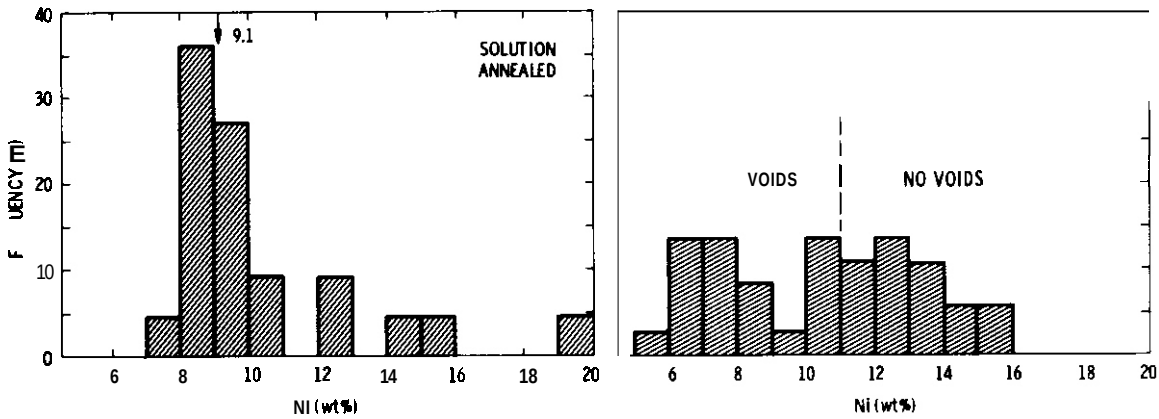

FIGURE 13. Distribution of Nickel Content at Different Locations in Irradiated AISI 316 Specimens Irradiated at 650°C to a Fluence of 1.0 x 10^{23} n/cm^2 (E>0.1 MeV).

average of 10.4% and the distribution is much broader. Other studies[1,3,4] have shown that the AISI 316 alloy in either the solution annealed or cold worked condition is proceding toward a matrix nickel content of about 9%, a level which is independent of temperature and starting condition.

Another important observation was made in the data field shown in Figure 13. The void swelling of the annealed specimen was about 8% and quite homogeneous, while the void swelling of the cold worked specimen was only 0.6% and quite heterogeneously distributed. In almost all cases, however, large area (about 0.5 μm in diameter) analyses of voided regions in the cold worked specimen showed the nickel content to be in the ≤10 wt.% range while regions which had not yet begun to swell contained ≥11 wt.% nickel. This in only one of several clues in these studies which indicate that the onset of void nucleation is determined more by microchemical considerations than by dislocation density or helium level.

4. Summary of the Microchemical Evolution

The complexities and heterogeneity of the microchemical evolution of AISI 316 have required that this study focus more on the techniques of data extraction rather than the relatively minor problems and equipment

modifications associated with the radioactivity of the specimens. This experience has also been typical of that encountered in the study of AISI 304[5] and various modified AISI 316 alloys.[3,4] Although the evidence compiled in the course of this and other related studies is too large to present here, a summary of the principles involved in the microchemical evolution of the 300 series alloys will be briefly presented to aid related studies by other researchers. These principles were revealed by combined TEM, diffraction and STEM/EDX techniques.

It appears that in the 300 series alloys the development of dislocation and loop microstructure (and to a lesser extent voids) proceeds toward a saturation state, comprised of number densities and component identities, which are independent of starting microstructure. The microchemical evolution induced by radiation also appears to proceed toward a saturation state but at a much more sluggish pace, although certain temperature paths or preirradiation treatments can short-circuit the sluggishness.[3,10]

The various microstructural components interact with the defect fluxes and lead to point defect gradients which function as the driving force for the segregation process. The element nickel seems particularly prone to concentrate at defect sinks in response to the inverse Kirkendall effect and perhaps other mechanisms. The matrix nickel content is then reduced, although not by much unless such as silicon and carbon are present. These elements coprecipitate with nickel at microstructural is then reduced, although not by much unless solutes such as silicon and carbon are present. These elements coprecipitate with nickel at microstructural sinks and form a microchemical reservoir capable of removing from the matrix approximately three atoms of nickel for each silicon (and possibly carbon) atom. In AISI 316 this leads to a reduction in matrix nickel content from 13.5 to 9 wt.%.

The most interesting feature of the precipitate-related segregation process is that the path by which the segregation process proceeds does not appear to influence the final outcome. A large variety of

phases can develop, depending strongly on irradiation temperature and history, minor variations in composition and preirradiation thermomechanical treatment. But all such phases either form as nickel and silicon-rich phases or become progressively richer in these elements as a result of the infiltration-exchange process. At fluences approaching 100 dpa even the Laves (Fe_2Mo) phase approaches a composition of Ni_3Si. If no other phase forms in the intermetallic temperature range centered at about 500°C, the "phase of last resort" forms eventually. This is the γ' phase (nominally Ni_3Si) which not only requires irradiation to form but once formed will dissolve in the absence of displacive irradiation.[3,4]

The consequences of the nickel segregation process are rather large. If the solute content is increased over the nominal specification for AISI 316, the matrix nickel content can be driven so low as to initiate the transformation of substantial amounts of matrix austenite to ferrite.[4] In AISI 304 the initial nickel level is only 9 wt.% and the nominal 0.5 wt.% silicon is sufficient to cause the transformation.[5]

It also appears that the nickel content (at levels below 30%) is the major determinant of the swelling and irradiation creep rates, once the saturation microstructure has developed. Just as the initial nickel content (C°_{Ni}) has been shown to be the major factor determining the magnitude of swelling,[3,4] the declining instantaneous nickel content in a specific alloy has been correlated with the acceleration of the creep and swelling rates.[3,4] When the average matrix nickel content reaches the level $C^{*}_{Ni} = C^{\circ}_{Ni} - 3(Si + C)$, then the steady state swelling and creep rate is established.

The many phases that can be involved in the segregation process all exhibit a different sensitivity to the host of variables which influence the evolution. Some are sensitive to cold work while others are not. In general, cold work decreases the rate of nickel removal in all precipitate phases in AISI 316 but accelerates the process for some phases in other

alloys, such as AISI 304 and 321.[12] The sensitivity of the microchemical evolution to variables such as stress,[13] temperature change,[10] and neutron flux[4] has been shown to be related to the response of the various second phases to these variables.

5. Conclusions

The radiation-induced microchemical evolution of 300 series stainless steel has been shown to be the major determinant of alloy behavior in response to the host of operating variables known to influence the evolution of dimensional and mechanical properties. Conventional transmission microscopy techniques are not in themselves sufficient to characterize this evolution, however, and the combined STEM/EDX technique is a necessary tool. The problem imposed by decay radioactivity can be solved by equipment modifications, and the problems associated with spatial resolution limitations and heterogeneity of alloy response can be overcome by developing a balance of data acquisition procedures which include the measurement of compositional profiles near sinks and statistical sampling of many matrix and precipitate volumes.

VI. REFERENCES

1. H. R. Brager and F. A. Garner, J. Nucl. Mat. 73, 9 (1978).

2. H. R. Braser. F. A. Garner. E. R. Gilbert. J. E. Flinn and W. G. Wolfer, in Radiation Effects in Breeder Reactor Structural Materials, M. L. Bleiberg and J. W. Bennett, eds., The Metallurgical Society of the American Institute of Mining, Metallurgical and Petroleum Engineers (1977) pp. 727-755.

3. H. R. Brager and F. A. Garner, "Dependence of Void Formation on Phase Stability in Neutron-Irradiated Type 316 Stainless Steel," Effects of Radiation on Structural Materials, ASTM STP 683, J. A. Sprague and D. Kramer, eds., ASTM (1979) pp. 207-232.

4. H. R. Brager and F. A. Garner, "Microchemical Evolution of Neutron-Irradiated 316 Stainless Steel," HEDL-SA-2001, Proceedings ASTM 10th International Symposium on Effects of Radiation on Materials, Savannah, Georgia (June 3-5, 1980).

5. D. L. Porter and E. L. Wood, J. Nucl. Mat 83, 90 (1979).

6. L. E. Thomas, "EDX Microanalysis of Neutron-Irradiated Alloys," Proceedings Symposium on Advanced Techniques for the Characterization of Irradiated Materials, Las Vegas, Nevada (February 1980).

7. N. J. Zaluzec, "Quantitative X-Ray Microanalysis: Microstructural Considerations and Applications to Materials Science," in Introduction to Analytical Electron Microscopy, J. J. Hren, J. I. Goldstein and D. C. Joy, eds., Plenum Press (1979) p. 121.

8. F. A. Garner and G. R. Odette, "Impact of Advanced Microstructural Characterization Techniques on Radiation Damage Modeling and Analysis," ibid., Reference 6.

9. A. D. Marwick, R. C. Pillar and P. M. Sivell, J. Nucl. Mat. 83, 35 (1979).

10. F. A. Garner, E. R. Gilbert, D. S. Gelles and J. P. Foster, "The Effect of Temperature Changes on Swelling and Creep of AISI 316 Stainless Steel," HEDL-SA-2003, ibid., Reference 4.

11. J. F. Bates and W. G. Johnston, "Effects of Alloy Composition on Void Swelling," ibid., Reference 2, pp. 625-644.

12. W. K. Appleby, E. E. Bloom, J. E. Flinn and F. A. Garner, "Swelling in Neutron-Irradiated 300 Series Stainless Steel," ibid., Reference 2, pp. 509-528.

13. F. A. Garner, E. R. Gilbert and D. L. Porter, "Stress-Enhanced Swelling of Metals During Irradiation," HEDL-SA-2004, ibid., Reference 4.

VII. FUTURE WORK

Analysis of data from the Breeder Reactor Program will continue as it becomes available in order to determine the nature of the radiation-induced phase development, its sensitivity to environmental and material variables, and the consequences of the phase evolution on dimensional and mechanical property changes. The techniques described in this paper will be applied toward material irradiated in HFIR, ORR and RTNS-II as specimens become available.

VIII. PUBLICATIONS

This paper will be published in the Proceedings of the AIME-sponsored symposium on Advanced Techniques for the Characterization of Irradiated Materials.

I. PROGRAM

Title: Irradiation Response of Materials

Principal Investigators: J. A. Spitznagel, S. Wood, and W. J. Choyke

Affiliation: Westinghouse Research and Development Center

II. OBJECTIVE

The objective of this work is to assess the phenomenology and mechanisms of microstructural evolution in materials exposed to simultaneous helium injection and creation of atomic displacement damage by a second ion beam.

III. RELEVANT DAFS PROGRAM TASK/SUBTASK

SUBTASK II.C.1, II.C.2, II.C.3, II.C.5, II.C.9, II.C.18

IV. SUMMARY

Temperature change experiments have been conducted to estimate the critical cavity size (r_c) for bias-driven growth. Good agreement with helium inventory measurements of r_c and theoretical predictions is observed. Data from dual ion bombarded targets of 316 SS in the aged condition (800°C - 10h) has been analyzed. Helium inventory measurements show a slow bubble growth regime at 600°C leading to a "double peak" in the temperature dependence of swelling. Cavity no. density is observed to be nearly independent of temperature and the nature of heterogeneous nucleation sites. Cavity and interstitial dislocation loop growth rates dominate microstructural evolution and are postulated to reflect changes in austenite matrix composition and helium partitioning to sinks.

V. ACCOMPLISHMENTS AND STATUS

A. The Use of Temperature Change Experiments to Determine the Maximum Equilibrium Bubble Size in 316 SS

Two important questions in alloy design for near term and longer term first wall and blanket applications involve the kinetics of helium partitioning to various microstructural sinks and what might be termed the "collection efficiency" or site stability of each sink. Dual-ion and HFIR studies have indicated that He atoms probably decorate growing interstitial loops, extended dislocations, surfaces of various carbide and intermetallic phase particles and grain boundaries. The effects of atomic displacement rate, He production rate, irradiation temperature and microstructure on He mobility and trapping site preference are not known. In fact, the actual spatial distribution of He has only been inferred from TEM observations of, what we believed to be, equilibrium gas bubbles.

Helium (and hydrogen) can be detected by a number of techniques and concentration vs depth profiles measured with a depth resolution of $\gtrsim$ 100 μm.[1] However, measurement of the partitioning of He or H to sinks requires a technique with lateral resolution which represents a small fraction of the average sink spacing. Divergence of the probing beam and minimum detectable mass constraints make the usual depth profiling techniques (SIMS, α-α scattering, nuclear reaction) unsuitable. Only the FIM-atom probe and, perhaps, electron energy loss spectroscopy techniques offer much promise of actually yielding intersink He or H concentration profiles for the materials and conditions of interest. In the interim, He partitioning and site occupancy must be inferred from TEM observations of "cavities", measurements of He and H release rates from surfaces during ion bombardment, mechanical measurements, modeling, etc.

In a previous report[2] we discussed the concept of a critical cavity size for a transition from gas-driven to bias-driven cavity growth. Observations of bimodal cavity size distributions in dual ion bombarded

stainless steel targets had suggested to us the possibility of estimating the critical cavity radius, $r_c = D_c/2$, by means of a helium "inventory". Cavities larger than the maximum possible equilibrium bubble size must have experienced bias-driven growth. Thus, the maximum bubble radius should be closely related to the critical cavity size. We attempted to determine which of the observable cavities in S.A. 316 SS or 20% C.R. 316 SS were truly equilibrium helium bubbles and which were "voids". A computerized data file system was used to calculate the maximum possible equilibrium bubble size class as shown schematically in Fig. 1. It was assumed that the gas obeyed the Van der Waals equation of state and that surface energy values could be obtained from zero-creep measurements. In every case analysis of cavity size distributions demonstrated that the size class where all of the implanted He was used up was smaller than the maximum cavity size observed. The maximum bubble radius obtained in this way increased exponentially with bombardment temperature and was in reasonable agreement with the theoretically predicted value.

The exponential temperature dependence of critical cavity size suggests that it should be possible to estimate r_c directly by changing the temperature during ion bombardment. Suppose one bombards a target at temperature T_1 for a time sufficient to establish a population of bubbles/cavities. If the temperature is then increased to T_2, for example, only those cavities having radii greater than r equal to r_c at T_2 will grow rapidly by bias-driven growth. The largest cavities not exhibiting rapid growth will be "subcritical" and should give a good estimate of r_c appropriate for the higher temperature. The process is shown schematically in Fig. 2 for a 200°C increase in temperature. To test this idea S.A. 316 SS targets were subjected to dual ion bombardment at 500°C to achieve a damage level of ~ 2 dpa. This was sufficient to establish a population of growing bubble/cavities and dislocation loops. The target temperature was then quickly changed to 700°C to alter the vacancy and helium diffusivities while maintaining the number and distribution of point defect sinks essentially constant. TEM measurements of the largest bubbles/cavities which did not undergo rapid growth at the second temperature were in good

agreement with critical cavity size estimates from the helium inventory (Method 1) and theoretical model calculations as shown by the value of r_c labeled "Method 3" in Fig. 3.

In addition to testing the validity of the "critical cavity size" concept, the helium inventory method and experiments involving in-situ changes in irradiation temperature are valuable for estimating the following:

1. Fraction of implanted He still in solution.
2. Frequency of association of equilibrium gas bubbles with various microstructural sinks as a function of irradiation temperature, He production and dpa rates.
3. Average He atom migration distance and velocity.
4. Coupling of He partitioning and microchemical segregation of other species.
5. 3-D mapping of probable He concentration profiles.

Analysis with the computerized data file is continuing for 316 SS in the solution annealed, 20% C.R. or aged conditions. Preliminary results for some of the items 1-5 above will be included in subsequent reports. The inventory method is being improved by incorporating geometrical He partitioning coefficients based on observed changes in the distribution of microstructural sinks.

B. Preliminary Numerical Analysis of the Temperature Dependence of Cavity and Dislocation Loop Formation in Aged 316 SS

To determine the effects of preirradiation aging and the presence of intergranular C.C. Cr-rich carbide ($M_{23}C_6$) particles in low-dose microstructural evolution under dual-ion bombardment, 316 SS from the MFE heat was given a 50% cold reduction, recrystallized by annealing at 1050°C for 0.5h and subsequently aged for 10h at 800°C. Targets were bombarded with

$\leqslant$ 2 MeV He and 28 MeV Si^{+6} ions at the High Energy Ion Bombardment Facility at the University of Pittsburgh. For all of the experiments helium was continuously implanted at rates from 3.2 x 10^{-3} to 5.7 x 10^{-3} appm/s at damage rates of 3.4 x 10^{-4} to 6.0 x 10^{-4} dpa/s. Bombardment temperatures were 550, 600, 650 and 700°C. Targets were sectioned to depths corresponding to damage levels of 8-16 dpa. TEM observations reported previously[3] showed:

1. Rapid growth of cavities associated with intergranular carbide particles at $T \geqslant 650$°C.
2. Appearance of faulted interstitial dislocation loops at $T < 600$°C and fewer acicular Ni_xSi_y precipitates with decreasing irradiation temperature.
3. Shift in cavity nucleation sites from acicular precipitates to dislocations with decreasing bombardment temperature.

Figure 4 summarizes the cavity size distributions for each bombardment temperature. Each histogram represents the weighted average of approximately 15 data sets normalized to a standard volume.

Table 1 gives the cutoff diameter, D_c, for the maximum equilibrium bubble size based on the helium inventory method. The numbers have not been corrected for gas partitioning based on geometric sink distributions and thus represent upper bound values. With the exception of bombardment at 600°C, D_c is observed to be smaller than the mean cavity diameter. At 600°C, however, this is not true and approximately 90% of the visible cavities are equilibrium gas bubbles. At 550°C fewer than 5% of the cavities are estimated to be gas bubbles. At 650 and 700°C, where cavity nucleation is highly heterogeneous and in association with an acicular Ni_xSi_y phase and grain boundary carbides, $\sim$40% of visible cavities are gas bubbles.

We note that, for S.A. 316 SS, a rapid cavity growth regime was observed at 600°C.[4] The effect in the same material aged at 800°C prior

TABLE 1. COMPARISON OF MAXIMUM EQUILIBRIUM BUBBLE SIZE (D_C) WITH MEAN ($\overline{D}$) AND MAXIMUM (D_{MAX}) CAVITY DIAMETERS FOR 316 SS AGED AT 800°C FOR 10 HOURS PRIOR TO DUAL ION BOMBARDMENT

BOMBARDMENT TEMPERATURE (°C)	ATOMIC DISPLACEMENTS (dpa)	IMPLANTED HELIUM CONCENTRATION (appm)	D_C (nm)	$\overline{D}$ (nm)	D_{max} (nm)
550	11.4	96	5	24	111
600	11.2	125	8	5	71
650	15.8	245	6	16	119
700	8.2	136	11	17	233

to irradiation is almost the exact inverse, namely, slow growth of near-equilibrium gas bubbles. It is suspected that initial or radiation-induced differences in austenite matrix composition may be related to the observed differences. This possibility is being investigated using energy dispersive x-ray analysis.

Swelling ($\Delta V/V_0$) determined from TEM micrographs by the usual techniques gave values of 3.8%, 0.3%, 7.8% and 2.8% for bombardment temperatures of 550, 600, 650 and 700°C, respectively. Many data sets have been analyzed and the statistical method used for combining heterogeneous cavity distributions is thought to be a reasonable averaging process. Cumulative errors from TEM particle sizing, stereo measurements of foil thickness, etc., however, result in a minimum uncertainty of $\sim$30% in each swelling value. The apparent "double peak" in swelling with temperature with a minimum at 600°C is qualitatively consistent with the observation of a large fraction of slow growing helium bubbles. Figure 5 demonstrates the slow cavity growth at 600°C.

Figure 6 supports the hypothesis that the temperature dependence of swelling reflects differences in cavity growth rates rather than differences in nucleation rates. Although the cavities become associated with different microstructural features as the temperature is lowered, the cavity no. density is relatively constant below 650°C for an appm He/dpa ratio of ∿12. Similar observations were reported previously for S.A. 316 and 20% C.R. 316.[4]

Growth of interstitial loops, as indicated by the variation of the mean loop diameter with temperature, Fig. 5, does not exhibit a monotonic increase with temperature. The mean loop diameter at 550°C (not shown) is ∿4 nm. Thus, with the exception of the 600°C value, d_ℓ would increase continuously with temperature in agreement with results from numerous neutron and charged particle irradiation experiments. Loop growth at 600°C appears to be very rapid and nearly equivalent to that observed at a much higher bombardment temperature. We note that this is accompanied by the appearance of faulted loops and a helium bubble dominated "cavity" population. Loop faulting suggests a lowering of the stacking fault energy, due perhaps to changes in austenite composition. The effect of a fine distribution of equilibrium gas bubbles on loop growth is not clear. Some decoration of the loops by bubbles is observed suggesting they may act as "pinning points" inhibiting loop expansion. From simple geometric arguments, however, it can be shown that the bubbles are the dominant sink for the continuously injected helium. Lowering the amount of helium in solution may result in faster loop growth as discussed elsewhere.[5]

The total dislocation line density did not vary with temperature within the uncertainty of the measurements, as shown in Fig. 6. Interstitial dislocation loop density decreased rapidly from a high value of $\sim 3 \times 10^{15}$ loops/cm^3 at 550°C to a value of $\sim 2 \times 10^{14}$/cm^3 at 600°C. Loop densities given in Fig. 6 agree well with those observed in S.A. 316 and 20% C.R. 316 (Fig. 7) although loop growth rates (not shown) are different. Analysis of the effects of helium partitioning and austenite composition changes on loop growth are continuing and will be discussed in a later report.

VI. REFERENCES

1. DOE Workshop on Techniques for Radiation Damage Analysis, Ed. P. Wilkes, J. A. Spitznagel, F. Nolfi, March 8-9, 1979, Oak Brook, Illinois, to be published.

2. S. Wood, J. A. Spitznagel and W. J. Choyke, DAFS Quarterly Report No. 8, October-December (1979).

3. S. Wood, J. A. Spitznagel and W. J. Choyke, DAFS Quarterly Report No. 6, April-June (1979).

4. S. Wood, J. A. Spitznagel and W. J. Choyke, DAFS Quarterly Report No. 7, July-October (1979).

5. W. J. Choyke, J. N. McGruer, J. R. Townsend, J. A. Spitznagel, N. J. Doyle and F. J. Venskytis, J. Nucl. Mater. 85 & 86 (1979), 647-651.

VII. FUTURE WORK

TEM-EDS and computerized data file analyses of dual ion experiments on S.A., 20% C.R. and aged 316 SS will be continued. Targets have been fabricated from Ti-modified 316 SS used in various HFIR experiments. Aging has produced a range of Ti-rich MC carbides. Dual ion studies will be conducted at appm He/dpa ratios of $\sim$0.2, 12 and 70 approximating EBR-II, CTR and HFIR conditions to determine the mechanisms of He trapping by such particles.

VIII. PUBLICATIONS

None

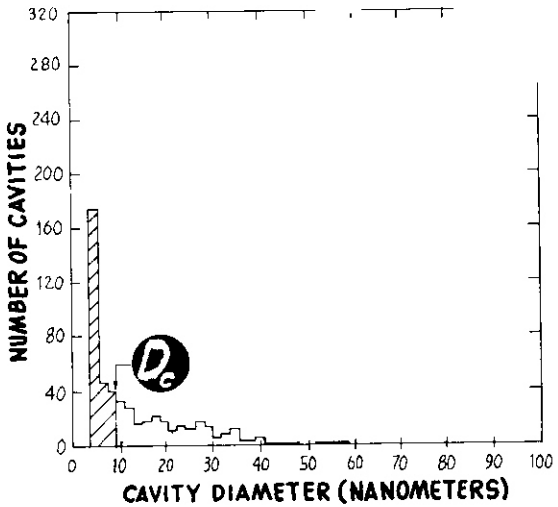

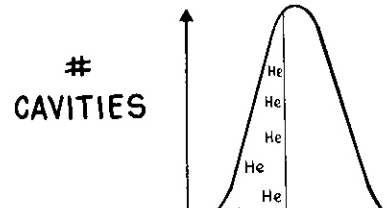

THE VAN DER WAALS EQUATION OF STATE

$$n = \frac{8\pi r^2 \gamma}{3(RT + 2B'\gamma/r)}$$

, Where n = # He atoms

IS USED TO INVENTORY ALL He IN BUBBLES AND CAVITIES BY MEANS OF A COMPUTER CODE.

$$\text{TOTAL He} = \sum_{i=1}^{c} \frac{N_i\, 8\pi r_i^2 \gamma}{3(RT + 2B'\gamma/r_i)} + \sum_{i=c}^{i_{MAX}} \frac{N_i\, 8\pi r_c^2 \gamma}{3(RT + 2B'\gamma/r_c)}$$

WHERE N_i = # CAVITIES IN CLASS i.

Fig. 1 - Schematic representation of the helium inventory method used to estimate the maximum equilibrium bubble size from measured cavity size distributions.

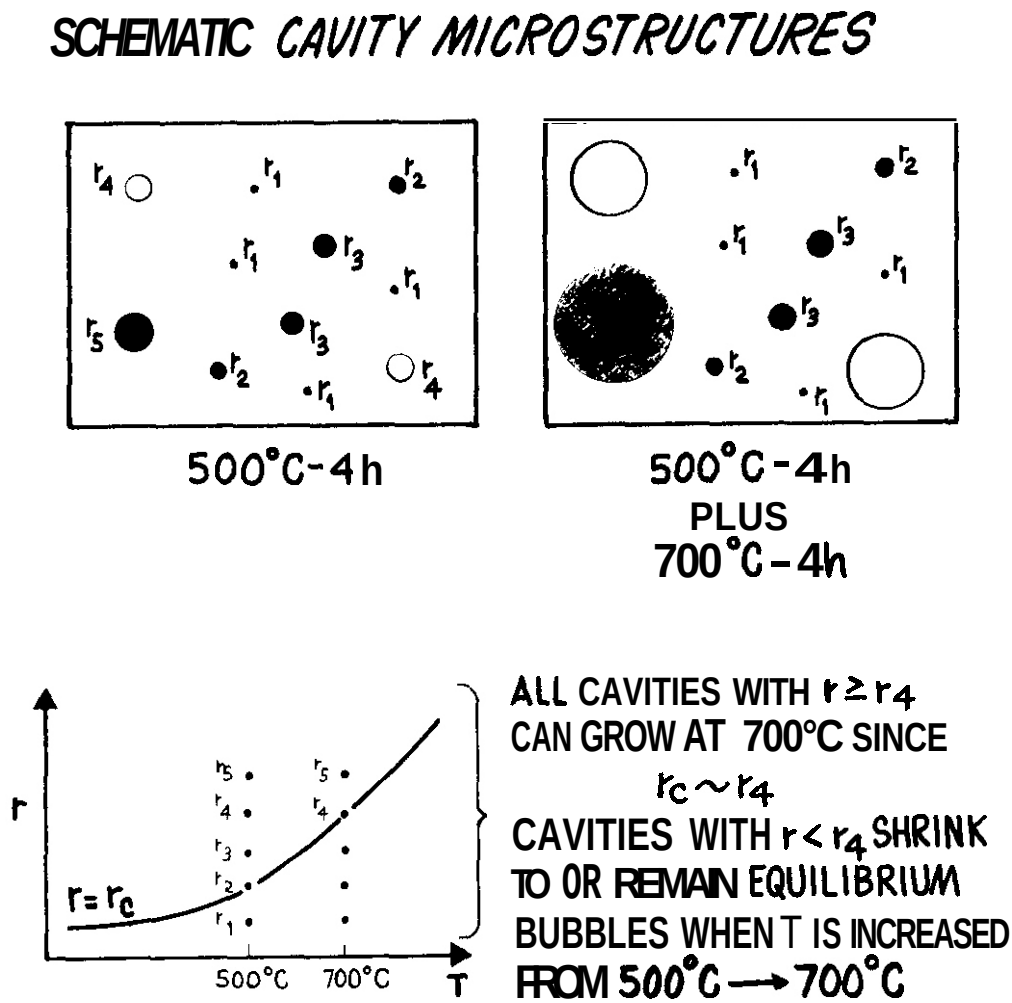

Fig. 2 - Schematic representation of the determination of the critical cavity size (r_c) by increasing the target temperature during dual-ion bombardment.

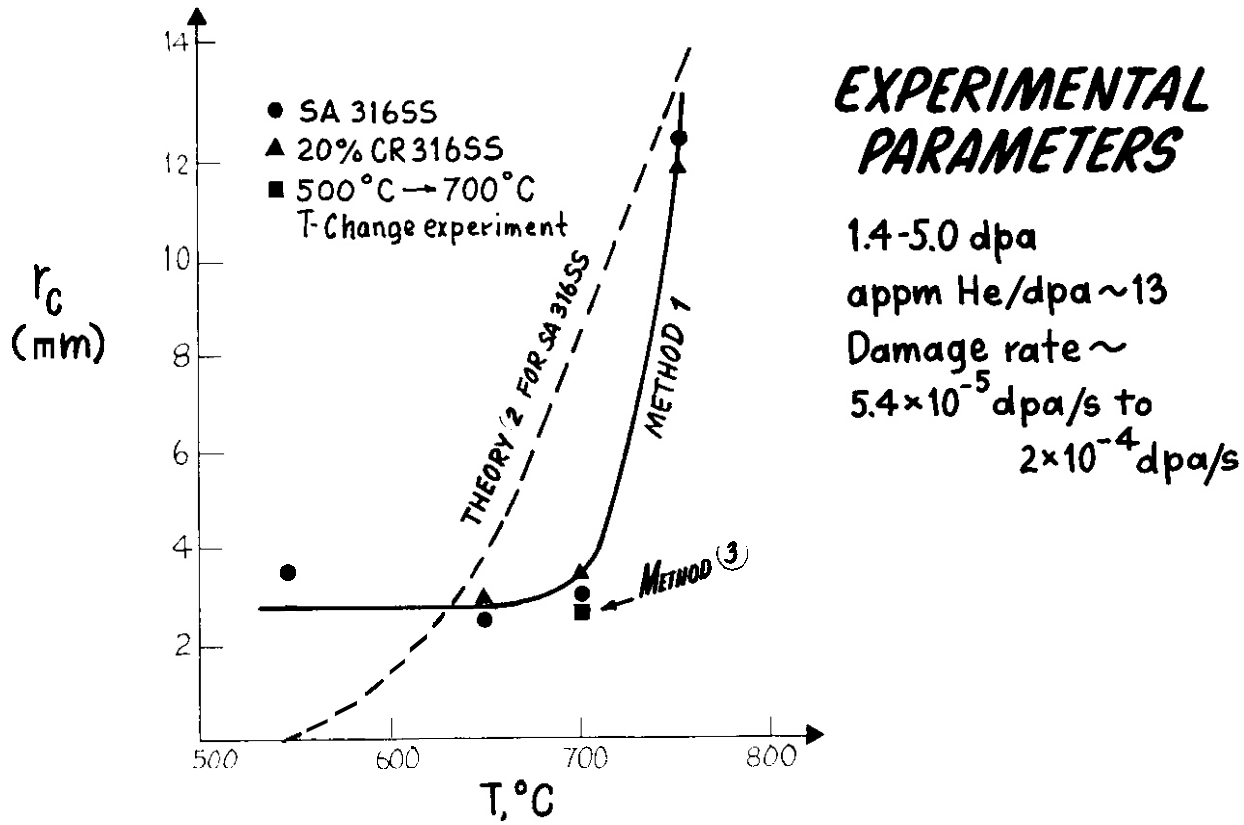

Fig 3 - Comparison of the temperature dependence of the critical cavity size for dual-ion bombarded S.A. 316 and 20% C.R. 316 from (1) helium inventory method, (2) theory and (3) temperature change experiment.

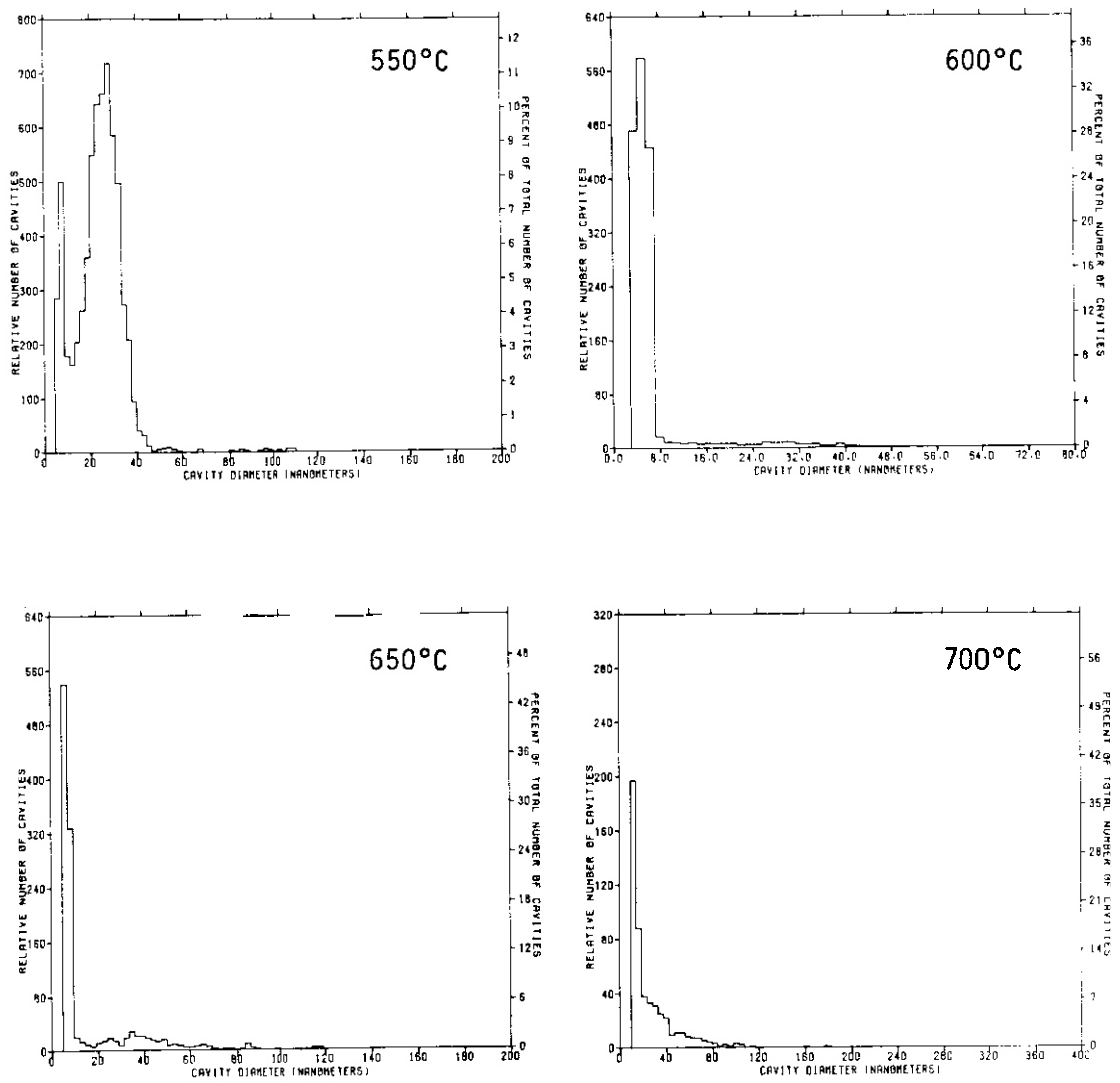

Fig. 4 - Cavity size distributions in aged 316 SS (800°C - 10 h) after dual-ion bombardment at temperatures from 550-700°C to fluences of 8-16 dpa (see Table I). Size distributions normalized to a standard volume.

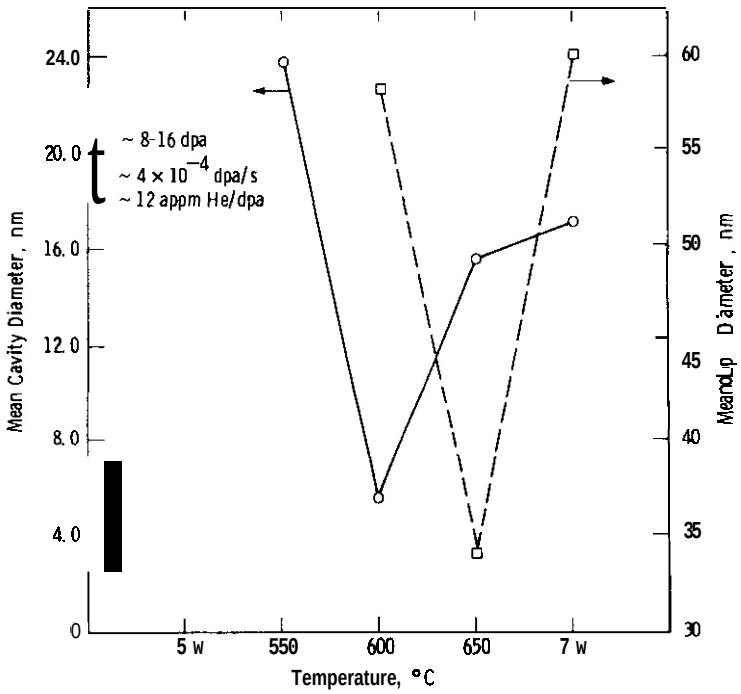

Fig. 5 - Temperature dependence of the mean cavity diameter and mean dislocation loop diameter in dual-ion bombarded, aged (800°C - 10 h) 316 SS.

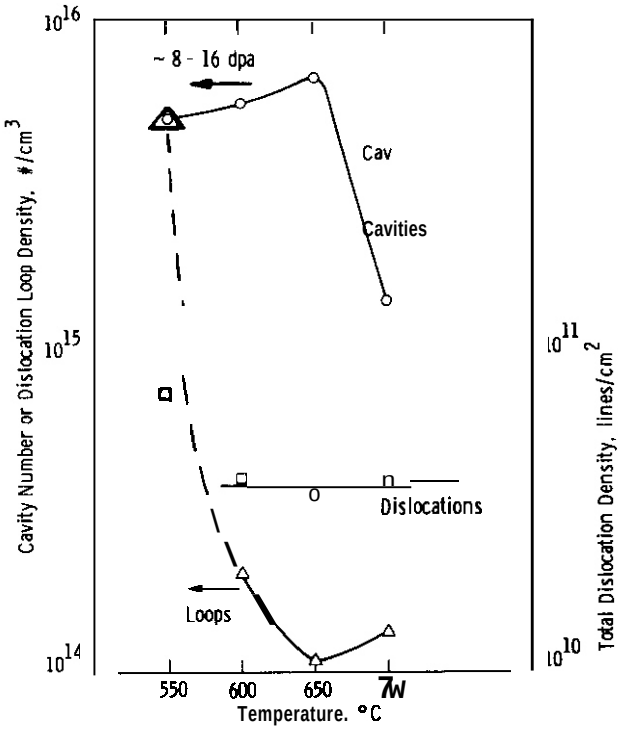

Fig. 6 - Variation of cavity number density, loop number density and total dislocation density with temperature for dual-ion bombarded, aged (800°C - 10 h) 316 SS.

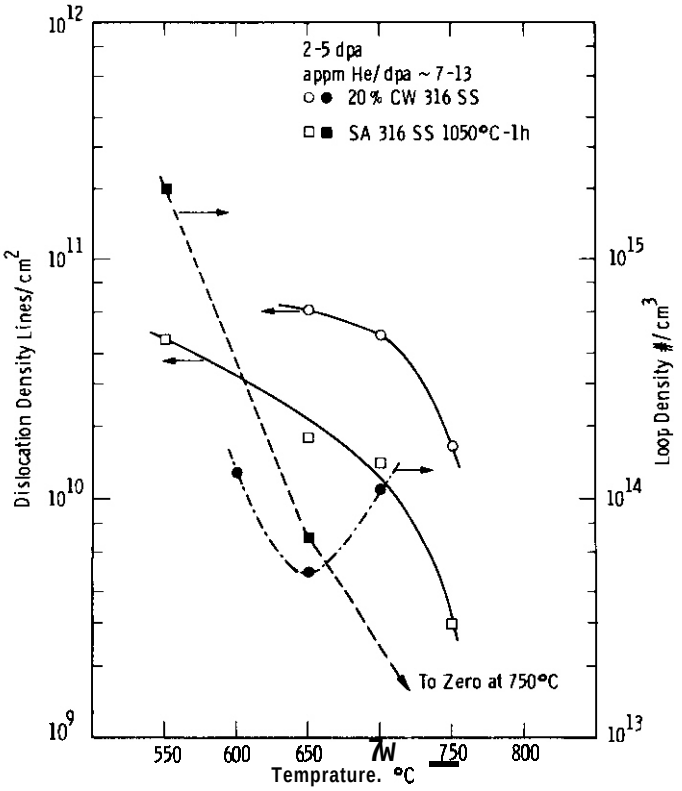

Fig. 7 - Variation of dislocation loop number density and total dislocation density with temperature for dual-ion bombarded S.A. 316 SS and 20% C.R. 316 SS.

I. PROGRAM

Title: Effects of Irradiation on Fusion Reactor Materials

Principal Investigators: F. V. Nolfi, Jr. and A. P. L. Turner
Affiliation: Argonne National Laboratory

11. OBJECTIVE

The objective of this work is to determine the microstructural evolution, during irradiation, of first-wall materials with special emphasis on the effects of helium production, displacement damage and rates, and temperature.

III. RELEVANT OAFS PROGRAM PLAN TASK/SUBTASK

SUBTASK II.C.2.1 Mobility, Distribution, and Bubble Nucleation

IV. SUMMARY

The dose and helium injection rate dependence of void swelling in 316 stainless steel irradiated simultaneously with Ni^{+} and He^{+} ions has been studied with TEM. Comparison is made to a parallel experiment on He preinjected and Ni^{+} ion irradiated material. For dual-ion irradiation, the size and number density of small cavities in a bimodal cavity size distribution did not appear to be strongly dose dependent, but the number density increased rapidly with increasing helium injection rate. For the large size cavities, the number density remained fairly constant with dose but the size increased rapidly with dose producing rapid increases in volume swelling. The preinjected samples exhibited the lowest swelling at all doses investigated. This is apparently due to a delay in the onset of the rapid swelling regime. In dual-ion irradiated samples, the large cavities formed preferentially at the ends of <100> oriented rod-shaped precipitates; TEM micrographs and diffraction patterns of the

precipitates are presented.

V. ACCOMPLISHMENTS AND STATUS

A. Dose and Helium Injection Dependence of Swelling in Single and Dual-Ion Irradiated 31G Stainless Steel -- G. Ayrault and H. A. Hoff

1. Introduction

A major question in the irradiation response of candidate fusion reactor structural materials is the influence of concurrent displacement damage and helium production. Dual-ion irradiation, using heavy-ions for damage production and helium ions to simulate gas production by transmutation events provides a means of investigating such effects in the absence of a high energy neutron source.

This report presents preliminary results on the dose dependence of swelling in preinjected single-ion and dual-ion irradiated 316 stainless steel, and on the helium injection rate dependence in dual-ion irradiated material. In addition, some observations are presented concerning acicular precipitates, which act as preferential cavity nucleation sites in dual-ion irradiated samples.

2. Irradiation Conditions

Type 316 stainless steel samples from the MFE heat were 50% cold-worked, then solution annealed at 1050°C for 0.5 h and aged at 300°C for 10 h. One set of samples was preinjected at room-temperature with 5 appm ^3He and single-ion irradiated with 3.0 MeV Ni^+. Three other sets of samples were dual-ion irradiated with 3.0 MeV Ni^+ and degraded 0.87 MeV He^+ at helium injection rates of 5:1, 15:1 and 50:1 appm He:dpa. For all samples the nominal doses were 3, 6, 12 and 25 dpa, and the nominal irradiation temperature was 625°C. After irradiation, the samples were

electrochemically sectioned to a depth of 4500Å (peak damage is at 5500Å), and backthinned for TEM inspection.

3. Qualitative Observations on Dose and Helium Injection Rate Dependence of Void Swelling

TEM results are now available for a complete set of the samples described above, but quantitative analysis of the micrographs has been performed only for preinjected samples and for 15:1 appm:dpa dual-ion specimens; analysis of the remaining micrographs is in progress. We therefore present a qualitative description of the dual-ion results in this section, and present the available quantitative data in the next section.

Typical microstructures for samples dual-ion irradiated at 5:1, 15:1 and 50:1 appm He:dpa to nominal doses of 6, 12 and 25 dpa are shown in Figs. 1, 2 and 3 respectively. Bimodal cavity size distributions were found in all dual-ion irradiated samples. In general, the number density of small cavities was much higher than that of large cavities, but the contribution of small cavities to volume swelling was almost negligable because of their size. The small cavities were found preferentially along dislocations and acicular precipitates, e.g. see Fig. 2b. Large cavities tended to appear at the ends of acicular precipitates, e.g. see Fig. 2a. It is not yet clear whether or not all of the large cavities are associated with precipitates; this point is discussed further in section 5.

As shown in Figs. 1, 2 and 3, the number density of small cavities increased rapidly with increasing helium injection rate but did not appear to change dramatically with dose. The mean size of the small-cavity population exhibited little change with either helium injection rate or dose. For the large-cavity population, the 50:1 He:dpa irradiations produced a higher number density of smaller cavities than either the 5:1 or 15:1 He:dpa irradiations; this was expected based on previous

results in Fe-20Ni-15Cr- [1]. But surprisingly, comparison of the large-cavity populations in 5:1 and 15:1 He:dpa samples shows a higher large-cavity number density for the lower He:dpa ratio, with fairly similar cavity size distributions at each dose. However, confirmation of this apparent minimum in the large-cavity number density between 5:1 and 50:1 He:dpa will have to await completion of quantitative analysis. For each He:dpa ratio, the primary effect of increasing dose appears to be growth of large cavities, with little change in the large-cavity number density, the small-cavity number density, or the small-cavity size.

4. Swelling in 15:1 He:dpa Dual-Ion and Preinjected Single-Ion Samples

Quantitative results for 15:1 appm He:dpa dual-ion irradiated samples and for preinjected (5 appm ^{3}He injected at room temperature) single-ion irradiated samples are presented in Figs. 4, 5 and 6; The small and large cavities of the bimodal cavity size distributions in the dual-ion samples are plotted separately in the size and number density plots, Figs. 5 and 6, as was done in our companion study of temperature dependence [2]. For dual-ion samples, the size and number density of small cavities was fairly constant with dose as described in the last section. The number density of large cavities increased slowly with dose, while the mean size increased rapidly, causing a rapid rise in volume swelling.

The behavior of preinjected samples was quite different from that of dual-ion irradiated samples. No cavities were observed at 3, 6 or 12 dpa for the 625°C temperature of this study, and the cavity number density at 25 dpa was low. Thus it appears that cavity nucleation was strongly suppressed in preinjected samples relative to dual-ion specimens, delaying the onset of the rapid swelling regime. This is in agreement with previous results in the austenitic ternary alloy Fe-20Ni-15Cr [1]. The reasons for the slow cavity nucleation are not clear at present, but for 316 stainless steel it may be related to a low number

density of acicular precipitates in the preinjected samples; these precipitates acted as preferential cavity nucleation sites in the dual-ion samples.

5. Acicular Precipitates

Acicular precipitates are present in most, if not all of the dual-ion irradiated samples; examples are seen in Fig. 2a. As mentioned above the precipitates act as preferential nucleation sites for cavities, with large cavities often found at the ends of the precipitates, and small cavities at ends and along the length. It will be shown below that the precipitates are directed along the three <100> directions, and for each <100> direction there are at least two equivalent crystallographic orientation variants of the precipitate lattice relative to the matrix; this means that there are at least six equivalent crystallographic orientations of the precipitate relative to the fcc host lattice. It is possible that all of the large cavities are assoicated with acicular precipitates, even though many do not appear to be in a given micrograph, since all crystallographic variants of the precipitate may not be simultaneously in contrast. To answer questions about cavity nucleation, and to aid in identification of the precipitates, we are studying the precipitates using microdiffraction and dark-field microscopy.

The precipitate diffraction spots are generally very weak, and are streaked in a direction normal to the <100> directions of the precipitate rods. So far only one set of precipitate lattice planes has been positively identified; diffraction spots from four sets of these planes are shown in Fig. 7c, and are labeled B, C, 0, and E in the diagram Fig. 7d. The matrix orientation where this pattern was recorded is along the [100] zone between the (001) and (013) poles, ~4° from (013). In the bright-field micrograph, Fig. 7a, Frank dislocation loops are in strong contrast, and the precipitates are in weak contrast. The dark-field micrograph, Fig. 7b, was recorded with spot D in Fig. 7d; the precipitate

images are aligned along the [100] direction. Additional dark-field micrographs (not shown) using spots B and E of Fig. 7 revealed two different sets of precipitates whose images were parallel to one another, and normal to the images in Fig. 7b. Thus all the precipitate images were consistent with <100> rods, and the fact that spots B and E are from different sets of precipitates aligned along the same <100> direction indicates that there are at least two equivalent crystallographic orientations for each <100> direction. Dark-field micrographs using spot C were identical to those with spot 0, suggesting that C and D form a pattern from a single set of precipitates; in this particular orientation the point is not proved, since a double diffraction 0 reflection should be superimposed upon C and vica versa. However, other dark-field micrographs using spots C and D, recorded in orientations where double diffraction should not occur, again showed the same set of precipitates for both diffraction spots, indicating that C and D do form a pattern. The other extra reflections in Figs. 7c and d are as follows: A and F are double diffraction E and B reflections, respectively, while the spots marked G are recipocal lattice rods which point in <111> directions, and are due to Frank dislocation loops. The origin of the diffuse rings marked H is unclear at present, but may be due to surface contamination.

since one set of lattice planes is insufficient to define the structure of the precipitates, we have assigned approximate fractional indices to the observed reflections, as if the precipitate planes were part of the fcc matrix; the indices define both the lattice spacing and orientation relative to the matrix. The indices of spot C in Fig. 7d are $\sim(\overline{1.0}, 1.2, \overline{0.29})$, while D $\sim(1.0, 1.2, \overline{0.29})$, B $\sim(\overline{1.2}, 1.0, \overline{0.29})$, and E $\sim(1.2, 1.0, \overline{0.29})$.

From the indices, we can determine the locations of these reciprocal lattice spots for any matrix orientation. For instance, spot C of Fig. 7d should appear in a matrix orientation along the $[11\bar{1}]$ zone between the (112) and (123) poles, $\sim 6°$ from (112). Micrographs taken in this orientation (in a different sample) are shown in Fig. 8; the sp

marked C in Fig. 8d is the same as spot C in Fig. 7d, and appears in the proper position in the diffraction pattern. In the dark-field micrograph, Fig. 8b, the precipitate images are oriented ∿51° from the $[11\bar{1}]$ direction, which is the correct projection for a [100] rod near a (112) orientation. As to the other extra spots in Figs. 8c and d spot J is a double diffraction C spot, and the spots marked G are <111> reciprocal lattice rods from Frank loops.

The diffraction information above should prove useful in establishing visibility criteria for all of the rod-shaped precipitates, and thereby aid in correlating cavity nucleation with the precipitates. Also, only a fairly limited amount of additional diffraction information is now needed for determination of the precipitate structure; the information at hand is sufficient to eliminate most structural possibilities.

VI. REFERENCES

1. S. C. Agarwal, G. Ayrault, D. I. Potter, A. Taylor and F. V. Nolfi, J. Nucl. Mater. 85 & 86, p. 653 (1979).

2. F. V. Nolfi, G. Ayrault and H. A. Hoff, DAFS Quarterly Report No. 7, July-September (1979).

VII. FUTURE WORK

Quantitative analysis of TEM micrographs is in progress for the remainder of the 316 stainless steel dose and helium injection rate samples described in this report. Similar analysis is being performed for temperature dependence samples, which will be added to the temperature dependence study reported previously [2]. Further insight into cavity nucleation will be sought through study of the radiation induced or enhanced precipitation.

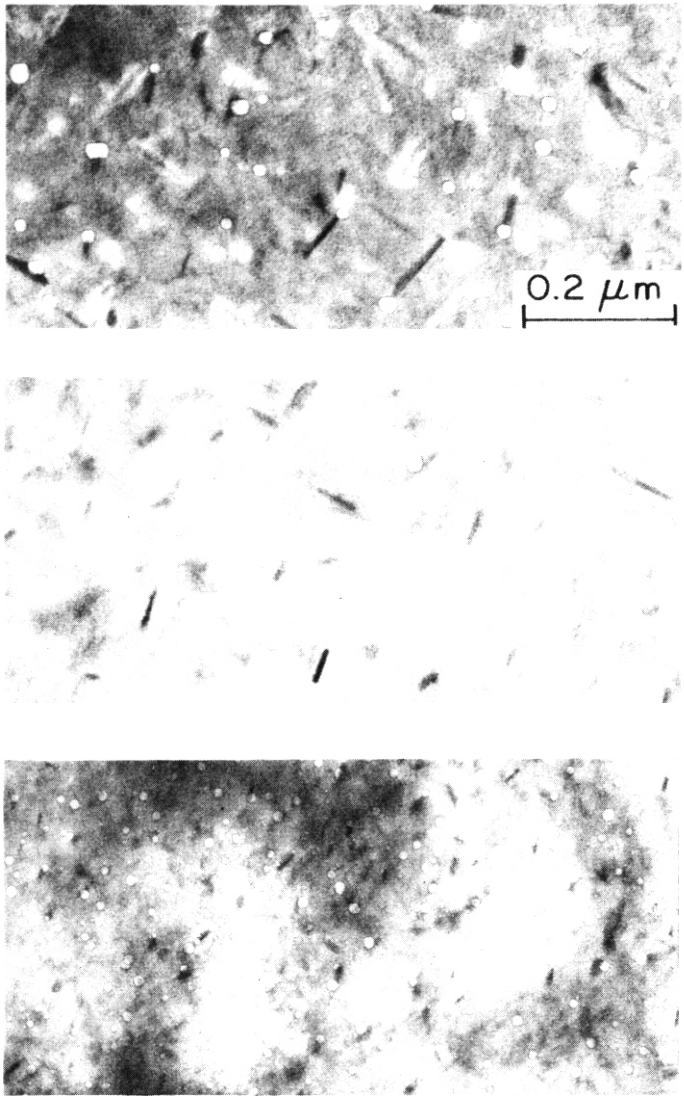

Figure 1. Absorption contrast micrographs of 316 stainless steel dual-ion irradiated at a nominal temperature of 625°C to a nominal dose of 6 dpa at different helium injection rates. (a) 5:1 He:dpa, 621°C, 8 dpa (b) 15:1 He:dpa, 620°C, 8 dpa and (c) 50:1 He:dpa, 612°C, 7 dpa.

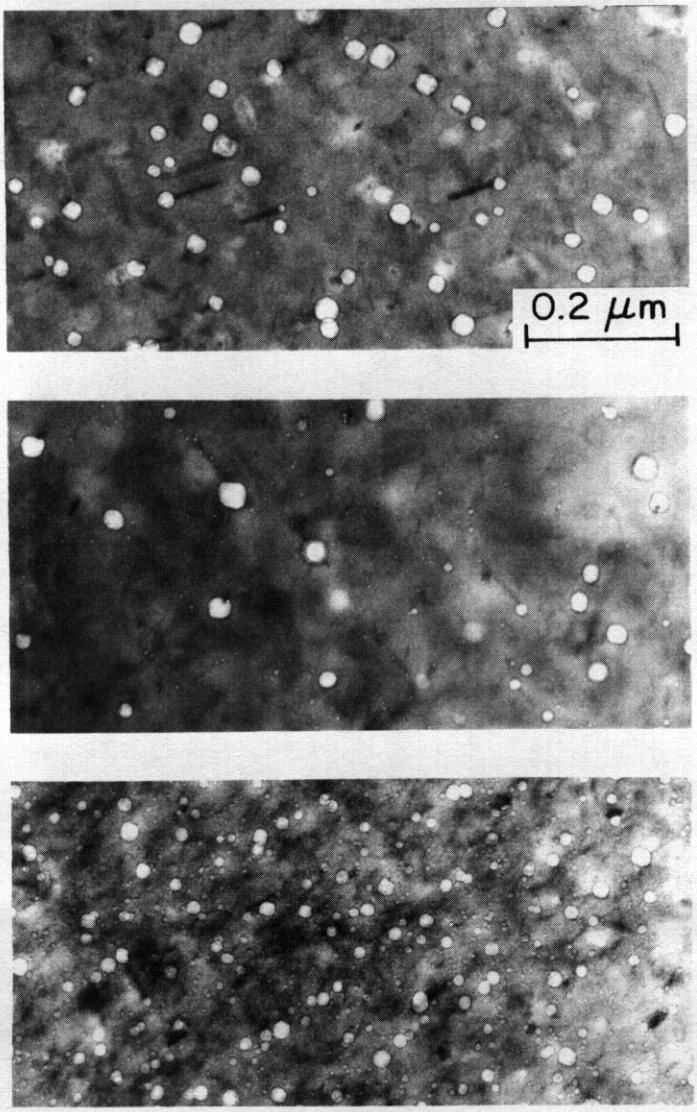

Figure 2. Absorption contrast micrographs of 316 stainless steel dual-ion irradiated at a nominal temperature of 625°C to a nominal dose of 12 dpa (a) 5:1 He:dpa, 619°C, 16 dpa (b) 15:1 He:dpa, 638°C, 15 dpa and (c) 50:1 He:dpa, 603°C, 14 dpa.

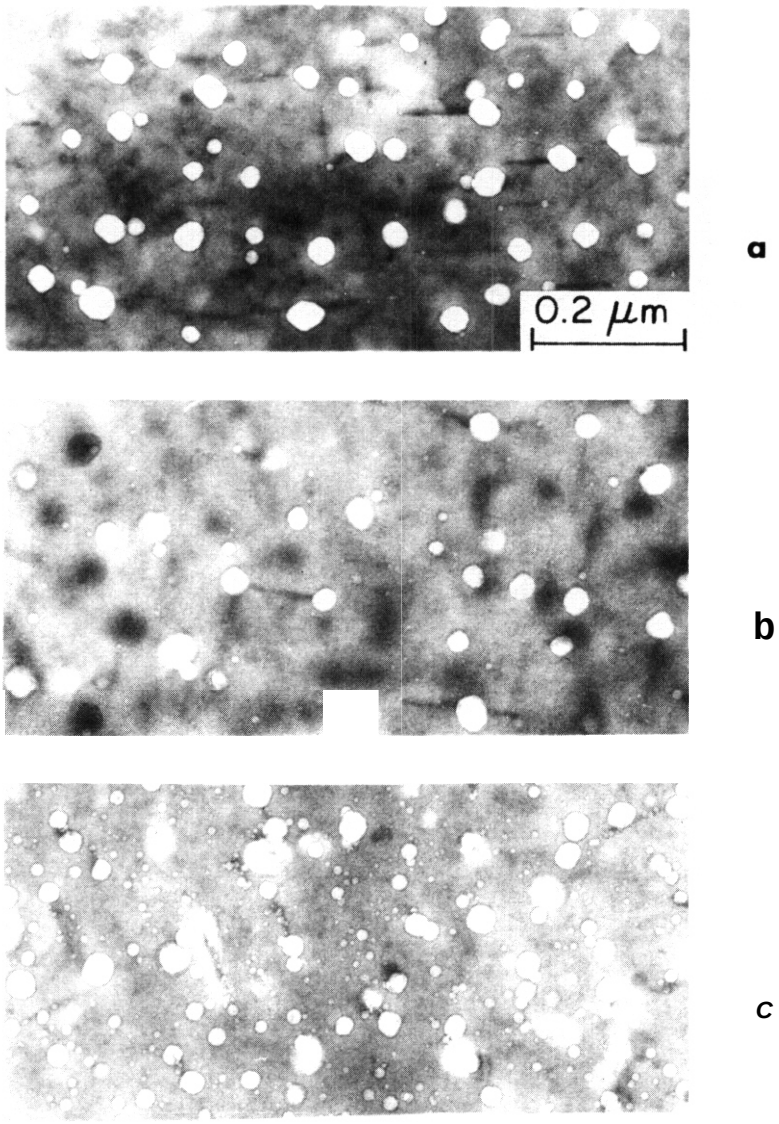

Figure 3. Absorption contrast micrographs of 316 stainless steel dual-ion irradiated at a nominal temperature of 625°C to a nominal dose of 25 dpa (a) 5:1 He:dpa, 615°C, 29 dpa (b) 15:1 He:dpa, 630°C, 29 dpa and (c) 50:1 He:dpa, 628°C, 22 dpa.

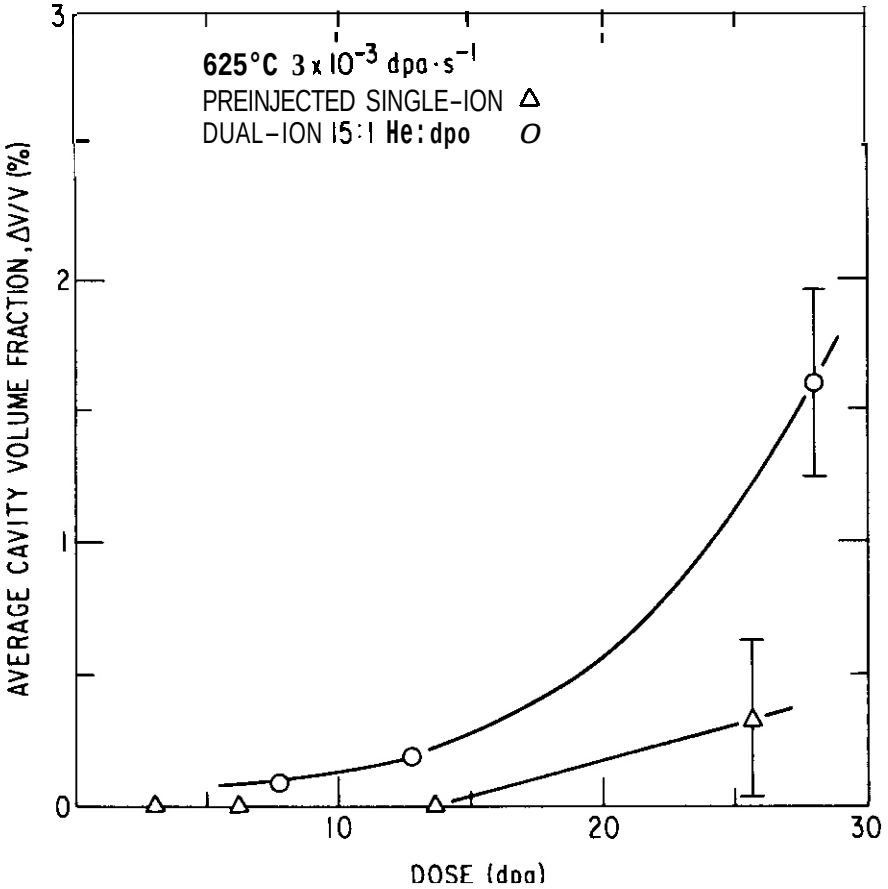

Figure 4. Dose dependence of swelling in preinjected single-ion and dual-ion irradiated 316 stainless steel.

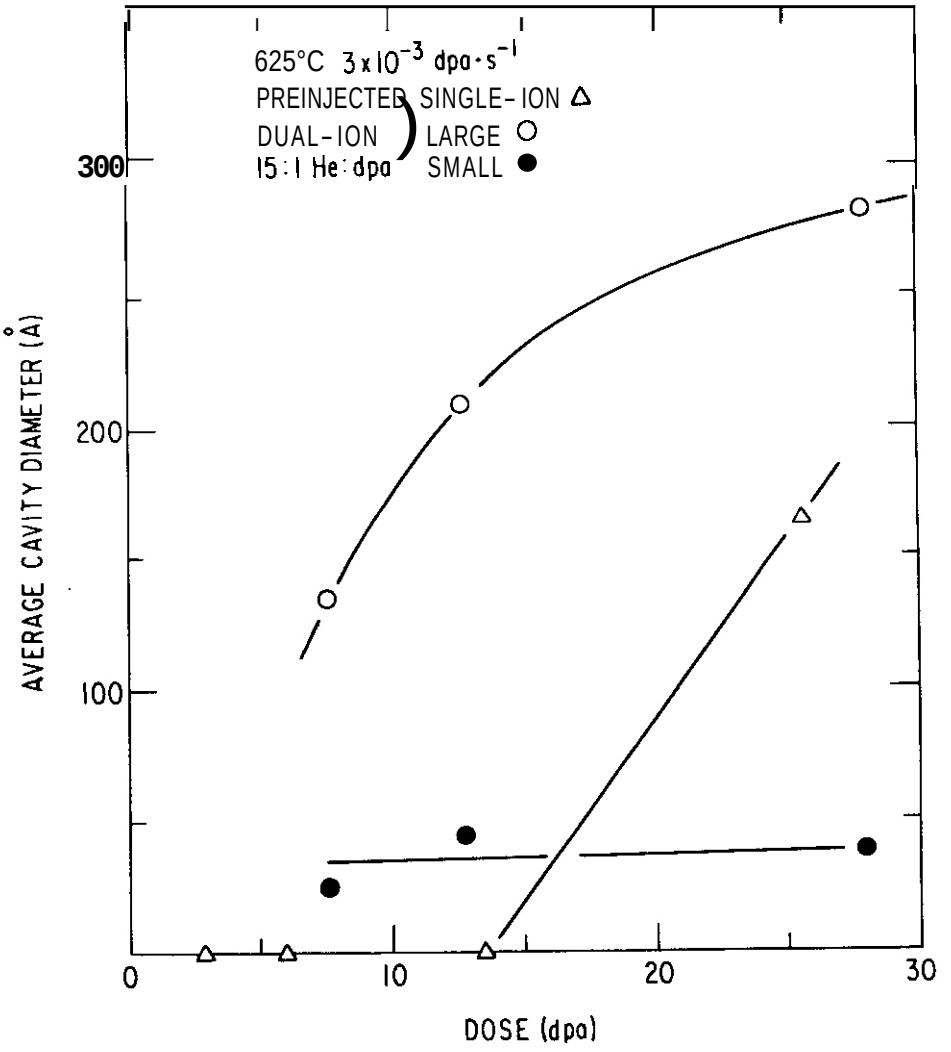

Figure 5. Dose dependence of cavity size in preinjected single-ion and dual-ion irradiated 316 stainless steel.

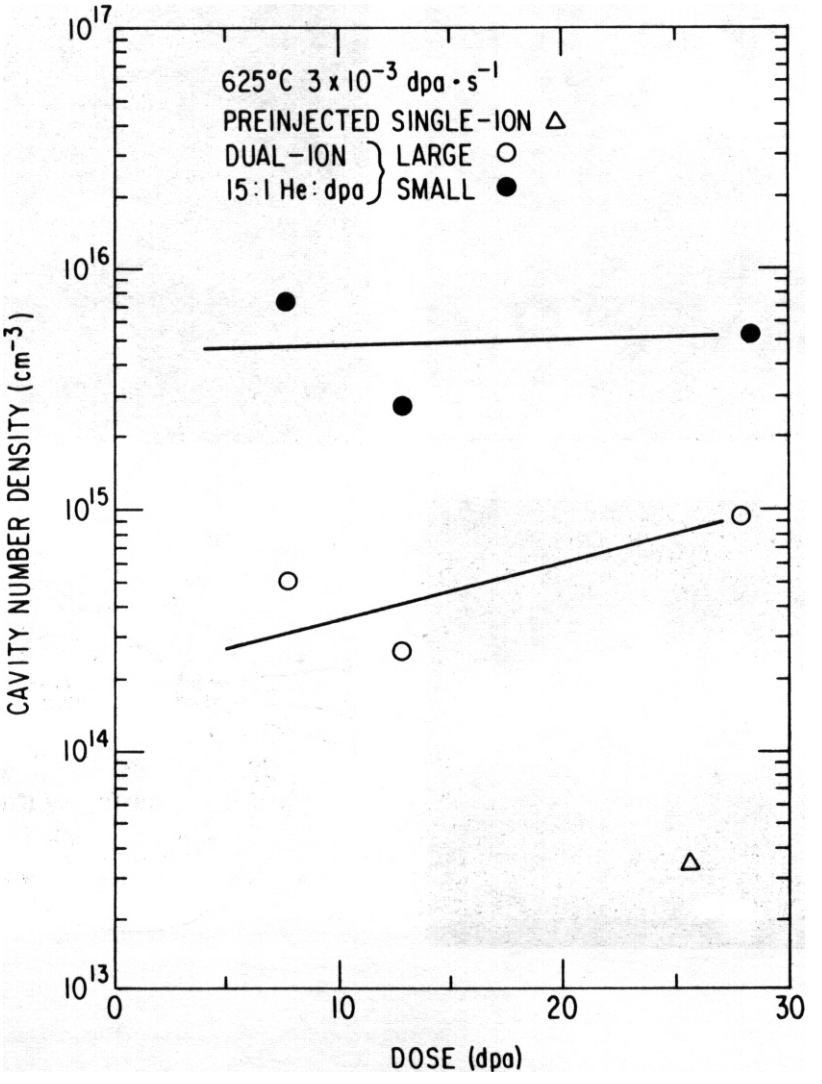

Figure 6. Dose dependence of cavity number density in preinjected single-ion and dual-ion irradiated 316 stainless steel.

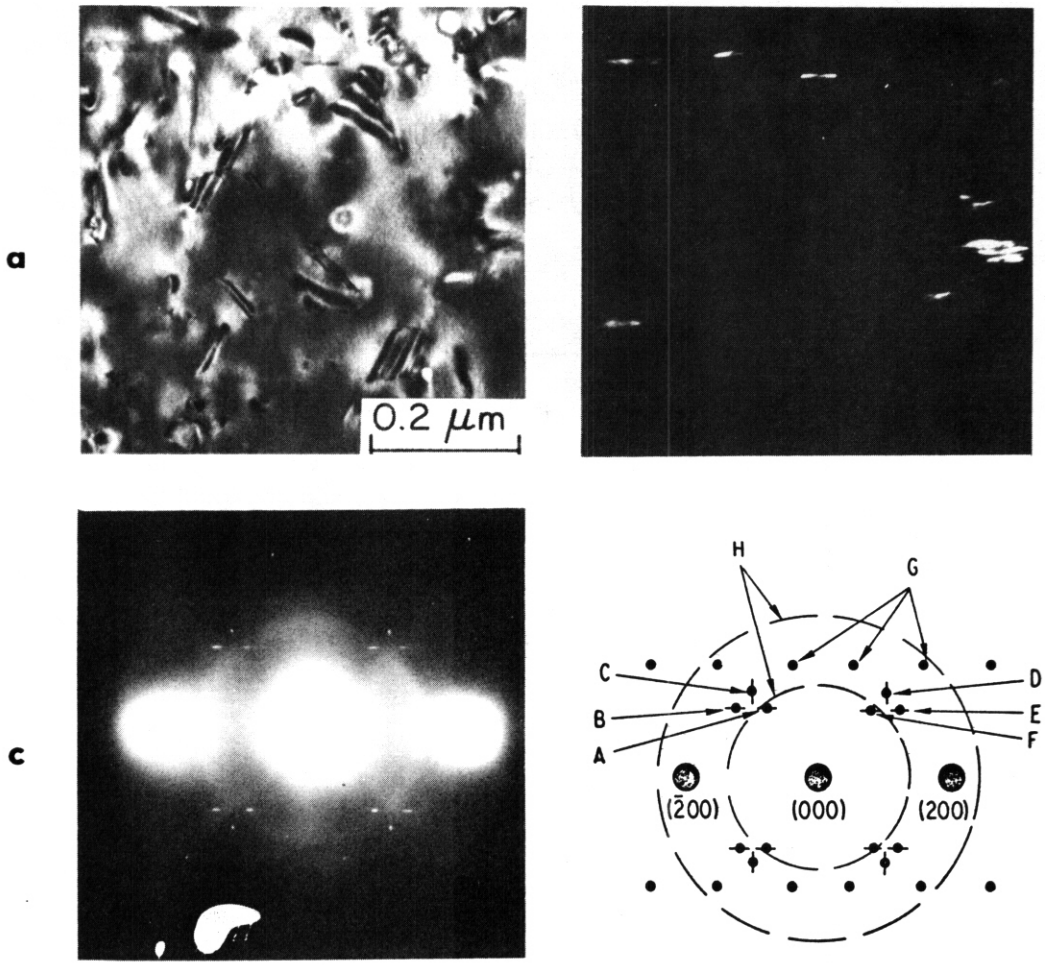

Figure 7. Acicular precipitates in a 316 stainless steel sample dual-ion irradiated to a 3 dpa dose at 610°C with 5:1 appm He:dpa. The orientation is along the [100] zone between (001) and (013), ∿4° from (013) (a) bright-field (b) dark-field using spot D in the diffraction pattern diagram (c) diffraction pattern and (d) diagram of the diffraction pattern.

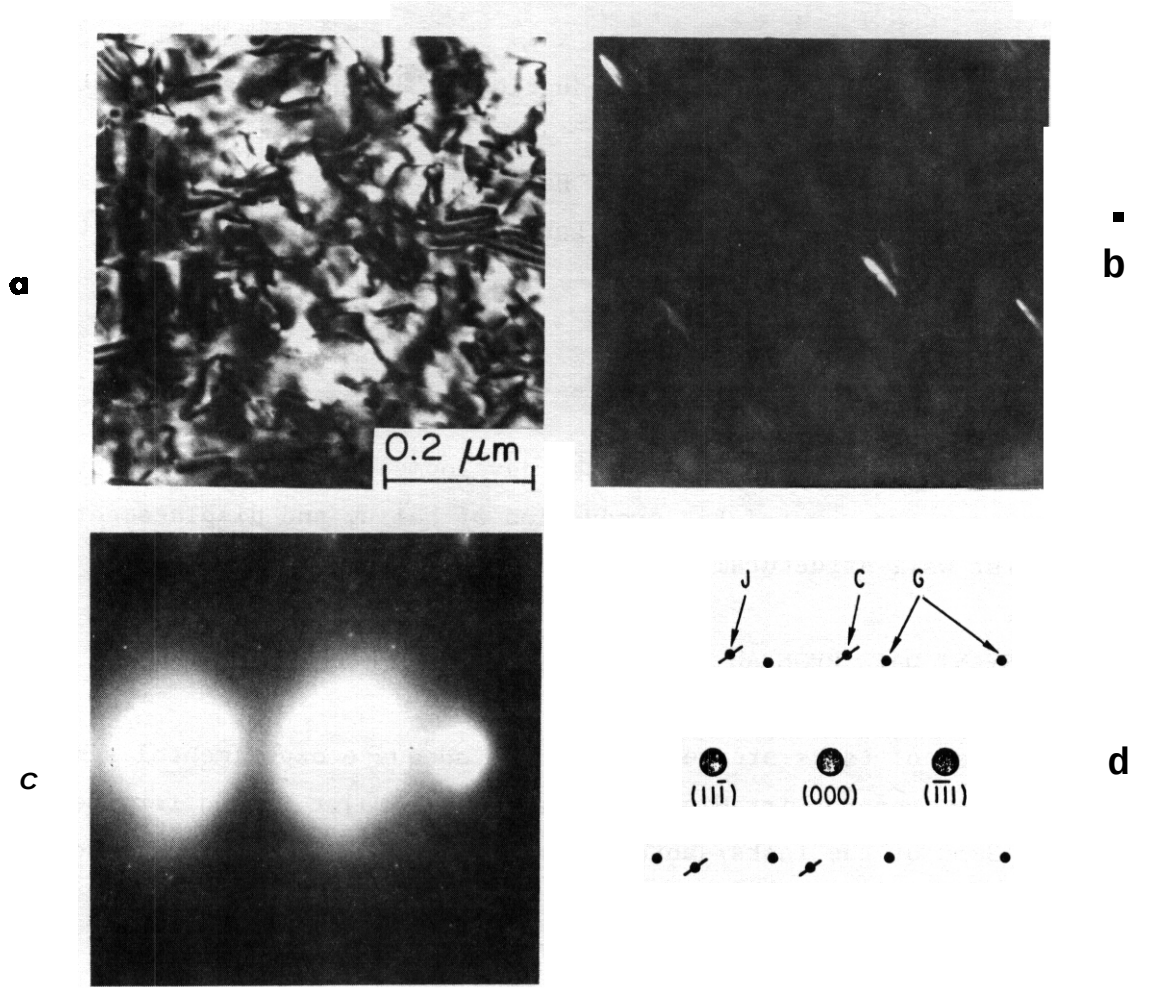

Figure 8. Acicular precipitates in a 316 stainless steel sample dual-ion irradiated to an 8 dpa dose at 621°C with 5:1 appm He:dpa. The orientation is along the [11$\bar{1}$] zone between (112) and (123), ~5° from (112) (a) bright-field (b) dark-field using spot C in the diffraction pattern diagram (c) diffraction pattern and (d) diagram of the diffraction pattern.

I. PROGRAM

Title: Synergistic Helium Production by Boron Doping of Splat Cooled Alloys

Principal Investigator: O. K. Harling

Affiliation: Nuclear Reactor Laboratory, Massachusetts Institute of Technology

11. OBJECTIVE

This work is directed toward the development of better simulation techniques for the synergistic production of helium and displacement damage in first wall structural materials.

III. RELEVANT DAFS PROGRAM PLAN TASK/SUBTASK

A number of tasks are relevant since adequate experimental simulation of fusion reactor irradiation effects is a major reason for the DAFS program. Some of the tasks/subtasks which are significantly affected are:

TASK II.A.4 Gas Generation Rates

II.C.2 Effects of Helium on Microstructure

II.C.8 Effects of Helium and Displacement on Fracture

II.C.13 Effects of Helium and Displacement on Crack Initiation and Propagation

IV. SUMMARY

Two type 316 stainless steels with different amounts of boron and zirconium have been rapidly solidified and thermomechanically treated. This report presents results from the microstructural characterization of these materials by meansoftransmission and scanning transmission electron microscopy, energy dispersive X-ray and electron energy loss spectroscopy and neutron autoradiography.

V. ACCOMPLISHMENTS AND STATUS

Characterization of Rapidly Solidified Boron Doped Stainless Steel for Synergistic Helium Production--L. Arnberg and O. Harling (M. I. T.)

1. Introduction

Today, large scale irradiation testing of candidate fusion reactor alloys has to be performed in fission reactors. A simulation technique which could make use of existing fission reactors to produce the simultaneous helium and displacement damage characteristic of fusion reactors may be achievable by alloying the material investigated with boron and by making use of the ^{10}B (nα) ^{7}Li reaction. In order to get a uniform helium production, the boron present in the material must be uniformly distributed and stay uniformly distributed at service temperatures and during irradiation. Since the equilibrium concentration of boron is low in many candidate alloys, conventional casting will produce substantial boron segregation, preferably to grain boundaries. By additions of elements which have a high affinity to boron, stable borides can instead be precipitated within the grains if the solidification rate is high enough.

To test these principles, two Type 316 stainless steels with different amounts of boron and zirconium have been rapidly solidified ($\sim 10^5$°K/sec) by means of a roller quencher.[1] The nominal compositions are given in Table 1. Only one of the alloys (I) with the nominal boron concentration 0.020 w/o ^{10}B was produced in a quantity large enough to permit consolidation. This alloy was extruded at 1065°C to a reduction of area of 23 to 1. It was then cold worked 42% by swaging and finally annealed at 850°C for 1/2 hr. The other alloy (II) with a nominal boron concentration of 0.100 w/o was not extruded but the roller quenched foils were annealed at 980°C for 1/2 hr. The bulk concentrations of boron and zirconium have been analyzed by plasma emission spectroscopy. These

TABLE 1

NOMINAL COMPOSITIONS OF THE BORON WPED STAINLESS STEELS

Concentrations are given in W/O

	Alloy I	Alloy II
Fe	balance	balance
Cr	16.73	16.73
Vi	16.49	16.49
Mb	2.27	2.27
Mn	1.21	1.21
Zr	0.170	0.845
Si	0.149	0.149
B	0.020	0.100
C	0.0054	0.0054
O	0.0052	0.0052
S	0.0035	0.0035
N	0.0016	0.0016

TABLE 2

MEASURED BORON AND ZIRCONIUM CONCENTRATIONS IN W/O

	Alloy I	Alloy II
B*	0.016	0.090
Zr	<0.002	0.450

* Alloy I contains enriched ^{10}B while Alloy II contains natural boron.

compositions are given in Table 2. There is a large discrepancy between the nominal and observed zirconium concentrations, especially for alloy I, where almost all zirconium has been lost, presumably due to oxidation during melting. It should be noted, however, that in alloy II the amount of Zr exceeds the stoichiometric concentration to form ZrB_2 with all boron in the alloy.

TEM discs from both alloys have been sent to **HEDL** to be included in the AD-2 EBR-II neutron irradiation. The test matrix is given in Table 3.

This quarterly report presents the pre-irradiation microstructural characterization of the two alloys.

2. Electron Microscopy and Microanalysis

The microstructures have been examined by transmission electron microscopy (TEM) and scanning transmission electron microscopy (STEM). The TEM investigations were carried out on a Siemens Elmiskop 101 operated at 100 KV. The STEM is a Vacuum Generators HB5 equipped with an energy dispersive X-ray detector and an electron energy loss spectrometer. The STEM microscope as well as the X-ray and electron spectrometers are described in Ref. 2. The alloy samples were thinned by electropolishing in a solution of 10% $HClO_4$ in CH_3OH at ~-45°C and 30V.

Fig. 1 shows the microstructure of alloy I. The average grain size is 5 μm. It can be seen that the material contains particles within the grains. Most particles are small, typically 100÷500 Å diameter but a few of them substantially larger ~0.5μm. The electron energy loss spectra (EELS) and the energy dispersive X-ray spectra (EDXS) show that most of the small particles are aluminum oxide (Fig. 2). This is probably due to contamination from alumina melting crucibles. Some small particles contain boron (Fig. 3) in the form of complex molybdenum-chromium borides.

TABLE 3

TEST MATRIX FOR NEUTRON IRRADIATION IN EBR-II

The table shows the number of TEM discs for Alloys I and II respectively

Temp. °C	Fast neutron dose n/cm^2 5.10^{22}	10^{23}
390	7,6	7,6
500	7,6	7,6
550	7,6	7,6

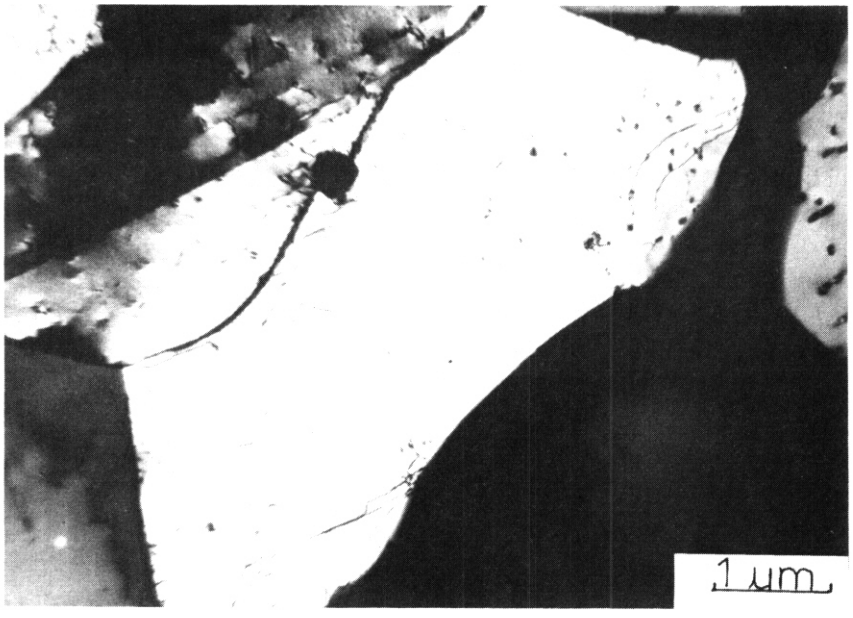

FIGURE 1. TEM micrograph of alloy I showing small intragranular particles and a large grain boundary precipitate (bright field).

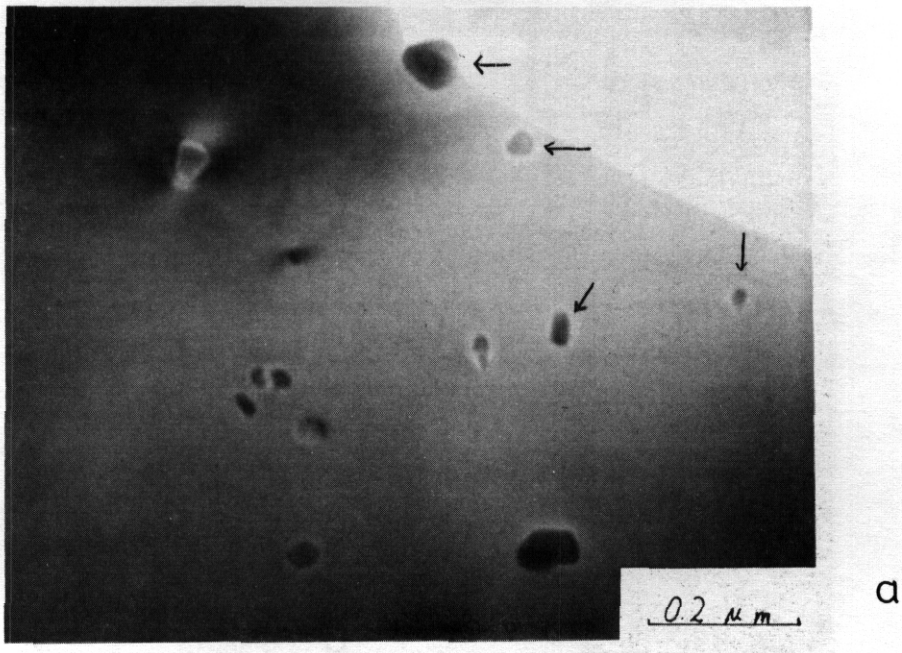

a

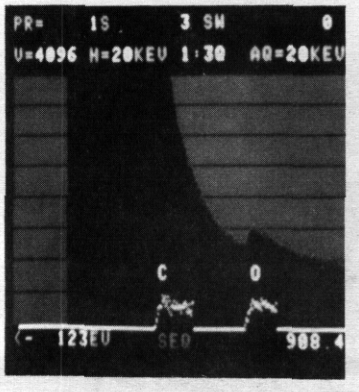

b

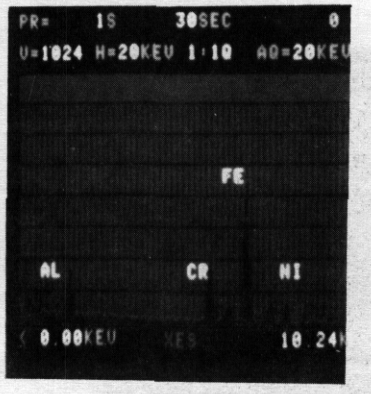

c

FIGURE 2a. STEM micrograph of alloy I. The arrowed particles have been analyzed and all show EELS and EDXS spectra like Fig. 2b and 2c respectively indicating that they are Al_2O_3. The carbon peak in the EELS spectrum is due to carbon contamination in the microscope.

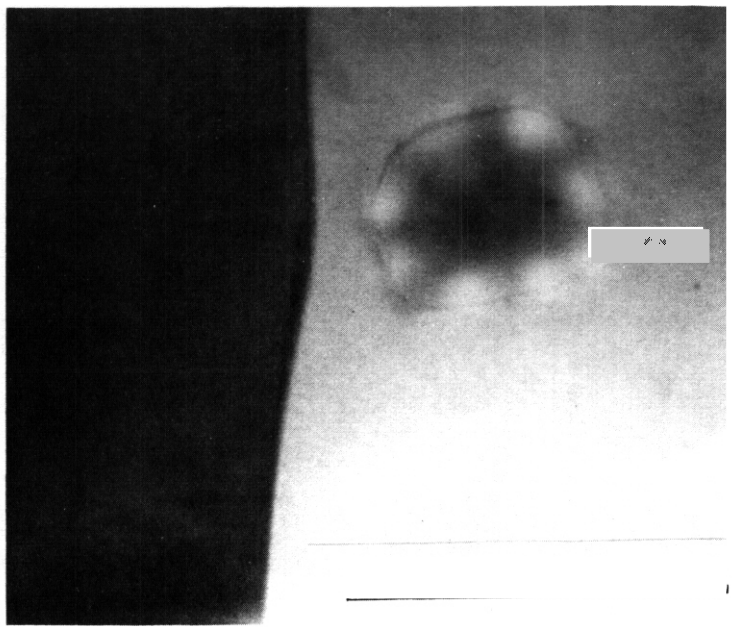

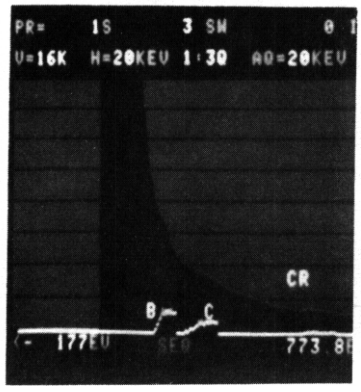

b

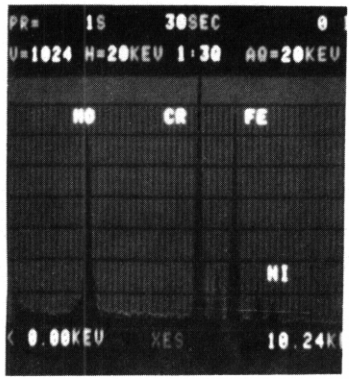

c

FIGURE 3a. STEM micrograph of a boron containing particle from alloy I.

b. EELS spectrum from the particle in Fig. 3a. The carbon peak is due to carbon contamination in the microscope.

c. EDXS spectrum from the particle in Fig. 3a.

There are very few Zr containing particles, which is consistent with the low zirconium concentration. The large particles are silicon and manganese rich (Fig. 4) and some of them contain small amounts of zirconium.

Alloy II exhibits a different microstructure from alloy I. The interdendritic precipitation of particles can easily be seen (Fig. 5) since this material has not been deformed after solidification. The major portion of the small particles, which are typically 250 Å diameter, contain Zr and B and are probably ZrB_2 (Fig. 6). A few complex Mo-Cr borides, as in Fig. 3, have also been found. A determination of the volume fraction of the boron containing particles made from micrographs like Fig. 5 agrees with the volume fraction calculated from the boron concentration within a factor of 2. No aluminum oxide particles have been found in alloy II.

3. Neutron Autoradiography

The boron content and distribution of both alloys has been investigated by neutron autoradiography at the MITR-II reactor. The track density of radiographs, e.g. Fig. 7, has been determined and found to be the same for alloys I and II within 20%, which is consistent with the fact that alloy II contains approximately five times as much boron as alloy I, while alloy I contains enriched boron with 92% ^{10}B and alloy II contains natural boron with 20% ^{10}B. The track distribution obtained from alloy II is very uniform, which is also true for alloy I with the exception of a few areas like in Fig. 8, showing an increased boron concentration.

VI. REFERENCES

1. J. P. Durand, "Properties of Splat Cooled 7075 Aluminum Alloys," M.S. Thesis, M. I. T. 1972
2. J. B. Vander Sande and E. L. Hall, "Applications of Dedicated Scanning Transmission Electron Microscopy to Nonmetallic Materials," J. Amer. Ceram. Soc. 62 [5-6] 246-254 (1979).

a

VII. FUTURE WORK

The time/temperature segregation behavior of the boron doped SS alloys will be determined. Boron doping of a candidate CTR alloy which does not have adequate Ni for the double nickel trick, e.g. HT9 will be considered. Complete microstructural characterization of the EBR-II irradiated boron doped SS will be carried out as soon as the irradiated material becomes available.

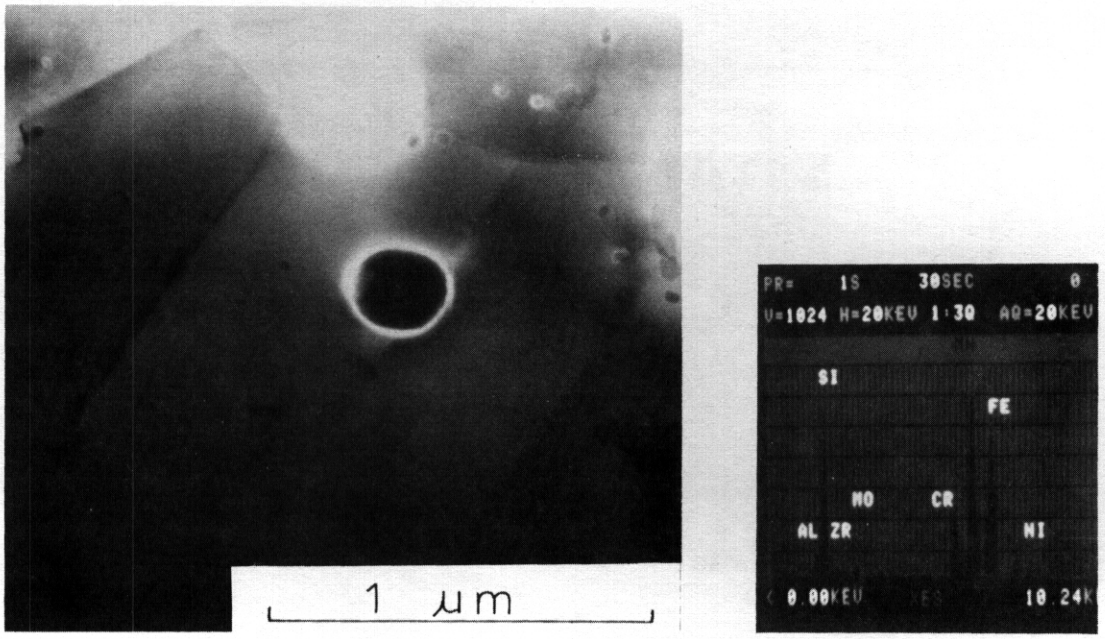

a b

FIGURE 4a. STEM micrograph of alloy I showing a large spherical particle.

b. EDXS spectrum obtained from the large particle in Fig. 4a.

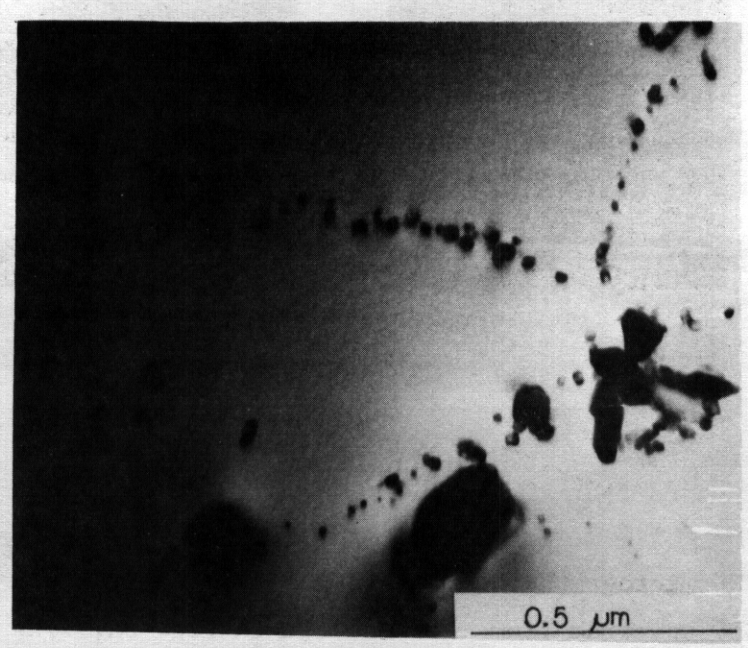

FIGURE 5. TEM micrograph of alloy II showing interdendritic precipitation of intermetallic particles (bright field).

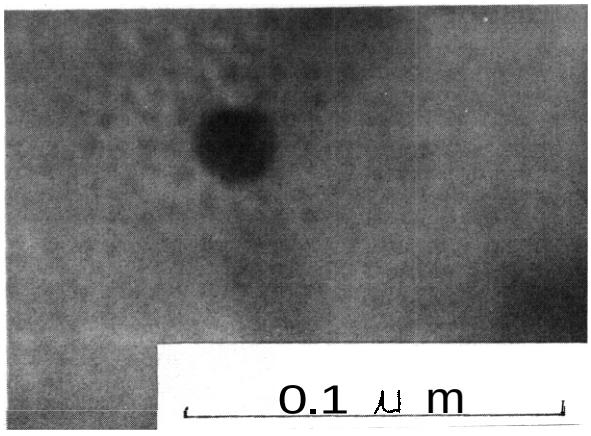

a

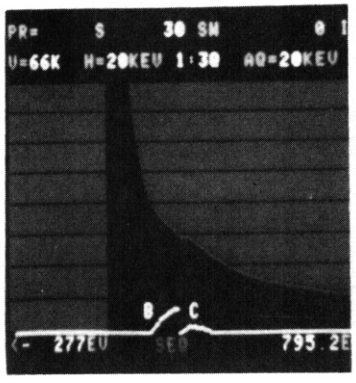

b

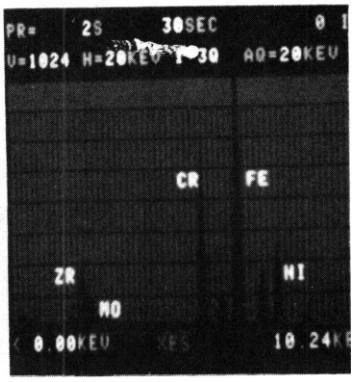

c

FIGURE 6a. STEM micrograph showing a 200 Å large particle.

b. EELS spectrum from the particle in Fig. 6a. The carbon peak is due to carbon contamination in the microscope.

c. EDXS spectrum from the particle in Fig. 6a.

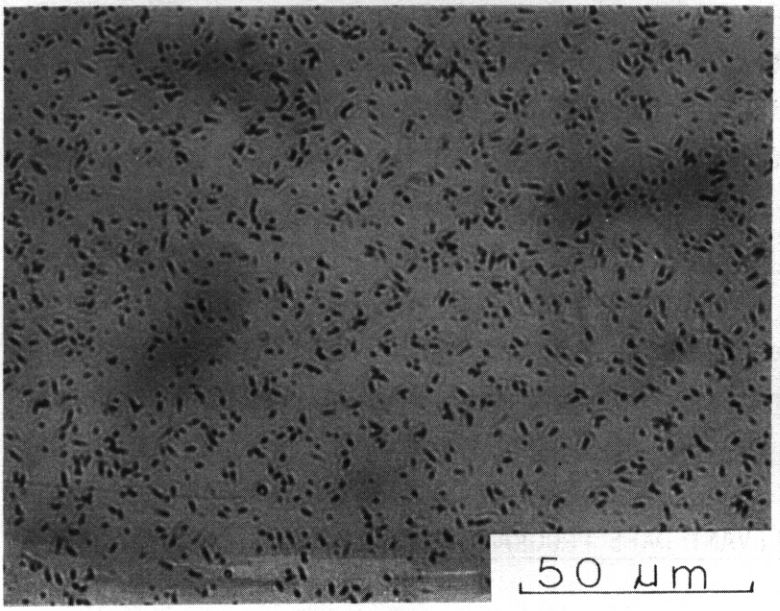

FIGURE 7. Neutron autoradiograph obtained from alloy I showing a uniform track distribution.

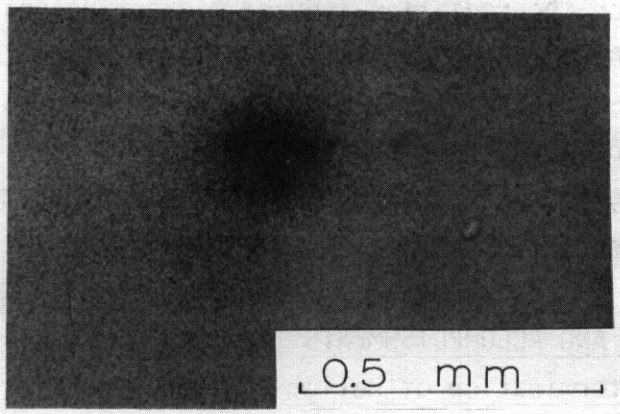

FIGURE 8. Neutron autoradiograph from alloy I showing a region of increased boron concentration.

I. PROGRAM

Title: Irradiation Effects Analysis (AKJ)
Principal Investigator: D. G. Doran
Affiliation: Hanford Engineering Development Laboratory

II. OBJECTIVE

The objective of this effort is to determine the effect of helium on the microstructural and microchemical evolution of metals during irradiation.

III. RELEVANT DAFS PROGRAM TASK/SUBTASK

SUBTASK II.C.2 Effects of Helium on Microstructure

IV. SUMMARY

Two single-variable experiments are proposed, both of which are designed to study the effect of helium generation rate (at constant displacement rate) on the radiation-induced microstructural and microchemical evolution of AISI 316 and other alloys. These are the helium halo technique and the recoil injection/pressurized tube technique. Both involve electron microscopy of irradiated specimens currently available from the Breeder Reactor Program. The analytical tools necessary to interpret the microscopy data have been developed.

V. STATUS AND ACCOMPLISHMENTS

A. Determination of Helium Influence on Microstructural Development: Two Experimental Methods - F. A. Garner (HEDL)

1. Introduction

One of the major differences between fast reactor and fusion reactor neutron environments is their large difference in helium generation rates. Many of the mechanical properties of metals as well as their swelling behavior are sensitive to the magnitude of the helium content developed during irradiation. There is some concern that the microchemical evolution of AISI 316 stainless steel is also strongly sensitive to the helium generation rate. Kenik has shown that during ion irradiation the phase stability of a modifed 316 stainless steel is altered by the presence of helium.[1] Maziasz found that in HFIR irradiations of AISI 316, the γ' phase observed in fast reactor irradiations does not develop, and other phases exhibit shifts in their temperature/fluence stability regimes.[2] (An alternate explanation of the data of Maziasz is presented in Reference 3.)

The role of helium in microstructural evolution must currently be inferred from two types of experiments, dual-ion irradiations and mixed spectrum/fast spectrum comparative irradiations. The first type of experiment necessarily includes some variables not typical of neutron irradiations and the analysis of data derived from this source is complex.[4] The second type of experiment may involve differences in damage rate and irradiation temperature, as well as complications arising from the differences in the source of the helium in the two environments. In addition, of course, the alloy must contain nickel in order to use the nickel two-step reaction to generate helium in a mixed spectrum.

The two methods proposed here for analysis of helium effects on microstructural development have the primary advantage that the He/dpa ratio is essentially the only variable. Furthermore, the specimen material is already available, having been irradiated in the Breeder Reactor Program at displacement rates and to fluences that are relevant to proposed fusion devices. The halo technique can also be employed on some specimens included in the MFE-1 experiment. The two methods share a common disadvantage in that the material volumes involved in the experiment are so small that only

microstructural data can be extracted.

2. The Helium Halo Technique

In an earlier report[5] a method was described which allows the determination of some aspects of the role of helium on microstructural evolution in complex alloys. It involves a direct comparison of the materials' response to the rate of helium generation. This is accomplished by irradiating specimens in either a fast or thermal reactor and conducting microstructural analyses on alloy matrix regions adjacent to precipitates rich in boron or nitrogen. Such precipitates generate well-defined atmospheres of helium (and other transmuted atoms) due to (n,α) reactions. Microstructural comparisons are made between the regions bearing implanted helium and those just beyond the helium range. The method takes advantage of the virtual absence of variations in alloy composition, pre-irradiation microstructure and displacement rate over short distances, and can be used to study any material of interest if the appropriate precipitates can be developed. A variety of helium/dpa ratios can be obtained in one specimen by using precipitates of various sizes.

As shown in Figure 1 the major disadvantage of this method is that the width of the helium-affected region must be 1.3 μm or less for a typical M_3B_2 precipitate in AISI 316 in order to keep the lithium-rich and helium-rich zones from overlapping. [Lithium has been shown to have a large effect on void nucleation and growth.[5]] This limits the size of the microstructural components which can be studied. At high irradiation temperatures (>550°C) this limitation will preclude effective study of the large voids and precipitates which develop. However, at the low temperatures typical of ETF applications[6] this consideration will not limit the use of the halo technique.

The previous analysis of the helium concentration profile[5] assumes that the ratio of the stopping powers of the M_3B_2 precipitate and the alloy matrix is m = 1.0. For AISI 316 this ratio is m = 1.06 and the

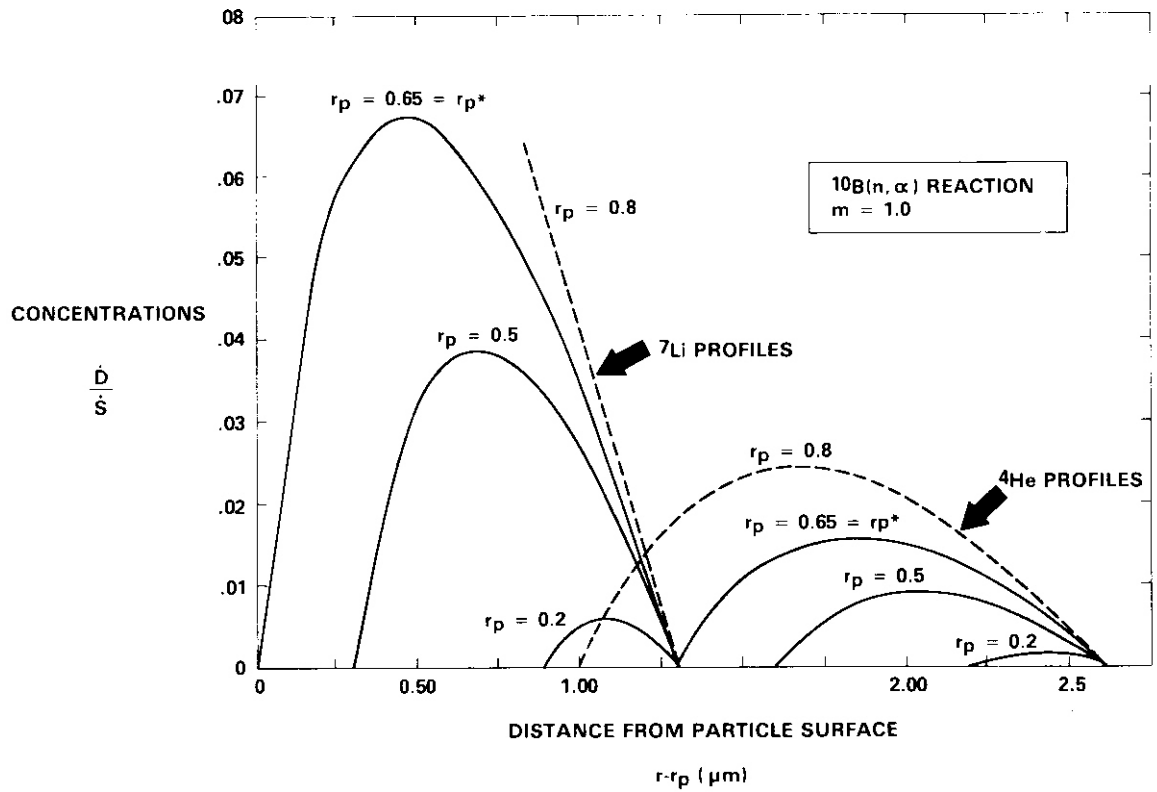

FIGURE 1. Influence of Particle Radius on Normalized Deposition Rate Profiles of Reaction Products for $^{10}B(n,\alpha)$ Events Occurring in Spherical Precipitates for Case Where the Energy Deposition Characteristics of Alpha Particles are the Same in Both Phases.

assumption is therefore reasonably valid. When m is significantly different from 1.0 however, the assumptions employed in the analysis are no longer valid and a more general treatment is required.

Since the use of other alloy/precipitate combinations is anticipated, analytical expressions have been developed for the general ($m \neq 1$) case. The simple derivation employed in Reference 5 assumed spherical geometry and will not suffice where $m \neq 1$.

For a precipitate of radius r_p the width of the helium-bearing region is defined as before,[5] where the inner and outer limits (R_i and R_o) of the halo can be defined for a given energy E_o in terms of ranges $R_p(E_o)$ and $R_m(E_o)$ in the precipitate and the matrix, respectively, and r_p. These relationships are shown in Figure 2.

$$R_o = R_m(E_o) + r_p \qquad [1]$$

$$R_i = R_m(E_o) + r_p(1 - 2m) \qquad [2]$$

$$m = \frac{\rho_p\sqrt{A_m}}{\rho_m\sqrt{A_m}} = \frac{R_m(E_o)}{R_p(E_o)} \qquad [3]$$

The quantity, m, is defined in terms of the molecular weight, A, and density, ρ, of both precipitate and matrix phases. Alternately, it is defined in terms of the ranges of a particle of energy E_o in each of the phases.

As shown in Figure 3, the surface within the precipitate which can contribute to deposition at point x within the halo is defined by a cone of revolution defined by the locus of those ranges $R(x,\theta)$ which satisfy the energy deposition requirements of two-phase travel.[5] The area of this surface, A_s, is

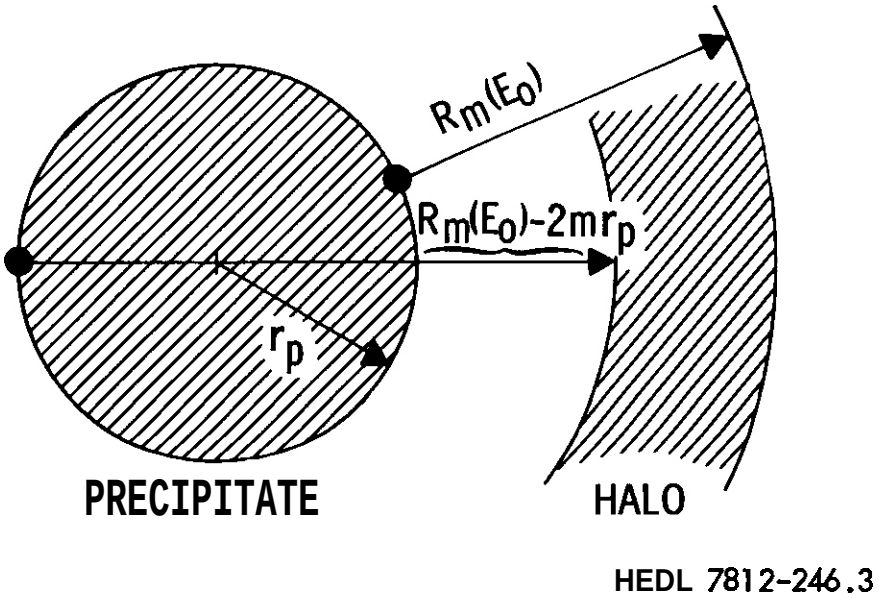

FIGURE 2. The Limits of the Halo are Determined by (n,α) Events Occurring on the Near and Far Surfaces of the Precipitates.

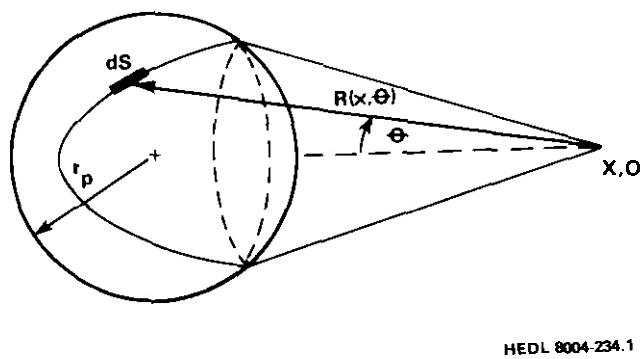

FIGURE 3. Schematic Illustration of Surface Within Precipitates Capable of Depositing Alpha Particles at Point **x,o** Within the Halo.

$$A_S = 2\pi \int_{\theta_1}^{\theta_2} R(x,\theta)\sin\theta \; ds, \qquad [4]$$

where

$$ds = \sqrt{R^2(x,\theta) + \left(\frac{dR}{d\theta}\right)^2} \; d\theta. \qquad [5]$$

The probability P of an alpha particle starting at ds and arriving at x is

$$P = \frac{1}{4\pi R^2(x,\theta)} \qquad [6]$$

For a source strength of S the deposition rate D(x) at x can be obtained by combining Equations 4, 5 and 6.

$$\dot{D}(x) = \frac{S}{2}\int_{\theta_1}^{\theta_2} \frac{\sin\theta}{R(x,\theta)} \sqrt{R^2(x,\theta) + \left(\frac{dR(x,\theta)}{d\theta}\right)^2}\, d\theta. \qquad [7]$$

The description of $R(x,\theta)$ must now be determined. Geiger[6] stated that the energy loss rate $\frac{dE}{dx}$ of an alpha particle was inversely proportional to the particle velocity. From this statement various forms of the "Geiger Rule" are found in the literature. Some of these are given below.

(a) $\frac{dE}{dx} \sim E^{-1/2}$	instantaneous energy loss rate at any energy E
(b) $R(E_o) \sim E_o^{1.5}$	total range in one phase
(c) $\frac{E(L)}{E_o} = [1 - \frac{L}{R(E_o)}]^{2/}$	residual energy at a distance $L \leq R(E_o)$

Consider now the obvious corollary *of* the Geiger Rule when the particle travels a distance d_p in the precipitate phase and then encounters the matrix phase, traveling a distance d_m. Statements (b) and (c) must hold in both phases; therefore

$$\frac{E(d_p)}{E_o} = [1 - \frac{d_p}{R_p(E_o)}]^{2/3} \qquad [8a]$$

at the precipitate boundary and

$$\frac{E(d_p)}{E_o} = \left[\frac{d_m}{R_m(E_o)}\right]^{2/3} \qquad [8b]$$

describes the remaining range in the matrix relative to the range of the original ion energy. Since $E(d_p) = E_o(d_m)$ at the precipitate boundary, equating these two expressions leads to

$$\frac{d_p}{R_p(E_o)} + \frac{d_m}{R_m(E_o)} = 1. \qquad [9]$$

Employing this criteria and the geometry shown in Figure 3 it can be shown that

$$R(x,\theta) = R_m + (1 - m)\,[x \cos e - \sqrt{r_p^2 - x^2 \sin^2\theta}]\ , \qquad [10]$$

and simple differentiation yields

$$\frac{dR(x,\theta)}{d\theta} = (1 - m)\,[-x \sin\theta + \frac{(x^2 \sin\theta \cos\theta)}{\sqrt{r_p^2 - x^2 \sin e}}\,]. \qquad [11]$$

Note that Equation [10] is only valid for $R_1 \leq x \leq R_o$. For $m = 1$, θ_1 is always zero, but that is not necessarily true when $m \neq 1$. The values of θ_1 and θ_2 change for each x and value of m. The integration of Equation [7] for all values of x within the halo does not appear to be possible without resorting to computer assistance. The value of m, of course, depends on the nature of the precipitate and the alloy in which it is embedded.

3. Recoil-Injection/Pressurized Tube Technique

The helium halo technique requires the use of alloys which possess reasonably high densities of boron-containing precipitates. While several developmental and experimental alloys meet this condition, most of the heats of AISI 316 used in the Breeder Reactor Program do not. The few precipitate particles are hard to find and are seldom found in a sufficient range of sizes in one grain to fully exploit the advantages of the technique. This problem can be overcome by using another type of irradiated specimen, however. This is the material close to the inner surface of pressurized tubes used to study irradiation creep. These tubes contained either helium or argon-helium mixtures. Any tube which contained helium was subjected to continuous implantation of helium across the tube inner surface during irradiation.

It has been demonstrated experimentally that substantial amounts of helium can be injected into a metal surface via recoil from neutron-helium scattering events near the gas-metal interface. Gaus, Migge, and Mirus[7] performed an experiment where an irradiation of only 4×10^{17} n/cm^2 (E>0.1 MeV) implanted 1.6×10^{12} atoms/cm^2 from helium gas at 80 kPa into silver foils. These authors calculated that an irradiation of 10,000 hours (2.7×10^{22} n/cm^2) in the British DFR reactor would yield 5.5×10^{-3} a/o helium in silver over a depth of 3.5 μm. However, the geometry of the helium-silver experiment was quite different from the geometry associated with a pressurized tube.

Near-surface implanted helium profiles have also been observed in the plenum and below-core regions of AISI 316 fuel pin cladding filled with helium cover gas.[8] More recently similar data have been obtained from pressurized creep tubes[8,9] such as those proposed for study in this report. Typical profiles measured in fuel pins are shown in Figure 4. It should be pointed out that the level of injected helium is much smaller in fuel pins than in pressurized tubes. This is due to the fact that fission gases shield the specimen surface from most recoil-generated alpha particles.

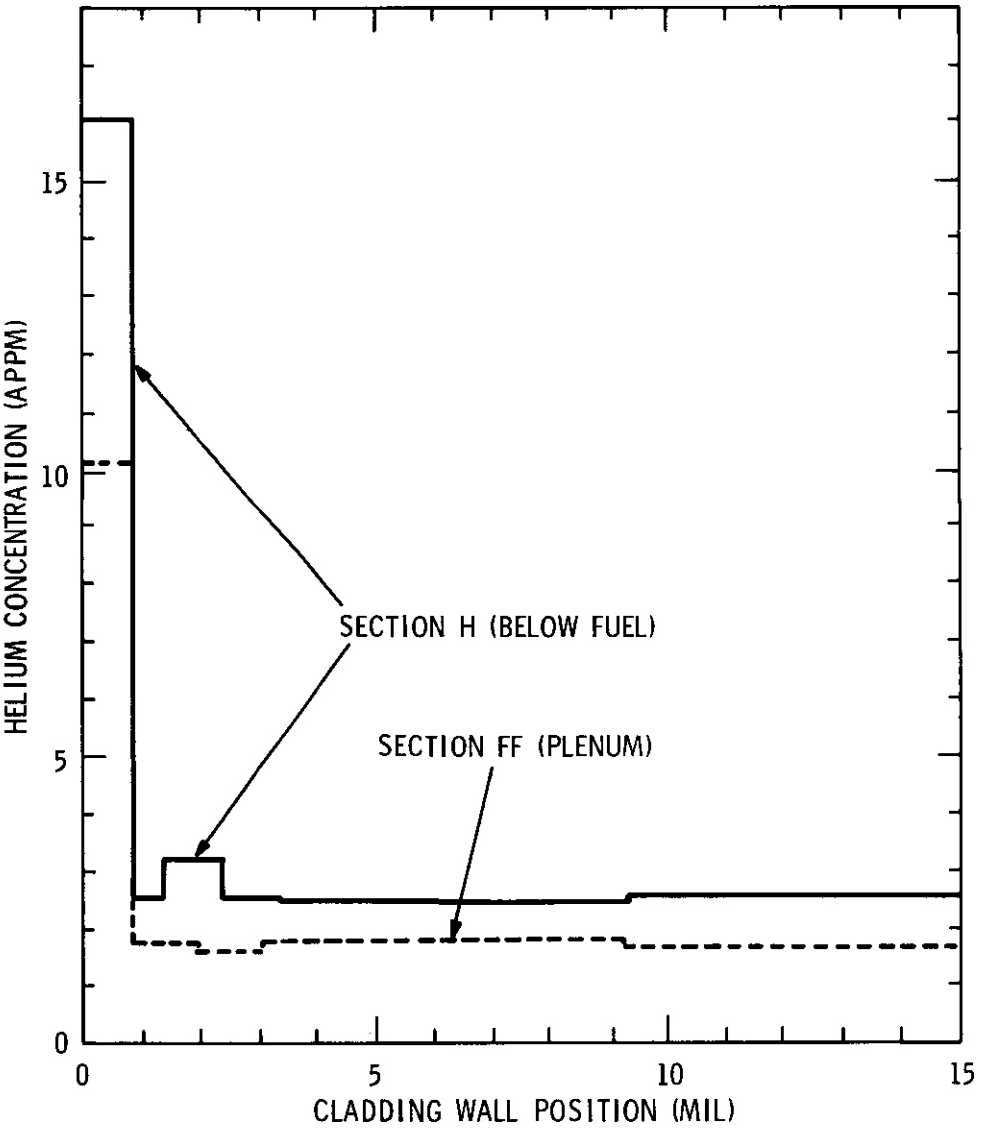

FIGURE 4. Near-Surface Helium Profiles Observed in AISI 316 Cladding at the Extremities of Fuel Pin P-23B-14A. Note that the near-surface increment was measured over a one-mil section, while the injected helium actually lies at depths shallower than 14 μm.

It can easily be shown that the helium is deposited very close to the surface. The maximum depth of penetration for a helium atom suffering a head-on collision with a 10 MeV neutron at the tube surface and directed along a radial path is about 14 μm. At shallower depths there is a steeply increasing concentration profile which arises from injection events that occur at lower neutron energies or with less efficient energy transfer, or which originate at deeper depths in the gas, or which follow non-radial paths. Surface concentrations of many thousands of ppm are reached in typical pressurized tubes at nominal fluence levels. The material beyond 14 μm contains typical fast reactor-generated microstructure for comparison. A large range of higher helium/dpa ratios exists at intermediate depths. Using the procedure developed earlier[5] it is possible to calculate the alpha contribution to the displacement rate, but in most cases it is negligible. The near-surface microstructure of evacuated tubes can be examined to insure that no pre-existing microstructural or compositional gradients influence the analysis.

Scoping calculations have been very successful in predicting the total helium content measured in fuel pin cladding[8] and detailed computer-generated profiles of injection rates in pressurized tubes have been calculated for planar surfaces by Yamada.[10] Yamada has agreed to supply profiles such as those shown in Figure 5 to interested researchers. It is anticipated that both TEM (with multiple depth sectioning) or full range HVEM studies can be employed to extract the dependence of the microstructural/microchemical evolution on helium.

4. Conclusions

It appears that both of these techniques can be used to obtain some insight on the role of helium in microstructural development. They can be used in elements which do not contain nickel. The analytical tools necessary to interpret the microscopy data have been developed.

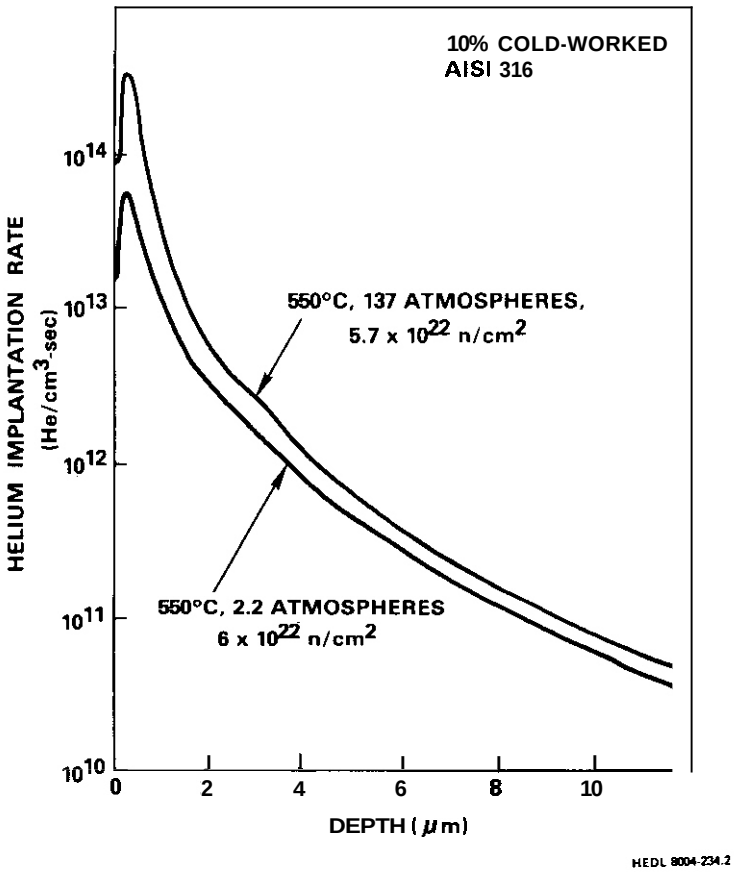

FIGURE 5. Profiles of Injected Helium Calculated **by** Yamada in Helium-Pressurized Creep Capsules Irradiated in EBR-II. The near-surface peak results from ignoring recoils below 30 keV.

VI. REFERENCES

1. E. A. Kenik, "The Influence of Helium on the Microstructural Evolution of an Ion-Irradiated Low-Swelling Stainless Steel," Proceedings of First Topical Meeting on Fusion Reactor Materials, Miami Beach, Florida, January 29-31, 1979.

2. P. J. Maziasz, "The Precipitation Response of 20% Cold-Work Type 316 Stainless Steel to Simulated Fusion Irradiation," ibid., Reference 1.

3. F. A. Garner, "Development of Fission-Fusion Correlations," this report.

4. F. A. Garner and J. J. Laidler, "Review of Factors Relevant to Intercorrelation Experiments," Proceedings of Workshop on Correlation of Neutron and Charged Particle Damage, Oak Ridge, Tennessee, June 4, 1976, CONF-760673, p. 177.

5. F. A. Garner and O. S. Gelles, "Analysis of the Helium Halo Effect in Neutron Irradiated Alloys," Damage Analysis and Fundamental Studies Quarterly Progress Report No. 4, DOE/ET-0065/5, p. 124, ibid., Reference 1.

6. H. Gieger, Proceedings of Royal Society of London, Series A, Volume 83 (1910) pp. 505-515.

7. H. Gaus, H. Migge and K. Mirus, "Implantation of Environmental Atoms Into Solids by Neutron Collision in Reactors," Rad. Effects 18 (1973) p. 79.

8. G. D. Johnson, C. W. Hunter, F. A. Garner, E. P. Lippincott, J. O. Schiffgens and H. Farrar, "Radial Helium Profiles in Fast Reactor Cladding," HEDL-SA-2068, March 1980.

9. H. Farrar IV, Rockwell International Technical Progress Reports, AI-ERDA-DOE-13181 and 13236.

10. H. Yamada, R. B. Poeppel, and R. H. Sevy, "Neutron-Induced Helium Implantation in GCFR Cladding," accepted for publication in Trans. ANS.

I. PROGRAM

Title: Irradiation Effects on Fusion Reactor Structural Materials
Principal Investigator: J. A. Sprague
Affiliation: Naval Research Laboratory

II. OBJECTIVE

The objectives of this work are to study the effects of composition on phase stability in titanium alloys and to study the effects of major element composition on the tensile properties of simple iron-nickel-chromium alloys.

III. RELEVANT DAFS PROGRAM PLAN TASK/SUBTASK

Task II.C.1 Effects of Material Parameters on Microstructure
Task II.C.7 Effects of Helium and Displacement on Flow
Task II.C.8 Effects of Helium and Displacement on Fracture

IV. SUMMARY

The AD-1 experiment was discharged from the EBR-II reactor after attaining peak fluences of 4 to 5 x 10^{22} n/cm^2 (E >0.1 MeV). The test contains transmission electron microscopy (TEM) specimens of a series of titanium alloys and tensile specimens of a series of simple iron-nickel-chromium ternary alloys. The capsule, irradiated at a design temperature of 500°C was opened and, after removal of the NaK, the Alloy Development for Irradiation Performance (ADIP) mechanical properties specimens (all of which are titanium alloys) showed evidence of corrosion. Consequently, the opening of the remaining two capsules has been delayed.

V. ACCOMPLISHMENTS AND STATUS

A. Status of the DAFS Specimens in the AD-1 Irradiation Test -- D. T. Peterson (HEDL) and J. A. Sprague (NRL)

1. Introduction

In July 1978 the AD-1 experiment was inserted in the EBR-II reactor. This test consists of three B-7c capsules designated B-284, B-285, and B-286. These are all isothermal capsules and were designed for irradiation temperatures of 394, 450, and 500°C, respectively. The DAFS portion of the experiment consists of a series of titanium alloys in the form of TEM disks and a series of simple iron-nickel-chromium ternary alloys in the form of tensile specimens.

2. Status

All three capsules have been removed from reactor and received at HEDL. Capsule B-284 (394°C) attained a peak fluence (at core midplane) of 4.2×10^{22} n/cm^2 (E >0.1 MeV) while capsules 8-285 (450°C) and B-286 (500°C) attained 5.0×10^{22} n/cm^2 (E >0.1 MeV).[1] The irradiation histories of these capsules are detailed in reference 1. Because of the limited available core space these capsules will not be reconstituted, as originally planned.

Capsule B-286 (500°C) was opened at HEDL. The ADIP mechanical properties specimens (all of which are titanium alloys) were observed to be corroded while the DAFS iron-nickel-chromium tensile specimens did not display any evidence of corrosion.[1] As the swelling packets in the capsule have not been examined, it is not known if the titanium alloy disks in them have also been corroded. The opening of the remaining two capsules has been delayed while the ADIP program studied the possible causes of the observed corrosion (see reference 1 for more details).

3. Specimen Matrix

The DAFS portion of the test is summarized in Tables 1 and 2 (additional details on these specimens can be found in reference 2). Two identical sets of TEM specimens were included in the test with a redundancy of three specimens within each set. A total of six tensile specimens were

TABLE 1

DAFS TEM SPECIMENS IN THE AD-1 TEST

Alloy	Thermomechanical Treatment*
Ti Sponge (High Purity)	800°C/2 hr/RC[+]
Ti Melt Control	800°C/2 hr/RC[+]
Ti-6Sn	800°C/2 hr/RC[+]
Ti-12Sn	800°C/2 hr/RC[+]
Ti-3A1	800°C/2 hr/RC[+]
Ti-2V	700°C/4 hr/FC
Ti-4Nb	700°C/4 hr/FC
Ti-6Al-4V	Commercial 8-Anneal
Ti-6Al	1040°C/0.5 hr/RC + 720°C/2 hr/RC
Ti-6Al-10Nb	1040°C/0.5 hr/RC + 720°C/2 hr/RC
Ti-6Al-20Nb	1040°C/0.5 hr/RC + 720°C/2 hr/RC

* All heat treatments were performed in vacuum.

[+] RC = Rapid cool (furnace removed from furnace tube).

TABLE 2

DAFS TENSILE SPECIMENS* IN THE AD-1 TEST

Alloy	Thermomechanical Treatment[t]
E20 (Fe-25Ni-15Cr)	30% CW + 950°C/15 min/AC
E37 (Fe-35Ni-7.5Cr)	30% CW + 950°C/15 min/AC
E22 (Fe-35Ni-15Cr)	30% CW + 950°C/15 min/AC
E25 (Fe-35Ni-20Cr)	30% CW + 950°C/15 min/AC
E23 (Fe-45Ni-15Cr)	30% CW + 950°C/15 min/AC

* SS-1 type specimen: 1.75" long, 0.030" thick, 0.060" wide gage, 0.195" wide grip.

[t] All heat treatments were performed in vacuum.

loaded for each of the ternary alloys. As the tensile specimens were loaded approximately eight inches from the core midplane their fluences are slightly lower than for the TEM specimens, which were loaded within one inch of the core midplane.

VI. REFERENCES

1. R. J. Puigh and E. K. Opperman, "Examination of Titanium Alloy Specimens Irradiated in EBR-II," ADIP Quarterly Report, DOE/ET-0058/8 October-December, 1979.

2. J. A. Sprague and R. W. Powell, "DAFS Test Matrix for the EBR-II Reactor Experiment," DAFS Quarterly Report, DOE/ET-0065/3 July-September, 1978.

VII. FUTURE WORK

After the remaining two capsules have been opened, a scoping study will be initiated on the titanium alloy specimens.

I. PROGRAM

Title: Irradiation Effects Analysis
Principal Investigator: D. G. Doran
Affiliation: Hanford Engineering Development Laboratory

II. OBJECTIVE

The objective of this work is to study the combined effects of displacement damage and helium generation rate on the microstructures and properties of iron-nickel-chromium alloys.

III RELEVANT DAFS PROGRAM PLAN TASK/SUBTASK

Task II.C.1.1	Effects of Material Parameters on Microstructures
Task II.C.2.2	Effects of Helium on Microstructure
Task II.C.7.2	Effects of Helium and Displacements on Flow
Task II.C.8.2	Effects of Helium and Displacements on Fracture

IV. SUMMARY

Specimens provided by the DAFS program have been included in the Oak Ridge Research Reactor (ORR) experiment designated MFE-IV. The specimens are transmission electron microscopy (TEM) disks and tensile flats of several simple iron-nickel-chromium ternary alloys and TEM disks of the Alloy Development for Irradiation Performance (ADIP) Path B alloys (precipitation strengthened iron-nickel-chromium alloys). These materials were selected to study the effects of composition and microstructure on the irradiation response of iron-nickel-chromium alloys. The effect of helium production rate will be assessed by comparison with similar specimens irradiated in other reactors.

V. ACCOMPLISHMENTS AND STATUS

A. DAFS Specimen Matrix for the ORR MFE-IV Test -- D. T. Peterson and R. W. Powell (HEOL)

1. Introduction

The MFE-IV fusion materials experiment is scheduledto begin irradiation in the ORR in April, 1980. The test matrix consists of four irradiation temperatures: 300, 400, 500, and 600°C with fluences of 9, 20, 30, and 50 dpa. This is the first test in the ORR designed to be discharged for interim examination and subsequently reconstituted. These reconstitutions will provide the opportunity to add materials to the test that were not included in the original specimen matrix.

2. Specimen Matrix

The DAFS specimens included in the test are listed in Tables 1 and 2. The TEM disks were loaded with a redundancy of two specimens. Only two fluences were included for the tensile specimens, with a redundancy of three specimensfor alloys E20, E22, and E38 and a redundancy of two specimens for alloy E23. With future reconstitutions it will be possible to pick up a third fluence for the tensile specimens.

The first group of alloys in Table 1 are simple iron-nickel-chromium ternary alloys. In the relatively low helium environment of EBR-II swelling in these types of alloys is decreased by increased nickel content and increased by increased chromium content. If these trends are maintained in high helium environments, then this series of alloys will provide some interesting comparisons. The alloys with constant chromium and increasing nickel contents will have increasing helium production with decreasing swelling. The series of alloys with constant nickel and increasing chromium contents will have constant helium production with increasing swelling. In addition, some alloys with different nickel and chromium contents, such as E23 and E37, will have different helium productions with similar swelling. Along with comparisons with EBR-II data on these alloys from the Breeder

TABLE 1

DAFS TEM SPECIMENS IN THE MFE-IV TEST

Alloy	Thermomechanical Treatment
E19 (Fe-20Ni-15Cr)	30% CW + 950°C/15 min/AC
E20 (Fe-25Ni-15Cr)	30% CW
E20	30% CW + 950°C/15 min/AC
E21 (Fe-30Ni-15Cr)	30% CW + 950°C/15 min/AC
E37 (Fe-35Ni-7.5Cr)	30% CW + 950°C/15 min/AC
E22 (Fe-35Ni-15Cr)	30% CW
E22	30% CW + 950°C/15 min/AC
E38 (Fe-35Ni-20Cr)	30% CW + 950°C/15 min/AC
E23 (Fe-45Ni-15Cr)	30% CW + 950°C/15 min/AC
AISI 316 (N-Lot)	1050°C/2 min/AC + 20% CW
B1	30% CW + 1025°C/5 min/AC + 750°C/8 hr/AC
B2	30% CW + 1025°C/5 min/AC + 800°C/8 hr/AC
B3	30% CW + 1025°C/5 min/AC + 750°C/8 hr/AC
B4	30% CW + 1025°C/5 min/AC + 850°C/3 hr/AC + 720°C/8 hr/FC to 620°C/10 additional hrs/AC

TABLE 2

DAFS TENSILE SPECIMENS* IN THE MFE-IV TEST

Alloy	Thermomechanical Treatment
E20	40% CW + 950°C/15 min/AC
E22	40% CW + 950°C/15 min/AC
E38	40% CW + 950°C/15 min/AC
E23	40% CW + 950°C/15 min/AC

* SS-2 type specimens: 1.25" long, 0.100" wide grip, 0.040" wide gage, 0.010" thick.

Reactor Program, this series of alloys will provide a means of studying the effects of helium production rate on swelling. Two of the alloys were included in the cold worked condition to determine the effect of pre-existing dislocations on their irradiation response. Specimens from the N-lot heat (87210) of AISI 316 were included as a control for comparison with the extensive data base already available on this heat of material.

Tensile specimens of some of the ternary alloys (Table 2) were included to permit comparison of changes in microstructure with changes in tensile properties. Comparison with specimens irradiated in the AD-1 test[1] will provide an assessment of the influence of helium production rate on the mechanical properties of these alloys.

The second group of specimens consists of four of the ADIP Path B alloys in solution treated and aged conditions (Table 1). Alloys B1 and B2 are molybdenum modified γ' strengthened alloys, B3 is a niobium modified γ' strengthened alloy, and B4 is a γ'/γ'' strengthened alloy. These alloys were included to study the stability and helium trapping characteristics of different precipitate phases in precipitation strengthened iron-nickel-chromium alloys. By comparison with similar specimens planned to be irradiated in HFIR, it will be possible to assess the influenceof helium production rate on the response of these alloys.

VI. REFERENCES

1. D. T. Peterson and J. A. Sprague, "Status of the DAFS Specimens in the AD-1 Irradiation Test," this report.

VII. FUTURE WORK

The first discharge of the MFE-IV experiment is planned for April, 1981. Prior to that time, specimens will be fabricated for the subsequent reconstitution of the test. Examination of selected specimens will be ini-, tiated shortly after the discharge.

I. PROGRAM

Title: Irradiation Effects Analysis
Principle Investigator: D. G. Doran
Affiliation: Hanford Engineering Development Laboratory

II. OBJECTIVE

The objective of this work is to assess the effect of irradiation environment on the irradiation response of simplified counterparts to the Path A and Path B alloys.

III. RELEVANT DAFS PROGRAM TASK/SUBTASK

Task II.C.l Effects of Material Parameters on Microstructure

IV. SUMMARY

Solid solution and precipitation strengthened iron-nickel-chromium model alloys have been selected and ordered. These model alloys are simplified versions of representative Path A and Path B alloys which are under development in the Alloy Development for Irradiation Performance (ADIP) program. They are intended to be irradiated in different reactor environments in order to study the effect of neutron flux-spectrum on phase stability and microstructural evolution. Completed round bar stock (1.31" diameter) is expected to be available in May 1980.

V. ACCOMPLISHMENTS AND STATUS

A. Path A and Path B Model Alloys -- D. T. Peterson and R. W. Powell (HEDL)

1. Introduction

Three classifications of materials are included in the DAFS program; representative alloys, model alloys, and mechanistic alloys. The representative alloys consist of selected alloys from each of the ADIP alloy paths. These alloys are intended to assess the effect of neutron environment on the phase stability and microstructural response of complex alloys. The model alloys are simplified counterparts to the representative alloys. By eliminating minor element additions in the model alloys, complex phase stability effects should be minimized. As with the representative alloys the model alloys will be used to study spectral effects. The mechanistic alloys are any alloys designed to study specific mechanisms.

2. Model Alloys

The representative Path A alloys are the MFE heat of 316 and the PCA (Ti modified 316). The Path A model alloys are designated MA1 and MA2. Alloy MA1 is a simple ternary alloy (Fe-20Ni-15Cr) and MA2 is a simple solid solution strengthened alloy (Fe-20Ni-15Cr-2Mo).

The representative Path B alloys are B2 (molybdenum modified γ' strengthened), B3 (niobium modified γ' strengthened) and B4 (γ'/γ'' strengthened). The Path B model alloys are designated MB1, MB2, MB3, and MB4. Alloys MB1 and MB4 have the same base compositions as alloys B1 and B4, respectively (the Si, Mn, B, and Zr additions have been deleted). Alloy MB2 has a lower molybdenum content than MB1, hence an increased γ'/γ misfit. Comparisons between MB1 and MB2 will make it possible to study the effect of the γ'/γ misfit on γ' redistribution and helium trapping. Besides not having the minor element additions, alloy MB3 has a slightly lower niobium content than B3. These changes will make MB3 less susceptible to Laves (Fe_2Nb) precipitation than B3.

3. Status

Two four inch diameter ingots of each of the six model alloys have been produced. Virgin materials were used for the melt stock. The

ingots were produced by vacuum induction melting followed by consumable electrode vacuum - arc remelting. The twelve ingots are currently being fabricated into 1.31" diameter round bar stock. One inch thick slices from the ingots have been received at HEDL and are available for specimen fabrication.

VI. FUTURE WORK

These alloys will be included in future DAFS irradiations

DISTRIBUTION

uc-20 (122)

uc-2oc (80)

DOE/RRT-HQ (7)
Mail Stop B-107
Washingtbn, OC 20545

Asst Director, Materials Tech
NA Oavies
JF Decker
PB Hemmig
KG Moses
RE Price
FT Scott

DOE/RL (3)
Richland, WA 99352

WA Burns
GM Chenevert
LA Pasquini

Argonne National Laboratory (4)
9700 South Cass Avenue
Argonne, IL 60439

L. R. Greenwood
A. Taylor
APL Turner
H. Wiedersich

Brookhaven National Laboratory
Associated Universities
Upton, NY 11973

Chairman, Nuclear Energy Dept

Columbia University
Plasma Physics Laboratory
New York, NY 10027

R. A. Gross

General Atomics Company (2)
P.O. Box 81608
San Diego, CA 92138

GR Hopkins
0. Stevenson

Lawrence Livermore Laboratory (2)
Universitv of California
P.O. Box 808
Livermore, CA 94550

MW Guinan
CM Logan

Los Alamos Scientific Laboratory (3)
University of California
P.O. Box 1663
Los Alamos, NM 87544

OJ Oudziak
CR Emigh
W. Green

Massachusetts Institute of Technology
Cambridge, MA 02139

L. Lidsky, Nuclear Engineering Dept

McDonnell-Douglas Astronautics
P.O. Box 516
St. Louis, MO 63166

D. Kummer

Mound Laboratory
P.O. Box 32
Miamisburg, OH 45342

Manager, Tech Appl and Development

National Bureau of Standards
Gaithersburg, MD 20760

CD Bowman

Naval Research Laboratory (2)
Metallurqy Division, Code 6390
Washington, DC 20375

I. Manning
JA Sprague

North Carolina State University
Department of Nuclear Engineering
Raleigh, NC 26707

JR Beeler, Jr.

Oak Ridge National Laboratory (7)
P.O. Box X
Oak Ridge, TN 37830

Director, Thermonuclear Div, (Bldg 9201-2)
RJ Colchin, Bldg 9201-2
FG Perey
M. Roberts, Bldg 9204-1
JO Stiegler
C. Weisbin
FW Wiffen

Pacific Northwest Laboratory (4)
P.O. Box 999
Richland, WA 99352

JL Brimhall
T. Chikalla
AB Johnson
LC Schmid

Princeton University (2)
Plasma Physics Laboratory
Forrestal Campus
P.O. Box 451
Princeton, NJ 08540

C. Osgood
K. Wakefield

Rockwell International Energy Systems
8900 DeSoto Avenue
Canoga Park, CA 91304

D. Kramer

Sandia Laboratories (2)
Albuquerque, NM 87115

FL Vook (2)

Sandia Laboratories
Livermore, CA 94550

WD Wilson

University of Michigan
Nuclear Engineering Department
Ann Arbor, MI 48105

T. Kammash

University of Virginia
Charlottesville, VA 22901

WA Jesser

University of Wisconsin
1500 W. Johnson Drive
Madison, WI 53706

P. Wilkes

Westinghouse R&D Center (2)
Beulah Road
Pittsburgh, PA 15234

HR Holland
JA Spitznagel

HEDL (38)

HR Brager	W/A-57	DL Johnson	W/A-4	RE Schenter	W/A-5
WL Bunch	W/C-47	FM Mann	W/A-5	FA Schmittroth	W/A-5
LL Carter	W/C-47	WN McElroy	W/C-39	WF Sheely	W/C-44
BA Chin	W/A-58	GH Moulthrop	W/C-115	RL Simons	W/A-57
DG Doran (5)	W/A-57	RE Nygren	W/A-58	AL Trego	W/E-15
EA Evans	W/JAD-6	EK Opperman	W/A-58	GL Wire	W/A-58
FA Garner	W/A-57	NF Panayotou	W/A-53	HH Yoshikawa	W/A-62
DS Gelles	W/A-58	EF Parker	W/E-18	Central Files (5)	W/C-110
R. Gold	W/C-39	RW Powell	W/A-57	Publ Services (2)	W/C-115
HL Heinisch	W/A-57	RJ Puigh	W/A-58		